

Freestanding Ultrathin Nanomembranes as Sample Supports for Structural Studies

Inauguraldissertation

zur
Erlangung der Würde eines Doktors der Philosophie
vorgelegt der
Philosophisch-Naturwissenschaftlichen Fakultät
der Universität Basel

von

Nadia Linda Lengweiler
aus Polen

Originaldokument gespeichert auf dem Dokumentenserver der Universität Basel

<https://edoc.unibas.ch>



Dieses Werk, ausgenommen Kapitel 1, ist unter dem Vertrag Creative Commons Namensnennung
– Keine kommerzielle Nutzung – Weitergabe unter gleichen Bedingungen 4.0 International
(CC BY-NC-SA 4.0) lizenziert.

Die vollständige Lizenz kann unter creativecommons.org/licenses/by-nc-sa/4.0 eingesehen werden.

Basel 2021

Genehmigt von der Philosophisch-Naturwissenschaftlichen
Fakultät

auf Antrag von

Prof. Dr. Henning Stahlberg (Fakultätsverantwortlicher)
Prof. Dr. Timm Maier (Co-Referent)

Basel, den 16. October 2018

Prof. Dr. Martin Spiess, Dekan

in memory of Joanna Roga
(1987-2014),
my high school chemistry class friend

“Jedno wiem, jedno jest pewne,
W nieskończoności tajemniczej
Muszą się spotkać - na to liczę,
Nawet równoległe”.

“I know one thing, I am sure about this one:
In the mysterious infinity
They have to meet each other, in fact, I count on it,
even parallel lines”.

From lyrics of the song “Równoległe “ (“Parallel lines”)



Summary

This thesis, entitled: “Freestanding ultrathin nanomembranes as sample supports for structural studies” reports on ultrathin films that have been investigated, developed and applied for fixing biological material (as protein crystals or single molecules) for experiments at synchrotrons, X-ray free electron lasers (XFELs) or in electron microscopes.

When utilized at XFELs these ultrathin membranes with the specimen serve as so-called: “fixed targets” a type of sample delivery system, an alternative to the commonly used liquid jets, initially developed for serial femtosecond crystallography (SFX). The main advantage of the fixed target approach is the possibility of the precise positioning of the sample in relation to the X-ray beam, which in ideal cases can provide 100% hit rate during diffraction data collection.

Low-dose X-ray fluorescence detection of metal markers localized onto the membrane supporting sample can additionally improve the precision and facilitate automation of the data acquisition in SFX, especially on non-regularly and non-uniformly distributed specimens.

Protein crystalline material can be either directly grown on the solid support, as demonstrated by using a model system on silicon nitride membranes on silicon chips or deposited from an aqueous suspension as well as lipidic cubic phase, alternatively another viscous matrix.

Relatively large *in situ* grown lysozyme crystals sandwiched between two X-ray transparent windows in microfabricated wells served as a sample for studying damage processes at the femtosecond scale in pump/probe measurements with split-and-delay X-ray optical setup.

Further development of two-dimensional materials towards increased performance especially should consider: the requirement of robust mechanical stability, high transparency to the radiation used in the structural study as well as compatibility of their physicochemical properties when preserving the native state of the investigated bio-material.

Keywords: freestanding ultrathin nanomembranes, X-ray free electron lasers, fixed targets, electron microscopy, diffraction, protein crystallography, JUNGFRU detector, self-assembly, 2D materials



Contents

Thesis Overview.....	A
Introduction to freestanding ultrathin nanomembranes.....	i
1. Direct protein crystallization on ultrathin membranes for diffraction measurements at X-ray free electron lasers.....	1
Abstract.....	2
1.1. Introduction.....	2
1.2. Experimental details.....	4
1.2.1. Microfabrication.....	4
1.2.2. Crystallization setup.....	6
1.2.3. Automatic deposition of the crystallization solutions.....	7
1.2.4. Screening crystallization conditions on the chip.....	7
1.2.5. Sandwich assembly.....	8
1.2.6. Structure refinement from the synchrotron diffraction data collected on <i>in situ</i> grown crystals.....	8
1.3. Results and discussion.....	9
1.3.1. Chip design.....	9
1.3.2. <i>In situ</i> crystallization.....	10
1.3.3. Multiwell silicon chips for screening crystallization conditions.....	11
1.3.4. Crystals from automated nanoliter dispensation.....	11
1.3.5. Crystal growth optimization for time-resolved measurements at the FEL.....	12
1.3.6. Assessment of <i>in situ</i> grown crystal quality by synchrotron radiation.....	15
1.3.7. Sample preparation for time-resolved measurements and the collection of diffraction data.....	16
1.4. Conclusions and outlook.....	17
1.5. Accession code.....	19
2. Demonstration of femtosecond X-ray pump X-ray probe diffraction on protein crystals.....	20
Abstract.....	21
2.1. Introduction.....	21
2.1.1. Protein crystallography as one of the XFELs' applications.....	21
2.1.2. Radiation damage mechanisms in protein crystals.....	22
2.1.3. Experimental approaches to radiation damage at XFELs.....	22
2.2. Experimental and computational methods.....	24
2.2.1. Experimental setup and diffraction geometry.....	24
2.2.2. Crystalline protein sample delivery.....	26
2.2.3. Pump-multiprobe femtosecond data collection.....	27
2.2.4. Procedure for calculating line profiles of diffraction intensities.....	28
2.3. Results and discussion.....	29

2.3.1. Estimation of the dose on the exposed crystals.....	29
2.3.2. Diffraction data collection.....	29
2.3.3. Data analysis.....	32
2.4. Conclusions.....	35
3. X-ray fluorescence detection for serial protein crystallography using a JUNGFRÄU pixel detector.....	38
Abstract.....	39
3.1. Introduction.....	39
3.2. Materials and Methods.....	41
3.2.1. Synchrotron data collection of fluorescence maps.....	42
3.2.2. Synchrotron data collection of absorption-edge scans.....	43
3.2.3. XFEL data collection of fluorescence maps.....	43
3.3. Results and discussion.....	44
3.3.1. Choice of data-collection parameters.....	44
3.3.2. Fluorescence maps.....	44
3.3.2.1. Scanning maps on model samples.....	44
3.3.2.2. Influence of collection parameters on model samples.....	45
3.3.2.3. Scanning maps on real-life samples.....	49
3.3.2.4. Precision of position determination.....	51
3.3.3. Absorption-edge scans.....	53
3.4. Conclusions.....	54
3.5. Related literature	
4. Supramolecular architectures of molecularly thin yet robust free-standing layers.....	56
Abstract.....	57
4.1. Introduction.....	57
4.2. Results and discussion.....	58
4.3. Conclusion.....	64
4.4. Materials and methods.....	65
4.4.1. Synthesis of 5,11,17,23-tetramethylcyano-25,26,27,28-tetrapropoxy calix[4]arene.....	65
4.4.2. X-ray crystallography.....	65
4.4.3. Langmuir monolayer, BAM, and LS deposition experiments.....	66
4.4.4. Near-edge X-ray absorption fine spectroscopy.....	66
5. The bright future of freestanding ultrathin nanomembranes.....	68
5.1. Conclusions.....	68
5.2. Outlook.....	69
5.2.1. Slit silicon chip.....	70
5.2.2. Polymer-based membrane supports.....	70
5.2.3. Composite-based sample support.....	71
5.3. Closing remarks.....	73
References.....	75
List of abbreviations	
Acknowledgements	
Publications and meetings	
Appendices:	
A: Femtosecond phase-transition in hard X-ray excited bismuth.....	I
B: Supporting information for the Chapter 1.....	XVII
C: Supporting information for the Chapter 2.....	XXVIII
D: Supporting information for the Chapter 3.....	XXXVII
E: Supporting information for the Chapter 4.....	LV



Overview

“Better to do something good and be late than bad and be early”
Elon Musk

The main aim of this dissertation is to summarize investigations conducted on the application of freestanding ultra-thin films as solid supports (a.k.a. fixed targets) for the biologically relevant samples. Diffraction-based measurements using large-scale facilities like synchrotrons, free-electron lasers as well as transmission electron microscopes are the selected methods covered in this thesis.

Introduction

Chapter 1 entitled: “Direct protein crystallization on ultrathin membranes for diffraction measurements at X-ray free electron lasers”, describes *in situ* crystallization on the silicon nitride membranes in silicon chip using lysozyme as a model system. Crystalline sample size and density together with preparation strategy was optimized for serial, room temperature diffraction data collection at synchrotrons and FELs.

Own contribution: design and microfabrication of supports, crystallization tests and production final optimized samples, development of the enclosure system, dehydration protection for the crystals (asymmetric sandwich), writing the manuscript.

Chapter 2 entitled: “Demonstration of femtosecond time-resolved X-ray diffraction on protein crystals”, presents femtosecond time-scale diffraction dynamics measurements in pump/probe mode using X-ray optics-based split-and-delay line on protein crystals prepared as described in chapter 1.

Own contribution: crystalline protein sample preparation, fabrication support membranes for X-ray optical gratings, participation in the assembly of the set-up and the diffraction data collection at the XCS

endstation of the X-ray Free-electron Laser LCLS, data analysis, evaluation and interpretation, writing the manuscript.

Chapter 3 entitled: “X-ray fluorescence detection for serial macromolecular crystallography using a JUNGFRÄU pixel detector”, describes development of the fiducial metallic markers for crystal localization before diffraction data collection at synchrotrons and XFELs. The applied method takes advantage of low-dose detection of heavy elements by X-ray fluorescence.

Own contribution: design and fabrication of the test samples, including iterative improvements; assembly of the final samples with protein crystals, writing M&M section of the manuscript, comments and corrections on the full text.

Chapter 4 entitled “Supramolecular architectures of molecularly thin yet robust free-standing layers”, reports on formation of free-standing, 2-dimensional, crystalline thin films based on calixarenes. Dipole-dipole interactions between the molecules provide stability of the material. Several methods, including X-ray crystallography, XPS, NEXAFS, AFM, TEM imaging and electron diffraction (ED) gives detailed description of the investigated supramolecular organic network.

Own contribution: investigation initiation of the free-standing calixarene-based membranes formation process, TEM imaging (data collection and interpretation), analysis of the ED data, comments and corrections on the manuscript.

Chapter 5 gives an outlook and perspective for further possible, alternative investigations as well as development of the optimal solutions for the sample delivery utilizing a fixed target approach in the future of the project and concludes the thesis.

Appendix A supplementary manuscript: “Femtosecond phase-transition in hard x-ray excited bismuth”, reports on ultrafast melting of bismuth crystal (femtosecond range). Lattice phase transition was triggered by intense 5 keV X-ray pulses and followed via observation of the (111) Bragg peak reflection decay.

Own contribution: Preparation of support membranes for X-ray optical gratings and assembly of the setup at XCS endstation of LCLS (*cf.* Ch2), commented on the manuscript.

Appendix B Supporting information for the **Chapter 1**

Appendix C Supporting information for the **Chapter 2**

Appendix D Supporting information for the **Chapter 3**

Appendix E Supporting information for the **Chapter 4**



Intro

“All imperfection is easier to tolerate if served up in small doses.”
- Wisława Szymborska, poet, Nobel Lecture Stockholm 7.12.1996

An introduction to freestanding ultrathin nanomembranes

Structural studies of biologically relevant molecules aim to find their shape at the atomic, molecular and supramolecular level. Together with protein function and mechanisms of interactions, structural information is highly desirable for biologists allowing them to understand in detail the building blocks of life.

Sample preparation is a key component of any analytical procedure. The properties of the support placed underneath or around the biological material, which delivers the sample to be structurally investigated plays an important role in diffraction measurements as well as imaging.

Most of the difficulties in preparation of the samples for structural studies on ultrathin materials, ensure high signal-to-noise ratio, are related to intrinsic properties of these films: they are very fragile, brittle, and challenging to handle by hand/tweezers. They are also generally sensitive to irradiation by X-rays or the electron beam. Cooling down to cryogenic temperatures of the specimen reduces the impact of radiation damage; however, this puts additional requirements on the sample support to withstand low temperatures. This usually makes ultrathin films even more brittle and possibly alters other, desired properties of the material like conductivity. Processes that require micro- (or nano-) fabrication and cleanroom conditions are expensive. However, mass-fabrication protocols once established, reduce the production costs of the sample support. Considering all of the above issues, selection of the optimal solution for sample delivery is non-trivial.

A new era in structural biology and protein crystallography started when X-ray free electron lasers came into operation [1], as these provide an intense source of X-rays that facilitates data collection in the “diffract-

before-destroy” regime and the possibility to investigate the ultra-fast dynamics of biomacromolecules using X-ray diffraction [I2].

Sample delivery methods for XFEL

Initially, so-called liquid jets providing hydrated streams of nanocrystals were developed and widely used as the main sample delivery method [I3]. This concept was followed by improvements of the injectors used in bringing protein crystals surrounded by much more viscous media [I4], like lipidic cubic phase or grease in a slower, well-controlled manner to the interaction spot with the X-ray beam. Conveyor belts with thin film tapes [I5], static mixers of mix-and-inject concept for diffusion-induced reactions [I6-I8] or lab on the chip drop ejection methods [I9] can be also employed in the experiments of specific requirements.

Alternatively, the development of the fixed-target approach included tests with silicon [I10] and silicon nitride-based technology [*cf.* Chapter 1]. Materials that are less brittle and easier to fabricate, but with less precision such as COC, Kapton foils, PDMS, or polycarbonate chips were also used [I11]. Amorphous materials give diffused signals and increase the detected noise, whereas the positions of reflections in the background from crystalline membranes can be easily predicted in reciprocal space and filtered out from the diffraction data or completely avoided (*e.g.* the case of silicon, graphene films [I12]) if located in low q (high resolution) range.

Thin films for transmission electron microscopy

Silicon nitride membranes over silicon frame assembled in a microfluidic chip [I13] have been reported before, especially for the samples in aqueous solutions in transmission electron microscopy (TEM) studies, as a so-called “nanoaquarium” approach. Other, commonly used materials as support films for biological TEM to date [I14] are: amorphous carbon (used as easy to prepare, continuous ultrathin film, or thicker, and holey/lacey/quantifoil[®] form with regularly placed openings – beneficial when automatic data collection performed), pristine graphene as a film [I15] or encapsulating material (*e.g.* graphene cell [I16]), graphene oxide, carbon-based nanomembranes [I17], metallic alloys, *e.g.* $\text{Ti}_{88}\text{Si}_{12}$ (due to its high electrical conductivity) [I18] or doped silicon carbide. Recent studies also include a novel method applying self-blotting gold nanowire grids which can produce even, thin, vitreous ice and improvement in overcoming preferred particle orientation crucial for data completeness of macromolecules in imaging and diffraction mode [I19-I20].

Different properties of ultrathin film materials

The thin films employed in structural studies can have different properties, belong to different types of materials: organic/inorganic, hydrophilic/hydrophobic, conductive (electric, thermal)/insulators; can be a monolayer of 2D material or form a composite, amorphous or crystalline. These parameters have to be carefully selected to match the desired properties of the sample support for structural studies, like stability, transparency and the most importantly, for it to be compatible with the investigated biomaterial.

References:

- [11] P. Ball, Europe's X-ray laser fires up. *Nature* **548**, 507-508 (2017).
- [12] B. D. Patterson, Crystallography using an X-ray free-electron laser. *Crystallography Reviews* **20**, 242-294 (2014).
- [13] U. Weierstall, Liquid sample delivery techniques for serial femtosecond crystallography. *Phil. Trans. R. Soc. B* **369**, 20130337 doi:10.1098/rstb.2013.0337 (2014).
- [14] U. Weierstall, D. James, C. Wang, T. A. White, D. Wang, W. Liu, J. C. H. Spence, R. Bruce Doak, G. Nelson, P. Fromme, R. Fromme, I. Grotjohann, C. Kupitz, N. A. Zatsepin, H. Liu, S. Basu, D. Wacker, G. Won Han, V. Katritch, S. Boutet, M. Messerschmidt, G. J. Williams, J. E. Koglin, M. Marvin Seibert, M. Klinker, C. Gati, R. L. Shoeman, A. Barty, H. N. Chapman, R. A. Kirian, K. R. Beyerlein, R. C. Stevens, D. Li, S. T. A. Shah, N. Howe, M. Caffrey, & V. Cherezov, Lipidic cubic phase injector facilitates membrane protein serial femtosecond crystallography. *Nat. Commun.* **5**, 3309 doi:10.1038/ncomms4309 (2014).
- [15] F. D. Fuller, S. Gul, R. Chatterjee, E. S. Burgie, I. D. Young, H. Lebrette, V. Srinivas, A. S. Brewster, T. Michels-Clark, J. A. Clinger, B. Andi, M. Ibrahim, E. Pastor, C. de Lichtenberg, R. Hussein, C. J. Pollock, M. Zhang, C. A. Stan, T. Kroll, T. Fransson, C. Weninger, M. Kubin, P. Aller, L. Lassalle, P. Bräuer, M. D. Miller, M. Amin, S. Koroidov, C. G. Roessler, M. Allaire, R. G. Sierra, P. T. Docker, J. M. Glowonia, S. Nelson, J. E. Koglin, D. Zhu, M. Chollet, S. Song, H. Lemke, M. Liang, D. Sokaras, R. Alonso-Mori, A. Zouni, J. Messinger, U. Bergmann, A. K. Boal, J. M. Bollinger Jr, C. Krebs, M. Högbom, G. N. Phillips Jr, R. D. Vierstra, N. K. Sauter, A. M. Orville, J. Kern, V. K. Yachandra & J. Yano, Drop-on-demand sample delivery for studying biocatalysts in action at X-ray free-electron lasers. *Nat. Methods* **14**, 443-449 doi:10.1038/nmeth.4195 (2017).
- [16] C. Kupitz, J. L. Olmos Jr., M. Holl, L. Tremblay, K. Pande, S. Pandey, D. Oberthür, M. Hunter, M. Liang, A. Aquila, J. Tenboer, G. Calvey, A. Katz, Y. Chen, M. O. Wiedorn, J. Knoska, A. Meents, V. Majriani, T. Norwood, I. Poudyal, T. Grant, M. D. Miller, W. Xu, A. Tolstikova, A. Morgan, M. Metz, J. M. Martin-Garcia, J. D. Zook, S. Roy-Chowdhury, J. Coe, N. Nagaratnam, D. Meza, R. Fromme, S. Basu, M. Frank, T. White, A. Barty, S. Bajt, O. Yefanov, H. N. Chapman, N. Zatsepin, G. Nelson, U. Weierstall, J. Spence, P. Schwander, L. Pollack, P. Fromme, A. Ourmazd, G. N. Phillips Jr. & M. Schmidt, Structural enzymology using X-ray free electron lasers. *Struct. Dyn.* **4**, 044003 (2017).
- [17] G. D. Calvey, A. M. Katz, C. B. Schaffer & L. Pollack, Mixing injector enables time-resolved crystallography with high hit rate at X-ray free electron lasers. *Struct. Dyn.* **3**, 054301 (2016).
- [18] J. L. Olmos Jr., S. Pandey, J. M. Martin-Garcia, G. Calvey, A. Katz, J. Knoska, C. Kupitz, M. S. Hunter, M. Liang, D. Oberthür, O. Yefanov, M. Wiedorn, M. Heyman, M. Holl, K. Pande, A. Barty, M. D. Miller, S. Stern, S. Roy-Chowdhury, J. Coe, N. Nagaratnam, J. Zook, J. Verburgt, T. Norwood, I. Poudyal, D. Xu, J. Koglin, M. H. Seaberg, Y. Zhao, S. Bajt, T. Grant, V. Mariani, G. Nelson, G. Subramanian,

- E. Bae, R. Fromme, R. Fung, P. Schwander, M. Frank, T. A. White, U. Weierstall, N. Zatsepin, J. Spence, P. Fromme, H. N. Chapman, L. Pollack, L. Tremblay, A. Ourmazd, G. N. Phillips Jr & M. Schmidt, Enzyme intermediates captured “on the fly” by mix-and-inject serial crystallography. *BMC Biol.* **16**, 59 (2018).
- [19] C. G. Burton, D. Axford, A. M. J. Edwards, R. J. Gildea, R. H. Morris, M. I. Newton, A. M. Orville, M. Prince, P. D. Topham & P. T. Docker, An acoustic on-chip goniometer for room temperature macromolecular crystallography. *Lab Chip* **17**, 4225-4230 doi: 10.1039/c7lc00812k (2017).
- [110] P. Roedig, I. Vartiainen, R. Duman, S. Panneerselvam, N. Stübe, O. Lorbeer, M. Warmer, G. Sutton, D. I. Stuart, E. Weckert, C. David, A. Wagner, & A. Meents, A micro-patterned silicon chip as sample holder for macromolecular crystallography experiments with minimal background scattering. *Sci. Rep.* **5**, 10451 (2015).
- [111] S. Muniyappan, S. O. Kim & H. Ihee, Recent advances and future prospects of serial crystallography using XFEL and synchrotron X-ray sources. *Biodesign* **3**, 98-110 (2015).
- [112] C. Seuring, K. Ayyer, E. Filippaki, M. Barthelmess, J.-N. Longchamp, P. Ringler, T. Pardini, D. H. Wojtas, M. A. Coleman, K. Dörner, S. Fuglerud, G. Hammarin, B. Habenstein, A. E. Langkilde, A. Loquet, A. Meents, R. Riek, H. Stahlberg, S. Boutet, M. S. Hunter, J. Koglin, M. Liang, H. M. Ginn, R. P. Millane, M. Frank, A. Barty & H. N. Chapman, Femtosecond X-ray coherent diffraction of aligned amyloid fibrils on low background graphene. *Nat. Comm.* **9**, 1836 (2018).
- [113] J. M. Grogan & H. H. Bau, *In Situ* Liquid Cell TEM/STEM with the Nanoaquarium. *Microsc. Microanal.* **17**, 532-533 (2011).
- [114] D. Rhinow, Nanomembranes for biological transmission electron microscopy. Chapter 6, in *Nanobiotechnology in Energy, Environment, and Electronics*, Pan Stanford Series on Nanobiotechnology ed. C. Nicolini, 137-153 CRC Press Taylor & Francis Group (2015).
- [115] R. R. Nair, P. Blake, J. R. Blake, R. Zan, S. Anissimova, U. Bangert, A. P. Golovanov, S. V. Morozov, A. K. Geim, K. S. Novoselov & T. Latychevskaia, Graphene as a transparent conductive support for studying biological molecules by transmission electron microscopy. *Appl. Phys. Lett.* **97**, 153102 (2010).
- [116] D. J. Kelly, M. Zhou, N. Clark, M. J. Hamer, E. A. Lewis, A. M. Rakowski, S. J. Haigh & R. V. Gorbachev, Nanometer Resolution Elemental Mapping in Graphene-Based TEM Liquid Cells. *Nano Lett.* **18**, 1168-1174 (2018).
- [117] A. Turchanin & A. Götzhäuser, Carbon nanomembranes from self-assembled monolayers: Functional surfaces without bulk. *Prog. Surf. Sci.* **87**, 108–162 (2012).
- [118] D. Rhinow & W. Kühlbrandt, Electron cryo-microscopy of biological specimens on conductive titanium-silicon metal glass films. *Ultramicroscopy* **108**, 698-705 (2008).
- [119] H. Wei, V. Dandey, Z. Zhang, A. Raczkowski, B. Carragher & C. S. Potter, Self-blotting nanowire grids for cryo-EM sample preparation. *Microsc. Microanal.* **23**, 848-849 (2017).
- [120] V. P. Dandey, H. Wei, Z. Zhang, Y. Zi Tan, P. Acharya, E. T. Enga, W. J. Rice, P. A. Kahn, C. S. Potter, B. Carragher, Spotiton: New features and applications. *J. Struct. Biol.*, **202**, 161-169 (2018).



Chapter 1

“Every big crystal was once small”
from lecture at BZ, University of Basel, Prof. J. P. Abrahams

Direct protein crystallization on ultrathin membranes for diffraction measurements at X-ray free electron lasers

Nadia Opara^{a,b,c}, Isabelle Martiel^a, Stefan A. Arnold^{b,c}, Thomas Braun^{b,c}, Henning Stahlberg^{b,c}, Mikako Makita^a, Christian David^a, and Celestino Padeste^{a,c}

^a Paul Scherrer Institute (PSI), 5232 Villigen, Switzerland

^b Center for Cellular Imaging and NanoAnalytics (C-CINA), Biozentrum, University of Basel, 4058 Basel, Switzerland

^c Swiss Nanoscience Institute, University of Basel, 4056 Basel, Switzerland

Available online:

<http://scripts.iucr.org/cgi-bin/paper?S1600576717005799>

Journal of Applied Crystallography **50**, 909-918 (2017)

PDB reference: lysozyme, 5ne0

This article has supporting information, in this thesis as Appendix B.
Reproduced with permission of the International Union of Crystallography.

Synopsis: *In situ* protein crystallization on highly X-ray transparent nanomembranes and an application for the collection of diffraction data at free electron lasers.

Abstract

A new era of protein crystallography started when X-ray free-electron lasers (XFELs) came into operation, as these provide an intense source of X-rays that facilitates data collection in the ‘diffract-before-destroy’ regime. In typical experiments, crystals sequentially delivered to the beam are exposed to X-rays and destroyed. Therefore, the novel approach of serial crystallography requires thousands of nearly identical samples. Currently applied sample-delivery methods, in particular liquid jets or drop-on-demand systems, suffer from significant sample consumption of the precious crystalline material. Direct protein microcrystal growth by the vapour diffusion technique inside arrays of nanolitre-sized wells is a method specifically tailored to crystallography at XFELs. The wells, with X-ray transparent silicon nitride windows as bottoms, are fabricated in silicon chips. Their reduced dimensions can significantly decrease protein specimen consumption. Arrays provide crystalline samples positioned in an ordered way without the need to handle fragile crystals. The nucleation process inside these microfabricated cavities was optimized to provide high membrane coverage and a quasi-random crystal distribution. Tight sealing of the chips and protection of the crystals from dehydration were achieved, as confirmed by diffraction experiments at a protein crystallography beamline. Finally, the test samples were shown to be suitable for time-resolved measurements at an XFEL at femtosecond resolution.

1.1. Introduction

Detailed structural information on proteins and other biomacromolecules is crucial to understand biochemical processes and design new medicines. Several methods are routinely used to obtain such information, *e.g.* nuclear magnetic resonance (NMR) [1.1-1.3] electron microscopy (EM) [1.4-1.6] or X-ray diffraction [1.7-1.9]. X-ray free electron lasers (XFELs) are rapidly becoming an indispensable addition [1.10]. The latter provide ultrahigh peak brilliance of femtosecond short X-ray pulses, which allows the detection of diffraction signals from crystals much smaller than those studied at synchrotron sources, *i.e.*, even from nano- and 2-dimensional (2D) crystals [1.11-1.12]. This is made possible by outrunning radiation damage in the “diffract-before-destroy” regime: compared to synchrotrons, a much higher dose is applied in a time shorter than that of typical X-ray induced molecular rearrangement or damage processes, and the diffraction signals arising from one single X-ray pulse are collected. However, when a pulse of the extremely intense radiation interacts with the sample, the crystal is damaged and no longer diffracts, which means that it cannot be used again. Thus, data collection has to be carried out in a serial approach where femtosecond diffraction experiments are performed on a large number of individual protein crystals [1.13]. Adequately prepared samples containing thousands of crystals, each of which can be smaller than 1 μm , have to be delivered to the beam in a short time. To this end, injector-based methods for aqueous suspensions

[1.14] and lipidic cubic phase (LCP) [1.15] have been successfully applied to achieve this for both, soluble and membrane proteins, in order to determine their structure. These methods, however, in particular the liquid jets, require large amounts of sample in order to obtain full and conclusive datasets due to the high flow speed. In an ideal case, when crystals are embedded in a slow flowing viscous medium such as agarose or LCP prior to injection, a flow rate of 160 nl per min was required, while typical flow rates for aqueous suspensions can be up to 100 times higher [1.16-1.17].

Alternatively, samples are immobilized on solid supports. This “fixed target” approach has the advantage that it uses significantly less biological material and allows a visual pre-selection of target sites. In one of the first time-delay holography experiments with an XFEL, polystyrene spheres 140 nm in diameter, were deposited on 20 nm silicon nitride membranes present in a silicon chip backed by a multilayer-coated plane mirror to form a sandwich-like packaging, and used for femtosecond time-delay X-ray holography [1.18]. Since then, there have been numerous attempts to optimize the fixed target approach. In particular, deterioration of the sample upon drying and the transparency of the support material have to be considered. In addition, protein crystals are very fragile. They are prone to lose quality due to dehydration and require preservation or waterproof protection. The methods used to maintain crystal quality while diffraction data is collected include sugar-embedding, *e.g.*, using trehalose [1.19], Paraton-N oil coverage [1.20], vitrification [1.21], “sandwich” enclosure [1.22] or wrapping in watertight graphene sheets [1.23].

The microfabrication strategy used to obtain relatively transparent thin freestanding silicon nitride membranes in silicon frames is well-established and widely applied, as described, *e.g.*, by Gibb & Ayub [1.24]. Windows of this type, in some cases with an octadecyltrichlorosilane (OTS) coating, and windows of thin carbon film with a poly(methyl methacrylate) layer [1.25] were used for the collection of diffraction data of 2D crystals of membrane proteins embedded in sugar [1.26]. Zarrine-Afsar *et al.* deposited concentrated suspensions of lysozyme and ferritin 3D crystals onto silicon nitride membranes for XFEL experiments [1.27]. Microfabricated silicon chips combined with a Mylar foil backing were also described as suitable for visual inspection as well as high-speed spectroscopy mapping for red myoglobin crystals [1.28]. Development towards full automation of the serial data collection has been shown with X-CHIP designs [1.29]. Goniometer-based serial femtosecond crystallography on polymeric meshes and grids has been also reported [1.30] as example of helical and raster scanning data-collection strategies avoiding XFEL exposure of a previously exposed sample area.

Recently, supports that allow the fixed target XFEL analysis of 3D microcrystals deposited in small wells [1.31-1.33] or enclosed in between thin polymer films [1.34-1.36] were developed. A microfluidic system that allows microcrystals grown elsewhere to be harvested and directly examined in an array of hydrodynamic traps is also available and provides an efficient way to capture individual crystals at defined positions [1.37].

Large 3D protein crystals can be obtained by various standard methods, *e.g.*, crystallization in gels [1.38], under microgravity [1.39] or by seeding [1.40]. The growth of crystals directly on the support subsequently placed in the FEL beam would be particularly attractive for 2D protein crystals, as these are easily deteriorated when handled. Such samples have been employed for atomic force microscopy (AFM) and EM studies. For example, 2D streptavidin crystals were grown on mica surfaces covered by phospholipids partially modified by biotin [1.41]; the morphology of the crystals obtained depended on the pH value of the mother liquid. Further, large (approximately 5 μm) 2D crystals and ultrathin 3D crystals of the H⁺-ATPase found in the plasma membrane of the red bread mould *Neurospora crassa* were grown directly on the surface of a carbon film supported gold-plated copper EM grid [1.42].

Here, we report the direct crystallization of proteins on silicon nitride nanomembranes for fixed target XFEL experiments. The design and microfabrication steps of silicon chips that can be used in combination with nanoliter-volume liquid handling systems are described. The growth of crystals by vapour diffusion methods on silicon nitride membranes and the use of a sealed asymmetric sandwich system developed to prevent crystals from drying before being probed by the XFEL beam are demonstrated. The described *in situ* crystal growth (as an example of the fixed target approach) is especially useful when large quantities of similar crystals are required, *e.g.*, for pump-probe experiments at XFELs. One specific aim of the crystallization experiments was to provide many crystals that are large enough to be hit in a split-delay X-ray optical setup for pump-probe experiments [1.43] by two sets of X-ray beams (pump-probe and reference) that respectively illuminate pumped and reference areas separated by approximately 70 μm .

1.2. Experimental details

1.2.1. Microfabrication

Single-crystal silicon <100> wafers, 240–260 μm in thickness and 100 mm in diameter, obtained by the Czochralski process (Si-Mat Silicon Materials, Germany) and polished on both sides, were covered with a 250 nm thick layer of low-stress amorphous silicon nitride grown by low-pressure chemical vapour deposition (CVD) (Centre de MicroNanoTechnologie, EPFL, Switzerland). Subsequently, a positive tone resist (S-1813, Microposit, USA) was spin-coated onto the silicon nitride layer on both sides of the wafer using a spin speed of 4000 rpm for 40 s and an initial ramp of 400 rpm/s. The deposited layer was soft-baked on a hot plate at 388 K for 90 s. The resist on one side of the wafer was then patterned [Fig. 1.1(a), part (i)] with the template for silicon nitride windows by a photolithography process (*cf.* Section 1.3.1. and Fig. BS1 in the supporting information). The regular pattern of squares was aligned with the cut primary flat of the wafer, which corresponds to the orientation of the crystal lattice planes and mounted in soft contact mode (*i.e.* no direct contact between the mask and the resist on the wafer) using

a mask aligner (MA6 Maskaligner, Karl Süss, Germany). The stack was exposed to UV light at a wavelength of 365 nm, 10 mW power. A multiple-exposure mode (2 x 10 s with a 15 s interval) was used to transfer the patterns from the specially designed polymeric photolithography mask (printed by Selba SA, Versoix, Switzerland) with a replication accuracy of 2 μm . Afterwards, the resist was developed in MF-321 solution (Microposit, USA) for 70 s, rinsed with water and dried in a stream of nitrogen [Fig. 1.1(a), part (i)]. In the next step, silicon nitride was completely removed from the areas not covered by the resist in a reactive-ion etching chamber (RIE 100, Oxford Instruments, UK) using fluorocarbon (CHF_3 , gas flow rate 40 s.c.c.m.; s.c.c.m. = standard cubic centimetre per minute) and oxygen (O_2 , gas flow rate 5 s.c.c.m.) as the process gases.

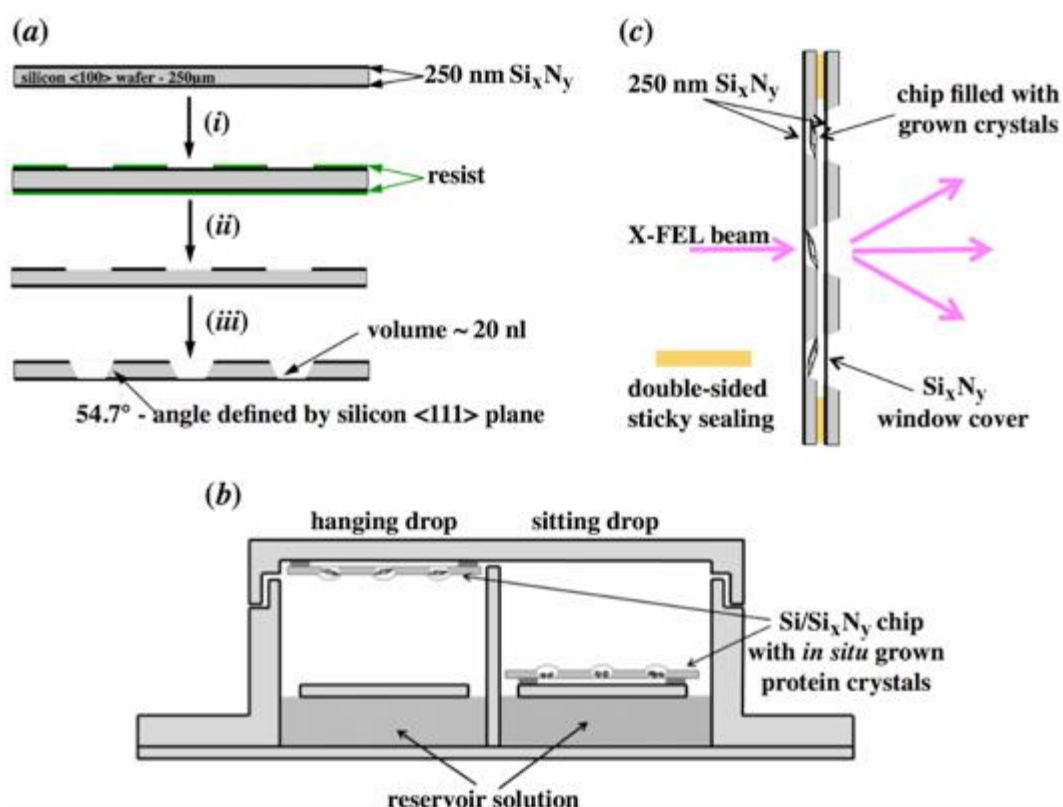


Figure 1.1 Microfabrication and use of a silicon chip with nanomembrane windows for serial crystallography. (a) The microfabrication steps carried out to obtain a **Multi-well Array Generated for *In situ* Crystallization (MAGIC)**: (i) photolithography to transfer a geometric pattern to a resist layer; (ii) reactive ion etching to form silicon nitride windows and resist removal in a solvent bath; (iii) potassium hydroxide etching to form thin silicon nitride membranes. (b) Setup for crystallization experiments on silicon nitride-membrane chips in the hanging-drop (left) and sitting-drop (right) arrangement. (c) The asymmetric sandwich assembly employed to protect crystals during XFEL (or synchrotron beamline) experiments. Note that the applied geometry allows wide-angle data collection; chips with larger membrane windows are used as lids.

An inductively coupled plasma was applied at a forward power of 800 W. Afterwards, the wafer was sequentially washed in filtered high-quality acetone (MOS PURANAL grade, Merck) and isopropanol (Micropur grade, Technic France) to remove the resist [Fig. 1.1(a), part (ii)]. Subsequently,

anisotropic wet etching was performed in 20% KOH solution at 353 K for approximately 3.5 h to form freestanding silicon nitride membranes [Fig. 1.1(a), part (iii)]. After this step, the wafer was immediately placed in water at 333 K and washed by soft agitation. All water used was of ultrapure quality (resistivity 18.2 M Ω *cm). The wafer was then washed in a fresh portion of water at 323 K, followed by 5 min in 10% hydrochloric acid (HCl) (diluted from 37% HCl, Sigma–Aldrich, Switzerland) at 313 K to avoid the formation of precipitates (contaminants) upon drying. Finally, the membranes were washed in water at room temperature and dried in a spin dryer (Polos SPIN150i/200i Infinite, SPS Europe BV, Netherlands) for 2 min at 500 rpm, or using a nitrogen gun with the gas stream running parallel to the membranes. Single chips were separated from the full wafer to form individual substrates by cleaving along fine lines that were included in the initial pattern on the lithography mask and created by partial etching into the wafer that took place during the anisotropic wet etching step (Fig. 1.1a).

1.2.2. Crystallization setup

The vapour diffusion method was employed to grow protein crystals *in situ* on the silicon nitride windows of the chips. Both sitting-drop (SD) and hanging-drop (HD) geometries were tested (Fig. 1.1b). Crystallization experiments were set up in double-bottomed transparent polymeric boxes (two-well μ -Slide, ibidi, Germany). All prepared solutions were kept on ice before deposition. A 200 mg ml⁻¹ stock solution of lysozyme from chicken egg white (AxonLab No. 9001-63-2, Switzerland) was prepared by gently agitating a suspension of the powder in water in a 1.5 ml Eppendorf tube by means of a pipette. The stock was diluted further with water to give concentrations ranging from 25 to 100 mg ml⁻¹.

A 20 μ l aliquot of the mixture of protein solution with precipitating agent (full details are given in Table BS1 in the supporting information) was pipetted onto the fenestrated chip (a 14 x 14 window array placed with 1 mm pitch) with square membranes of a = 100, 200, 300, 400 or 500 μ m in size and spread over all 196 wells with a cut pipette tip held by curved tweezers. To enable monitoring of crystal growth without the risk of the sample drying out or overheating (melting) in the microscope light, chips with deposited solutions were mounted on the inner part of the ibidi box lid (HD geometry) or base (SD geometry) and secured with Scotch tape at the corners.

A small spacer was used to ensure that the silicon nitride membranes did not come into direct contact with the box. This was either a rolled piece of Scotch tape or a small piece of silicon wafer (thickness 250 μ m) placed on a thin strip of the double-sided adhesive tape (thickness 100 μ m) fixed to the inner side of the crystallization chamber lid or base. Several chemical conditions were tested, including the addition of a few microlitres of 50% polyethylene glycol (PEG, Sigma–Aldrich) in H₂O or 100% ethylene glycol (EG, Sigma–Aldrich) to the aqueous lysozyme solution (full details are given in Table BS1 in the supporting information). A 1 ml aliquot of

reservoir solution (precipitating agent) prepared from 1 M sodium acetate (NaAc, Sigma–Aldrich) pH 4.5, 3 M sodium chloride (NaCl, Sigma–Aldrich) and water in the proportion 1:2:7, resulting in final concentrations of 0.1 M NaAc and 0.6 M NaCl, was pipetted at the very bottom of the ibidi boxes (Fig. 1b). After incubation for several hours to allow crystal growth, the chips were imaged with a Leica M205C stereo microscope (Mannheim, Germany).

1.2.3. Automatic deposition of the crystallization solutions

To have more control over the sample volume, a dispensing device equipped with a microcapillary nozzle and able to handle liquid volumes down to 5 nl [1.44] was used to deposit the sample in the individual wells of a silicon chip. To avoid evaporation of minute amounts of the deposited solutions, the silicon chip was placed on a temperature-controlled stage and cooled to the dew point of the environment during this process. Initially, 500 nl of the solution to be dispensed were aspirated by a dispensing nozzle (New Objective, USA, FS360-100-30, inner diameter 100 μm with a tapered tip of 30 μm diameter) with a flow rate of 1 $\mu\text{l}/\text{min}$. The wells, with volumes of about 20 nl, were filled either with 50:50 mixtures of an aqueous 50 mg/ml lysozyme solution and precipitating agent solution with the same composition as the reservoir solution above (0.1 M NaAc, 0.6 M NaCl, pH 4.5) or in sequential order (first with the protein and then with the precipitating agent solution or *vice versa*) with a deposition flow rate of 10 $\mu\text{l}/\text{min}$. Once loaded, the chips were mounted in a large VDX 24-well crystallization plate (Hampton Research) in the SD geometry and incubated at room temperature *versus* 0.5 ml of reservoir solution placed at the bottom of the plate wells. After several hours of incubation at room temperature, they were observed using a light microscope (Axiophot, Zeiss, USA) to assess crystal growth.

1.2.4. Screening crystallization conditions on the chip

To demonstrate the feasibility of using the silicon nitride membrane chips for screening experiments carried out to establish the optimal conditions for crystal growth, a chip with 500 μm x 500 μm membranes was loaded with the following lysozyme solutions: (i) lysozyme at a concentration of 50 mg ml^{-1} in 50 mM NaAc buffer pH 4.5; (ii) the solution in (i) plus 50% PEG aqueous solution and reservoir solution (0.1 M NaAc and 0.6 M NaCl pH 4.5) in the proportions 9:1:1; or (iii) lysozyme at a concentration of 50 mg ml^{-1} in H_2O . A pipette was used to deposit 8 μl aliquots of the solutions on the different regions of the chip. Each single drop covered approximately 25 wells. Once loaded, the chips were mounted in HD geometry in an ibidi box as described above, incubated *versus* 1 ml of reservoir solution and imaged after 8 h using a Leica ML95 light microscope (Mannheim, Germany) equipped with a Moticam 5.0 MP camera (Motic, Hong Kong).

1.2.5. Sandwich assembly

Double-sided 100 μm thick adhesion tape (Laminex spacer, Molecular Dimensions, MD11-50) was used to assemble asymmetric (contact well to membrane side) watertight chambers out of two chips. A thin adhesive frame (2 mm wide) was cut out of a continuous foil and placed on one side of one chip. This chip serving as a lid was first fixed, adhesive side up, on a cube of soft Styrofoam-like material (Hobbyatelier Brugg, Switzerland) using 400 μm thick needles inserted through 400 μm x 400 μm square orifices ('knockout' membranes; *cf.* Fig. BS1 in the supporting information) at its corners. A second grid was used for an SD or HD crystallization run. Once the run was complete, the second grid with crystals grown on its membrane was aligned to the lid using the needles and squeezed gently together around the frame with tweezers to form a sealed 'sandwich' (Fig. 1.1c).

1.2.6. Structure refinement from the synchrotron diffraction data collected on *in situ* grown crystals

Diffraction data from several lysozyme crystals prepared in HD geometry (*cf.* Table BS1 in the supporting information, chip 48) and enclosed in a sandwich were collected at room temperature on the X06SA PX-I beamline at the Swiss Light Source at the Paul Scherrer Institute, Switzerland, using a 40 μm x 20 μm beam at a wavelength of 1.00 Å. The full flux of 1.5×10^{12} photons s^{-1} was attenuated to 0.3% for data collection. Data were collected with an EIGER X 16M photon-counting detector placed 200 mm from the sample with a rotation of 0.1° per frame and exposure of 0.1 s per frame. Owing to geometric constraints, the total rotation range of the chip was limited to about 50°. Data from two individual crystals from one chip were merged to obtain a full data set. Data indexing was done with the program package XDS [1.45], and scaling and merging with XSCALE [1.46]. Structure solution was done by molecular replacement with the program MOLREP [1.47], using the Protein Data Bank (PDB) code 2lyz as search model. Structure refinement was done using REFMAC [1.48], BUSTER [1.49] and phenix.refine [1.50], and model validation using MOLPROBITY [1.51].

1.3. Results and discussion

1.3.1. Chip design

The chip layout (Fig. BS1 in the supporting information) was designed for serial femtosecond crystallography, which requires several hundreds to thousands of similarly placed crystals. A number of quality and microfabrication requirements influenced the final geometry of the chip.

The chip had to (i) be compatible with double-bottomed crystallization chambers (Fig. 1.1c), (ii) be strong enough to be handled manually during crystallization experiments and mounting in the XFEL beam, (iii) facilitate *in situ* crystallization, (iv) allow the microwells to be sealed by stacking two chips, and (v) enable fast shifts from window to window during data acquisition. Regarding these points, we found the following limitations: the geometry of the wells is defined by the anisotropic etching process and the angle between the crystallographic planes of the single-crystal silicon; in addition, the applied photolithographic process requires the application of sufficiently wide lines (at least 50 μm) between the patterned features, limiting the well density. For example, a minimal distance of 550 μm is required between the centres of 200 μm^2 windows in a 250 μm thick silicon wafer. Thinner wafers are much more difficult to handle during the microfabrication processes, as silicon is brittle and fragile. The overall size of the chips was 17 mm x 17 mm, so that they would fit into 20 mm x 20 mm crystallization chambers (Fig. 1.1b). They were patterned with fully symmetric arrays of 196 square-bottomed cavities (14 x 14) placed with a distance of 1 mm between the centres of the squares (Fig. BS1 in the supporting information). The microfabrication process started with polished silicon <100> wafers coated with a 250 nm thick layer of silicon nitride on both sides, and consisted of three major steps: (i) photolithography on the reverse of the wafer to define the pattern; (ii) reactive ion etching to transfer the pattern into the silicon nitride; and (iii) anisotropic wet etching in 20% KOH solution through the silicon wafer to create deep cavities defined by the thickness (250 μm) of the silicon wafer (Fig. 1.1a, and see Section 1.2.1). Their mechanically stable bottoms were formed by the remaining 30–250 nm thick amorphous low-stress and smooth silicon nitride layer. The square membranes had an area of 40 000–250 000 μm^2 and were uniform in size over each chip. The wells had an approximate volume of 38–117 nl, which gives an overall chip capacity between 7448 and 22 932 nl when the wells are filled to the rim. Chips with larger (500 and 1000 μm) silicon nitride membrane windows could be used as ‘lids’, *i.e.* they were stacked on top and sealed (Fig. 1.1c), allowing wide-angle data collection. Large silicon nitride membranes, which formed at defined positions in all four corners of the 2 mm wide outer frame of every chip at an equal distance from the edge (Fig. BS1 in the supporting information), were removed with a thin needle. These openings served as alignment aids when asymmetric sandwiches were assembled (Fig. 1.1c).

1.3.2. *In situ* crystallization

The chips described above were used as solid supports for the *in situ* crystallization of lysozyme and fixed-target XFEL data collection. Direct crystallization on ultrathin silicon nitride freestanding films by vapour diffusion was performed in the HD and SD geometries (Fig. 1.1b). The first crystals were usually visible under a light microscope a few hours after deposition of the crystallization solution (minimum 6 h).

The size and crystal form of the growing crystals depended on the crystallization conditions in the silicon wells. Crystals with different shapes and sizes were obtained and were positioned in a wide range of crystallographic orientations on the silicon nitride membranes; full details are given in Table BS1 in the supporting information. The average coverage of the wells with crystals of the desired size was more than 90%. The balance between the formation of new crystals and crystal growth is related to the amount of protein available. In the vapour diffusion method, the protein and salt concentrations increase as the drop equilibrates with the reservoir solution. Once the protein reaches supersaturation, nucleation and crystal growth are in competition. It is known that several critical factors affect the dimensions of the protein crystals obtained [1.11]. The concentration of a protein in the crystallization solution is an important variable. When the concentration was too low in the HD and SD experiments, the nucleation rate was low and few crystals grew. This low crystal density led to insufficient coverage of the membrane, but usually favoured the formation of large crystals. When the protein concentration was too high, nucleation rates were high, leading to clusters of many small crystals. When the concentration of the protein was much too high, *i.e.* close to the solubility limit, precipitation without crystal formation was observed.

During crystallization experiments in the chamber, the difference between the concentration in the protein solution and that in the reservoir solution was the driving force that caused water to evaporate from the drop. This led to nucleation and further crystal growth. The crystallization process proved to be critical for the mechanical stability of freestanding ultrathin silicon nitride membranes during the incubation period (Fig. BS2 in the supporting information), which also depended on their thickness, uniformity and lack of pinholes, *i.e.* the quality of the CVD coating. The very thin intact membranes (30 nm) fabricated initially tended to break. The probability of nucleation and the growth of crystals were increased in the corners of the wells, as smaller crystals were observed to cluster in these areas. Presumably, the membranes broke when the forces exerted on the film were too high during formation of the crystals. As a result, samples intended for time-resolved XFEL measurements were prepared on 250 nm thick membranes.

1.3.3. Multiwell silicon chips for screening crystallization conditions

Microfabricated multiwell chips are suitable for nanovolume crystallization screening and allow the optimum crystallization conditions to be determined with minimal protein consumption. Their use together with XFELs promises to facilitate the structural analysis of proteins that are difficult to obtain in large quantities. As an initial proof of concept, 8 μ l portions of three lysozyme solutions in buffers with different pHs were pipetted by hand onto selected areas of a multiwell chip. Each

sample covered an area of approximately 25 wells. Crystallization was carried out in the HD geometry. Crystals were evident after 8 h, and had different morphologies (habits) in the three regions of the chip (Fig. 1.2).

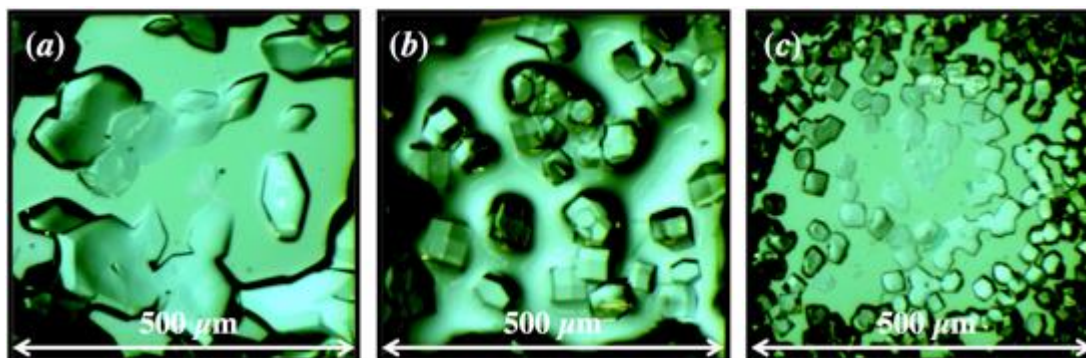


Figure 1.2 Crystals grown under different conditions on silicon nitride membrane windows of the same chip. The size and shape of the crystals obtained depended on the composition of the sample buffer. (a) Lysozyme concentration: 50 mg ml⁻¹ in 50 mM NaAc buffer pH: 4.5. (b) Solution as in part (a) modified with 50% PEG solution and reservoir solution (0.1 M NaAc and 0.6 M NaCl, pH: 4.5) in proportion 9:1:1, (c) 50 mg ml⁻¹ lysozyme solution in miliQ H₂O.

1.3.4. Crystals from automated nanolitre dispensing

Nanoliter sample volumes have to be dispensed to make full use of the chips for screening and to allow the crystallization conditions to be varied from well to well. This requires the use of a robot such as the one described by Arnold *et al.* [1.44]. This automated unit was employed in the present study and is equipped with a glass capillary nozzle with a 30 μm orifice (inner diameter), and with a dew-point stage to reduce liquid evaporation (Fig. 1.3). It was used to deposit precise volumes ranging from 5 to 15 nl into each well. As the capacity of the wells used in these experiments was approximately 22 nl, the concave meniscus formed by the liquid was below the rim and mixing of the solutions deposited in different wells was avoided.

The deposition of nanolitre-volume drops from the tip of the nozzle proved difficult, especially when dispensing 5 nl volumes. The droplet crept along the nozzle and foreclosed deposition in the silicon well. It has been reported that the application of a hydrophobic coating to the nozzle can be used to overcome this problem [1.44].

Alternatively, contact-mode deposition of 15 nl volumes was employed. This was achieved by touching the inclined wall of the silicon well, formed by anisotropic etching of the single-crystal chip, with the tip of the nozzle and allowing the liquid to flow down the sides to the silicon nitride membrane at the bottom (Fig. 1.3b) (a short film showing the deposition is provided as online supporting information). Contact between the nozzle and the fragile membrane was avoided. However, this approach increased the time required to fill the chip.

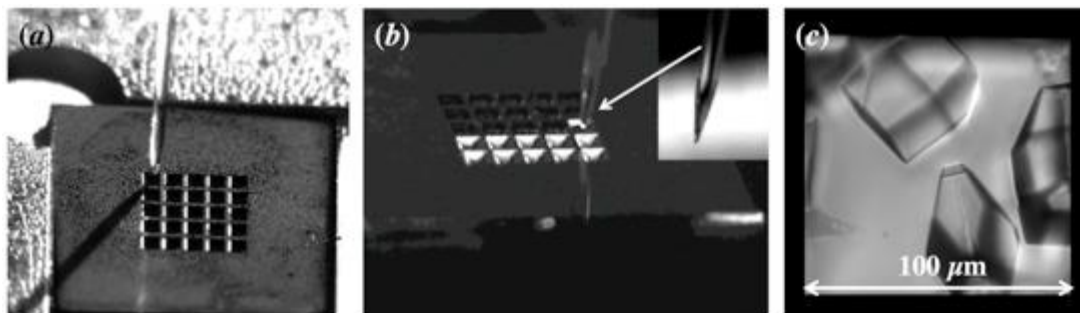


Figure 1.3 Crystal growth in nanoliter wells: (a) Top view of the silicon chip on the dew point stage; the 5 x 5 well array is 2 mm x 2 mm in size. (b) Nanoliter wells being filled with protein solution by contact-mode deposition. The dark wells at the top are filled, while the bright wells at the bottom empty. It took about 2 min to fill the array. The inset shows the capillary when moved away from the chip surface. (c) Lysozyme crystals grown on the 100 µm x 100 µm 30 nm thin silicon nitride membranes from deposited nanoliter volumes of 50 mg ml⁻¹ lysozyme mixed 1:1 with precipitating agent (0.1 M NaAc, 0.6 M NaCl, pH 4.5). Crystallization was carried out in the SD geometry.

1.3.5. Crystal growth optimization for time-resolved measurements at the FEL

Protein crystals grown *in situ* as described in Section 1.3.2, and protected from dehydration by a second silicon nitride membrane as described in Section 1.2.5, were used to investigate radiation damage processes in the femtosecond range at the FEL X-ray source at the Linac Coherent Light Source (LCLS, Menlo Park, California, USA; Section 1.3.6). In the course of the crystallization trials (Table BS1 in the supporting information), crystal growth was optimized to maximize the probability of X-ray interaction with the crystals, *i.e.* to maximize the expected hit rate during data collection. Conditions giving the maximum coverage of the membrane window by crystals with large lateral dimensions (150–200 µm) (Fig. 1.4a) or by a high density of smaller crystals (approximately 50 µm) (Fig. 1.4b) were sought. The crystals observed on 200 µm x 200 µm membranes were usually the largest and had the optimum dimensions and distribution density for time-resolved measurements (Fig. 1.4a).

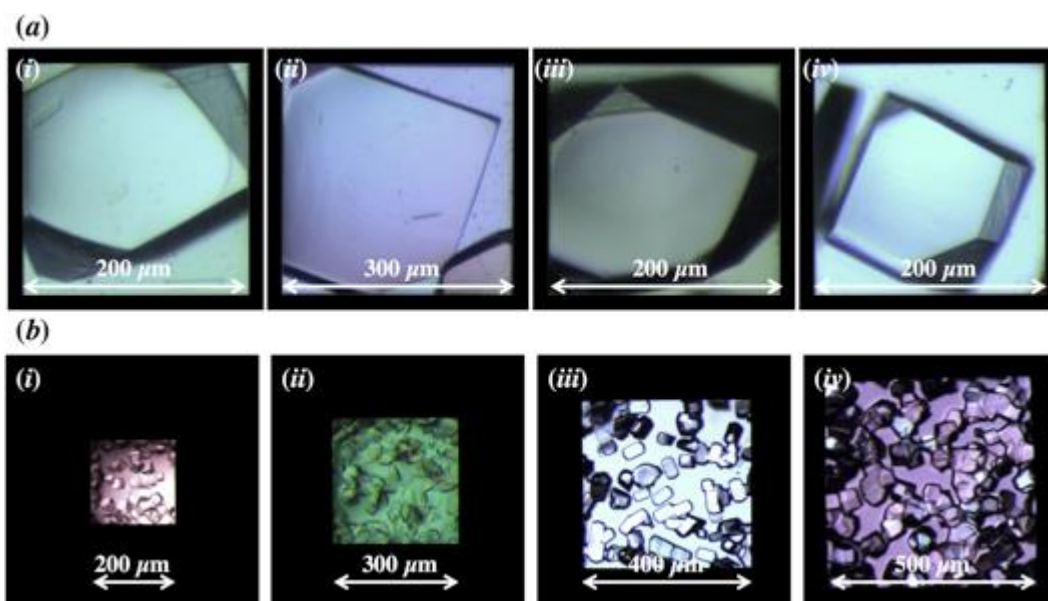


Figure 1.4 *In situ* crystal growth on silicon nitride membranes with density optimization. (a) Single protein crystals grown on membranes filling majority of the membrane window – the ideal case that will provide almost 100% hit rate on serial diffraction data collection. The crystals shown were grown (HD geometry) at room temperature under different conditions as detailed in Table BS1 in the supporting information: (i) chip 30, (ii) chip 31, (iii) chip 20, (iv) chip 36. (b) Protein crystals grown (HD geometry) at RT from solutions (mixtures with precipitating agent) incubated beforehand overnight at 277 K are shown on membranes of various sizes. The conditions are detailed in Table BS1 in the supporting information: (i) chip 11, (ii) chip 12, (iii) chip 4, (iv) chip 6.

A strong influence of the crystallization solution storage temperature before deposition on the chip on the crystal growth was observed. Performing crystallization at room temperature from solutions previously stored at 277 K overnight usually resulted in growth of a higher density of smaller crystals compared with experiments run under the same conditions with freshly prepared solutions (Fig. BS3 in the supporting information). It turned out that storage at lower temperatures leads to protein aggregation and the formation of clusters of protein acting as nucleation centres as soon as supersaturation is reached. These clusters seem to be stable enough to sustain an elevated temperature during setup of the crystallization. Increased density and reduced size of crystals grown from solutions conditioned at lower temperatures were observed independent of other parameters, including the size of the membrane (Fig. 1.4b).

Growth initiated from the window corners was often observed. As a consequence, using much larger membrane windows with single crystals resulted in poor coverage of the centre of the window (Fig. BS5 in the supporting information). Therefore, when aiming for high coverage of the membrane by single crystals, the crystal size and window should be similar. Growth initiating from the window corners can also lead to maximal coverage of the membrane, when a single crystal grows over the single membrane and the crystal size matches the membrane dimensions. As expected, the chemical composition of the salt solution was a further important crystallization parameter. Using salt solutions of different pH is

known to influence the crystallization of lysozyme, leading to different morphologies [1.52]. The final size of the crystals obtained is also affected by the pH value, since it is directly related to the net surface charge of the molecule (isoelectric point). Moreover, additives such as PEG or EG that interact with the solvation shell of protein molecules have an impact on the final crystal shape. Indeed, the addition of such surface-active substances in the present study modified the shape of the protein crystals formed and tended to change their aspect ratio, resulting in elongated rod-like crystals (Fig. 1.5).

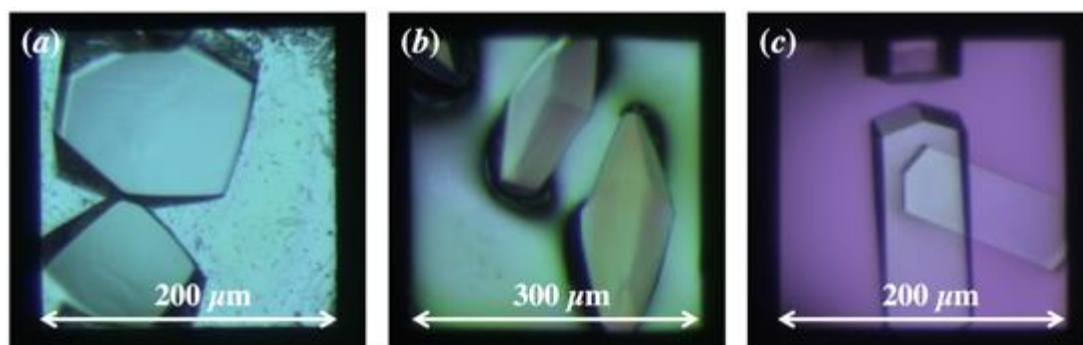


Figure 1.5 The influence of additives on the direct crystallization of lysozyme on silicon nitride membranes. The presence of additives in the protein buffer resulted changed the aspect ratio of the crystals. (a) 50 mg ml⁻¹ lysozyme in 50 mM NaAc buffer. (b) As in part (a) but plus PEG. (c) As in part (a) but plus EG. For details, see Table BS1 in the supporting information, chips (a) 20, (b) 17 and (c) 13.

Table 1.1 Data collection (beamline PX-I) and refinement statistics for *in situ* grown crystals.

Data collection	
Temperature (K)	293
Wavelength (Å), phasing method	1.00, MR (PDB ID 2lyz)
Total range collected per crystal (°)	50
Number of crystals merged	2
Space group	P4 ₃ 2 ₁ 2
Unit cell parameters <i>a</i> , <i>b</i> , <i>c</i> (Å), <i>α</i> = <i>β</i> = <i>γ</i> (°)	79.50, 79.50, 37.81, 90
Resolution (Å)	50-1.57 (1.61-1.57)
R _{meas}	0.05 (0.847)
<I/σ(I)>	13.74 (1.04)
Completeness	0.954 (0.952)
CC _{1/2}	99.9 (70.5)
Mosaicity (°)	0.033
Refinement	
R _{work} /R _{free}	0.1656/0.1840
Bond lengths RMS (Å), bond angles RMS (°)	0.005, 0.77
Ramachandran favored (%)	99.25
Ramachandran outliers (%)	0
Rotamer outliers (%)	0
Clashscore	1.00
Average B-factor (Å ²)	30.44
PBD code	5ne0

1.3.6. Assessment of *in situ* grown crystal quality by synchrotron radiation

In order to assess the quality of lysozyme crystals grown *in situ* and their preservation in the sandwich-type enclosure (Section 1.2.5.), diffraction experiments were carried out at room temperature on the PX-I beamline at the Swiss Light Source (SLS, PSI). Data were collected from individual 50–100 μm crystals selected using an inline microscope (Fig. BS6 in the supporting information) on a chip assembly that was mounted on the goniometer head. The sample could be tilted by about $\pm 30^\circ$ without shadowing the crystals by the supports. Data were collected under crystal rotation by about 50° , leading to high-quality data sets (Table 1.1), although with limited completeness depending on the crystal orientation. Merging data sets from two tetragonal crystals with different orientations on the support yielded complete crystallographic data at 1.57 Å resolution. Structure solution and refinement provided a high-quality electron-density map (Fig. 1.6).

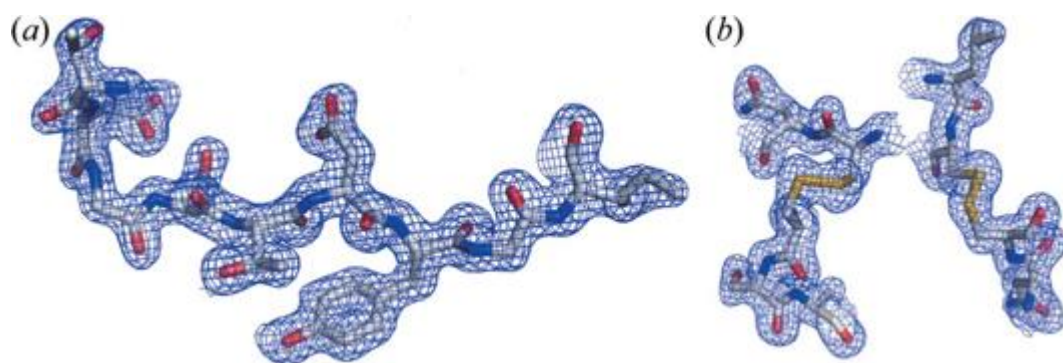


Figure 1.6 Details of the electron density obtained from the 1.57 Å room-temperature data set collected from lysozyme crystals enclosed between silicon nitride membranes (PDB code 5ne0). (a) Residues THR47–ILE55. (b) Disulfide bonds between CYS64–CYS80 and CYS76–CYS94. The difference maps showed no residual density on the disulfide bonds, which indicates that the bonds remained intact and that the protein structure suffered no significant radiation damage. The $2F_o - F_c$ maps are shown as blue meshes contoured at 1σ . Stick models show N atoms (blue), O atoms (red), S atoms (yellow) and C atoms (grey).

For full data set statistics and refinement details, see Fig. BS7 and Table BS2 in the supporting information. All quality parameters of the obtained data and model compare favourably with other lysozyme entries in the PDB. The low mosaicity given by XDS (0.033°) and the sharpness of the peaks (Fig. BS7 in the supporting information) are consistent with room-temperature crystals in a good state of conservation. This proves that the crystals were satisfactorily protected by the silicon nitride enclosure.

1.3.7. Sample preparation for time-resolved measurements and the collection of diffraction data

Large protein crystals on solid supports were produced for time-resolved measurements aimed at the investigation of X-ray induced damage in the femtosecond range using a split-delay X-ray optical setup similar to the one described earlier [1.43]. A detailed report, including a full description of the experiment and the results of the ongoing data evaluation, is in preparation. In brief, fractions of an X-ray pulse delivered by the XFEL were split off using a set of diamond gratings in the optical path. A second set of gratings redirected the split beams to the sample, where they arrived under an angle of up to 6 mrad and with a time delay in the range of 20–300 fs. The setup was designed in such a way that one set of split beams overlapped with the ‘direct’ primary pulse on the sample (pump-and-probe area), while a second symmetric set of split beams was focused on an area approximately 70 μm away (reference area). The setup was adapted to diffraction geometry where the primary ‘pumping’ beam and the probing and reference beams were diffracted by the same Bragg plane within the protein crystal. The slightly different incident angles of the delayed pulses translate into slightly different positions on the detector (delayed peaks). Optimization of the sample-to-detector distance for the resolution of the delayed peaks led to limitation of the accessible q range (8–14.5 \AA). As a consequence, only single Bragg peaks (with their accompanying delayed peaks) were observed from individual X-ray pulses. The samples were kept at room temperature and atmospheric pressure. Being sealed between two silicon nitride windows (Fig. 1.1c, Section 1.2.5) prevented them from dehydrating. The chip ‘sandwich’ was mounted on a fast XY stage, aligned, and moved stepwise through the XFEL beam (step size 1 mm) to irradiate the membrane array window by window (Section 1.3.1) at a rate of up to 1 Hz until the whole sample area had been covered (14 mm x 14 mm). Under these conditions, Bragg reflections and the time-delayed peaks were collected with sufficient spatial resolution and with very good contrast owing to the high X-ray transparency of the silicon nitride membranes (Fig. 1.7a). The reference experiments with blanked primary beams showed only the delayed peaks (Fig. 1.7b). The high quality of the registered signal showed that the protection provided by the ‘sandwich’ chip assembly was sufficient to prevent dehydration of the crystals before the measurement.

Furthermore, the single crystals were large enough to be hit simultaneously by the two sets of beams separated by 70 μm . However, the samples dried out slowly during data collection, because the pulses of intense X-rays created holes in the silicon nitride membranes leading to slow evaporation from adjacent wells. Sealing each of the wells individually would help to overcome this problem.

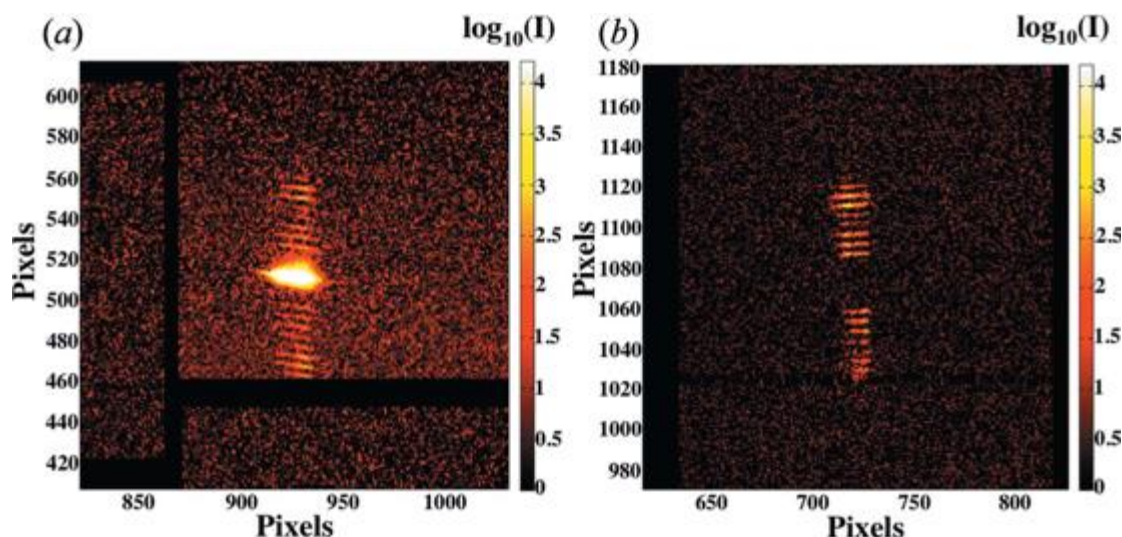


Figure 1.7 Examples of diffraction data collected on a CSPAD pixelated detector [1.53] during time-resolved pump-probe experiments with the split-delay X-ray optics line on large lysozyme crystals. (a) The set of Bragg reflections stemming from the pump beam (central intense peak) and the decreased intensity delayed peaks. (b) The pumping beam has been blanked out, leading to sets of delayed peaks in both the probing (top) and the reference (bottom) region. The views shown here are limited to a small part of the detector, but they contain full signal registered during single shots (the detector was placed off-axis in the horizontal direction at an angle of approximately 13° from the direct beam and at a distance of 122 cm from the sample). Images are plotted on a log₁₀ scale and pixels with the intensity (I) <1 counts were set to 0. A high contrast was obtained between the registered signal and the background owing to the high X-ray transmission of the used silicon nitride membranes. The membrane supporting the crystals and the membrane in the sandwich lid were 250 nm thick.

Application of the other materials commonly used for *in situ* data collection at synchrotrons (like *e.g.* cyclic olefin copolymer or Kapton foil, see Fig. BS8 in the supporting information) would significantly increase the background, especially given their partially ordered structures, and would most likely indispose the observation of weak delayed peaks. Moreover, very thin plastic foils are water permeable and not suitable for long-term data collection. Also, the previously reported examples of fixed targets, *i.e.* vapour diffusion crystallization plates or microfluidic chips [as described by Feld *et al.* (2015) [1.54], Huang *et al.* (2015, 2016) [1.34-1.35], Axford *et al.* (2016) [1.36], Lyubimov *et al.* (2015) [1.37] and Murray *et al.* (2015)[1.33]] provide much higher background levels, mainly due to the applied thicknesses and/or (semi-)crystalline materials. Silicon nitride fabrication technology is unique in this respect in providing thin films in the sub-micrometre range, which gives an ultralow continuous (amorphous) background in X-ray diffraction, as shown in Fig. BS8 in the supporting information.

1.4. Conclusions and outlook

Protein crystals of the desired size could be efficiently grown with the required distribution density on silicon nitride membrane substrates,

protected from dehydration by the formation of a silicon nitride membrane chamber and analysed *in situ* by an XFEL beam. This opens many possibilities for the time-resolved investigation of phenomena occurring in the femtosecond regime. The silicon nitride membranes employed are highly X-ray transparent (composed of light chemical elements), ultrathin, self-supporting, stable and water impermeable, and allow the production of multiple copies of large protein crystals at defined places for serial measurement in quasi-random crystallographic orientations. In an ideal case, the chips would provide a 100% guarantee of hitting the crystalline sample during data collection at an XFEL, *i.e.* when the membrane windows are completely covered by single crystals grown with lateral dimensions matching the window size or with a high density of small crystals. The applied technology has the potential for the production of supports with about one order of magnitude higher density of the wells using thinner wafers and adapted designs. This makes them attractive for application at XFELs with repetition rates in the 100 Hz range, such as at the planned fixed-target instrument for protein crystallography at Experimental Station B of the SwissFEL. Using a few tens of chips of area 1 cm x 1 cm should be sufficient for the collection of a full data set of an unknown protein. However, when addressing higher repetition rate sources an even higher sample density is required, which could for instance be achieved with elongated windows [1.20] in which a whole series of crystals are sequentially probed during a fast one-directional movement. Given the notable improvements that allow the more efficient collection of diffraction data from fixed targets at XFEL sources [1.54], the key to obtaining high-resolution protein structures now lies in the material quality and the sample preparation and handling procedures. When crystals are grown on the fixed-target support they can be delivered directly to the beam. *In situ* measurements avoid the mechanical stress incurred during handling and thus help to maintain the quality of the sample until data collection. Importantly, the method used to grow crystals on silicon nitride membranes significantly reduces the sample volume required. In particular, automatic handling of the liquid allows for nanoliter deposition and for crystallization conditions to be screened on the nanoliter scale. The principles and techniques presented here can be applied to a wide range of proteins and promise to extend the list of structures solved using XFELs. In the future, this crystallization procedure, which requires minimal volumes, could be adapted for nanocrystal growth as well as for deposition of crystal suspensions. In spite of the demonstrated success of the method described here, the use of polymers and other materials to make the chips easier to mass-produce and to reduce their cost needs to be investigated further [1.54]. The membranes should be composed of light elements so that they are essentially transparent to the X-ray beam, thin to reduce absorption and diffuse scattering, and less brittle than silicon nitride membranes.

1.5. Accession code

The coordinates and structure factors of the room-temperature structure of lysozyme between silicon nitride membranes have been deposited in the PDB under accession code 5ne0.

Acknowledgements

The authors would like to thank Dario Marty and Christopher Wild for technical assistance in microfabrication. We are grateful to Marcin Sikorski and his team for experiment support and data acquisition at the XCS endstation. Parts of this research were carried out at the Linac Coherent Light Source (LCLS) at the SLAC National Accelerator Laboratory. LCLS is an Office of Science User Facility operated for the US Department of Energy Office of Science by Stanford University. Use of the LCLS, SLAC National Accelerator Laboratory, is supported by the US Department of Energy, Office of Science, Office of Basic Energy Sciences, under contract No. DE-AC02-76SF00515. We also acknowledge the Paul Scherrer Institut, Switzerland, for provision of synchrotron radiation beamtime on beamline PX-I of the SLS. Istvan Mohacsi and Shirley Müller helped in manuscript preparation.

Funding information

Funding for this research was provided by: Swiss Nanoscience Institute (project No. P1305).



Chapter 2

“You cannot teach a man anything; you can only help him discover it in himself”.
Galileo

Demonstration of femtosecond X-ray pump X-ray probe diffraction on protein crystals

Nadia Linda Opara^{a,b,c}, Istvan Mohacsia^{a,d}, Mikako Makita^{a,e}, Daniel Castano-Diez^b, Ana Diaz^a, Pavle Juranić^a, May Marsh^a, Alke Meents^d, Christopher J. Milne^a, Aldo Mozzanica^a, Celestino Padeste^a, Valérie Panneels^a, Marcin Sikorski^f, Sanghoon Song^f, Henning Stahlberg^{b,c}, Ismo Vartiainen^a, Laura Vera^a, Meitian Wang^a, Philip R. Willmott^a, Christian David^a

^a Paul Scherrer Institut, CH-5232 Villigen-PSI, Switzerland

^b C-CINA, Biozentrum, University of Basel, CH-4058 Basel, Switzerland

^c Swiss Nanoscience Institute, CH-4056 Basel, Switzerland

^d Deutsches Elektronen-Synchrotron DESY, Notkestrasse 85, D-22607 Hamburg, Germany

^e European XFEL GmbH, Holzkoppel 4, D-22869, Schenefeld, Germany

^f LCLS, SLAC National Accelerator Laboratory, 2575 Sand Hill Road, CA94025 Menlo Park, USA

Available online:

<https://aca.scitation.org/doi/10.1063/1.5050618>

Structural Dynamics **5**, 054303 (2018)

This article has supporting information: Appendix C.

All article content, except where otherwise noted, is licensed under a Creative Commons Attribution (CC BY) license (<http://creativecommons.org/licenses/by/4.0/>).

Synopsis: Pump-multiprobe X-ray optics delay line has been applied for demonstration of the time-resolved, femtosecond scale diffraction data collection on large lysozyme crystals.

Abstract

The development of X-ray free-electron lasers (XFELs) has opened the possibility to investigate the ultrafast dynamics of biomacromolecules using X-ray diffraction. Whereas an increasing number of structures solved by means of serial femtosecond crystallography at XFELs is available, the effect of radiation damage on protein crystals during ultrafast exposures has remained an open question. We used a split-and-delay line based on diffractive X-ray optics at the Linac Coherent Light Source XFEL to investigate the time dependence of X-ray radiation damage to lysozyme crystals. For these tests, crystals were delivered to the X-ray beam using a fixed-target approach. The presented experiments provide probe signals at eight different delay times between 19 and 213 femtoseconds after a single pump event, thereby covering the time-scales relevant for femtosecond serial crystallography. Even though significant impact on the crystals was observed at long time scales after exposure with a single X-ray pulse, the collected diffraction data did not show significant signal reduction that could be assigned to beam damage on the crystals in the sampled time window and resolution range. This observation is in agreement with estimations of the applied radiation dose, which in our experiment was clearly below the values expected to cause damage on the femtosecond time scale. The experiments presented here demonstrate the feasibility of time-resolved pump-multiprobe X-ray diffraction experiments on protein crystals.

2.1. Introduction

2.1.1. Protein crystallography as one of the X-ray free-electron lasers' (XFELs) applications

Research on biomolecular systems is a rapidly developing application of X-ray free-electron laser (XFEL) facilities [2.1]. These ultra-bright X-ray sources provide pulses on the femtosecond timescale with millijoule pulse energies, which allow pump-probe experiments to investigate fast dynamic processes in proteins [2.2-2.8]. In addition to providing feasibility of time-resolved measurements on proteins, the ultrashort pulses of XFELs can overcome the radiation damage limitations encountered when using synchrotron radiation. In this case, the investigation of microcrystals is limited by the fact that radiation damage often prevents the collection of useful diffraction datasets when using very intense, tightly focused X-ray beams. Due to the femtosecond pulse lengths of XFELs, recording of high-quality diffraction patterns from the probed crystals is possible before structural damage sets in. By sequentially collecting diffraction patterns from newly supplied crystals with identical structure and random orientation, it was demonstrated that it is possible to collect diffraction data suitable for solving the molecular structure of proteins [2.9]. More recently, there has been a growing interest of structural biology in serial protein crystallography at XFELs facilities, and the method has led to increasing numbers of solved structures [2.10-2.18].

2.1.2. Radiation damage mechanisms in protein crystals

Protein crystals consist mostly of only low-Z atoms and significant amounts of solvent (water) [2.19-2.20]. They usually have large unit cells. Destruction of these radiation sensitive samples [2.21] is based mostly on photoelectric absorption. Classification of the radiation damage within an irradiated protein crystal can be based on the location within the crystal in which it occurs in. Namely, they are considered global when large displacements of the protein molecules are observed and therefore there is an increase of the mosaicity, the unit cell constants change, and the loss of the resolution occurs. On the point/local scale, the most prominent damage processes include the cleavage of the disulphide bonds (S-S), decarboxylations of the amino acids or photo-reduction of redox systems. All these phenomena occur on their characteristic time scales [22-23].

The fastest time-scale of radiation damage processes gives the limit for serial femtosecond crystallography (SFX) and so-called “diffract-and-destroy” data collection mode [2.24-2.25], where the sample is blasted by the X-ray laser pulse, but only after the scattering process has taken place which can be registered as diffraction pattern on the detector. Theoretical investigations have been performed in order to quantify the damage effects and to reveal the relevant mechanisms [2.26-2.28]. First simulations reported by Neutze *et al.* on protein lysozyme molecules approximate femtosecond X-ray induced Coulomb explosion to occur on sub-100 fs time scales [2.29].

2.1.3. Experimental approaches to radiation damage at XFELs

Experimental approaches have focused on the effects of pulse duration and fluence in SFX and comparison to data obtained at synchrotrons [2.30-31]. Chapman *et al.* reported on SFX data on lysozyme crystals collected with 200, 70 and 10 fs pulse lengths [2.32]. It was found that the Bragg-peak intensity drops by about one order of magnitude when comparing 200 fs to 70 fs pulses or shorter. These findings indicate that only the photons arriving during the first tens of femtoseconds of an X-ray pulse interact with an intact crystal. Photons arriving later interact with a sample of decaying crystallinity, which contributes less and less to the diffraction peaks and merely adds to the diffuse background. This self-terminating diffraction mechanism [2.33] is predicted to greatly help in the collection of SFX data even with pulse length exceeding the time scales of structural damage.

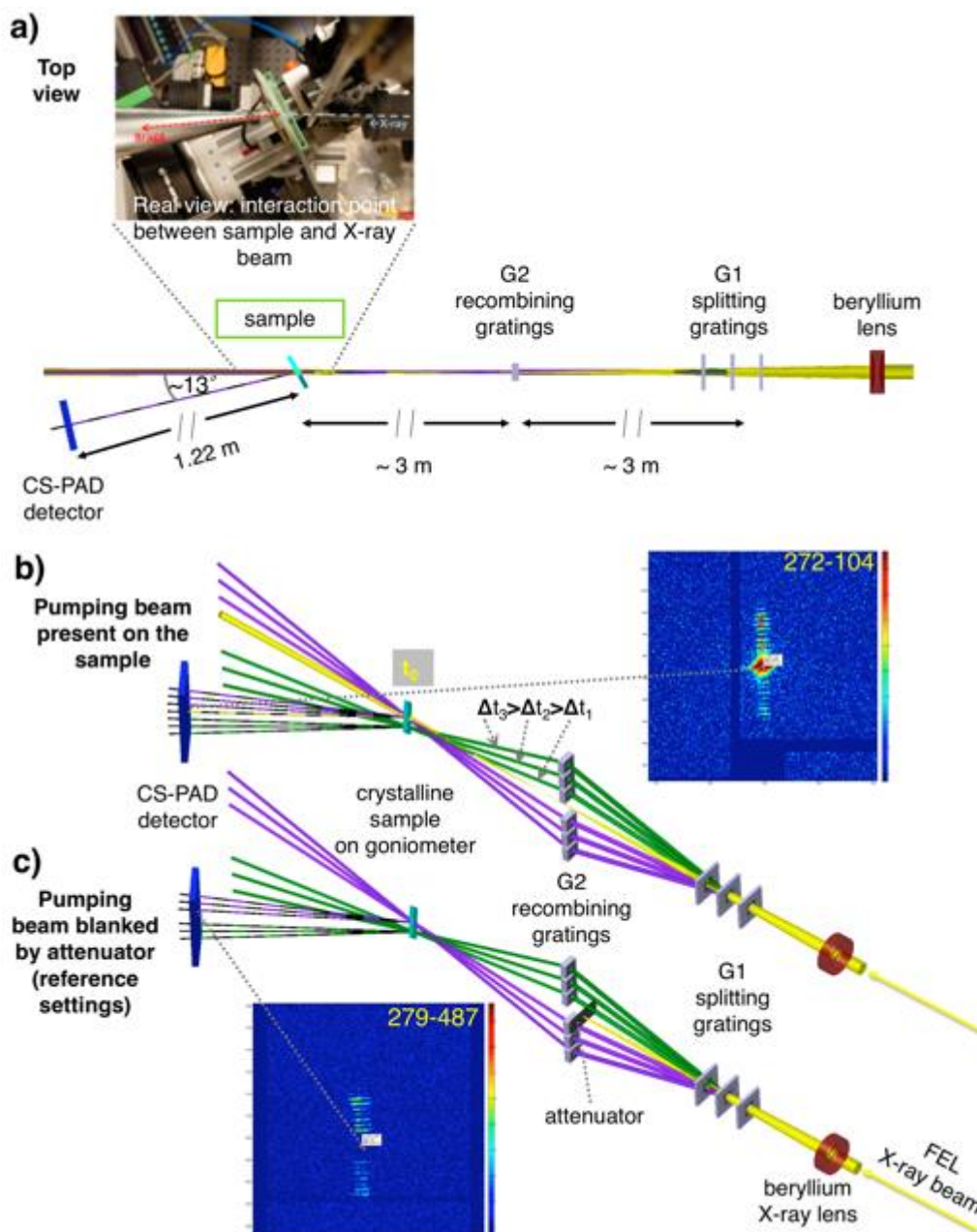


Figure 2.1 Scheme of the X-ray optics set-up (adapted from ref. 2.34), showing the data collection in transmission geometry for protein crystal diffraction. The detector was placed off-axis at an angle of 13° at a 122 cm distance from the sample. a) Top view, b) perspective view, pumping beam on (spot size focused down to $40\text{-}50\ \mu\text{m}$), and c) perspective view, pumping beam blanked. The dashed lines (— — —) indicate diffracted beams from the crystals collected ideally on the single tile of the CSPAD. The inset shows only a part of the detector with the signal. The purple probing beams run through the region of the sample hit by the pump beam, while the green probing beams run through a region of the sample not overlapped with the X-ray pump (b).

So far, no direct measurements of the dynamics of femtosecond radiation damage in protein crystals have been demonstrated. There are two main obstacles that have impeded such experiments in a classical pump-probe manner. Firstly, it is very difficult to provide an intense X-ray pump beam and an X-ray probe beam onto the same sample location but with a defined delay on the femtosecond scale. Secondly, the repetitive data collection at varying delays would require delivering fresh, undamaged crystals for every shot, under precisely the same Bragg angles.

Application of the pump/multi-probe setup, as reported here, can directly access femtosecond events in crystalline protein samples using X-ray diffraction. Our new approach to investigate the ultrafast X-ray damage processes in protein crystals covers, in this case, a time-scale from tens to up to a few hundred of femtoseconds and presents a proof of concept experiment. The investigated time window is of particular importance to explore the effects of beam damage in protein crystals probed with XFEL radiation with ultrashort pulses. For this purpose, the split-and-delay setup [2.34] was adapted for measurements in transmission (Laue) geometry [Fig 2.1]. Experiments performed with this setup allow for studying the effect of X-ray interaction with biological matter by observation of the measured diffracted signal collected on an integrating pixel array detector. The delayed peaks accompanying the main Bragg reflections from the probed protein crystal reveal the evolution of the Bragg-reflected intensity in time.

2.2. Experimental and computational methods

2.2.1. Experimental setup and diffraction geometry

For the experiments presented here, the set-up follows the design of an X-ray optical delay line as described by David *et al.* [2.34] [Fig. 2.1]. This provides the possibility to measure multiple discrete delayed probes with the same X-ray pumping beam using geometrically defined, jitter-free timing. A set of beryllium lenses was used for focusing/defocusing the direct beam to approximately 40-50 μm (ϕ) spot size on the crystals, and a set of delayed beams was generated from the main beam by a split-and-delay type of setup. It consists of an arrangement of X-ray diffraction gratings (“G1 gratings”) that splits a multi-keV X-ray pulse into an intense pump pulse and a fan of delayed probe beams, which are redirected by a second set of gratings (“G2 gratings”) to intersect at the target position, where the sample is placed. Due to the longer paths the probe pulses arrive with precisely defined time delays at slightly different incident angles. Moreover, a second symmetrically arranged set of delayed reference beams arrives at the sample with a spatial offset of 70 μm with respect to the pump beam and irradiates a part of unpumped sample area to serve as reference to the measurement. The obtained delay times (*cf.* Table 2.1.) corresponded directly to the grating pitches and distances. The 4th time delay of 77.7 fs was obtained by using the 2nd diffraction order of the 1st grating.

After being diffracted from the same crystal plane, the pump, probe and reference beams reach the detector at slightly different positions [Fig. 2.3]. This allows for registering the time-resolved diffraction signal without the need of an ultra-fast detector. Thus, the femtosecond dynamics of the excited sample can be detected for a single X-ray pump pulse as a streak of delayed peaks around the main Bragg peak originating from the beams of the intensity approximately 10^6 times fainter than the pump beam.

Table 2.1. Length of individual time delays.

No. #	1	2	3	4	5	6	7	8	9	10	11
Delay time [fs]	19.4	34.0	53.8	77.7	106.3	138.1	173.0	212.2	256.5	307.0	357.3

The experiments were performed at the X-ray coherent scattering (XCS) end-station of the Linac Coherent Light Source (LCLS) XFEL source, operated at a nominal photon energy of 5 keV with a spectral bandwidth of the single shot of about 10-15 eV FWHM [2.35-2.36] and a nominal pulse duration of about 45 fs, meaning that the first probes are arriving at the pumped area while pumping still occurs.

Technical modifications as described below were made to the original design [2.34] to provide a better match towards the investigations of protein crystals during the first few hundred femtoseconds after excitation. The setup was reduced in length by almost a factor of two, *i.e.* to approximately 6.6 m from the G1 gratings to the sample position. The new design was used at slightly increased photon energy of 5 keV and produced 11 delayed beams covering a time window of up to 357 fs with denser sampling instead of the previous 15 beams reaching up to 1200 fs delay.

As typical for protein crystallography experiments, the measurements were performed in transmission (Laue) geometry. The G1 diamond beam-splitting gratings were equally spaced by 16 mm along the beam axis, each mounted on a rotational stage for an alignment performed around the beam axis with assistance of beam spots visualization on the scintillator screen.

To increase the efficiency of the narrowest pitch gratings (8th, 9th and 10th) they were filled with iridium [2.37]. The G2 gratings set, which recombines the split beams and brings them to the sample at the incident angles with up to 5.7 mrad differences, was slightly asymmetric. This resulted in the lateral shift on the sample of the probe and reference parts of the split beam of approximately 70 μm . This set-up is also described in more detail by Makita *et al.* [2.38] showing its application for studying dynamics on bismuth single crystals in reflection (Bragg) geometry. These experiments also confirmed the spatial overlap of the pump and probe beams originating from the used X-ray optics setup.

The diffracted patterns from protein crystals were recorded at room temperature on a Cornell-SLAC Pixel Array Detector (CSPAD) 2.3 M, a pixelated detector (pixel size: 110 μm x 110 μm) with an overall size of about 20 cm x 20 cm [2.39-2.40]. It was placed off-axis in the horizontal direction at an angle of approximately 13° from the direct beam and at

a distance of 122 cm from the X-ray/sample interaction region, as schematically shown in Fig. 2.1. A shorter detector distance would not have given enough angular resolution to resolve the delayed beams and would have concentrated too much scattered intensity on too few pixels, potentially causing damage to the detector. On the other hand, placing the detector too far from the sample would have reduced the probability of capturing relevant reflections. The detector position was calibrated using silver behenate ($\text{AgC}_{22}\text{H}_{43}\text{O}_2$), a crystalline powder with 58.380 Å d-spacing [2.41], sandwiched between two pieces of adhesive Kapton tape. The resulting equally spaced arcs of powder diffraction pattern confirmed that the geometry was chosen in a way to cover a part of the solid angle corresponding to the d-values ranging from 8 Å to 15 Å (corresponding to a q-range between 0.4 Å⁻¹ and 0.7 Å⁻¹) [Fig. CS1]. This covers the reciprocal space where lysozyme crystals yield the most intense Bragg reflections.

2.2.2. Crystalline protein sample delivery

For diffraction data collection, protein crystals of chicken egg-white lysozyme with sizes between 50 and 400 µm were prepared by three different procedures. Two of them used *in situ* growth of the crystals. Crystallization was carried out on arrays of ultrathin silicon nitride membranes in microfabricated silicon chips from manually deposited solutions. For taking measurements, the samples were hermetically sealed with a second chip with silicon nitride windows as described previously in detail [2.42]. Protein origin of the grown crystals has been confirmed with UV test after XFEL exposure [*cf.* Fig CS9]. Alternatively, drops of protein solution were automatically dispensed using a Mosquito® crystallization robot on 25 µm thick cyclic olefin copolymer (COC) bottom of standard-dimension 96-position microtiter well plates [2.43]. The procedure was applied as follows: lysozyme protein from chicken egg-white (Sigma-Aldrich L6876-10G) at a concentration of 50 mg/ml (in 50 mM sodium acetate, pH 4.5) was crystallized by vapor diffusion against the precipitant solution (2M NaCl, 5% poly(ethylene) glycol monomethyl ether 5000, 50 mM sodium acetate pH 4.5, 25% ethylene glycol). A 200 nl drop of lysozyme was dispensed at the bottom of each CrystalDirect™ Plate well (MiTeGen LLC) [2.44] together with a 200 nl drop of the precipitant. The crystallization mixture was equilibrated against 500 µl of precipitant. The plate was efficiently sealed using a ClearVue Sheet (Molecular Dimensions) and incubated for one day at room temperature. The sealing cover was replaced immediately before the XFEL measurement by a less watertight but X-ray transparent 25 µm-thick Kapton® foil (Kapton type HN, DuPont™, USA), attached with 141 µm-thick 96-well adhesive gaskets from Saunders®. This approach provided a perfect environment for each crystal to grow to the desired dimensions, until precisely located and probed. A third type of sample was also prepared with the use of the silicon nitride membrane chips. The difference is that the crystals were initially grown in a crystallization plate then fished and transferred by

hand between two silicon nitride membranes. Successful data collection is feasible from each kind of tested samples. However, the silicon/silicon nitride chip approach provided the most suitable environment for efficient serial data collection, due to the much lower background level [Fig. CS2] originating from crystal packaging. This is due to the very thin membranes and limited amount of mother liquor around the crystals, as well as the regular placing of crystals on a small area.

2.2.3. Pump-multiprobe femtosecond data collection

Two different types of data sets were recorded, one with the main direct beam at its highest intensity (full XFEL beam) running through the sample (pump) [Fig. 2.1a] and the other with the pump beam blanked out [Fig. 2.1b, *cf.* Figs. 2.3a and 2.3d] to serve as an unpumped reference. A total number of 10905 shots were collected during the 12 h of an LCLS beamtime shift. The collected images of the exposures were visually inspected and individually selected. This resulted in a set of 289 shots with visible diffraction signals originating from protein crystals supported by the silicon nitride substrates. Figure 2.2a shows the full set of these shots, which have been used after initial filtering for further analysis. In Figure 2.2b a zoomed view is presented, showing a selection of reflections close to the detector center including some of the characteristic delayed peaks.

Since no rotation of the crystal was possible during the exposure to the X-ray pulses (crystal damaged after each shot) and due to the limited solid angle covered by the detector, the resulting diffraction patterns contain only a single or at maximum two Bragg peaks. Partial signals, meaning that only probe or reference sides were visible next to the Bragg peak, frequently occurred. This is due to the fact that only one series of the delayed beams reached the crystalline sample. The reason for this was either that the size of the protein crystal was smaller than the distance between the probe and the reference area spots (70 μm) or that the location of the crystal on the chip was such that part of the beams missed the crystal.

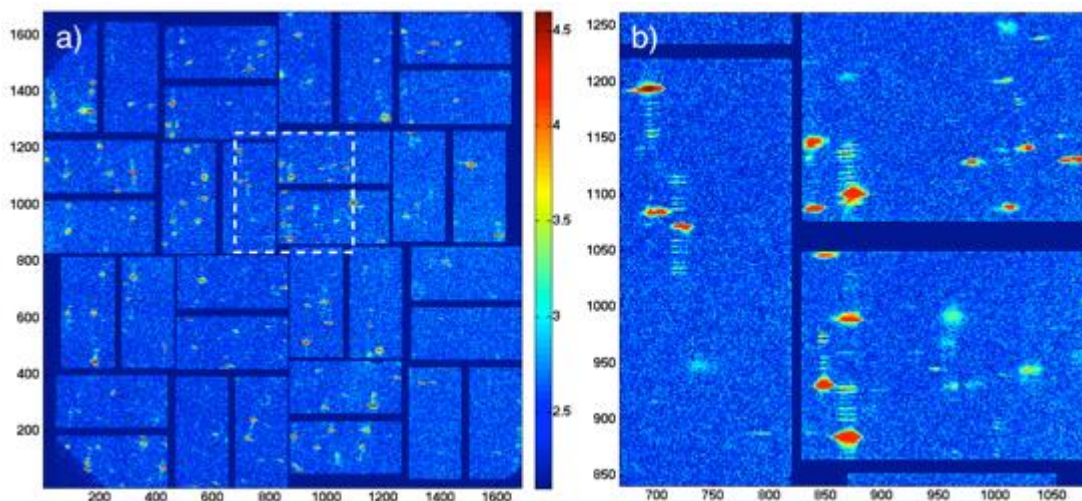


Figure 2.2 Summed signal of the 289 shots selected for analysis after initial filtering. The diffraction signals originate from the lysozyme crystals grown/deposited on silicon nitride windows. The intensity scale of the images is $\log_{10}(I)$, a) Full view of the CSPAD and b) zoomed view of the marked region.

The images with visible patterns were graded A, B or C depending on the quality of the signal intensity and then selected for further processing [Fig. CS3]. Individual images with well-visible and separated delayed peaks signals (Grade A shots) of the delays on the probe-side, the reference-side, or on both sides together (“complete” shots [Fig. CS4a]) were further analyzed. They created the following four data sets: probe pumped 60, probe unpumped 29, reference pumped 37, and reference unpumped 33 exposures.

2.2.4. Procedure for calculating line profiles of diffraction intensities

Following the visual inspection and manual determination of the positions of the collected signals, further processing was performed on this limited dataset. Signal profiles were extracted by means of MatLab scripts [Fig. 2.3c-f]. The applied algorithms are able to identify the position of the signal on the basis of manually given input coordinates on the center of the 6th (the most intense out of registered) delay peak. From this, they determine the integrated intensities of the delayed peaks [Fig. 2.3]. Data treatment involved: (i) correction of the angle originating from the position on the detector by rotation, (ii) obtaining line profiles of the signal by summing up the selected region of interest over the width of the signal [Fig. 2.3], and (iii) subtraction of the background for each peak separately.

2.3. Results and Discussion

2.3.1. Estimation of the dose on the exposed crystals

The relatively large area of the pump beam (40-50 μm , *v.s.* Section 2.2.1.) was kept to ensure lateral overlap of both the pump and the probe beams on the crystal. Focusing to a smaller spot size would have increased the local dose at the risk of incomplete beam overlap.

XFEL pulses of approximately 45 fs, at an average of 3.2 mJ energy, at a wavelength of 2.48 \AA (5 keV) were used for the pump-probe experiments on protein crystals grown on the solid supports. However, a substantial part of the initial energy of the XFEL pulses was lost on the way to the sample, mainly because of the absorption by the optical elements in the X-ray path. About half of the initial intensity was lost by absorption and diffraction by the diamond membranes of the G1 gratings (each 10 μm thick) and a similar fraction was absorbed by the beryllium focusing lenses. Additional photon intensity losses occurred in the 125 μm thick diamond exit window and in the helium-filled flight tubes, which are placed between the G1 gratings and the sample as well as between sample and detector. The out-of-vacuum beam path further contributed to the reduced level of delivered dose. The final X-ray energy arriving at the sample was measured to be approximately 100 μJ . For this purpose, a calorimeter has been placed at the sample position with all the optics in the X-ray path (including compound refractive lenses, G1 gratings, direct beam focusing lens, no aluminum filters inserted).

Taking into account the approximated 5 keV photon energy X-ray transmission through lysozyme crystals with about 45%-98% (for thicknesses of the crystals between 5-200 μm), the density of the crystals ($\approx 1.2 \text{ g/cm}^3$) and the incoming pulse energy of 100 μJ , result in an estimated dose in the spot area of about 0.1-0.2 MGy.

2.3.2. Diffraction data collection

During the initial alignment runs and final tuning of the experimental set-up, large crystallization plates backed with kapton foil with grown lysozyme crystals (*cf.* Section 2.2.2.) were probed in “by hand” mode, aligning each crystal individually. This method of collecting diffraction images resulted in a high hit rate but was very time-consuming. Subsequently, the silicon nitride membrane arrays with large lysozyme microcrystals (50-200 μm) were scanned through the XFEL beam and were exposed window by window in an automatic fast scanning manner with a repetition rate of 1 Hz. Due to the quasi-random position, the crystallographic orientation of the crystals in the windows, and placing of shots in a regular pattern the hit rate was lower.

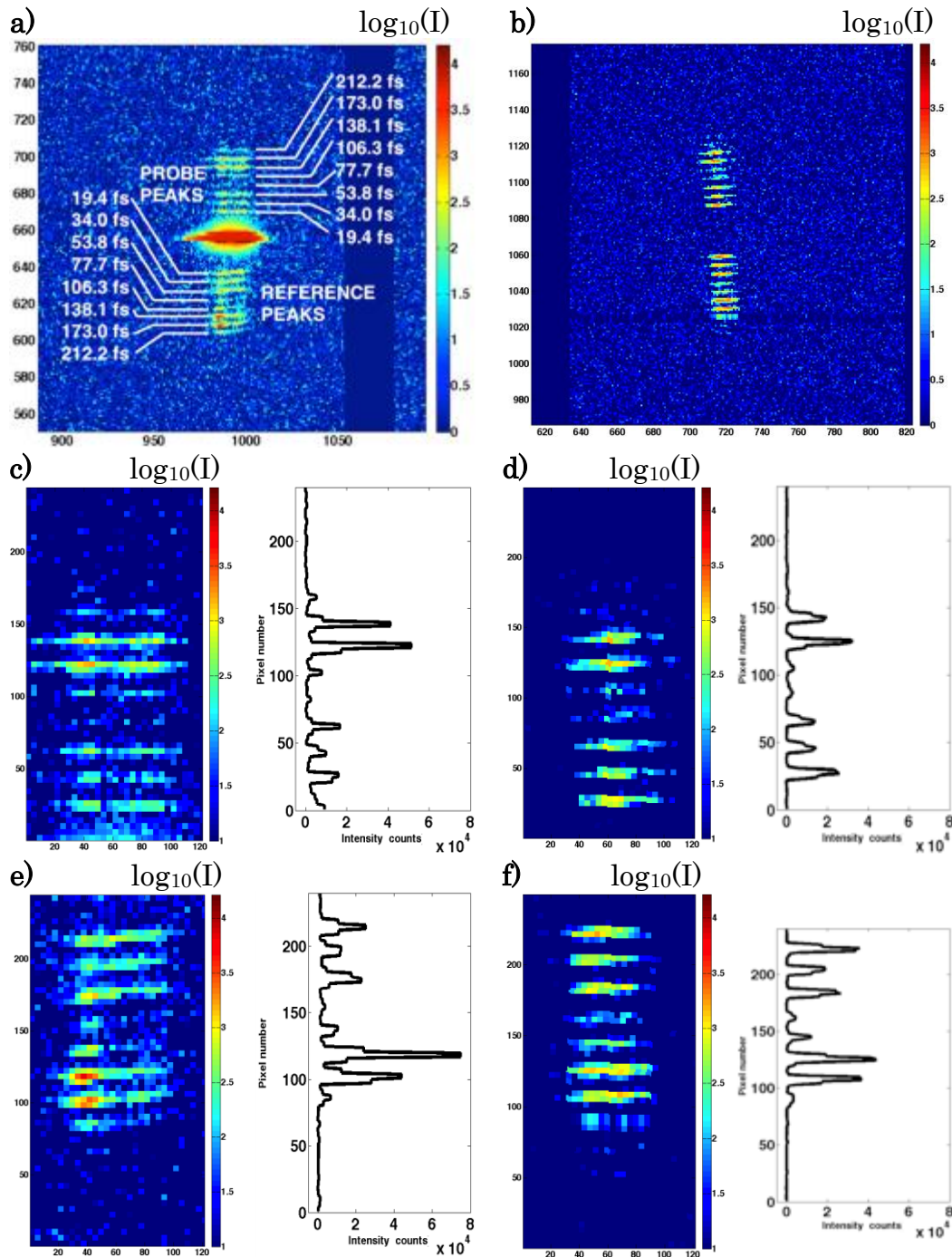


Figure 2.3 Examples of registered diffraction signals of (a) a pumped shot (Run 275 – Shot 136) and (b) an unpumped shot (Run 277 – Shot 326). c) - f) Regions of interest selected for intensity integration after resizing (images in logarithmic scale $\log_{10}(I)$, resizing factor: 4, original size: 30 px x 40 px) and delayed peaks' intensity profiles (linear scale representing values of counts registered on the detector after integration in x direction) of measured intensity distribution for all visible delays in a shot. c) and d) Probe and e) and f) reference part of the signal of a) and b) respectively.

However, the overall yield of diffraction patterns was much higher compared to manual strategy described above due to the significantly increased repetition rate. Even though the sealed sandwiches with regularly placed samples were open to the ambient environment after the first shot, it appears that the dehydration caused by vapor exchange with the normal atmosphere was slow enough that it did not affect the quality of the subsequent shots. Ultimately, diffraction data could be collected from a whole chip (196 wells/windows). During the data collection, all the samples were kept at ambient conditions (RT, normal pressure). Two sets of experiments were run, one with the pump and one without (*i.e.* delayed peaks only), with the latter being used to evaluate the relative intensity of the delayed peaks and also possibly for calibration purposes.

Due to the small solid angle in the chosen detector geometry, only one or two Bragg peaks could be recorded from a single X-ray pulse. Therefore, the determination of the approximate d-values corresponding to the lysozyme Bragg peaks was possible, but no indexing. The main Bragg peak of the registered signal was in most cases either saturating the detector [Fig. CS4a], or not present in the unpumped shots [Fig. CS4b].

This saturation, visible in the set of the pumped shots resulted in a locally increased background (flare) around the main Bragg peak. The spatial separation of the delayed peaks on the CSPAD detector proved to be sufficient for the quantification of the intensity of the delayed peaks. The delayed peaks were visible up to the 10th delay (307.0 fs), but the lower intensity delays (9th, 10th and 11th) were often lost in the noise and did not provide usable data.

Unfortunately, only rarely were both probe and reference sides of the diffraction signal been registered from the same crystal [Fig. CS4]. These few acquired complete data frames confirm the possibility to collect simultaneous pump and reference information with our method. Since the statistical relevance of this sparse dataset is questionable, we pursued the alternative approach for data processing that considers delayed peaks from the probe and reference side separately. In future experiments, the yield of the registered diffraction peaks could be increased by using larger crystals in width and length (but not in thickness), and by applying a better (automated) alignment procedure as well as prelocation methods.

Additionally, some shots had to be excluded from further analysis, as they partially fell on the inactive gaps between the detector tiles. High signal rotation and loss of part of the delayed peaks occurred when the signal was diffracted under high angle away from the main X-ray propagation axis resulting in landing at a largely off-centered position on the detector. In such cases, delayed peaks are prone to falling off of the rocking curve, meaning they do not fully fulfil Bragg's law [Fig S5]. However, in favorable conditions (intense Bragg peak, thick region of the crystal) it was also possible to reach intensity values close to the detector saturation level with the delayed peaks and clearly observe the weakest or the longest delay (4th, 9th, 10th) peaks [Fig. CS6].

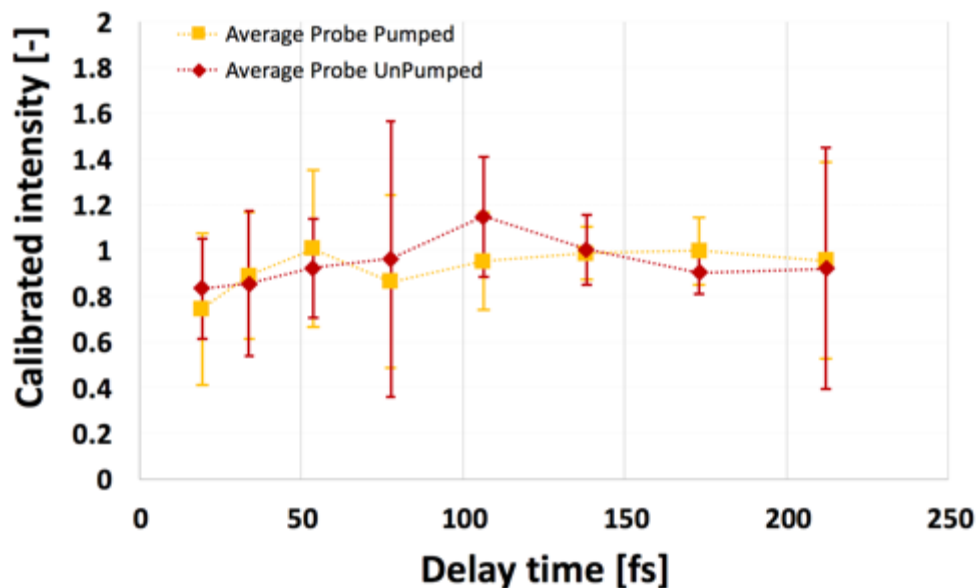
2.3.3. Data analysis

During the manual pre-selection and grading process [*cf.* Fig. CS3], a limited set of data packages [*cf.* Section 2.2.3., Fig. CS7] were chosen for further evaluation. They consist of the following numbers of A-graded shots: 60 for probe pumped, 29 probe no pumped, 37 reference pumped and 33 reference no pumped shots [Fig. CS7]. Following the manual localization of the delayed peaks at the detector readout images, further processing was performed using automated Matlab scripts on these relevant shots. Signals were corrected for small rotations and integrated on the horizontal axis [Fig. 2.3b-c,e and f]. Peak positions were automatically refined and their total intensity integrated after background subtraction. As no information was available about the absolute Bragg-peak intensity, the intensities of the delayed peaks were normalized by their total intensity (sum of the first 8 delays) as an internal reference.

Moreover, due to the different diffraction efficiencies of each grating, there is a large fluctuation between the characteristic relative intensity [Fig. CS7, S8] of the different delay peaks. Factors include: limited amount of available data, differences in protein arrangement, and fluctuations in the X-ray pulse spectrum contribute to the high level of signal scattering within a single time data-point [Fig. CS8].

The relative intensities of the shots in each dataset were subsequently reduced into an average (single) value per delay [Fig CS8]. Error bars for each time step were determined separately and represent ± 1 standard deviation from the calculated average. The averaged values of the relative intensities are different for each time point, due to the different diffraction efficiencies of the used gratings. The strongest signals are found for the 6th and 7th delay representing delay times of 138.1 and 173 fs. The weakest signals were registered in the 4th delay (77.7 fs), because the second order diffraction of a G1 grating was used. It also showed for the longest (*e.g.* 8th) delays, as the fabrication of the gratings with the feature spacing, which was close to the technical limits resulted in low diffraction efficiencies. Delays number 9 and 10 were only rarely visible, and the 11th delay was never detected. These relative intensities follow similar trends in the pumped and unpumped sets for both the probe [Fig. CS8a] and the reference [Fig. CS8b] sides and their ratio show no clear changes beyond statistical noise. Attempts to divide the experimental intensity values of the “pumped” scenario by the average of “unpumped” (plots not shown) give graphs of approximately constant functions at the level of 1, with relatively large errors for all the data points.

a)



b)

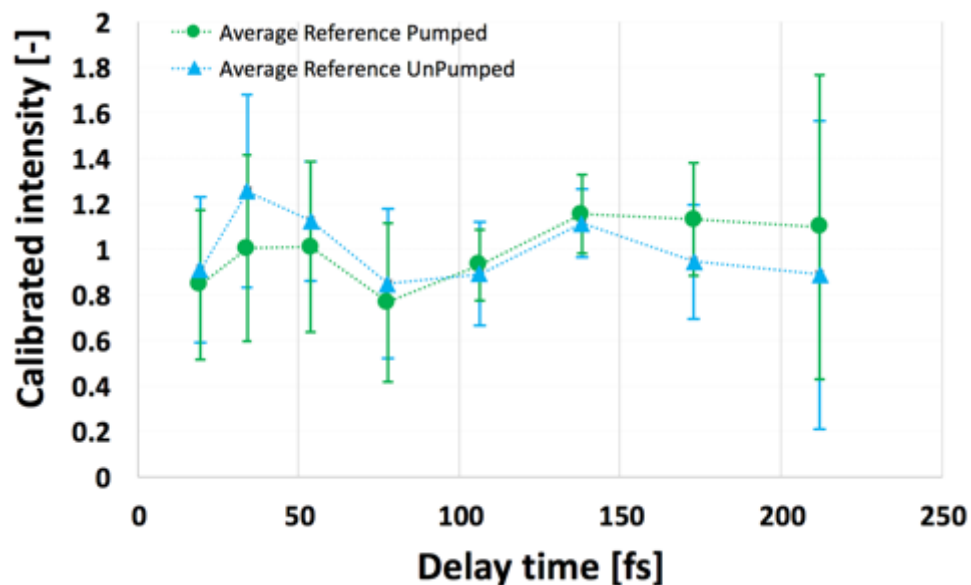


Figure 2.4 The average intensity based on measurements on protein crystals for individual 8 time points (19.4; 34; 53.8; 77.7; 106.3; 138.1; 173; 212.2 fs). It has been calibrated with factors obtained from unpumped reference measurements on silicon single crystals. Data shown separately for the parts of the registered signal are: a) Probe-side pumped/no pump, b) reference-side pumped/no pump sets. Experimental data is marked by a geometric figure; thin, dotted lines connecting experimental time points are a visual guide and facilitates comparison of the curves. Error bars show +/- 1 standard deviation of the individual shots from the average truncated to 80% of all the population of the data (sigma value 1.282 applied for shot or single peak intensity value deviating from average).

Specifically, significant errors were observed for the weak signals (4th and 8th delay), as the applied data treatment strategy attaches more importance to the intense values.

The obtained results indicate no change in signal that could be assigned to the impact of the pump beam within the studied time window. This can be seen on the intensity plots based on protein crystal diffraction data [Fig. 2.4] which were calibrated with factors based on unpumped reference measurements on silicon single crystal [*cf.* Supplementary Table CS1] collected with the same X-ray optics set-up [Fig. 2.1], but in reflection geometry. Details about these Si-based results will be published elsewhere. Thus, the data analysis gives no evidence of damage occurring within the studied time window at the applied dose of 0.1-0.2 MGy (*cf.* Section 2.3.1.).

By applying the data treatment described above, we see no apparent change between the values of the relative calibrated intensities of the delayed peaks for the pumped shots as compared to the corresponding data for the unpumped shots [Fig. 2.4]. Damage of the protein crystal structure on the femtosecond time scale would manifest itself as decaying Bragg reflectivity over time. Chapman *et al.* described this effect previously [2.32], where a strong reduction of the signal intensity was recorded in the resolution-range (15 to 8 Å), corresponding to the same resolution observed here. The fact that there is no clear decay of the registered signal in our experiment indicates that the dose deposited by the pump beam is too low to cause substantial damage on the probed femtosecond time scale.

However, microscopic inspection of the shot crystals shows evident changes resulting from evaporation of the probed volume of the crystals. The damage in the center of the probed areas is well visible, while the rest of the crystal appears intact. In case of crystals grown on the silicon chips, the silicon nitride was often cracked or broken due to the impact of the pump beam [Fig. 2.5].

For further optimization of the method for probing protein crystals, the following modifications would be beneficial i) using prelocation of the crystals before exposures can be used for maximizing hit rate; ii) running the diffracted beam in vacuum would reduce scattering; iii) selection of a bigger detector (for higher surface area) would result in covering more of the scattering solid angle, enabling the collection of more than a single Bragg peak per exposure; and iv) additionally, a second detector placed closer to the sample and therefore covering a larger solid angle would enable collection of a sufficient number of diffraction spots to allow their indexing on the back detector.

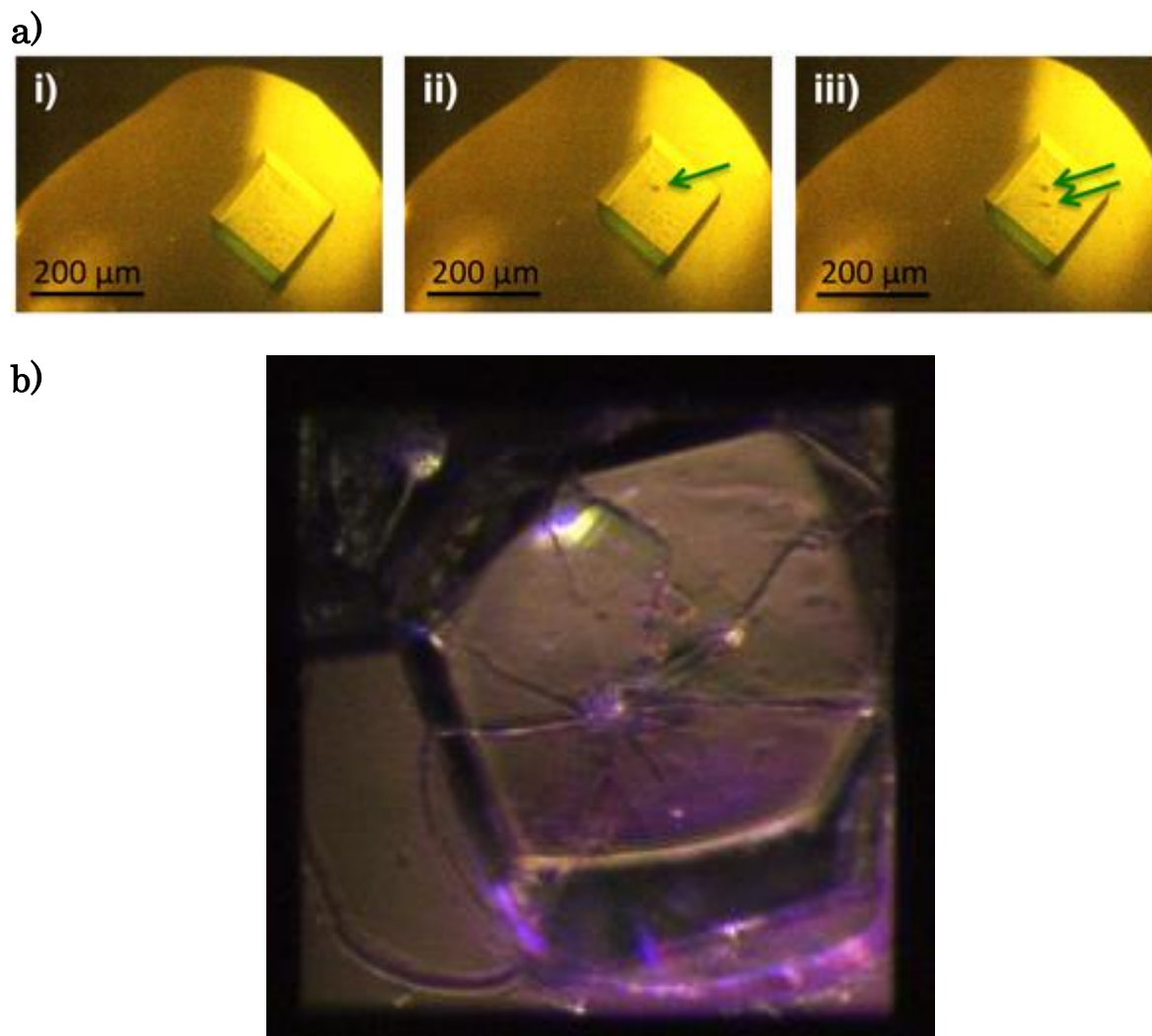


Figure 2.5 a) Lysozyme crystal grown on a kapton foil in a plate mounted in the sample position as seen in the mother liquor drop by a video camera: i) Before exposure to the X-ray beam, ii) after first shot (indicated by the arrow), and iii) after a second shot on the same crystal. b) Lysozyme crystal grown on the silicon nitride membrane of Chip no. 30, membrane size: $200\ \mu\text{m} \times 200\ \mu\text{m}$; cracked after a shot by 5keV XFEL photons.

2.4. Conclusions

This study demonstrates the feasibility of diffraction data collection on protein crystals by utilizing an X-ray diffraction grating-based multiple beam split-and-delay line. The applied streaking method can be used to perform time-resolved studies on crystals of macromolecules aiming at a better understanding of the damage processes at femtosecond time scales.

The significant advantages of this approach over conventional pump-probe experiments include: (i) no temporal jitter between the pump and the probe pulse, thus the possibility to measure several precisely known delays for each individual pump event [34]. Moreover, (ii) the ability to control focus/defocus of the pump and probe beams separately allows for

an independent adjustment of the pump intensity, and for an optimization of pump and probe spatial overlap. This is not found in any other X-ray probe and X-ray pump methods [2.45-2.48]. The former point is important in the context of protein crystallography, as a conventional pump-probe approach following the response for a single delay only would require renewing the sample for each pump event. Repeating the diffraction experiment for different delays on protein crystals is difficult, as one needs to hit the sample at exactly the same crystal orientation.

The selected sample delivery system based on fixed targets proved to be suitable in providing sufficient amounts of crystalline material at pre-defined positions for serial, automated exposures. Microfabricated silicon nitride membrane chips containing sandwiched crystals were also providing protection of the sample from dehydration. Background scattering from the packaging of protein was much less in the case of the silicon nitride (total thickness: 0.5 μm) in comparison to the thick polyimide (Kapton) foils [*cf.* Fig. CS8, Ref 2.42]. Application of the helium-filled flight tubes further reduced air scattering in the setup.

We were able to record Bragg reflections from lysozyme crystals in the 8 to 15 \AA resolution range that featured clear streaks of delayed reflections. The probed time window here covered 19-213 fs in 8 measurement time points after the initial excitation provided by the main pump beam. Further probe beams with longer delays (9th, 10th, 11th channel) exist; however, they gave too weak intensities to be taken into account for data analysis. The collected diffraction data give no proof of any radiation damage on this time scale, which is the most relevant time scale for serial femtosecond crystallography. If there were damaging effects of FEL X-rays on protein crystals within the probed time range, they must have been smaller than the error bars of our measurements. These findings are consistent with the approximate values of radiation doses deposited on the crystals in our experiment of 0.1-0.2 MGy (*cf.* Section 2.3.1.), which are at least one order of magnitude below the dose required for femtosecond damage and also at least three orders of magnitude lower than in the studies described by Chapman *et al.*, [2.32]. Doses applied in our experiment are also relatively low in comparison to doses reported to cause damage in synchrotron measurements that showed no apparent change of the Bragg peak intensity below 1 MGy [2.49].

The following improvements can be made for the future attempts of similar experiments, especially addressing the issue of increasing the deposited radiation doses on the probed crystals: (i) Increase of the pulse energy by application of a brighter X-ray source; (ii) Increase the transmission of the setup, which was limited to $\sim 10\%$ in our experiment, *e.g.*, by reducing absorption losses in the diamond exit window of the beamline, or the support membranes of the G1 gratings; (iii) focusing the photon beam to a smaller spot. Reducing the illuminated area from the 50 μm in diameter as in our experiment to, *e.g.*, 1.5 μm would increase the dose by more than 3 orders of magnitude. Such spot sizes are routinely achieved at XFELs; however, this would put more stringent requirements

on alignment to assure sufficient spatial overlap of pump and probe beams.

The presented study is a proof of concept of the single-shot collection of diffraction data from protein crystals probed with several delays after excitation by an XFEL laser pulse. This method, once further optimized, can be applied for studying ultrafast dynamics in proteins.

Supplementary material

See supplementary material for additional figures: Appendix C.

Acknowledgements

Diffraction experiments were carried out at the Linac Coherent Light Source, a national user facility operated by Stanford University (USA) and at the Swiss Light Source (beamline X06DA), Paul Scherrer Institute (Villigen, Switzerland). The diffraction gratings were tested at the cSAXS (X12SA) beamline of the Swiss Light Source.

Use of the Linac Coherent Light Source (LCLS), SLAC National Accelerator Laboratory, is supported by the U.S. Department of Energy, Office of Science, Office of Basic Energy Sciences under Contract No. DE-AC02-76SF00515. Part of this work was performed under the auspices of the U.S. Department of Energy by Lawrence Livermore National Laboratory under Contract No. DE-AC52-07NA27344.

The research leading to these results has received funding from the European Community's Seventh Framework Programme (FP7/2007-2013) under grant agreement no. 290605 (PSIFELLOW/COFUND) and from the Swiss Nanoscience Institute *via* the Ph.D. school Project No. P1305.

We thank Brian Kobilka, Stanford University School of Medicine for the access to his Mosquito® dispensing robot suitable for protein crystallization on the Kapton-backed plates. We acknowledge support from Gabriella Carini related to setting up parameters of CSPAD detector. We thank: Eugen Deckardt for technical support in constructing the delay line; Helena David for crystalline sample preparation at DESY; Xavier Donath for technical support during the test experiments at the cSAXS beamline; René Lengweiler for help in preparation schemes for Figure 2.1 in CAD-based 3D modelling software; Andri Fränkl for careful proofreading the manuscript; and Thomas Braun for fruitful discussions during manuscript preparation.



Chapter 3

“I was taught that the way of progress was neither swift nor easy.”
Maria Skłodowska-Curie

X-ray fluorescence detection for serial macromolecular crystallography using a JUNGFR AU pixel detector

Isabelle Martiel ^a, Aldo Mozzanica ^a, Nadia L. Opara ^{a,b,c}, Ezequiel Panepucci ^a, Filip Leonarski ^a, Sophie Redford ^a, Istvan Mohacsi ^a, Vitaliy Guzenko ^a, Dmitry Ozerov ^a, Bernd Schmitt ^a, Bill Pedrini ^a and Meitian Wang ^a

^a Paul Scherrer Institute, Forschungsstrasse 111, Villigen 5232, Switzerland

^b Center for Cellular Imaging and NanoAnalytics (C-CINA), Biozentrum, University of Basel, Basel 4058, Switzerland

^c Swiss Nanoscience Institute, University of Basel, Basel 4056, Switzerland

Available online:

<https://journals.iucr.org/s/issues/2020/02/00/ig5086/ig5086.pdf>

Journal of Synchrotron Radiation **27**, 329-339 (2020).

This article has supporting information at <https://doi.org/10.1107/S1600577519016758/ig5086sup1.pdf> consisting of Materials and Methods, edge scan detailed information, and various figures and tables (edge scan values), in this thesis as Appendix D.

All article content, except where otherwise noted, is licensed under a Creative Commons Attribution (CC-BY) license.

Synopsis: Method for precise positioning of the sample in the XFEL beam is demonstrated. X-ray fluorescence signal method can be measured with charge-integrating detector.

Abstract

Detection of heavy elements, such as metals, in macromolecular crystallography (MX) samples by X-ray fluorescence is a function traditionally covered at synchrotron MX beamlines by silicon drift detectors, which cannot be used at X-ray free-electron lasers because of the very short duration of the X-ray pulses. Here it is shown that the hybrid pixel charge-integrating detector JUNGFRAU can fulfill this function when operating in a low-flux regime. The feasibility of precise position determination of micrometre-sized metal marks is also demonstrated, to be used as fiducials for offline prelocation in serial crystallography experiments, based on the specific fluorescence signal measured with JUNGFRAU, both at the synchrotron and at SwissFEL. Finally, the measurement of elemental absorption edges at a synchrotron beamline using JUNGFRAU is also demonstrated.

3.1. Introduction

X-ray free-electron lasers (XFELs) are highly brilliant X-ray sources that deliver X-ray pulses with a duration of femtoseconds. These ultra-short pulses are attractive for macromolecular structure determination by crystallography because they allow the study of small crystals down to submicrometre sizes and give access to radiation-damage-free structures by the ‘diffract-before-destroy’ approach [3.1-3.3]. Because of the high peak intensity of the pulses, the sample is locally destroyed and data collection must be performed in a serial manner while replacing the sample between pulses [3.4]. The XFEL beam time and protein samples are both extremely valuable, which means that both the hit rate (*i.e.* the proportion of useful images) and the sample consumption must be optimized. In fixed-target approaches, it is possible to reach high hit rates, either by prepositioning the crystals at specific positions [3.5-3.8] or by prelocating the crystals on their support and addressing them at their positions with the beam in a precise manner [3.9].

In the crystal prelocation approach, the crystal positions are identified prior to diffraction data collection. Possible prelocation methods include X-ray based methods such as diffraction-based rastering [3.10] or X-ray imaging [3.10-3.11], and optical imaging methods such as UV-visible fluorescence [3.12], cross-polarization or second harmonic generation imaging [3.13]. The prelocation step can be performed online, meaning that the crystals are prelocated immediately before data collection without unmounting the sample from the goniometer or scanning stage used for data collection. This requires integration of the prelocation and diffraction data-collection setup. The prelocation step can alternatively be performed offline with a separate instrument, in which case the prelocated crystal coordinates must refer to fiducials on the sample support [3.5]. The fiducials are then identified when the sample is mounted on the diffraction setup and data collection can take place based on the calculated crystal coordinates. The precise positioning of fiducials is therefore a key step on

which the accuracy of the subsequent data-collection process relies. Positioning inaccuracies larger than the beam size would result in missing the crystals while locally damaging the sample with the XFEL beam. Positioning of fiducials, or more generally coordinate retrieval, at the beamline has been achieved by visual identification on the online viewing system [3.14], either letting the user manually select them on the graphical user interface or using automatic pattern recognition schemes on the chip [3.15]. However, in some samples the fiducials may be hardly visible. Manually indicating their position on the user interface, *e.g.* by mouse clicking, may be too imprecise or time-consuming and is not amenable to automation. We propose to employ metal fiducials placed on the chips to serve as coordinate references and use their fluorescence signal as a fiducial detection method at the beamline. The advantages of this approach are that the energy-specific fluorescence signal cannot be hidden by the protein sample and support, *i.e.* the marks can be detected even if they are not visible, and the precision of the position determination relies solely on the hardware precision. This method is also easily amenable to automation. A prerequisite is that the metal fiducials also appear in the prelocation step used to find the crystal positions offline so that coordinate matching can be performed. This is the case in particular in X-ray imaging methods, as we will separately show (manuscript in preparation).

The silicon drift detectors (SDDs) commonly used at synchrotron beamlines cannot serve at XFELs since they count single photons only at microsecond rates [3.16]. Spectral recording at XFELs is currently often carried out using specialized setups such as bent crystal spectrometers, *e.g.* in von Hamos geometry [3.17-3.18], or reflective zone plates [3.18]. The angular footprint of such spectrometers is not negligible so their integration in the measurement setup must be carefully planned and compromises must be found for collecting diffraction data simultaneously [3.17-3.18]. The spectral resolution and performance offered by these instruments is higher than that required for certain applications such as simple detection of a known metal's presence by fluorescence. However, bent crystal spectrometers certainly remain indispensable for other advanced macromolecular crystallography (MX)-related experiments requiring the detection of subtle signal modulations, for instance for the detection of oxidation states in protein-bound ions and functional clusters [3.18]. Energy-discriminating measurements have also been demonstrated at XFELs using pnCCDs [3.19-3.20].

The low noise and high sensitivity of modern hybrid pixel X-ray detectors make them good candidates for metal-detection applications. Hybrid pixel X-ray detectors are composed of a sensor, usually made of silicon for the conventional energy range for MX applications, directly bump-bonded to an application-specific integrated circuit (ASIC). Detectors with two classes of ASICs are available: photon counting and charge integrating. Photon-counting detectors increase a digital counter by one when the signal exceeds a defined threshold because of a photon hit. In the case of photon counters with a single threshold like PILATUS and EIGER [3.21],

the pixel output corresponds to the number of events where the photon energy was higher than the defined threshold. This allows the suppression of dark and read-out noise and of lower-energy fluorescence by placing the threshold between the fluorescence energy and the incoming beam energy, though it does not allow for detecting only lower-energy fluorescence photons while ignoring higher-energy photons at the incoming beam energy. However, such a filtering of photons by energy could be achieved with photon counters having more than one threshold (color mode), *e.g.* Medipix3 [3.22] and EIGER2 [3.23-3.24]. But the photon-counting technology would remain inadequate for XFEL applications because of the pulse brilliance, because after counting a photon the electronic signal needs to decay below the threshold value before another photon can be detected, resulting in a ‘dead time’ and photon pile-up limitations. This is extremely severe for XFEL pulses, where the photon-counter dead time is orders of magnitude longer than the duration of a single pulse. In charge-integrating detectors such as JUNGFRÄU, the total charge generated by the photons is collected during the integration time in each pixel and read out for each acquisition. This makes charge-integrating detectors optimal for XFEL applications, as the incoming photon number can be determined even if photons arrive within a short pulse. The pixel output is directly proportional to the energy of the incoming photons. If the flux is low enough that most pixels record single photons, individual photon energies can be readily measured. Alternatively, the number of photons can be determined as the total charge divided by the charge generated by a single photon.

Here we demonstrate practically that the JUNGFRÄU hybrid pixel charge-integrating detectors that are installed at SwissFEL, among other facilities, are suitable for the detection of energy-dispersive fluorescence signals for two major fluorescence-based MX applications. We make use of the charge-integration technology in a regime of very low photon flux, and therefore very low dose, to determine the energy of single incoming photons on single pixels and combine the full detector area information into a fluorescence spectrum from scanning maps. We also show here that JUNGFRÄU is suitable for recording fluorescence absorption-edge scans on standard samples, suggesting that it could fulfill the function traditionally devoted to SDDs at MX synchrotron beamlines. The application of JUNGFRÄU for synchrotron crystallography data collection has been developed recently [3.25].

3.2. Materials and Methods

For concision, experimental details about the preparation of samples, data processing and absorption-edge scans are given in the supporting information. Fig. DS13 in the supporting information is a schematic with the distances of the experimental setup.

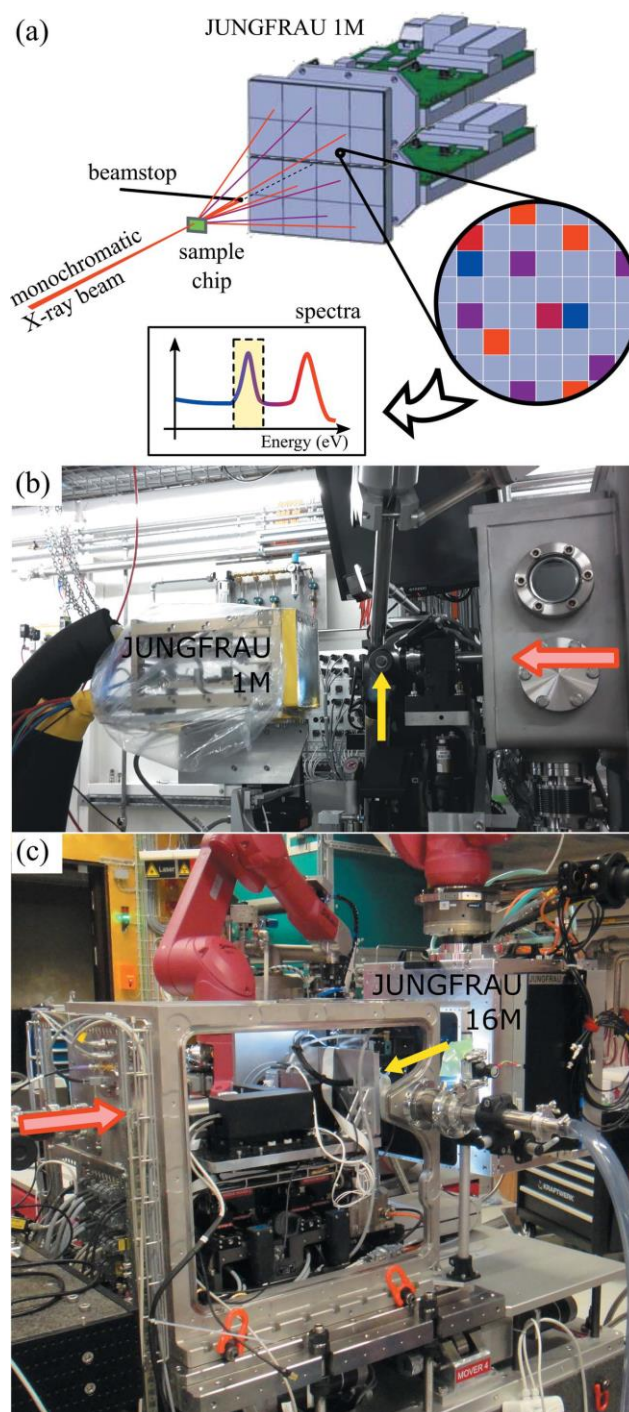


Figure 3.1 (a) Schematic of the geometry of the experiment and how spectra are obtained. (b) Photograph of JUNGFRAU 1M installed at the X06SA PXI beamline, with external cooling and nitrogen environment. (c) Photograph of JUNGFRAU 16M in operation at SwissFEL Bernina with the SwissMX instrument. The red arrows show the direction of the X-ray beams and the yellow arrows show the sample positions.

3.2.1. Synchrotron data collection of fluorescence maps

The JUNGFRAU 1 megapixel (1M) detector was installed at the X06SA PXI beamline at Swiss Light Source (SLS), Villigen, Switzerland [Fig. 3.1(b)]. It consists of two 0.5 megapixel modules stacked vertically, with a horizontal gap of 2.7 mm and total dimensions of 77 mm x 80 mm.

The sensitive surface is protected by a 20 μm aluminized mylar film. External cooling was applied to reduce the noise level in long integration times, set at a temperature of minus 12°C. A protective plastic film filled with nitrogen gas was wrapped around the detector to prevent condensation. The detector was placed on a stack of xyz stages, with the z stage (beam direction) motorized. The silicon sensor thickness was 320 μm . Pedestals were recorded for all datasets with the X-ray shutter closed and detector calibration was performed in the laboratory prior to the experiments [3.26]. The beamline energy was set to 12.398 keV. The beam size was 5 μm x 5 μm with a full flux of 1.13×10^{11} photons s^{-1} . The sample-to-detector distance was 40 mm and the sample-to-beamstop distance was 15 mm.

Mapping was performed using the D3 goniometer [3.27], similar to the rastering procedure described by Wojdyla *et al.* [3.10]. The grid-cell dimensions were identical to the beam size, 5 μm x 5 μm , except for oversampled scans where the cells were 2 μm x 2 μm and 1 μm x 1 μm . Unless stated otherwise, the beam transmission was 4% and the detector was triggered at the beginning of each row to collect images at a rastering rate of 100 Hz, while the detector was operated with a 1.0 kHz repetition rate and a duty cycle of 0.25 (*i.e.* 250 μs integration time per image), meaning that ten images were collected per cell of the raster grid.

Fluorescence maps were also collected with the photon-counting EIGER X 16M (Dectris, Baden-Daettwil, Switzerland) using the standard rastering procedure of the X06SA PXI beamline [3.10], using a single image per cell without changing the automatically set internal threshold of half of the incoming photon energy, which is below the fluorescence energy of the investigated metals for the incoming radiation of 12.389 keV. The detector distance for the EIGER 16M measurements was 135 mm.

3.2.2. Synchrotron data collection of absorption-edge scans

The setup was essentially similar to that used for the fluorescence maps. Complete details are given in Section DS2.1 of the supporting information. The JUNGFRÄU 1M detector was operated at 2.2 kHz, since this operating condition had become available at the time of the measurement.

3.2.3. XFEL data collection of fluorescence maps

Fluorescence data were also collected at the SwissFEL Bernina station [3.28], using the JUNGFRÄU 16 megapixels (16M) operated at room temperature and mounted on a robot arm attached to the ceiling [Fig. 3.1(c)]. The beam parameters were 9.06 keV photon energy, 250 μJ pulse energy (full beam) and 25 Hz repetition rate. The beam was focused slightly smaller than 5 μm x 5 μm FWHM and attenuated to typically 0.64% transmission. Samples were scanned using the SwissMX instrument for fixed-target MX [3.17, 3.28]. The integration time of the detector was 10 μs . The sample-to-detector distance was 0.2 m and the entrance of the post-sample tube (2 mm outer diameter) was placed 25 mm

after the sample. Each pulse was recorded in a separate image and corresponds to a unique scanning position and grid cell, in contrast to the SLS experiment where several images were summed for each cell of the grid.

3.3. Results and discussion

3.3.1. Choice of data-collection parameters

The data-collection parameters were carefully chosen to guarantee that the number of incoming photons per pixel per frame was well below 1, both at the synchrotron and at the XFEL. This is necessary to ensure that the maximum charge detected by each pixel corresponds to an isolated photon so that the final spectrum reflects the incoming radiation as accurately as possible. In these low-flux conditions, double counts are minimized; however, charge-sharing effects between neighboring pixels are still present. A typical image contained more than 90% of pixels with no apparently detected photon (Fig. DS9). The suitable range of conditions corresponds in practice to several orders of magnitude attenuation of the X-ray beam, which are realistic parameters for XFELs in normal self-amplified spontaneous emission (SASE) mode or using a monochromator. Another important parameter is the dose received by the protein samples. With the typical beam parameters used here for collecting fluorescence maps with JUNGFRAU, the dose received by a crystal with the same size as the beam is of the order of 1 kGy. This dose is two orders of magnitude lower than the dose received by the same crystal during a standard diffraction rastering at 100 Hz with full beam, which is about 0.1 MGy. In the absorption-edge measurements at the synchrotron, the exposure conditions were comparable with those of an SDD measurement.

3.3.2. Fluorescence maps

3.3.2.1. Scanning maps on model samples

Fluorescence maps were first measured at the SLS by raster-scanning samples on a regular grid at very low incident flux and summing the pixels which recorded a photon with an energy around the expected metal fluorescence energy [Fig. 3.1(a)]. Map scanning was initially performed on model samples carrying only metal marks of 1 μm thickness, consisting of 3 μm -sized crosses with 1 μm branches [Fig. 3.2(a)]. Representative spectra are shown in Fig. 3.2(b) and Fig. DS4 of the supporting information. The peak at the incoming photon energy is present in all curves and results from elastic scattering from the direct beam. A second peak at the fluorescence energy of the metal is visible in the presence of the metal (dark blue curves). All the spectra also display a charge-sharing baseline signal extending from the highest incoming energy down to zero (see Section 3.2.3). Fig. 3.2 shows representative maps obtained from the Au and Ni samples [Figs. 3.2(e) and 3.2(g)] with a comparison with the

online microscope view where the grid has been defined [Figs. 3.2(f) and 3.2(h)]. With the fluorescence maps, metal dots are easily distinguished from dust particles [purple arrows in Figs. 3.2(e) and 3.2(f)] deposited on the membrane surface, which are present in the optical image but do not give rise to a fluorescence signal at the expected energy. The signal-over-background ratio (SBR) for the mapping scans presented in Figs. 3.2(e) and 2(g) is 10.2 ± 0.2 and 7.3 ± 0.2 for Au and Ni, respectively.

After this successful proof-of-principle demonstration at the SLS, the viability of the detection was confirmed at SwissFEL. Fluorescence map scans were performed at SwissFEL during commissioning time, using the SwissMX fixed-target station [3.17, 3.28] and JUNGFRÄU 16M of the Bernina endstation, on the nickel model samples. Because of time limitations, only a few scans were recorded and only on small areas around individual marks. Fig. 3.2(c) shows a scan over a single nickel mark and Fig. 3.2(d) shows the corresponding representative spectra with a SBR of 21.5. The enhanced SBR at SwissFEL compared with the SLS seems to result from the relatively lower intensity of the direct-beam scattering, which may come from subtle differences in the measurement endstations (Fig. DS13), such as the beamstop or post-sample tube size and distance to the sample, as well as the slightly different beam sizes. The higher counts read in Fig. 3.2(d) compared with Fig. 3.2(b) results from a factor 50 in the incoming flux between both setups.

The SwissMX scanning stages can be enclosed in a chamber for operation in a helium or air environment. In helium, low-energy X-rays such as fluorescence signals from Fe or Ni may be detected more easily since they are not absorbed in the long path in air until they reach the detector. However, this effect will be partly compensated by the kapton back-window closing the He chamber, as well as the possibly increased thickness of the protective aluminized kapton foil on the detector.

3.3.2.2. Influence of collection parameters on model samples

A systematic study of several parameters was undertaken to evaluate the robustness of the detection method. At the synchrotron, the X-ray beam transmission was varied between 0.04% and 100% to investigate the influence of the number of photons per exposure [Fig. 3.3(a)]. An optimal transmission was observed because of the competition between increased background noise at low transmission and progressive departure from the conditions of a single photon per pixel at high transmission, where the energy of the incoming photons can no longer be determined reliably.

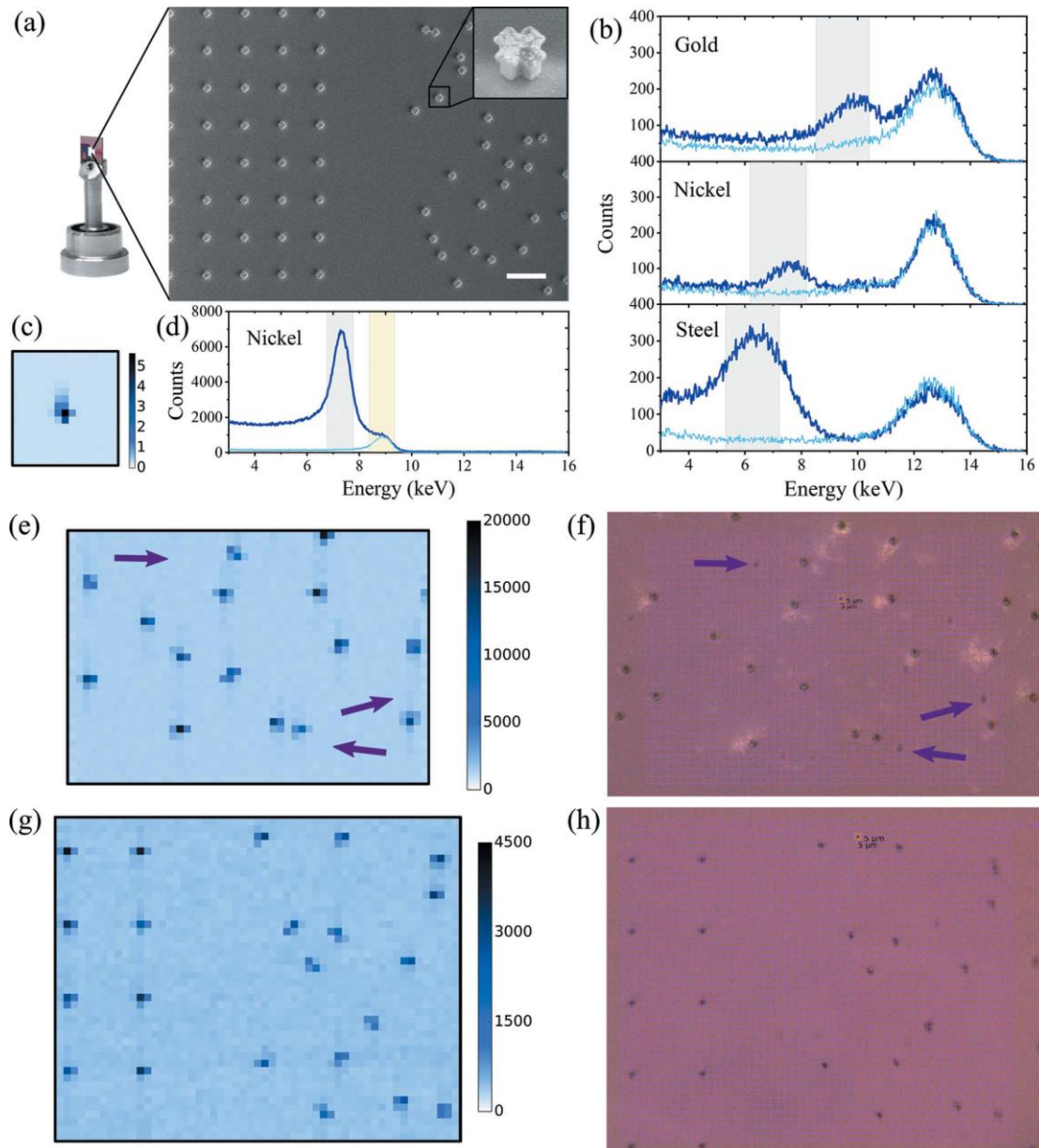


Figure 3.2 (a) Si_xN_y membrane fixed on a chip pin and a scanning electron microscopy (SEM) image of the electroplated metal structures on the Si_xN_y membrane; the scale bar is 20 μm . Inset: magnified view on a 3 μm gold cross with a 35.6° tilt. (b) and (d) Representative spectra, cumulated from all detector pixels, for different metals investigated: (b) from representative samples sandwiched between Si_xN_y windows at the SLS (JUNGFRAU 1M) and (d) from a model nickel sample at SwissFEL (JUNGFRAU 16M). The thick dark blue curves correspond to a grid cell where the metal was present; the thin light blue curves correspond to another cell of the same grid where the metal was absent. The gray areas represent the ROI used for extracting the fluorescence signal. (c) and (e)–(h) Examples of maps obtained from gold [(e) and (f)] and nickel [(c), (g) and (h)] model samples. (c) Fluorescence map from a JUNGFRAU 16M at the SwissFEL. The color scale shows the ratio of fluorescence to direct-beam ROI counts. For this FEL case, the signal from the fluorescence ROI was normalized to the counts in the direct-beam energy ROI [shown as gray and yellow, respectively, in (d)]. (e) and (g) Fluorescence maps from a JUNGFRAU 1M at the SLS. The corresponding inline camera view is shown in (f) and (h). The purple arrows point to dust particles present on the membranes. The color scales show summed ROI counts (arbitrary unit of fluorescence signal).

Representative maps are shown in the supporting information (Fig. DS5). Table 3.1 shows the SBR obtained while varying other collection parameters on the same grid. The duty cycle was compared at 0.25 and 0.01 to investigate detector noise levels. In this case, a moderate loss of SBR is observed with the longer integration time because of the accumulation of noise. The rastering speed was compared at 10 Hz and 100 Hz while keeping the number of photons constant. A slightly lower fluorescence signal was observed at the lower rastering speed (Fig. DS5), which caused a moderate drop in SBR. This might be caused by imprecision in the transmission settings or by a more precise sampling of the metal mark with the partial duty cycle used here. Generally, situations where the overall number of incoming photons is reduced give noisier spectral curves (*cf.* Fig. DS6). However, within a certain range of variation of experimental parameters, the SBR obtained from the summed region of interest (ROI) counts remains relatively unchanged and reliable. This indicates that the detection technique is robust and could be employed over a wide range of measurement conditions.

In the data collected at SwissFEL, the large area of the 16M detector makes it possible to study the effects from the positioning and area of the sensitive surface. In Fig. 3.3(b), the fluorescence was measured on square 1M spatial ROIs placed on the 16M area with offsets to the center in the vertical and horizontal directions [Fig. DS11(a)]. The SBR increases with the offset to the center because the fluorescence photons are scattered essentially isotropically and therefore are overrepresented compared with elastic scattering which takes place predominantly in the forward direction. On the edge of the detector, the two curves slightly separate: the fluorescence counts and SBR become higher for a horizontal offset than for a vertical offset, possibly reflecting the polarization of the X-ray beam. Fig. 3.3(c) shows that the detected signal essentially does not depend on the area of the detector over the wide range studied. The rectangular ROIs were chosen to preserve comparable radial symmetries [Fig. DS11(b)] in order to eliminate the angular effects presented in Fig. 3.3(b). This becomes difficult at large areas, where high-angle pixels are slightly overrepresented, thus increasing slightly the measured SBR above 2 megapixels.

For comparison, scanning maps were also performed at the synchrotron using a detector without energy-dispersive detection features, *i.e.* a large-area single-photon-counting detector EIGER 16M (Table 3.1), using as close as possible parameters (see Section 3.2), in particular the same solid angle and incoming flux per cell. The obtained fluorescence SBRs are substantially lower and are strongly influenced by the integration geometry (Fig. DS12). In particular, in the forward direction (*i.e.* when integrating close to the direct beam), the SBR is so low that fluorescence detection becomes impossible with EIGER [Fig. DS12(a)], whereas the SBR remains high with JUNGFRÄU [Fig. 3.3(b)].

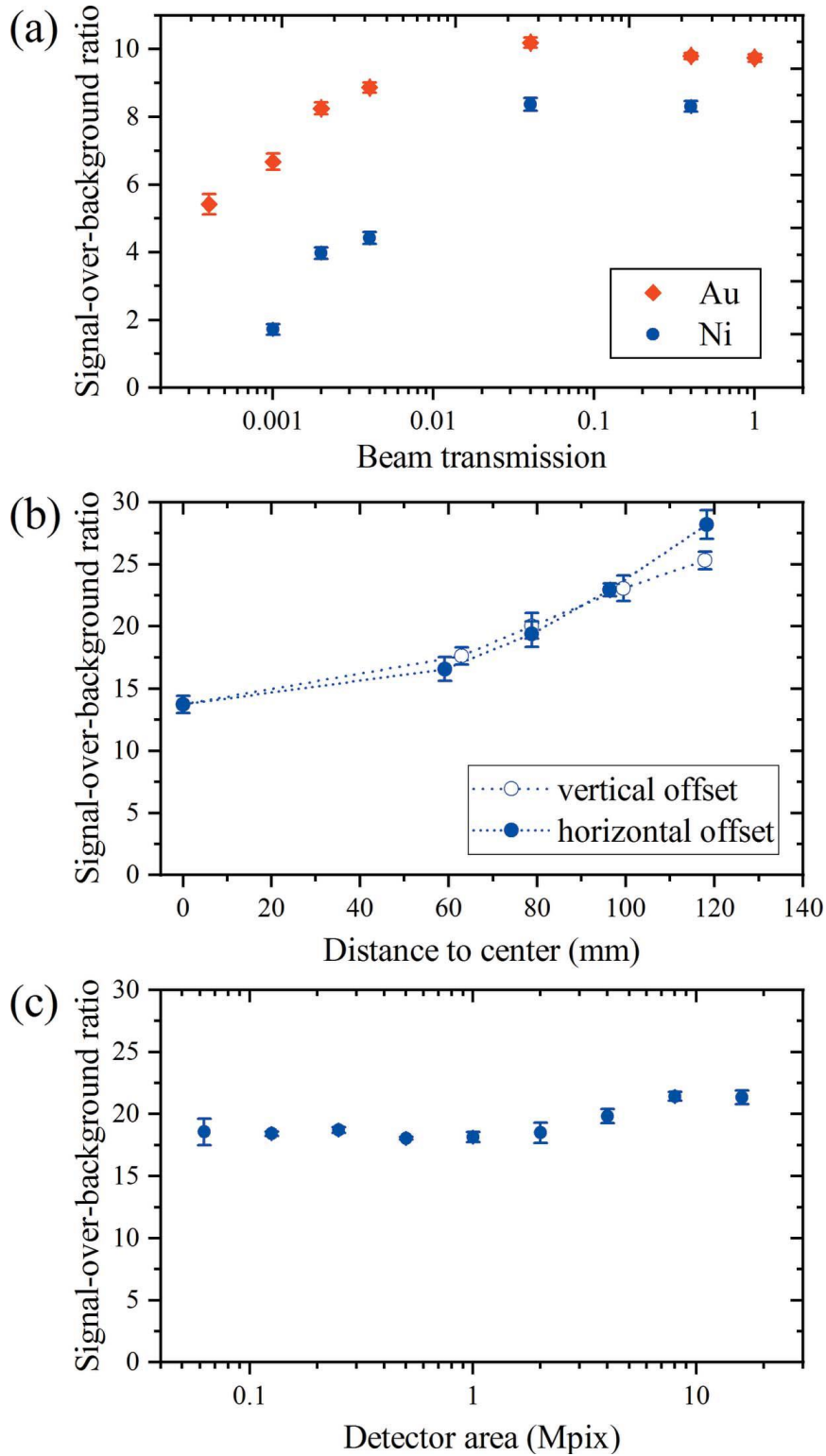


Figure 3.3 (a) SBR as a function of the beam transmission for gold and nickel model samples measured at the SLS with a JUNGFRAU 1M. (b) SBR from a nickel model sample as a function of the vertical and horizontal offset of a 1M spatial ROI on the JUNGFRAU 16M at SwissFEL. (c) SBR from a nickel model sample as a function of the area of the spatial ROI on the JUNGFRAU 16M at SwissFEL.

Table 3.1 Influence of various detection parameters on the SBR for the gold and nickel model samples, measured at the SLS.

n.d = not determined. The duty cycle is the ratio between the integration time and period associated with the detector frequency of operation.

	Varying parameter	Experimental conditions	SBR (Au)	SBR (Ni)
Duty	0.01	100% T, 100Hz	11.4 ±0.1	n.d.
cycle	0.25	100% T, 100Hz	9.7 ±0.1	-
Raster	10 Hz (100 images cell ⁻¹)	0.4% T, duty cycle 0.25	6.6 ±0.1	n.d.
speed	100 Hz (10 images cell ⁻¹)	4% T, duty cycle 0.25	10.2 ±0.2	-
Detector	JUNGFRAU 1M (energy dispersive)	4% T, 100Hz, duty cycle 0.25	10.2 ±0.2	7.3 ±0.2
type	EIGER 16M (total photon counts)	0.1% T, 10Hz, duty cycle 1	4.2 ±1	1.8 ±0.2

3.3.2.3. Scanning maps on real-life samples

To assess the practical usefulness of the method, it is required to evaluate the impact of the presence of other materials in the beam path, which increases the elastic signal by scattering the incoming X-rays and reduces the SBR. The real-life protein-containing samples investigated here are representative of in situ methods [3.29-3.30] where the matrix or mother liquor is not removed from the support, thus resulting in a high elastic scattering signal. In other experimental methods, it is possible to remove the mother liquor to decrease the background and to improve the diffraction SBR [3.6-3.7]. The fluorescence signal from such samples would also benefit from the mother-liquor removal and resemble more the SBR obtained from model samples. The choice of high-background real-life protein-containing samples in our experiments exemplifies the applicability of the method presented here to a broad range of samples.

In the scope of this work on fluorescence detection, no diffraction data were collected from the embedded protein crystals. Demonstration of MX data collection from prepositioned protein crystals using fiducials on the same samples will be the topic of a separate publication. Characterization of the MX data-collection performance of JUNGFRAU has been reported elsewhere [3.25]. The fluorescence signal is used solely to detect the metal fiducials and never to detect the crystals themselves, as the offline prelocation process implies that these are detected using a different technique.

Two types of representative real-life samples containing protein crystals were investigated. In the first sample, the micrometre-thick Au or Ni fluorescent marks on Si_xN_y, previously investigated as model samples, were used as one side of a 140 μm sandwich of lipidic cubic phase (LCP) containing protein crystals [Figs. 3.4(a)–(e)] to determine whether the uniformly spaced marks could still be detected in the presence of increased background. In the second sample, steel microbeads of 1 to 22 μm diameter were randomly embedded in the crystal-containing LCP to

simulate iron fluorescent marks with unknown spacing and sandwiches were prepared from both Si_xN_y membranes without metal marks [Figs. 3.4(f) and 3.4(g)] and 25 μm -thick cyclic olefin copolymer (COC) films [total thickness 190 μm , Figs. 3.4(h) and 3.4(i)]. In all cases, the positions of metal objects were readily identified in the fluorescence map, while they were not always clearly visible in the online camera view, for instance inside the frozen bolus. The bolus edges clearly appeared as a drop in the background counts. For the Si_xN_y sandwich with gold and nickel marks, the SBR was 2.6 ± 0.1 and 2.5 ± 0.1 respectively, compared with 10.2 ± 0.2 and 7.3 ± 0.2 , respectively, for the model samples measured in identical conditions. The drop in SBR is caused by the higher absorption and signal from X-ray scattering in the LCP matrix. For the steel beads in Si_xN_y and COC sandwiches, the SBR was 16.0 ± 0.2 and 29.3 ± 0.1 , respectively. The SBR values for the steel beads cannot be directly compared with the gold and nickel cases because the steel beads are much larger than the thickness of the microfabricated gold and nickel patterns. With the EIGER 16M, the fluorescence could not be readily detected on the same real-life protein-containing samples (Fig. DS10).

Hybrid pixel detectors display charge-sharing effects, *i.e.* when a photon hits the edge or the corner of a pixel the energy deposited is collected by up to four pixels. Because of this charge-sharing effect, charge-integrating hybrid pixel detectors always provide a distribution of energies based on single pixels which extends below the true photon energy all the way to zero as a continuous energy background in the spectrum, in addition to the main energy peak. Charge summation of neighboring pixels is often used to obtain a correct energy distribution, albeit at the cost of a higher noise level. In order to assess the potential for improvement of SBR, clustering analysis was performed on the Si_xN_y gold protein-containing-sample scan (Fig. DS6). By summing energy readouts of clusters of neighboring pixels instead of considering energy readouts of individual pixels, the low energy baseline of counts induced by charge sharing is strongly reduced. This results in an improvement of the SBR, from 2.6 ± 0.1 to 5.7 ± 0.1 on this fluorescence map.

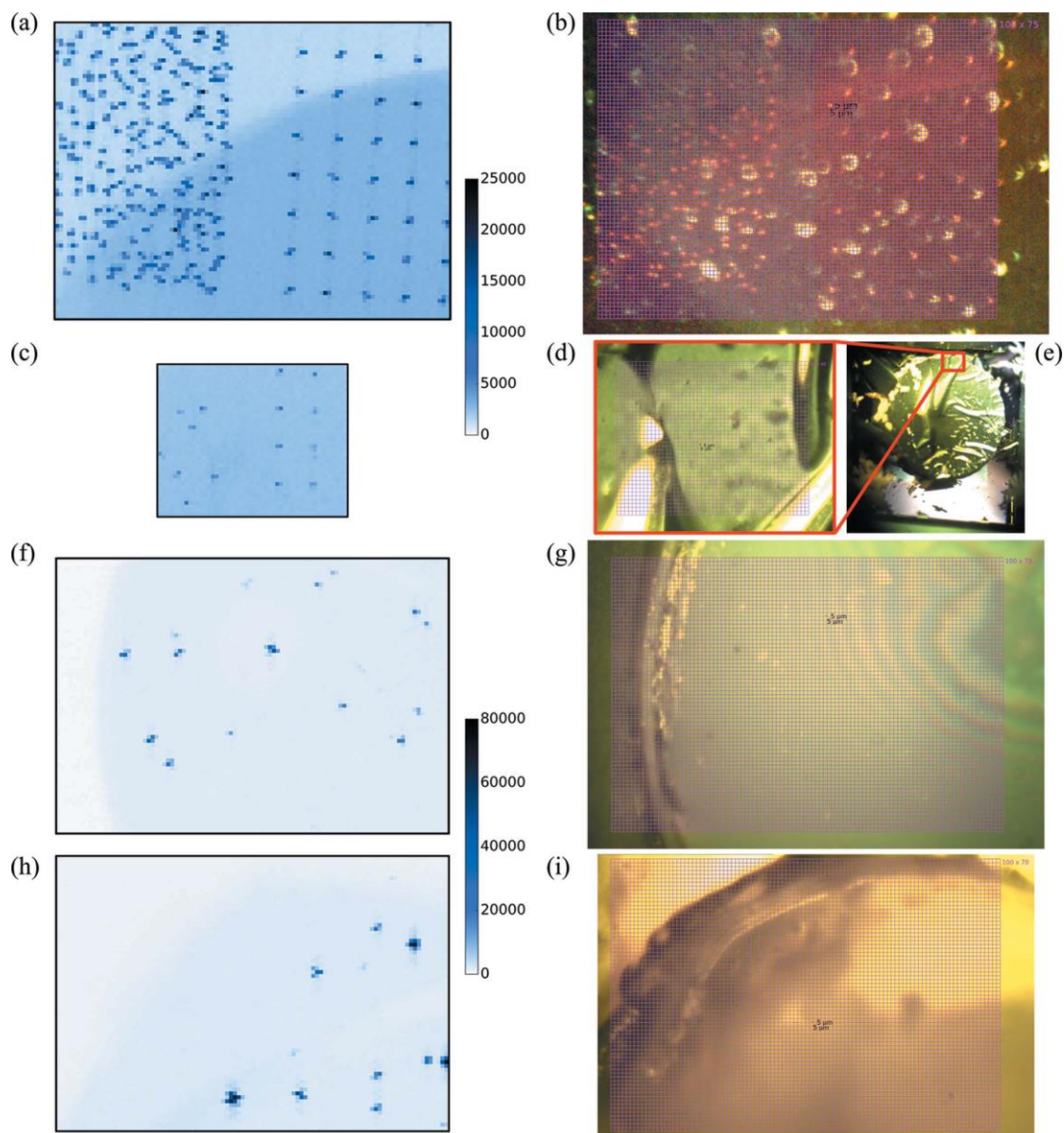


Figure 3.4 JUNGFRUA 1M fluorescence maps from real-life protein-containing samples [(a), (c), (f) and (h)] with corresponding views on the online camera [(b), (d), (e), (g) and (i)]. (a) and (b) Au marks. (c)–(e) Ni marks, where the Si_xN_y membrane was partially destroyed around the LCP bolus. (e) A low-magnification view. (f) and (g) Steel microbeads embedded in LCP within Si_xN_y sandwich and (h) and (i) within COC sandwich. Maps (a) and (c), and (f) and (h) are plotted in the same scale of summed ROI counts.

3.3.2.4. Precision of position determination

For high hit-rate data collection on prelocated samples, the fiducial marks must be precisely located. To assess the potential for accurate mark position determination, scans were also performed on the same samples (Figs. 3.2 and 3.4) in oversampled conditions, where the grid-cell dimensions were reduced compared with the beam size. This resulted in a slower scanning speed but more precise sampling of the fluorescence profile of the mark with overlapping frames. Fig. 3.5 shows map details and one-dimensional sections of the oversampled maps (blue dots), and

examples of complete oversampled maps are given in Fig. DS6. In order to determine the position of the center of mass of the metal marks, a theoretical fluorescence profile was calculated by convoluting the beam Gaussian intensity profile with the known shape of the mark, using a simple overlap model (Fig. 3.5, framed inset): the convolution of the 3 μm -wide cross shape and the 5 μm FWHM Gaussian beam was performed by summing the intersection volume while displacing the two objects relative to each other. The center of mass of the marks was then determined by fitting the theoretical curves to the experimental curves (Fig. 3.5, red curves) in both horizontal and vertical directions.

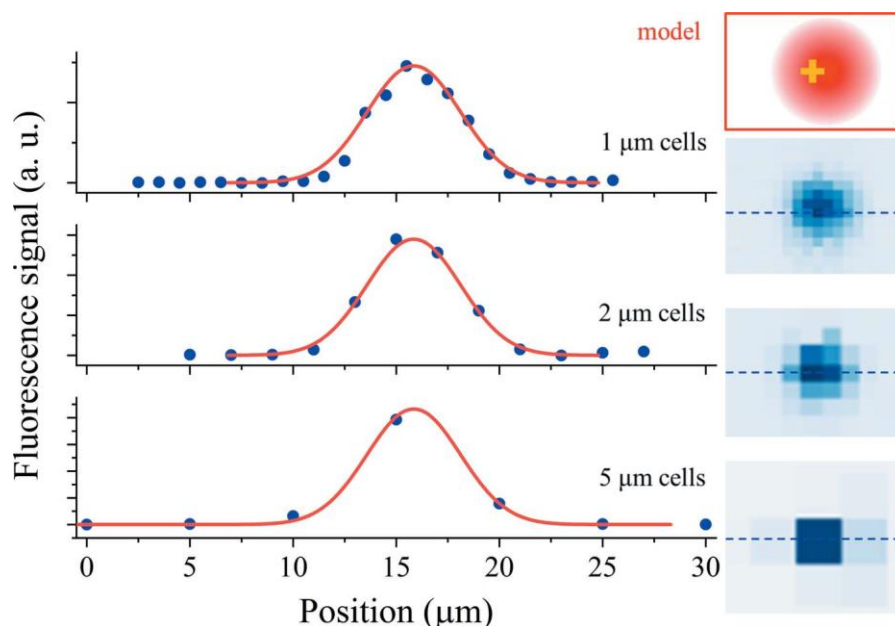


Figure 3.5 Cross section of a gold cross fluorescence map with (from top to bottom) 1 μm , 2 μm and 5 μm cell size, showing the experimental (blue dots) fluorescence profile and fitted overlap model (red curve). The horizontal slices on the left panel correspond to the dashed blue lines on the fluorescence maps on the right panel. Framed inset (top right), schematic of the overlap model used for modeling the experimental signal: convolution of the 3 μm -wide cross shape and the 5 μm FWHM Gaussian beam.

Table 3.2 Effect of oversampling on the differences between the measured and expected distances between marks, in model and real-life protein-containing samples.

		Au		Ni	
	Number of distances measured	Average absolute difference (μm)	Standard deviation (μm)	Average absolute difference (μm)	Standard deviation (μm)
1 μm cells, model sample	≥ 3	0.49	0.17	0.28	0.20
2 μm cells, model sample	≥ 10	0.60	0.41	0.45	0.26
5 μm cells, model sample	≥ 10	0.82	0.86	1.58	1.24
5 μm cells, real-life sample	≥ 10	1.31	1.49	2.24	1.64

A good agreement was obtained between the experimental and the theoretical profiles. For prelocation processes, distances are a relevant measurement because the spacings between fiducials matter more than their individual absolute positions. The quality of the position determination was assessed by measuring all distances between marks on a map and comparing with the expected values of the pattern design. Statistics were calculated on the values of the differences between measured and expected distances, taking the absolute differences to avoid error-compensation effects (Table 3.2). From these results, we concluded that the achieved precision of position determination is in all cases better than the size of the grid cells. Oversampling increases the position-determination precision, which makes it possible to reach submicrometric precision with a moderate oversampling. The lower SBR obtained from protein-containing real-life samples decreases the position-determination precision. The precision observed with the nickel protein-containing sample is worse than expected. As seen in Figs. 3.4(d) and 3.4(e), this sample was broken around the bolus and the mark-bearing membrane was wrinkled, which may partly explain the worsening of the precision of position determination.

3.3.3. Absorption-edge scans

Proof-of-principle absorption-edge scan measurements were performed at the SLS on large protein crystals representative of standard synchrotron rotation experiments (Fig. 3.6). Experimental methods and results are detailed and discussed in the supporting information (Section DS2, Fig. DS8, Tables DS1 and DS2). A 90 μm x 50 μm crystal of selenomethionine containing protein was chosen as an example displaying a clear white line above the absorption edge. Experimentally determined curves (Fig. 3.6) and values (Table DS1) are in excellent agreement with the measurement performed with SDDs on the same sample, and within the variation observed between SDD measurements at two different beamlines [Fig. DS8(d)]. The example of a mercury-soaked model crystal, an element for which the peak is not prominent, is also shown in the supporting information [Figs. DS8(c) and DS8(e), Table DS2].

A charge-integrating pixel detector like JUNGFRU, with small pixels and a relatively high noise, is arguably no match for a dedicated energy-dispersive detector like a commonly used SDD. Charge sharing produces a continuous background at all energies below the measured energy and the higher electronic noise gives photon-energy peaks which are a factor of five broader compared with peaks typically obtained with a SDD [Fig. DS8(a)].

However, in the scope of this work, it is important to note that, in spite of this reduced spectrum quality, JUNGFRU provides enough information to reliably retrieve edge scans of sufficient quality for the investigated purposes. A main JUNGFRU detector installed at a synchrotron beamline could in principle also take over the function of a fluorescence detector for the applications presented above, thus freeing space in the

crowded sample environment in MX beamlines. In addition, the high-angle scattering recorded in a typical diffraction image in MX experiments carried out in a low-dose and fine-phi slicing manner is usually very weak. Therefore, when JUNGFRAU is used as the main X-ray detector at an MX beamline, an analysis of high-angle background scattering could in principle be used to detect most bio-metals. In a multiwavelength anomalous dispersion (MAD) experiment, such utility could provide continuous monitoring of the beam energy and detect potential energy drifts around the absorption edge of interest throughout the entire data collection.

Regarding the possibility of measuring absorption edges at XFELs, it is important to note that the recording of absorption-edge scan data at the XFEL would require reducing the energy bandwidth of the XFEL beam by using a monochromator or a seeded injection scheme. XFEL SASE beams are characterized by a certain energy spread varying from pulse to pulse [3.31-3.33]. The pulse-by-pulse monitoring of the incoming energy spectrum would also need to be included in the data analysis in order to preserve the quality of the resulting fluorescence spectra [3.34].

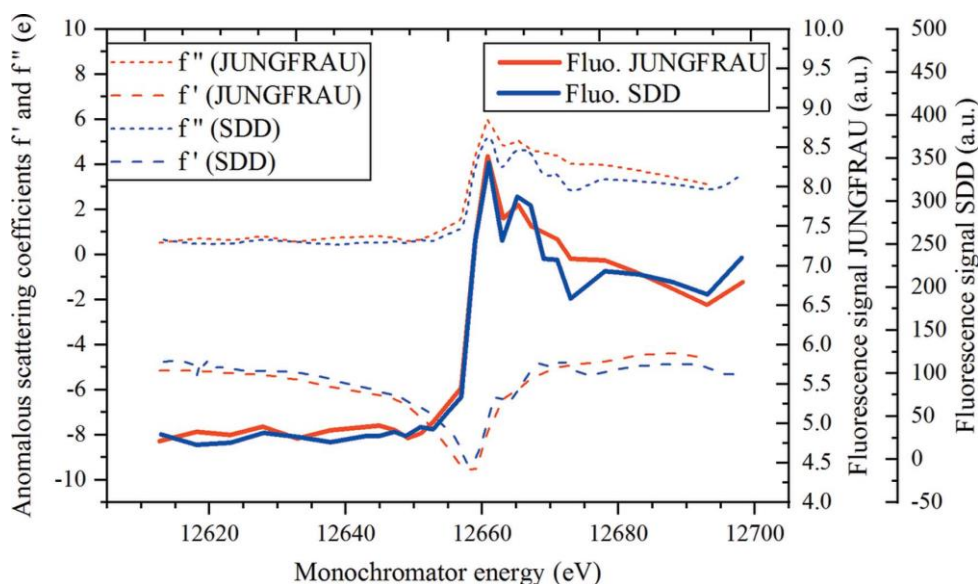


Figure 3.6 Edge scan over the Se edge on a 90 μm x 50 μm crystal showing a comparison between JUNGFRAU and an SDD measurement.

3.4. Conclusions

We have practically demonstrated that the hybrid pixel charge-integrating detector JUNGFRAU can fulfill the functionalities of a spectrometer for X-ray fluorescence detection applications in macromolecular crystallography, thanks to its native energy-dispersive capabilities. The method presented here is valid over a wide range of beam attenuation, allowing low-dose fluorescence detection and therefore protein sample preservation. Two different MX-related applications were investigated: the accurate spatial detection of micrometre-sized metal marks in both model and

representative protein-containing samples, and absorption-edge scans for anomalous data collection. The wide variety of metals used proves the versatility and robustness of the detection. In the case of fluorescence maps, sub-cell precision was obtained by fitting a theoretical fluorescence profile.

Our results are of practical importance considering that the SDDs commonly employed at synchrotron MX beamlines cannot be used at XFELs, whereas JUNGFRÄU detectors are permanently installed or available on request at a number of facilities including SwissFEL. The energy-dispersive capacities of charge-integrating detectors such as JUNGFRÄU could be useful in other types of imaging experiments where the energy-dispersion requirements are similar.

3.5. Related literature

The following references are cited in the supporting information for this article: 3.35-3.43.

Acknowledgments

We acknowledge the SLS X06SA PXI beamline staff for the use of beamline development beam time, the crystallization facility at the SLS for providing lysozyme crystals, Jérôme Basquin (MPG) for providing the selenomethionine-containing crystal, Karol Nass for stimulating discussions and help during the SwissFEL data collection, Dario Marty for technical support when using the PSI-LMN facilities, and Carola Alampi (BioEM Lab) for technical support with SEM imaging. Jan Hora and coworkers at PSI AIK constructed the sample pin used for the model samples.



Chapter 4

“Sir, the impossible we do at once, miracles take a little longer.”
Origin unknown

Supramolecular architectures of molecularly thin yet robust free-standing layers

Mina Moradi^{a,b}, Nadia L. Opara^{b,c}, Ludovico G. Tulli^a, Christian Wäckerlin^d, Scott J. Dalgarno^e, Simon J. Teat^f, Milos Baljovic^b, Olha Popova^g, Eric Van Genderen^c, Armin Kleibert^h, Henning Stahlberg^c, Jan Pieter Abrahams^{i,j}, Philippe F.-X. Corvini^a, Thomas A. Jung^{b,g}, & Patrick Shahgaldian^a

^aInstitute of Chemistry and Bioanalytics, School of Life Sciences, University of Applied Sciences and Arts Northwestern Switzerland, Hofackerstrasse 35, CH-4132 Muttenz, Switzerland

^bLaboratory for Micro- and Nanotechnology, Paul Scherrer Institute, Villigen CH-5232, Switzerland

^cCenter for Cellular Imaging and NanoAnalytics (C-CINA), Biozentrum, University of Basel, Mattenstrasse 26, CH-4058 Basel, Switzerland.

^dEmpa - Swiss Federal Laboratories for Materials Science and Technology, CH-8600 Dübendorf, Switzerland.

^eInstitute of Chemical Sciences, Heriot-Watt University, Riccarton, Edinburgh, Scotland EH14 4AS, UK.

^fAdvanced Light Source, Lawrence Berkeley National Laboratory, 1 Cyclotron Rd, Berkeley, CA 94720, USA.

^gDepartment of Physics, University of Basel, Klingelbergstrasse 82, 4056 Basel, Switzerland

^hSwiss Light Source, Paul Scherrer Institute, CH-5232 Villigen, Switzerland

ⁱBiozentrum, University of Basel, Switzerland and Laboratory of Biomolecular Research, Paul Scherrer Institute, Villigen, Switzerland

^jInstitute of Biology Leiden, Leiden University, Sylviusweg 72, 2333 BE Leiden, Netherlands

Available online: <https://advances.sciencemag.org/content/5/2/eaav4489>
Science Advances **5**, eaav4489 (2019)

This article has supporting information: Appendix E.
Distributed under a Creative Commons Attribution NonCommercial License 4.0 (CC BY-NC).

Synopsis: Synergistically acting weak molecular interactions create robust, free-standing, single molecular layers with ~ 1nm thickness via an interfacial self-assembly process.

Abstract

Stable, single-nanometer thin and free-standing two-dimensional layers with controlled molecular architectures are desired for several applications ranging from (opto-)electronic devices to nanoparticle and single-biomolecule characterization. It is, however, challenging to construct such stable single-molecular layers via self-assembly, as the cohesion of those systems is ensured only by in-plane bonds. We herein demonstrate that relatively weak non-covalent bonds of limited directionality such as dipole-dipole ($\cdot\text{CN}\cdots\text{NC}\cdot$) interactions act in a synergistic fashion to stabilize crystalline monomolecular layers of tetra-functional calixarenes. The monolayers produced, demonstrated to be free-standing, display a well-defined atomic structure on the single-nanometer scale and are robust under a wide range of conditions including photon and electron radiation. This work opens up new avenues for the fabrication of robust, single-component and free-standing layers via bottom-up self-assembly.

4.1. Introduction

The ambition to produce materials with meticulous control over the organization of molecular building blocks has, for decades, attracted chemists and material scientists and triggered their efforts. This longstanding challenge has been met, to a great extent, with the development of reticular chemistry allowing for the design of complex and chemically programmed crystalline materials, namely metal-organic and covalent-organic frameworks (MOFs and COFs) [4.1-4.2]. The strong resurgence of interest in 2-dimensional (2D) materials triggered MOF design strategies to be adapted for the production of 2D networks [4.3-4.10]. The two-dimensional nature of this class of materials considerably limits their stability, however, a substrate is required. Thus, the possibility to produce stable and, *a fortiori*, free-standing monolayers remains a challenge. It is remarkable that currently existing methods do not allow for the fabrication of crystalline and free-standing monolayers of organic building units exclusively via supramolecular interactions between their constituent molecules, in the absence of chemical linkers. Here, we challenge the accepted paradigm endorsing strong and directional interactions for the design of stable supramolecular architectures: we report a strategy to construct stable and free-standing monomolecular layers using weak non-covalent bonds of limited directionality (*i.e.*, dipole-dipole interactions).

4.2. Results and discussion

The design of the molecular building block chosen for our first demonstration of a free-standing layer architecture has been inspired by our previous work on calixarene macrocycles in their function of organizing molecular entity [4.9]. At the phenolic rim of the parent calix[4]arene macrocycle short alkyl chains were attached in order to reinforce the hydrophobic character of the amphiphile while preserving its interfacial crystallization propensity. We decided to restrict the work to four-membered ring macrocycles because of their higher level of symmetry and their relative conformational rigidity. To endow this calixarene derivative with the ability to form 2D supramolecular networks, chemical moieties capable of dipole-dipole interactions have been introduced. Methyl-cyano functional groups have been chosen as they have been widely studied for their ability to establish this type of supramolecular interaction [4.11-4.12]. 5,11,17,23-tetra-methylcyano-25,26,27,28-tetrapropoxycalix[4]arene (**1**) was synthesized and fully characterized (see synthesis section in the SI and Fig. ES1).

The crystallization of **1** from methanol yielded single crystals suitable for X-ray diffraction studies with synchrotron radiation. Inspection of the structure showed that both molecules of **1** are in the pinched-cone conformation and that all methyl-cyano functionalities point away from the calixarene cavities. Symmetry expansion reveals a bilayer system [Fig. ES2] akin to those found in the vast majority of structures containing p-sulfonatocalix[4]arene [4.10-4.11], with hydrophobic layers alternating within the extended structure. The relative conformational flexibility of **1** is likely to be a contributory factor to bilayer formation; examination of the extended structure shows that the symmetry equivalents of **1** pack in an interdigitated manner, forming a series of identifiable CH \cdots N and CH \cdots π interactions (Table ES1-ES8).

The formation of layers of **1** at the air-water interface was studied using the Langmuir balance technique and Brewster angle microscopy (BAM, Fig. 4.1 & Table ES9). The compression isotherm shows that **1** here forms stable monolayers, characterized by a relatively high collapse pressure of 28 mN m $^{-1}$ and a limiting area of 90 Å 2 molecule $^{-1}$. It is noteworthy that, unlike the large majority of amphiphilic calixarenes at the air-water interface, the interfacial behavior of **1** displays two main phase transitions at surface pressure values of 3.4 and 17.9 mN m $^{-1}$ (Fig. 4.1, the points labeled α and β on the isotherm, respectively). Before monolayer compression, BAM analysis of the monolayer of **1** at the air-water interface shows no contrast; this is characteristic of a 2D gas-phase (Fig. 4.1D). At the isotherm take off ($A_0 = 102$ Å 2 molecule $^{-1}$), the monolayer exhibits a homogeneous morphology in BAM (Fig. 4.1D). After the first phase transition observed at 3.4 mN m $^{-1}$, the morphology of the monolayer changes to yield large needle-like crystalline structures (Fig. 4.1E&F).

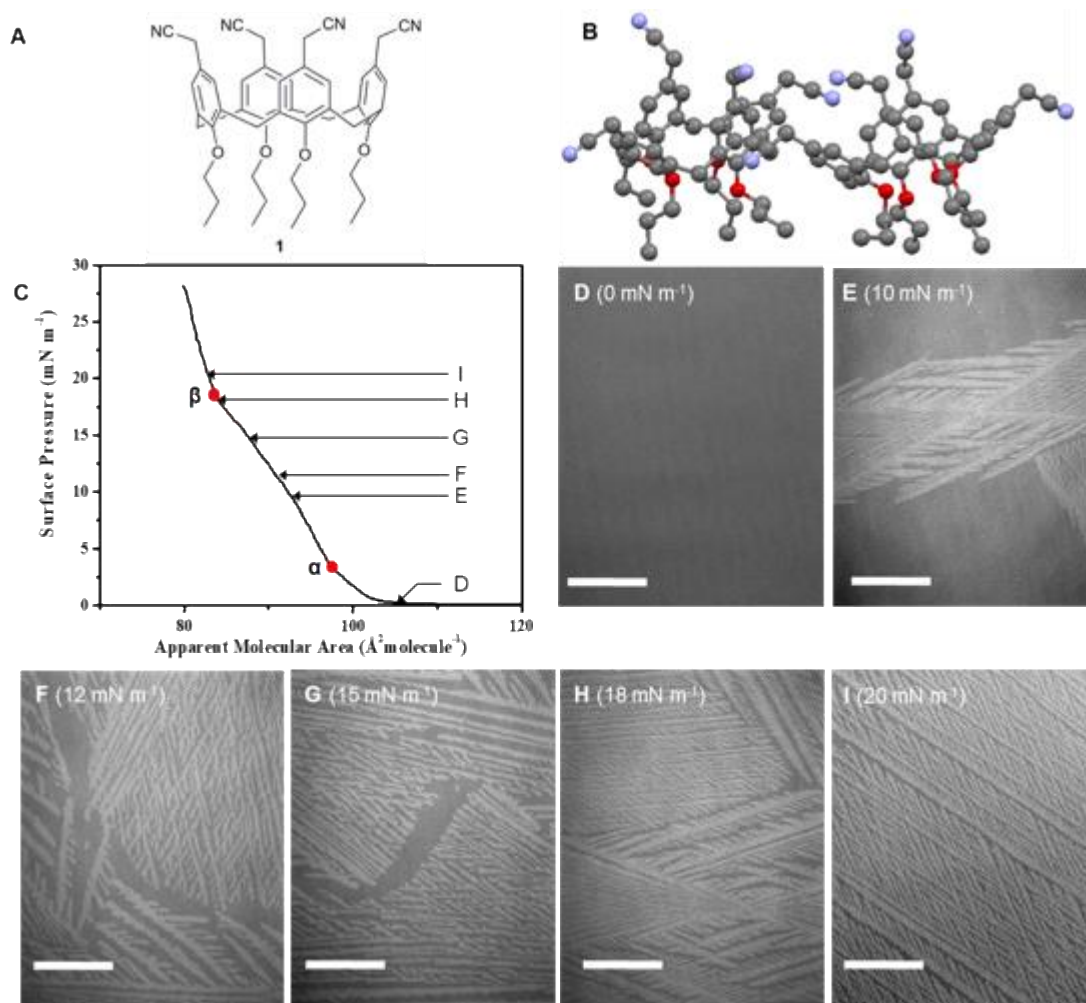


Figure 4.1 Chemical structure and interfacial self-assembly characterization of 1. (A) Molecular structure of *para*-methyl-cyano-tetra-propoxy-calix[4]arene, **1**. (B) Extended structure found in the crystal structure of **1** showing methyl-cyano functionalities pointing away from macrocycle cavities. Color code: C – grey, N – blue, O – red. Hydrogen atoms are omitted for clarity. (C) Surface pressure-area compression isotherm of **1** on pure water displayed three distinct phases with phase transitions at surface pressure values of 3.4 (α) and 17.9 mN m^{-1} (β), corresponding to molecular area values of 97 and 84 $\text{\AA}^2 \text{ molecule}^{-1}$, respectively. Letter labels indicate the position on the isotherm where the corresponding BAM micrographs were acquired. (D-I) BAM micrographs of the monolayer of **1** on pure water. Large crystalline monolayer domains grow after the first phase transition (10 mN m^{-1}). Upon further compression, the crystalline network expands and covers the whole available area at the air-water interface. Scale bar represents 100 μm .

Upon further compression, the second phase transition is reached; large dendritic crystalline structures appear and gradually cover the whole surface available (Fig. 4.1G & H). Further compression increases the density of those crystalline domains (Fig. 4.1I) until the monolayer collapses.

Notably, BAM results confirms that **1** self-assembles as a crystalline layer at the interface in the absence of organic/inorganic nodes. The addition of transition metal salts (*i.e.*, CuCl_2 , NiCl_2 and CrCl_3) did not cause any relevant change in the compression isotherm or BAM micrographs. As cyano moieties are known to be capable of metal coordination, this result strongly suggests that in-layer interactions are largely favored (Fig. ES3)

and that the formation of the crystalline network of **1** is due to intermolecular (-CN ···NC-) dipole-dipole interactions. The influence of van der Waals interactions can be neglected because of the short length of aliphatic chains at the lower rim of the macrocycle. To further verify the nature of the intramolecular interaction stabilizing this layer, compression isotherms were carried out in the presence of a competitor molecule capable of (-CN ···NC-) interactions, namely acetonitrile (ACN), in the subphase (Fig. ES4). The dissociation constant (K_d) of single dipole-dipole interactions, calculated using reported Gibbs' free energy of interaction values (ΔG_0 , ranging from -5 to -20 kJ mol⁻¹) of -CN ···NC- [4.13], is expected to range from 0.3 to 100 mM. In our experiments, we used acetonitrile concentrations of 10 and 10⁻² mM. At the lowest tested concentration of 10⁻² mM (expected to be below K_d), the Langmuir compression isotherm did not reveal any relevant change with regard to that measured on pure water. This confirms that no significant interaction occurred between **1** and ACN. Oppositely, at an ACN concentration of 10 mM, only a very unstable monolayer is formed (with a collapse pressure below 4 mN m⁻¹), indicating that the interactions of **1** with the cyano group in ACN totally disrupted the self-assembly process. This result further confirms the dipole-dipole nature of the intermolecular forces stabilizing the monolayer of **1**.

The monomolecular layer of **1** was transferred, using the Langmuir Schaefer (LS) method, at the surface pressure of 20 mN m⁻¹, from the air-water interface onto two different solid substrates, *i.e.*, highly oriented pyrolytic graphite (HOPG) and silicon/silicon dioxide coated with octadecyltrichlorosilane (OTS). In both cases, transfer ratio values were close to unity; surface ellipsometry and contact angle measurements confirmed the successful transfer of the monolayer onto the solid substrates tested (Table ES10). To avoid interferences with the alkyl chains of OTS, HOPG has been chosen as the substrate for surface analytical experiments described hereinafter.

The element-specific chemical analysis of the monolayer of **1** transferred onto HOPG was carried out using X-ray photoelectron spectroscopy (XPS). The N1s spectrum showed only a single peak at 399.7 eV, which is a characteristic value for the cyano CN group attached to carbon [4.14]. The single sharp N peak, with a full width at half maximum of 1 eV, provides evidence that all N atoms have the same chemical environment in the monolayer. The O:N ratio, calculated from the O1s and N1s spectra, is ~ 1, in agreement with the chemical structure of **1**. The amount of water in the transferred monolayer is negligible, as calculated from the O1s spectrum. This provides further counterevidence against H-bonding of **1** with water driving the self-assembly of the monolayer of **1** (Fig. 4.2A-C). To further explore whether dipole-dipole interactions between the CN groups are responsible for stabilizing the layer, we transferred the monolayer by LS transfer after assembly on aqueous solutions containing 10 μ M CuCl₂, NiCl₂, or CrCl₃ (Fig. ES3). XPS revealed, in all these cases, the absence of any metal linkers (Fig. ES5). These results confirm that the CN groups in the calixarene have a higher propensity to interact with one

another via dipole-dipole interaction than via coordination bond with metal ion linkers.

To further characterize **1**-based networks transferred on a solid substrate and to establish a molecular model of the monolayer on the surface, near-edge X-ray absorption fine structure (NEXAFS) measurements at the N-K edge were carried out (Fig. 4.2D-F). The spectra exhibited a very simple line shape consisting only of the signals of transitions into the π^* (400.6 eV) and σ^* (approximately 425 eV) molecular orbitals (MOs) of CN [4.15, 4.16]. Only one peak is observed because the CN MO is not hybridized with the π system of the phenyl group because of the linking sp^3 hybridized carbon [4.17]. The linear dichroism (LD) spectrum revealed a slight polarization of the π^* signal rising to $\sim 4\%$ at 70° X-ray incidence angle. The small negative LD implies that, in average, the cyano groups are oriented in an angle γ greater than the magic angle (54.74°) with respect to the surface normal. The angle dependence of the π^* LD is modeled as a plane type orbital (see NEXAFS section in SI) [4.17-4.18]. Also, we find an average angle of the CN group with respect to the surface normal $\langle \gamma \rangle = 57 \pm 1^\circ$.

Atomic force microscopy (AFM) studies of the 2D supramolecular systems provided a substantial challenge; this may be caused by the weak interactions between the short apolar part of **1** (*i.e.*, propyl chains) and the substrate [4.19-4.20]. AFM micrographs of the monolayer of **1**, transferred onto HOPG under ambient conditions, were acquired (Fig. 4.3). The layer thickness has been determined by measuring the z-profile after scratching the layer with the AFM at high constant force. The thereby obtained value of 1.0 ± 0.4 nm further confirms the presence of only a single layer of **1** on HOPG (Fig. ES6) also consistent with surface ellipsometry measurements that show the value of 1.0 ± 0.2 nm. AFM imaging at molecular resolution revealed large areas covered with molecules of **1** packed in a square fashion with an average lattice constant of 1.5 nm (Fig. 4.3A and B). This confirms that the layer is sufficiently stable to be transferred from the liquid to the solid surface without being disrupted by the process despite the above evidenced absence of covalent or coordination bonding.

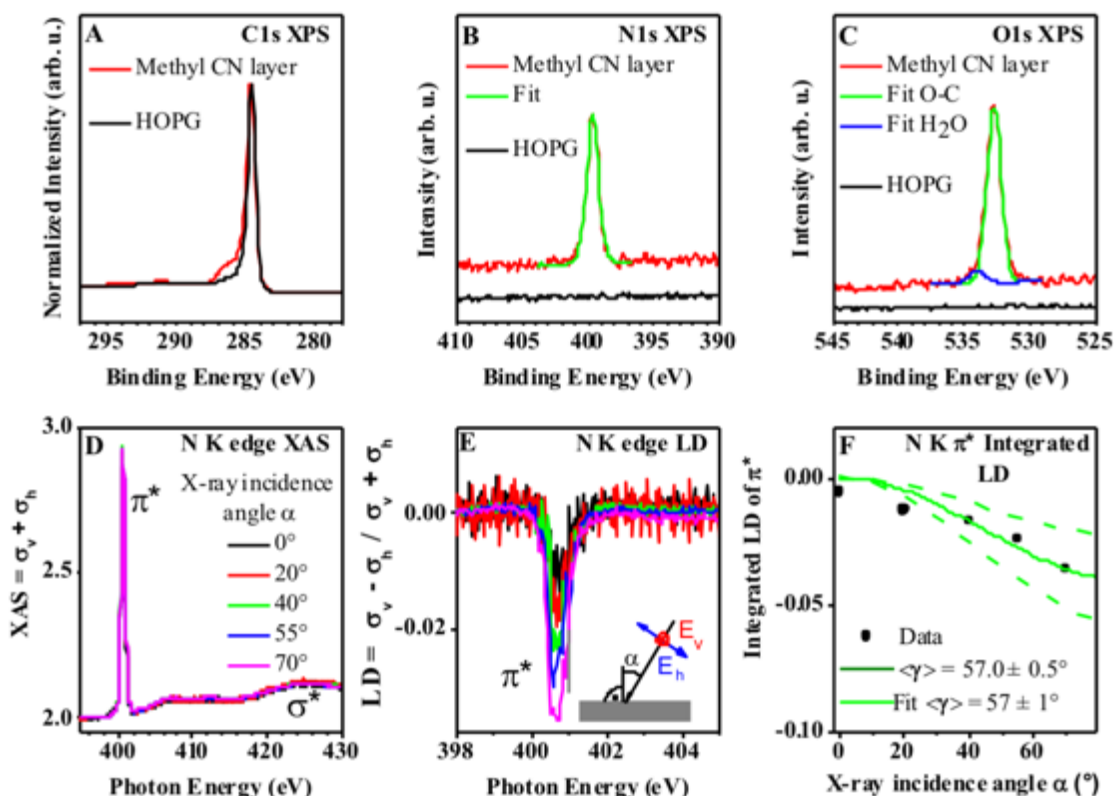


Figure 4.2 Surface spectroscopy analysis of 1-based monolayers. (A, B & C) X-ray photoelectron spectra of the monolayer of **1** transferred onto HOPG by the LS method for C1s, N1s and O1s peaks. (C) The O1s spectrum can be fitted with two peaks, 532.5 and 533.2 eV representing O-C of **1** and an insignificant amount of H₂O (~6% of the O1s spectrum) [4.14]. A precise interpretation of the C1s spectrum is challenging because of multiple peaks overlapping for different C entities of **1**. (D, E, & F) Room temperature N-K edge X-ray absorption spectra ($E_v + E_h$) and linear dichroism (LD) of the monolayer of **1** on HOPG. (D) The transition into the unoccupied π^* MO of the CN groups is visible as a distinct peak at 400.6 eV. (E) Integrated intensity of the LD of the π^* signal as a function of the X-ray incidence angle with respect to the surface normal. (F) The data is consistent with an average orientation of $\langle \gamma \rangle = 57^\circ$ of the CN groups. The dashed line corresponds to $\langle \gamma \rangle = 57 \pm 1^\circ$.

Combining Langmuir isotherm results, XPS, NEXAFS and AFM, we propose a model for the molecular packing of **1**-based monolayers (Fig. 4.3C & D). In this model, every single building block of **1** interacts with its nearest neighbors via $-\text{CN} \cdots \text{NC}-$ dipole-dipole interactions. Interatomic distances and angles of the CN groups agree with the values reported by Allen *et al.* [4.13] for dominant antiparallel geometry of dipole-dipole interaction of CN functional groups. The angle of the CN functional groups of **1** with regard to the surface normal, extracted from the molecular model, is 58.4° , which is in agreement with the NEXAFS data.

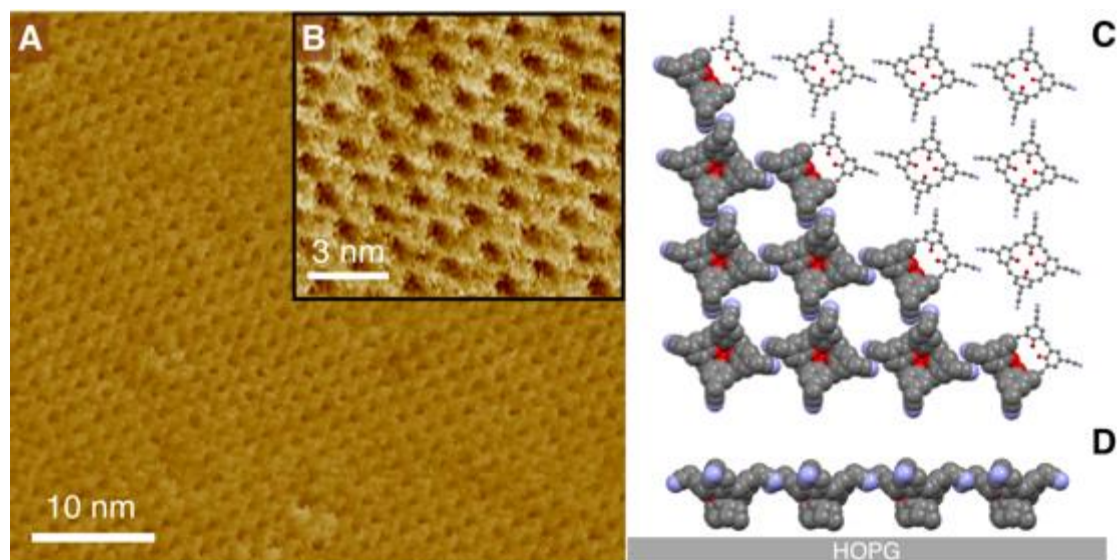


Figure 4.3 Molecular resolution AFM imaging of the monolayer of 1. (A) AFM images of the monolayer of **1** transferred onto HOPG via the LS method. (B) High resolution image of the crystalline network of the monolayer shows a highly ordered network formed from the single molecules of **1**. (C) top view and (D), side view). Molecular model of the building blocks of **1** interacting via the proposed dipole-dipole interaction in the well-ordered monolayer.

To further investigate the stability of the layer under different environmental conditions, cryo-transmission electron microscopy (TEM) investigations have been performed of the monolayer of **1** after a successful transfer from the air-water interface onto a lacey carbon copper grid by the LS method (Fig. 4.4). Lacey carbon grids are hydrophobic by nature and have a mesh structure displaying more than 80% of open areas. The LS transfer was carried out using the same conditions than in the case of HOPG and the transfer ratio measured was again close to unity. Cryo-TEM investigations of the monolayer of **1**, shown in Fig. 4.4, revealed the presence of homogeneous free-standing layers across areas as large as $3 \times 3 \mu\text{m}$, without rupturing and shrinking. Thus, the bonding between the molecules in the monolayer is sufficiently stable that it can be transferred as a free-standing film. We attribute this remarkable level of stability to the synergistic action of the dipole-dipole interactions. The diffraction pattern of the free-standing layer shows only one characteristic lattice (Fig. 4.4B). This, together with the absence of higher order Laue zones and the high degree of Friedel symmetry in the electron diffraction patterns (also in the shape of the Bragg peaks), confirms that the free-standing layers are indeed monolayers and not ordered or disordered stacks. The electron diffraction patterns of the free-standing monolayer (Fig. 4.4B) reveals a square lattice with a unit cell size of 15 \AA (Fig. ES7). This result is in agreement with the AFM data and our molecular model.

It has been widely reported that 2D monolayers of organic molecules suffer from decomposition and loss of stability under high electron beam intensity [4.21-4.24]. Notably, our results show that the free-standing

monolayer of **1** remains intact also during extensive sessions of cryo-TEM imaging.

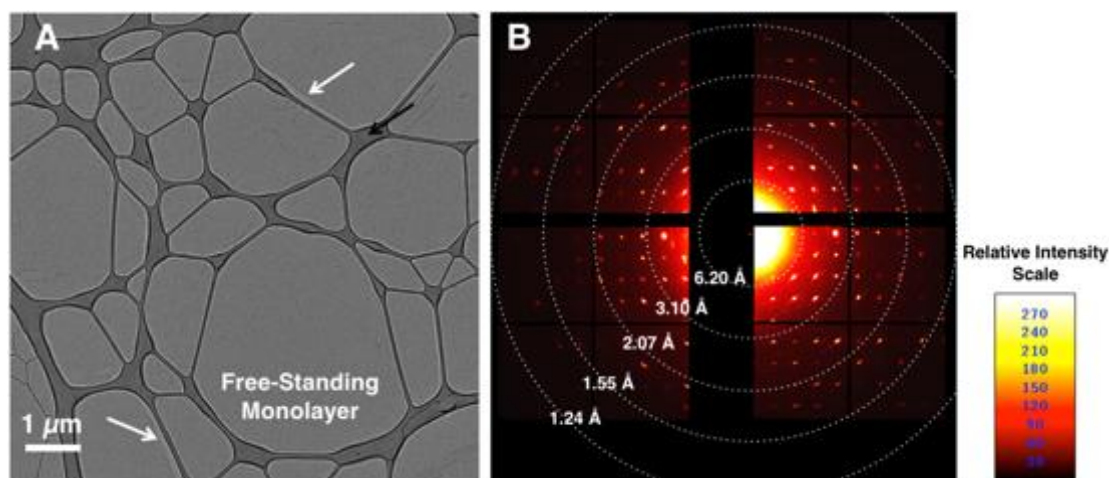


Figure 4.4 Cryo-TEM investigation of the free-standing monolayer of **1.** (A) TEM analysis of the monolayer of **1** transferred via the LS method on a Lacey carbon TEM grid (dark areas in the picture are areas of thick carbon from the “lacey carbon” substrate as it is widely used as a TEM substrate for its non-uniform and wide openings, black arrow). The layer has fractured and lost contact in some areas with the lacey carbon. In these areas, the free-standing monolayer can be visualized, as shown with white arrows. (B) The electron diffraction pattern of the free-standing monolayer of **1** confirms the square symmetric packing structure of the crystalline layer. The profile lines across the diffraction pattern, Fig. ES7, reveal a unit cell size of 15 Å consistent with the AFM acquired and the molecular model of the self-assembled monolayer of **1**.

4.3. Conclusion

In conclusion, we demonstrated the formation of a crystalline, free-standing supramolecular organic network produced in absence of coordination or covalent bonds. Thereby we go beyond the current paradigm endorsing strong and directional interactions for the design of stable supramolecular architectures. The remarkable stability of the layer, despite the absence of covalent bridging of the constitutive building blocks, is reflected in the observation of undistorted free-standing layers and surface-supported layers with the same square crystalline lattice in molecular-resolution AFM and high-resolution TEM data, respectively. On the basis of surface chemical analysis and a model, the cohesion between the building blocks of the layer has been attributed to noncovalent dipole-dipole interactions between the functional CN groups of **1**. We expect our chemical design strategy to be versatile so that it could be expanded to a broader range of multivalent building blocks capable of establishing in plane dipole-dipole interactions. These building blocks should support multiple synergistic dipole-dipole interactions, minimize other less directional interactions such as van der Waals, and form single molecular layers at the solid-liquid interface. The latter is important to gain single molecular layers and not amorphous polymer layers with far less structural and thickness control. The stability of the free-standing layers

produced, when exposed to photon-, photoelectron-, and electron irradiations, makes them systems suitable to serve as supporting layers for single-protein and single-nanoparticle analyses and imaging [4.25]. Furthermore, the findings reported here pave the way toward the design of robust 2D layers with molecularly precise architectures and controllable physicochemical properties.

4.4. Materials and methods

4.4.1. Synthesis of 5,11,17,23-tetramethylcyano-25,26,27,28-tetrapropoxy calix[4]arene

Compound Cl-C₄A-OC₃ (Fig. ES1) was synthesized as previously described [4.26].

5,11,17,23-tetramethylcyano-25,26,27,28-tetrapropoxy calix[4]arene, **1**, was synthesized using a modified procedure adapted from that described for analogs nonalkylated at phenolic positions [4.27], as follows. Sodium cyanide (0.38 g, 7.63 mmol) was added to a mixture of Cl-C₄A-OC₃ (1 g, 1.27 mmol) in dimethyl sulfoxide (150 ml). The reaction mixture was kept under N₂ atmosphere and magnetic stirring at 80°C for 3 hours. The resulting pale yellow solution was cooled down and added to 500 ml of ice/water, yielding a milky solution. This mixture was acidified with an aqueous HCl solution (2M). The resulting white precipitate was filtered and crystallized from MeOH to yield **1** as white crystals (0.32 g, 34%; mp 200° to 205°C).

¹H NMR (nuclear magnetic resonance) (300 MHz, CDCl₃): δ 6.62 (s, 2, ArH), 4.45 to 4.41 (d, J = 13.3 Hz, 1, Ar-CH₂-Ar), 3.87 to 3.81 (t, J = 13.3 Hz, 2, O-CH₂-CH₂-CH₃), 3.50 (s, 2, Ar-CH₂-CN), 3.16 to 3.12 (d, J = 13.5 Hz, 1, Ar-CH₂-Ar), 1.98 to 1.86 (m, J = 7.5 Hz, 2, O-CH₂-CH₂-CH₃), and 1.02 to 0.97 (t, J = 7.4 Hz, 3, O-CH₂-CH₂-CH₃). ¹³C NMR (75 MHz, CDCl₃): δ 156.21, 135.39, 127.81, 123.52, 118.40, 30.87, 23.18, 22.89, 10.26. Mass spectroscopy (electrospray ionization) mass/charge ratio: [M + Na]⁺, calculated for [C₄₈H₅₂N₄O₄+Na]⁺ 771.4; found 771.3. Elemental analysis (%) calculated for C, 76.98, H, 7.00; N, 7.48; found, C (76.50, 76.52), H (7.01, 7.05), N (7.42, 7.45).

4.4.2. X-ray crystallography

Data were collected at 100(2) K by shutterless scans using a Bruker D8 diffractometer equipped with a PHOTON 100 detector and operating with a silicon 111 monochromator and synchrotron radiation of wavelength 0.77490 Å. Diffraction data on the crystal powder of **1** were collected using a Bruker D8 Advance powder diffractometer, operating with Ge-monochromated Cu K_{α1} radiation (wavelength = 1.5406 Å) and a LynxEye linear detector. Data were collected over the angular range of 5° to 85° in 2θ.

4.4.3. Langmuir monolayer, BAM, and LS deposition experiments

Surface pressure area compression isotherms were recorded using a NIMA112D Langmuir system. For each series of experiments, the trough and barriers were thoroughly cleaned with analytical grade chloroform and nanopure water (resistivity of 18.2 megohm·cm). Nanopure water was used as a subphase. The monolayer was prepared by spreading a solution of **1** (13 ml, 0.5mg ml⁻¹) in chloroform at the water surface using a gastight microsyringe. After solvent evaporation and equilibration of amphiphiles at the interface (15 min), barriers were symmetrically closed at a speed rate of 5 cm² min⁻¹. The accuracies of π_c and A_0 measurements were of $\pm 0.1 \text{ mNm}^{-1}$ and $\pm 1 \text{ \AA}^2 \text{ molecule}^{-1}$, respectively. Each condition was repeated three times to ensure reproducibility of the isotherms.

BAM was performed by using a Nanofilm_ep3 system (Accurion) equipped with an internal solid-state laser at a wavelength of 658 nm. The images were acquired using a charge-coupled device camera (768 Å~562 pixels) and a 10Å~ objective, equipped with an automatic focus scanner yielding 1- μm lateral resolution.

LS transfer was carried out using a NIMA deposition system. HOPG and hydrophobic silicon wafers (coated with OTS) [4.28] were used as solid substrates for the LS deposition of the monolayer of **1**. The substrates were brought toward the interface at a controlled speed of 1 mm min⁻¹ and touched the monolayer compressed at 20 mN m⁻¹. After 15 min, the substrates were slowly removed from the aqueous solution at a constant speed of 1 mm min⁻¹.

4.4.4. Near-edge X-ray absorption fine spectroscopy

Near edge X-ray absorption fine spectroscopy was measured at the N-K edge at room temperature in a total electron yield mode using linearly polarized X-rays (E_v and E_h) for different incidence angles α [4.18]. $\alpha = 0^\circ$ implies normal incidence, E_v is always parallel to the surface plane, and E_h is perpendicular to E_v . The degree of polarization is 100% [4.18]. Each spectrum was divided by a matching (same polarization σ and incidence angle α) spectrum obtained on clean HOPG and normalized to unity at the pre-edge (395 to 398 eV).

The angle dependence of the CN π^* signal was modelled according to an established procedure [4.17], assuming a plane-type orbital (suitable for the cyano π^* MO) for a threefold or higher substrate symmetry. The equations for the intensities I_p and I_n of the absorption, where the electric field of I_n is normal with respect to the surface normal (*i.e.*, in the surface plane) and where I_p is perpendicular to I_n , are as follows:

$$I_p = 1 - \cos^2\theta \cos^2\gamma - \frac{1}{2} \sin^2\theta \sin^2\gamma$$
$$I_n = \frac{1}{2} (1 + \cos^2\gamma)$$

Here, γ is the angle between the plane normal to the plane orbital (*i.e.*, the CN vector) and the surface normal, and θ is the angle between the electric polarization of I_p and the surface normal [4,17]. The theoretical LD is then calculated as $(I_n - I_p)/(I_n + I_p)$. Note that the photon energy was not exactly calibrated.

Acknowledgments

We thank R. Schelldorfer for technical support for XPS and AFM measurements and M. Clabbers for the electron diffraction data conversion (from the direct electron detector format). Part of this work was performed at the Surface/Interface: Microscopy (SIM) beamline of the Swiss Light Source, Paul Scherrer Institute, Villigen, Switzerland. Funding: The financial support of the Swiss Nanoscience Institute (grant nos. P1305 and P1308) is gratefully acknowledged. C.W. acknowledges financial support by the University Research Priority Program LightChEC of the University of Zürich, Switzerland. M.B. and T.A.J. acknowledge the Swiss National Science Foundation (grant nos. 200020-153549, 200020-175800, and 206021-113149). This research used resources of the Advanced Light Source, which is a DOE Office of Science User Facility under contract no. DE-AC02-05CH11231. This research was in part supported by the SNF [grant no. 5204.23000.160.02; “SwissFEDI, a free electron diffraction instrument for nano-diffraction of biological specimens” (2016–2019) to J.P.A.].

Author Contributions

P.S. and T.A.J. conceived the research. M.M. and L.G.T. performed LB, BAM, LS, contact angle, ellipsometry and AFM experiments and analyzed the data. N.L.O. and M. M. initiated investigation of the formation free-standing monolayers. M.M. and M.B. conducted XPS experiments and analyzed the data. N.L.O. and E.v.G. performed EM data collection and with H.S. and J.P.A. interpreted the data. L.G.T. and M.M. synthesized the molecule. C.W., M.B., O.P. and A.K. acquired the NEXAFS data and analyzed the data. S.J.D. and S.J.T. performed the single crystal X-ray diffraction work. M.M., T.A.J., P.F.-X.C., and P.S. wrote the paper. All authors commented on the manuscript

Competing interests

The authors declare that they have no competing interests.

Data and materials availability

All data needed to evaluate the conclusions in the paper are present in the paper and/or the Supplementary Materials. Additional data related to this paper may be requested from the authors. Crystallographic data for the structure of compound **1**, reported in the Supplementary Materials, have been deposited at the Cambridge Crystallographic Data Centre under deposition no. CCDC 1586569. Copies of the data can be obtained free of charge at www.ccdc.cam.ac.uk/data_request/cif.



Chapter 5

“I’m making a note here: Huge success!”
from lyrics: “Still alive” – Portal

The bright future of freestanding ultrathin nanomembranes

Synopsis: Freestanding membranes (thin films) applied as specimen support together with selected examples of directions for their further development in structural studies.

5.1. Conclusions

In this thesis an example of amorphous, freestanding, ultrathin silicon nitride membranes fabricated on a silicon chip (Chapter 1) with a specific application for unprecedented X-ray pump/ X-ray multiprobe XFEL measurements on protein crystals (Chapter 2) is presented. Dehydration protection of crystalline material, which contain significant amounts of solvent (water), has been achieved, and is essential to keep the diffraction properties of the sample during data collection. Well-sealed packaging consisting of materials highly transparent to X-rays [examples: Appendix B, Fig. BS8] is indispensable for the collection of high-quality diffraction patterns obtained from protein crystals deposited on or *in situ* grown onto a fixed-target delivery system.

Chapter 3 gives insight on the X-ray fluorescence detection on JUNGFRU detector applied to model samples, consisting of metal markers supported by an ultrathin membrane, as well as real, protein-containing samples. This approach of precise sample prelocation permits development towards high throughput XFEL diffraction data collection with high sampling precision and no beam-induced damage.

Further developments towards obtaining novel, freestanding material (Chapter 4) compatible with TEM measurements [Fig. 5.1b], with its analysis, have also been shown in detail.

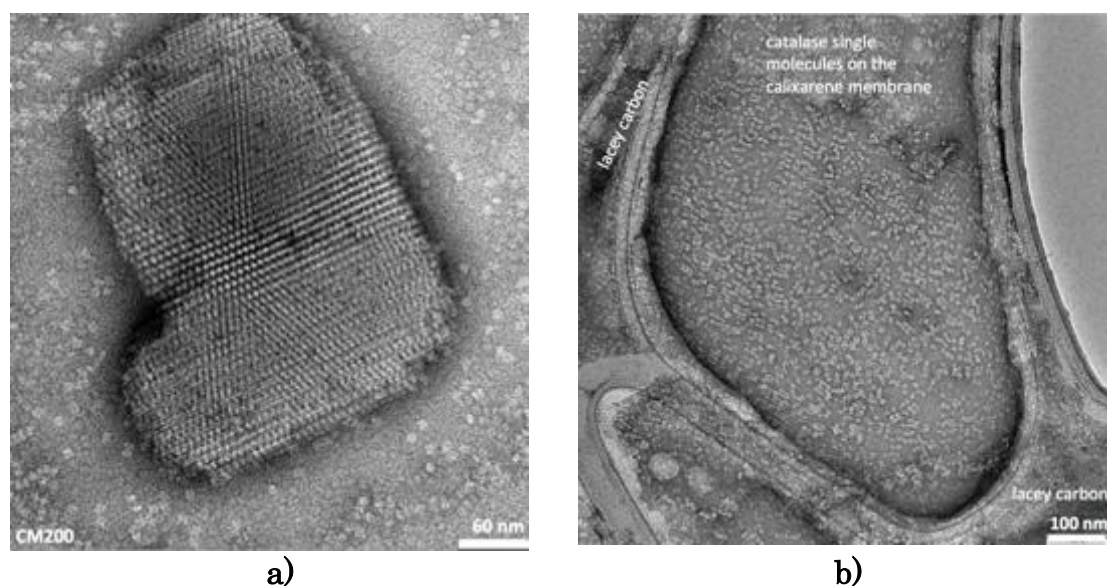


Figure 5.1 Negative stain TEM imaging of a) catalase nanocrystal on ultrathin carbon film in the EM grid, surrounded by single molecules, b) single molecules of catalase on the calixarene-based freestanding membrane suspended over lacey carbon in the EM grid. CM200 machine operating at 200 keV.

5.2. Outlook

Considering the further development of freestanding ultrathin nanomembranes for structural biology, the main requirements for an optimal solid support applied in diffraction studies are as follows:

- i) high transparency (to X-rays/electron beam) to ensure a sufficient signal to noise ratio of the collected data;
- ii) mechanical stability during data acquisition;
- iii) economic and easy to mass-fabricate for cost-efficient high-throughput measurements;
- iv) high metallic conductivity, especially for TEM and not only at room temperature but also under cryogenic conditions;
- v) prevents preferential orientation of the specimen (*e.g.*, non-flatness);
- vi) compatibility with vacuum in case of TEM or ambient conditions for RT XFEL data collection.

To accomplish the optimization of the specimen support for better performance I would suggest some of the following specific directions that could be taken:

5.2.1. Slit silicon chip

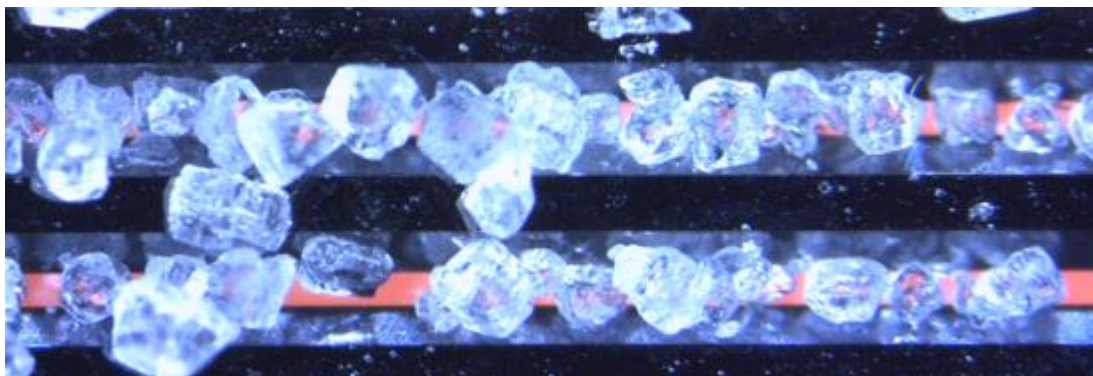


Figure 5.2 Silicon slit chip (Silson Ltd., UK), loaded with high-density microcrystals for serial diffraction data collection. The crystalline material was grown *via* batch crystallization and deposited in the V-shaped cavities. Scale: width of the slits (orange) is 100 μm , Leica Microscope at CF, SLS, PSI.

The slit chip [Fig 5.2.] is an example of fixed-target design, which allows for continuous scanning over the sample, using fast goniometers. It is compatible with kHz speeds of scans with an ultrafast stage [5.1] and high repetition rate of the source (for European XFEL designed value: 2700 pulses/s). It allows for obtaining high hit-rates; however, it gives high risk of preferential orientation of the sample resulting in low completeness of the diffraction data. Thus, further improvements of this approach are needed, especially with regard to scaling down the dimensions, for a solution compatible with nanocrystals [Fig. 5.1a].

5.2.2. Polymer-based membrane supports

Polymeric supports [Fig 5.3. (prototypes)] are generally flexible and less brittle than silicon-based materials. Their main advantage is a relatively large working area compatible with automatic, grid-based, serial scanning by the XFEL beam. They can serve as single-use chips since they would be cheaper once a mass-fabrication protocol is well-established.

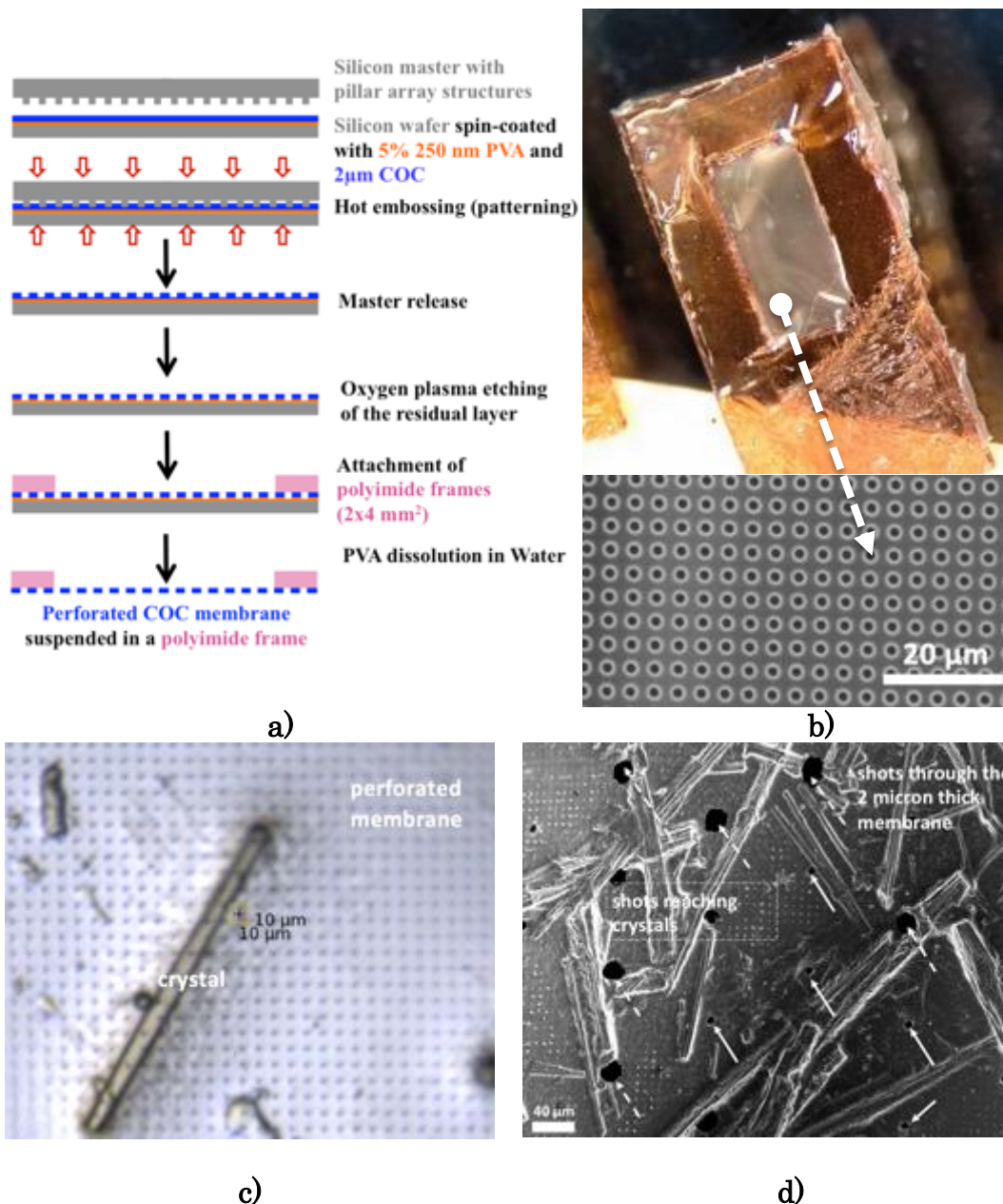


Figure 5.3. Serial crystallography supports with large area of freestanding polymeric membranes (cryo-mesh): a) fabrication protocol [5.2, SNI Annual Report 2017, p.38, Project: P1305], b) 2 µm thick holey membrane in the polyimide frame, c) membrane protein crystal deposited on the support, imaged in frozen state, d) *postmortem* view of the support with membrane protein crystals after exposure to the XFEL (LCLS) beam in Nov 2017, MFX end station (sample covered with ultrathin layer or chromium for contrast enhancement in SEM imaging).

[Further experiments on polymeric supports have been described in publication: Karpik *et al.*, *Micro and Nano Engineering* 7 1000532020 (2020)]

5.2.3. Composite-based sample support

Developments towards minimisation of the background originating from the support is particularly desirable for weakly scattering samples (like proteins). Application of ultrathin freestanding membranes, especially exploitation of the 2D materials, (for instance: graphene, or graphene-

based composites) is promising. Apart from the high transparency to X-rays or electrons graphene serves as a waterproof layer. Therefore, it can be used in the microfabrication process as the bottom of the wells in the silicon chip [Fig 5.4 a-b] for direct protein growth (*cf.* Chapter 1) on ultrathin membranes, *i.e.* holey carbon-supported graphene membranes, suspended on a silicon chip providing “zero-background” signal during diffraction experiment [Fig 5.4c].

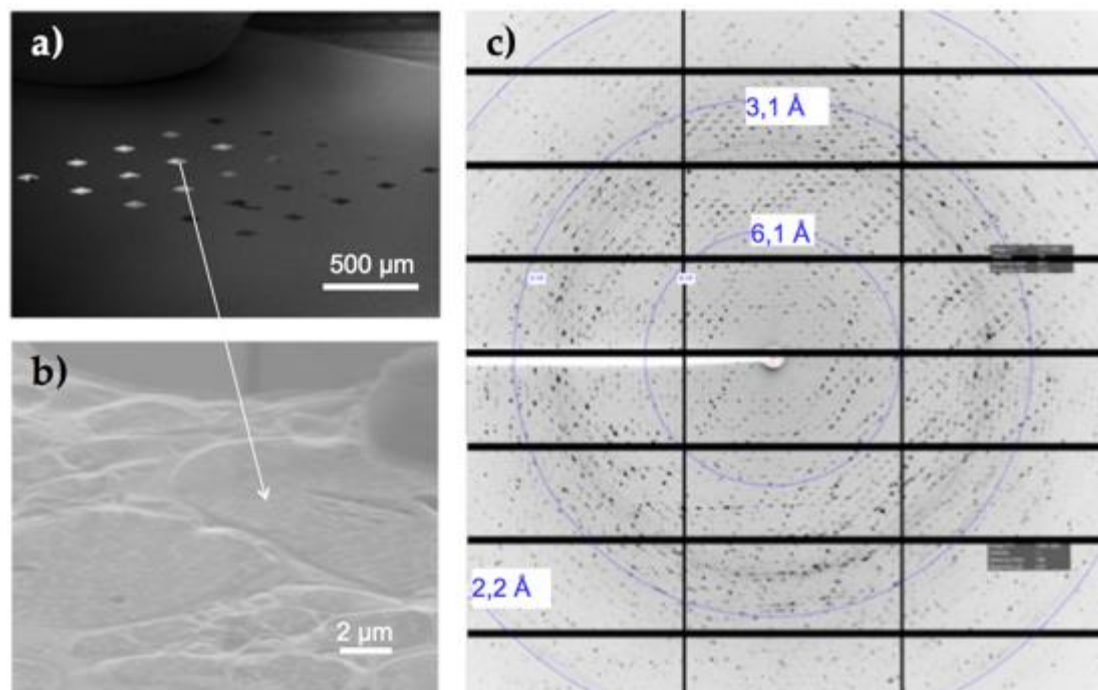


Figure 5.4 Minimal background supports for protein crystal diffraction studies a) microfabricated silicon chip with graphene on holey carbon over windows of 100 μm x 100 μm in size, b) closer view on the membrane, c) diffraction pattern measured using synchrotron radiation (SLS, PXI) on lysozyme crystals directly grown on a graphene/holey carbon support.

Apart from its desirable properties, graphene is hydrophobic (when hydrocarbon contaminated) and a direct contact of the macromolecule with its surface can lead to damage of the protein structure. For that reason, the combination of graphene with a soft, ultrathin, hydrophilic and protein compatible surface (serving as a “buffer” interlayer) would be beneficial. This concept leads to exploration of novel composites [Fig. 5.5] as specimen supports, especially those consisting of polymeric 2D materials [5.3]. The main advantage of this approach is reducing the risk of denaturation of the protein molecules due to unsuitable support surface.

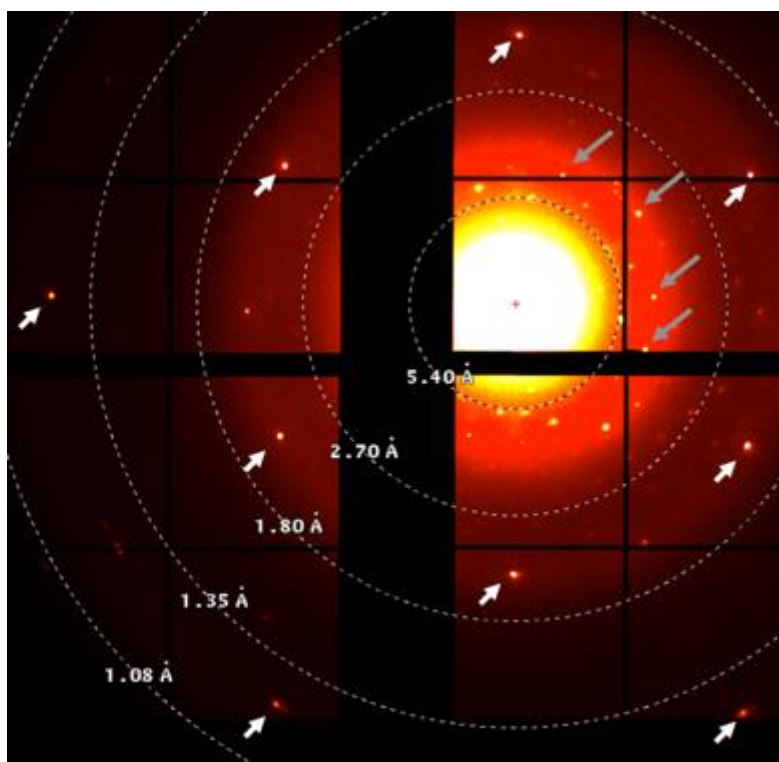


Figure 5.5 Electron diffraction pattern from the composite crystalline material: calixarene-based nanomembrane (low resolution reflections indicated with grey arrows) on graphene (high resolution hexagonally located reflections at $\approx 2.1 \text{ \AA}$ and $\approx 1.2 \text{ \AA}$ indicated with white arrows).

Finally, the optimal solution, which should be selected for structural studies of biological materials, depends on many factors, the most important of which are:

- i) parameters of the investigated samples (size, sensitivity, *etc.*),
- ii) type of radiation used (analytical method),
- iii) parameters of the data acquisition (RT *vs* cryocooling; atmospheric pressure *vs* vacuum; initial tests *vs* final tuning, *etc.*) and most importantly
- iv) the research question to be answered.

5.3. Closing remarks

XFEL-based and electron microscopy techniques have undergone unprecedented development in recent years, resulting in high-resolution structure determination of many proteins using cryo-EM single particle imaging (recognized with Chemistry Nobel Prize in 2017) and visualization of the excited, intermediate states of the protein molecules, thanks to time-resolved, pump-probe experiments [*e.g.* 5.4-5.7]. What was a dream in structural biology decades ago, has now become reality. The thoughts towards the future of emerging technologies bring hope for new exciting discoveries.

Acknowledgements

The following people greatly contributed to preparation of the figures presented in Chapter 5: Philippe Ringler provided biological material of the crystalline catalase, Isabelle Martiel collected diffraction patterns at PX-I beamline (SLS) from *in situ* grown crystals on graphene composite membrane and designed the polymeric chip (microfabrication: Konrad Vogelsang, Vitaliy Guzenko) following the concept described before by Gel *at al.* [5.2], Kishan Thodkar grew CVD graphene and imaged freestanding graphene membranes with SEM. Membrane protein crystals exposed to LCLS XFEL (MFX end-station scientist: Aina Cohen) were prepared by Jonas Mühle and Filip Pamula; project of Ching-Ju Tsai, SEM image: Vitaliy Guzenko. Graphene EM grids were prepared by Radosav Pantelic, Mina Moradi transferred the calixarene-based material (*cf.* Chapter 4). Eric van Genderen helped with ED data acquisition on direct electron detector, Max Clabbers converted data from binary files.

References

- [1.1] M. Billeter, G. Wagner, & K. Wüthrich, Solution NMR structure determination of proteins revisited. *J Biomol NMR* **42** (3), 155-158 (2008).
- [1.2] K. Wüthrich, Protein Structure Determination in Solution by NMR Spectroscopy. *J. Biol. Chem.* **265**, 22059-22062 (1990).
- [1.3] F. M. Marassi, & S. J. Opella, NMR structural studies of membrane proteins. *Curr. Opin. Struct. Biol.* **8** (5), 640-648 (1998).
- [1.4] E. Binshtein & M. D. Ohi, Cryo-Electron Microscopy and the Amazing Race to Atomic Resolution. *Biochemistry* **54**, 3133-3141 (2015).
- [1.5] J. Ruprecht, & J. Nield, Determining the structure of biological macromolecules by transmission electron microscopy, single particle analysis and 3D reconstruction. *Prog. Biophys. Mol. Biol.* **75**, 121-164 (2001).
- [1.6] K. R. Vinothkumar, Membrane protein structures without crystals, by single particle electron cryomicroscopy. *Curr. Opin. Struct. Biol.* **33**, 103-114 (2015).
- [1.7] A. L. Lamb, T. J. Kappock, & N. R. Silvaggi, You are lost without a map: Navigating the sea of protein structures. *Biochim. Biophys. Acta*, **1854**, 258-268 (2015).
- [1.8] I. Moraes, G. Evans, J. Sanchez-Weatherby, S. Newstead, & P. D. S. Stewart, Membrane protein structure determination — The next generation. *Biochim. Biophys. Acta*, **1838**, 78-87 (2014).
- [1.9] A. Wlodawer, W. Minor, Z. Dauter, & M. Jaskolski, Protein crystallography for non-crystallographers, or how to get the best (but not more) from published macromolecular structures. *FEBS J.* **275** (2007).
- [1.10] P. Fromme, XFELs open a new era in structural chemical biology. *Nat Chem Biol*, **11**, 895–899, (2015).
- [1.11] J. C. Falkner, A. M. Al-Somali, J. A. Jamison, J. Zhang, S. L. Adrianse, R. L. Simpson, M. K. Calabretta, W. Radding, G. N. Phillips, Jr. & V. L. Colvin, Generation of Size-Controlled, Submicrometer Protein Crystals. *Chem. Mater.* **17**, 2679-2686 (2005).
- [1.12] R. W. Martin, & K. W. Zilm, Preparation of protein nanocrystals and their characterization by solid state NMR. *J. Magn. Reson.* **165**, 162-174 (2003).
- [1.13] I. Schlichting, Serial femtosecond crystallography: the first five years. *IUCrJ.* **2**, 246-255 (2015).
- [1.14] M. S. Hunter, & P. Fromme, Toward structure determination using membrane-protein nanocrystals and microcrystals. *Methods* **55** (4), 387-404 (2011).
- [1.15] U. Weierstall, D. James, C. Wang, T. A. White, D. Wang, W. Liu, J. C. H. Spence, R. B. Doak, G. Nelson, P. Fromme, R. Fromme, I. Grotjohann, C. Kupitz, N. A. Zatsepin, H. Liu, S. Basu, D. Wacker, G. Won Han, V. Katritch, S. Boutet, M. Messerschmidt, G. J. Williams, J. E. Koglin, M. Marvin Seibert, M. Klinker, C. Gati, R. L. Shoeman, A. Barty, H. N. Chapman, R. A. Kirian, K. R. Beyerlein, R. C. Stevens, D. Li, S. T. A. Shah, N. Howe, M. Caffrey, & V. Cherezov, Lipidic cubic phase injector facilitates membrane protein serial femtosecond crystallography. *Nat. Commun.* **5**, 3309 (2014).
- [1.16] C.E. Conrad, S. Basu, D. James, D. Wang., A. Schaffer, S. Roy-Chowdhury, N. A. Zatsepin, A. Aquila, J. Coe, C. Gati, M. S. Hunter, J. E. Koglin, C. Kupitz, G. Nelson, G. Subramanian, T. A. White, Y. Zhao, J. Zook, S. Boutet, V. Cherezov, J. C. H. Spence, R. Fromme, U. Weierstall, P. Fromme, A novel inert crystal delivery medium for serial femtosecond crystallography. *IUCrJ*, **2**, 421-430 (2015).
- [1.17] M. Sugahara, C. Song, M. Suzuki, T. Masuda, S. Inoue, T. Nakane, F. Yumoto, E. Nango, R. Tanaka, K. Tono, Y. Joti, T. Kameshima, T. Hatsui, M. Yabashi, O. Nureki, K. Numata & S. Iwata, Oil-free hyaluronic acid matrix for serial femtosecond crystallography. *Sci. Rep.* **6**, 24484 (2016).
- [1.18] H. N. Chapman, S. P. Hau-Riege, M. J. Bogan, S. Bajt, A. Barty, S. Boutet, S. Marchesini, M. Frank, B. W. Woods, W. H. Benner, R. A. London, U. Rohner, A. Szöke, E. Spiller, T. Möller, C. Bostedt, D. A. Shapiro, M. Kuhlmann, R. Treusch, E. Plönjes, F. Burmeister, M. Bergh, C. Caleman, G. Huldt, M. M. Seibert, J. Hajdu, Femtosecond time-delay X-ray holography. *Nature* **448**, 676-679 (2007).

- [1.19] C. Schebor, M. F. Mazzobre, & M. del Pilar Buera, Glass transition and time-dependent crystallization behavior of dehydration bioprotectant sugars. *Carbohydr Res.* **345**, 303-308 (2010).
- [1.20] M. S. Hunter, B. Segelke, M. Messerschmidt, G. J. Williams, N. A. Zatsepin, A. Barty, W. H. Benner, D. B. Carlson, M. Coleman, A. Graf, S. P. Hau-Riege, T. Pardini, M. M. Seibert, J. Evans, S. Boutet & M. Frank, Fixed-target protein serial microcrystallography with an X-ray free electron laser. *Sci. Rep.* **4**, (2014).
- [1.21] K. Sader, D. Studer, B. Zuber, H. Gnaegi, & J. Trinick, Preservation of high-resolution protein structure by cryo-electron microscopy of vitreous sections. *Ultramicroscopy* **110**, 43-47 (2009).
- [1.22] N. Coquelle, A. S. Brewster, U. Kapp, A. Shilova, B. Weinhausen, M. Burghammer, & J.-P. Colletier, Raster-scanning serial protein crystallography using micro- and nano-focused synchrotron beams. *Acta Cryst. D* **71**, 1184-1196 (2015).
- [1.23] J. L. Wierman, J. S. Alden, C. U. Kim, P. L. McEuen, & S. M. Gruner, Graphene as a protein crystal mounting material to reduce background scatter. *J. Appl. Cryst.* **46**, 1501-1507 (2013).
- [1.24] T. Gibb, & M. Ayub, Engineered Nanopores for Bioanalytical Applications. *Micro Nano Technol. Series*, pp. 121-140. USA: Elsevier (2013).
- [1.25] M. Frank, D. B. Carlson, M. S. Hunter, G.J. Williams, M. Messerschmidt, N. A. Zatsepin, A. Barty, W. H. Benner, K. Chu, A.T. Graf, S. P. Hau-Riege, R. A. Kirian, C. Padeste, T. Pardini, B. Pedrini, B. Segelke, M. M. Seibert, J. C. H. Spence, C-J Tsai, S. M. Lane, X. Li, G. Schertler, S. Boutet, M. Coleman, & J. E. Evans, Femtosecond X-ray diffraction from two-dimensional protein crystals. *IUCrJ* **1**, 95-100 (2014).
- [1.26] B. Pedrini, C.-J. Tsai, G. Capitani, C. Padeste, M. S. Hunter, N. A. Zatsepin, A. Barty, W. H. Benner, S. Boutet, G. K. Feld, S. P. Hau-Riege, R. A. Kirian, C. Kupitz, M. Messerschmitt, J. I. Ogren, T. Pardini, B. Segelke, G. J. Williams, J. C. H. Spence, R. Abela, M. Coleman, J. E. Evans, G. F. X. Schertler, M. Frank, & X. Li, 7 Å resolution in protein two-dimensional-crystal X-ray diffraction at Linac Coherent Light Source. *Phil. Trans. R. Soc. B* **369**, (2014).
- [1.27] A. Zarrine-Afsar, T. R. M. Barends, C. Müller, M. R. Fuchs, L. Lomb, I. Schlichting, & R. J. D. Miller, Crystallography on a chip. *Acta Cryst. D* **68**, 321-323 (2012).
- [1.28] S. Oghbaey, A. Sarracini, H. M. Ginn, O. Pare-Labrosse, A. Kuo, A. Marx, S. W. Epp, D. A. Sherrell, B. T. Eger, Y. Zhong, R. Loch, V. Mariani, R. Alonso-Mori, S. Nelson, H. T. Lemke, R. L. Owen, A. R. Pearson, D. I. Stuart, O. P. Ernst, H. M. Mueller-Werkmeister and R. J. D. Miller Fixed target combined with spectral mapping: approaching 100% hit rates for serial crystallography. *Acta Cryst. D* **72**, 944–955 (2016).
- [1.29] G. Kisselman, W. Qiu, V. Romanov, C. M. Thompson, R. Lam, K. P. Battaile, E. F. Pai, & N. Y. Chirgadze, X-CHIP: an integrated platform for high-throughput protein crystallization and on-the-chip X-ray diffraction data collection. *Acta Cryst. D* **67**, 533–539 (2011).
- [1.30] A. E. Cohen, *et al.*, Goniometer-based femtosecond crystallography with X-ray free electron lasers. *Proc. Natl Acad. Sci. USA*, **111**, 17122–17127 (2014).
- [1.31] P. Roedig, I. Vartiainen, R. Duman, S. Panneerselvam, N. Stübe, O. Lorbeer, M. Warmer, G. Sutton, D. I. Stuart, E. Weckert, C. David, A. Wagner, & A. Meents, A micro-patterned silicon chip as sample holder for macromolecular crystallography experiments with minimal background scattering. *Sci. Rep.* **5**, 10451 (2015).
- [1.32] E. L. Baxter, L. Aguila, R. Alonso-Mori, C. O. Barnes, C. A. Bonagura, W. Brehmer, A. T. Brunger, G. Calero, T. T. Caradoc-Davies, R. Chatterjee, W. F. Degrado, J. S. Fraser, M. Ibrahim, J. Kern, B. K. Kobilka, A. C. Kruse, K. M. Larsson, H. T. Lemke, A. Y. Lyubimov, A. Manglik, S. E. McPhillips, E. Norgren, S. S. Pang, S. M. Soltis, J. Song, J. Thomaston, Y. Tsai, W. I. Weis, R. A. Woldeyes, V. Yachandra, J. Yano, A. Zouni, & A. E. Cohen, High-density grids for efficient data collection from multiple crystals. *Acta Cryst. D* **72**, 2-11 (2016).
- [1.33] T. D. Murray, A. Y. Lyubimov, C. M. Ogata, H. Vo, M. Uervirojnangkoorn, A. T. Brunger, & J. M. Berger, A high-transparency, micro-patternable chip for X-ray diffraction analysis of microcrystals under native growth conditions. *Acta Cryst. D* **71**, 1987-1997 (2015).

- [1.34] C.-Y. Huang, V. Olieric, P. Ma, E. Panepucci, K. Diederichs, M. Wang, & M. Caffrey, *In meso in situ* serial X-ray crystallography of soluble and membrane proteins. *Acta Cryst. D* **71**, 1238–1256 (2015).
- [1.35] C.-Y. Huang, V. Olieric, P. Ma, N. Howe, L. Vogeley, X. Liu, R. Warshamanage, T. Weinert, E. Panepucci, B. Kobilka, K. Diederichs, M. Wang, & M. Caffrey, *In meso in situ* serial X-ray crystallography of soluble and membrane proteins at cryogenic temperatures. *Acta Cryst. D* **72**, 93–112 (2016).
- [1.36] D. Axford, P. Aller, J. Sanchez-Weatherby, & J. Sandy, Applications of thin-film sandwich crystallization platforms. *Acta Cryst. F* **72**, 313–319 (2016).
- [1.37] A. Y. Lyubimov, T. D. Murray, A. Koehl, I. E. Araci, M. Uervirojnangkoorn, O. B. Zeldin, A. E. Cohen, S. M. Soltis, E. L. Baxter, A. S. Brewster, N. K. Sauter, A. T. Brunger, & J. M. Berger, Capture and X-ray diffraction studies of protein microcrystals in a microfluidic trap array *Acta Cryst. D* **71**, 928–940 (2015).
- [1.38] H. Matsumura, S. Sugiyama, M. Hirose, K. Kakinouchi, M. Maruyama, R. Murai, H. Adachi, K. Takano, S. Murakami, Y. Mori, & T. Inoue, Approach for growth of high-quality and large protein crystals. *J. Synchrotron Rad.* **18**, 16–19 (2011).
- [1.39] A. McPherson, & L. J. DeLucas, Microgravity protein crystallization. *npj Microgravity* **1**, 15010 (2015).
- [1.40] N. Shimizu, S. Sugiyama, M. Maruyama, H.Y. Yoshikawa, Y. Takahashi, H. Adachi, K. Takano, S. Murakami, T. Inoue, H. Matsumura and Y. Mori, Growth of Large Protein Crystals by Top-Seeded Solution Growth Together with the Floating and Solution-Stirring Technique. *Cryst. Growth Des.* **9** (12), 5227–5232 (2009).
- [1.41] C. Lou, M. Shindel, L. Graham, & S.-W. Wang, Molecular Self-Assembly of Solid-Supported Protein Crystals. *Langmuir* **24**, 8111–8118 (2008).
- [1.42] M. Auer, G. A. Scarborough, & W. Kühlbrandt, Surface Crystallisation of the Plasma Membrane H⁺-ATPase on a Carbon Support Film for Electron Crystallography. *J. Mol. Biol.* **287**, 961–968 (1999).
- [1.43] C. David, P. Karvinen, M. Sikorski, S. Song, I. Vartiainen, C. J. Milne, A. Mozzanica, Y. Kayser, A. Diaz, I. Mohacsi, G. A. Carini, S. Herrmann, E. Färm, M. Ritala, D. M. Fritz, & A. Robert, Following the dynamics of matter with femtosecond precision using the X-ray streaking method. *Sci Rep* **5**, doi: 10.1038/srep07644 (2015).
- [1.44] S. A. Arnold, S. Albiez, N. Opara, M. Chami, C. Schmidli, A. Bieri, C. Padeste, H. Stahlberg, & T. Braun, Total Sample Conditioning and Preparation of Nanoliter Volumes for Electron Microscopy. *ACS Nano* **10** (5), 4981–4988 (2016).
- [1.45] W. Kabsch, XDS. *Acta Cryst. D* **66**, 125–132 (2010).
- [1.46] W. Kabsch, Integration, scaling, space-group assignment and post-refinement. *Acta Cryst. D* **66**, 133–144 (2010).
- [1.47] A. Vagin, & A. Teplyakov, MOLREP: an Automated Program for Molecular Replacement. *J. Appl. Cryst.* **30**, 1022–1025 (1997).
- [1.48] G. N. Murshudov, A. A. Vagin, & E. J. Dodson, Refinement of Macromolecular Structures by the Maximum-Likelihood Method. *Acta Cryst. D* **53**, 240–255 (1997).
- [1.49] G. Bricogne, E. Blanc, M. Brandl, C. Flensburg, P. Keller, P. Paciorek, P. Roversi, A. Sharff, O. Smart, C. Vonrhein, T. Womack, BUSTER Version 2.10.2. Global Phasing Ltd, Cambridge, England (2016).
- [1.50] P. V. Afonine, R. W. Grosse-Kunstleve, N. Echols, J. J. Headd, N. W. Moriarty, M. Mustyakimov, T. C. Terwilliger, A. Urzhumtsev, P. H. Zwart, & P. D. Adams, Towards automated crystallographic structure refinement with *phenix.refine*. *Acta Cryst. D* **68**, 352–367 (2012).
- [1.51] V. B. Chen, W. B. Arendall III, J. J. Headd, D. A. Keedy, R. M. Immormino, G. J. Kapral, L.W. Murray, J. S. Richardson, & D. C. Richardson, *MolProbity*: all-atom structure validation for macromolecular crystallography. *Acta Cryst. D* **66**, 12–21 (2010).
- [1.52] S. Basso, A. N. Fitch, G. C. Fox, I. Margiolaki, J. P. Wright, High-throughput phase-diagram mapping via powder diffraction: a case study of HEWL versus pH. *Acta Cryst. D* **61**, 1612–1625 (2005).
- [1.53] P. Hart, S. Boutet, G. Carini, A. Dragone, B. Duda, D. Freytag, G. Haller, R. Herbst, S. Herrmann, C. Kenney, J. Morse, M. Nordby, J. Pines, N. van Bakel, M. Weaver, G. Williams, The Cornell-SLAC Pixel Array Detector at LCLS. SLAC

Publication, SLAC-PUB-15284, In Nuclear Science Symposium, Medical Imaging Conference IEEE NSS/MIC, 538-541 (2012).

[1.54] G. K. Feld, M. Heymann, W. H. Benner, T. Pardini, C-J. Tsai, S. Boutet, M. A. Coleman, M. S. Hunter, X. Li, M. Messerschmidt, A. Opathalage, B. Pedrini, G. J. Williams, B. A. Krantz, S. Fraden, S. Hau-Riege, J. E. Evans, B. W. Segelke, & M. Frank, Low-Z polymer sample supports for fixed-target serial femtosecond X-ray crystallography. *J. Appl. Cryst.* **48**, 1072-1079 (2015).

[2.1] P. Ball, Europe's X-ray laser fires up. *Nature* **548**, 507-508 (2017).

[2.2] C. Kupitz, S. Basu, I. Grotjohann, R. Fromme, N. A. Zatsepin, K. N. Rendek, M. S. Hunter, R. L. Shoeman, T. A. White, D. Wang, D. James, J.-H. Yang, D. E. Cobb, B. Reeder, R. G. Sierra, H. Liu, A. Barty, A. L. Aquila, D. Deponte, R. A. Kirian, S. Bari, J. J. Bergkamp, K. R. Beyerlein, M. J. Bogan, C. Caleman, T.-C. Chao, C. E. Conrad, K. M. Davis, H. Fleckenstein, L. Galli, S. P. Hau-Riege, S. Kassemeyer, H. Laksmono, M. Liang, L. Lomb, S. Marchesini, A. V. Martin, M. Messerschmidt, D. Milathianaki, K. Nass, A. Ros, S. Roy-Chowdhury, K. Schmidt, M. Seibert, J. Steinbrener, F. Stellato, L. Yan, C. Yoon, T. A. Moore, A. L. Moore, Y. Pushkar, G. J. Williams, S. Boutet, R. B. Doak, U. Weierstall, M. Frank, H. N. Chapman, J. C. H. Spence & P. Fromme, Serial time-resolved crystallography of photosystem II using a femtosecond X-ray laser. *Nature* **513**, 261-265 (2014)

[2.3] A. Aquila, M. S. Hunter, R. B. Doak, R. A. Kirian, P. Fromme, T. A. White, J. Andreasson, D. Arnlund, S. Bajt, T. R. M. Barends, M. Barthelmess, M. J. Bogan, C. Bostedt, H. Bottin, J. D. Bozek, C. Caleman, N. Coppola, J. Davidsson, D. P. DePonte, V. Elser, S. W. Epp, B. Erk, H. Fleckenstein, L. Foucar, M. Frank, R. Fromme, H. Graafsma, I. Grotjohann, L. Gumprecht, J. Hajdu, C. Y. Hampton, A. Hartmann, R. Hartmann, S. Hau-Riege, G. Hauser, H. Hirsemann, P. Holl, J. M. Holton, A. Hömke, L. Johansson, N. Kimmel, S. Kassemeyer, F. Krasniqi, K.-U. Kühnel, M. Liang, L. Lomb, E. Malmerberg, S. Marchesini, A. V. Martin, F. R.N.C. Maia, M. Messerschmidt, K. Nass, C. Reich, R. Neutze, D. Rolles, B. Rudek, A. Rudenko, I. Schlichting, C. Schmidt, K. E. Schmidt, J. Schulz, M. M. Seibert, R. L. Shoeman, R. Sierra, H. Soltau, D. Starodub, F. Stellato, S. Stern, L. Strüder, N. Timneanu, J. Ullrich, X. Wang, G. J. Williams, G. Weidenspointner, U. Weierstall, C. Wunderer, A. Barty, J. C. H. Spence, & H. N. Chapman, Time-resolved protein nanocrystallography using an X-ray free-electron laser. *Opt. Express* **20**(3), 2706-2716 (2012)

[2.4] M. Levantino, G. Schirò, H. Till Lemke, G. Cottone, J. M. Glowia, D. Zhu, M. Chollet, H. Ihee, A. Cupane & M. Cammarata, Ultrafast myoglobin structural dynamics observed with an X-ray free-electron laser. *Nat. Commun.* **6**, 6772 (2015).

[2.5] A. Shimada, M. Kubo, S. Baba, K. Yamashita, K. Hirata, G. Ueno, T. Nomura, T. Kimura, K. Shinzawa-Itoh, J. Baba, K. Hatano, Y. Eto, A. Miyamoto, H. Murakami, T. Kumasaka, S. Owada, K. Tono, M. Yabashi, Y. Yamaguchi, S. Yanagisawa, M. Sakaguchi, T. Ogura, R. Komiya, J. Yan, E. Yamashita, M. Yamamoto, H. Ago, S. Yoshikawa, T. Tsukihara, A nanosecond time-resolved XFEL analysis of structural changes associated with CO release from cytochrome c oxidase. *Sci. Adv.* **3**, e1603042 (2017).

[2.6] M. Schmidt, A short history of structure based research on the photocycle of photoactive yellow protein. *Struct. Dyn.* **4**, 032201 (2017).

[2.7] J. Tenboer, S. Basu, N. Zatsepin, K. Pande, D. Milathianaki, M. Frank, M. Hunter, S. Boutet, G. J. Williams, J. E. Koglin, D. Oberthuer, M. Heymann, C. Kupitz, C. Conrad, J. Coe, S. Roy-Chowdhury, U. Weierstall, D. James, D. Wang, T. Grant, A. Barty, O. Yefanov, J. Scales, C. Gati, C. Seuring, V. Srajer, R. Henning, P. Schwander, R. Fromme, A. Ourmazd, K. Moffat, J. Van Thor, J. H. C. Spence, P. Fromme, H. N. Chapman & M. Schmidt, Time-resolved serial crystallography captures high resolution intermediates of photoactive yellow protein. *Science* **346**(6214), 1242-1246 (2014).

[2.8] E. Nango, A. Royant, M. Kubo, T. Nakane, C. Wickstrand, T. Kimura, T. Tanaka, K. Tono, C. Song, R. Tanaka, T. Arima, A. Yamashita, J. Kobayashi, T. Hosaka, E. Mizohata, P. Nogly, M. Sugahara, D. Nam, T. Nomura, T. Shimamura, D. Im,

- T. Fujiwara, Y. Yamanaka, B. Jeon, T. Nishizawa, K. Oda, M. Fukuda, R. Andersson, P. Båth, R. Dods, J. Davidsson, S. Matsuoka, S. Kawatake, M. Murata, O. Nureki, S. Owada, T. Kameshima, T. Hatsui, Y. Joti, G. Schertler, M. Yabashi, A.-N. Bondar, J. Standfuss, R. Neutze & S. Iwata, A three-dimensional movie of structural changes in bacteriorhodopsin. *Science* **354** (6319), 1552-1557 (2016).
- [2.9] S. Boutet, L. Lomb, G. J. Williams, T. R. M. Barends, A. Aquila, R. B. Doak, U. Weierstall, D. P. DePonte, J. Steinbrener, R. L. Shoeman, M. Messerschmidt, A. Barty, T. A. White, S. Kassemeyer, R. A. Kirian, M. M. Seibert, P. A. Montanez, C. Kenney, R. Herbst, P. Hart, J. Pines, G. Haller, S. M. Gruner, H. T. Philipp, M. W. Tate, M. Hromalik, L. J. Koerner, N. van Bakel, J. Morse, W. Ghonsalves, D. Arnlund, M. J. Bogan, C. Caleman, R. Fromme, C. Y. Hampton, M. S. Hunter, L. C. Johansson, G. Katona, C. Kupitz, M. Liang, A. V. Martin, K. Nass, L. Redecke, F. Stellato, N. Timneanu, D. Wang, N. A. Zatsepin, D. Schafer, J. Defever, R. Neutze, P. Fromme, J. C. H. Spence, H. N. Chapman, I. Schlichting, High-Resolution Protein Structure Determination by Serial Femtosecond Crystallography. *Science* **337**, 362-364 (2012).
- [2.10] J.C.H. Spence, XFELs for structure and dynamics in biology. *IUCrJ* **4**, 322-339 (2017).
- [2.11] H. M. Ginn, M. Messerschmidt, X. Ji, H. Zhang, D. Axford, R. J. Gildea, G. Winter, A. S. Brewster, J. Hattne, A. Wagner, J. M. Grimes, G. Evans, N. K. Sauter, G. Sutton & D. I. Stuart, Structure of CPV17 polyhedrin determined by the improved analysis of serial femtosecond crystallographic data. *Nat. Commun.* **6**:6435 (2015).
- [2.12] A. Y. Lyubimov, M. Uervirojnangkoorn, O. B. Zeldin, Q. Zhou, M. Zhao, A. S. Brewster, T. Michels-Clark, J. M. Holton, N. K. Sauter, W. I. Weis, A. T. Brunger, Advances in X-ray free electron laser (XFEL) diffraction data processing applied to the crystal structure of the synaptotagmin-1 / SNARE complex. *eLife* **5**:e18740 (2016).
- [2.13] J. L. Thomaston, R. A. Woldeyesb, T. Nakane, A. Yamashita, T. Tanaka, K. Koiwai, A. S. Brewster, B. A. Barad, Y. Chen, T. Lemmin, M. Uervirojnangkoorn, T. Arima, J. Kobayashi, T. Masuda, M. Suzuki, M. Sugahara, N. K. Sauter, R. Tanaka, O. Nureki, K. Tono, Y. Joti, E. Nango, S. Iwata, F. Yumoto, J. S. Fraser, and W. F. DeGrado, XFEL structures of the influenza M2 proton channel: Room temperature water networks and insights into proton conduction. *Proc. Natl. Acad. Sci. U.S.A.* **114** (51), 13357-13362 (2017).
- [2.14] Y. Fukuda, K. M. Tse, T. Nakane, T. Nakatsu, M. Suzuki, M. Sugahara, S. Inoue, T. Masuda, F. Yumoto, N. Matsugaki, E. Nango, K. Tono, Y. Joti, T. Kameshima, C. Song, T. Hatsui, M. Yabashi, O. Nureki, M. E. P. Murphy, T. Inoue, S. Iwata & E. Mizohata, Redox-coupled proton transfer mechanism in nitrite reductase revealed by femtosecond crystallography. *Proc. Natl. Acad. Sci. U.S.A.* **113**, 2928-2933 (2016).
- [2.15] Y. Kang, X. E. Zhou, X. Gao, Y. He, W. Liu, A. Ishchenko, A. Barty, T. A. White, O. Yefanov, G. W. Han, Q. Xu, P. W. de Waal, J. Ke, M. H. E. Tan, C. Zhang, A. Moeller, G. M. West, B. Pascal, N. Van Eps, L. N. Caro, S. A. Vishnivetskiy, R. J. Lee, K. M. Suino-Powell, X. Gu, K. Pal, J. Ma, X. Zhi, S. Boutet, G. J. Williams, M. Messerschmidt, C. Gati, N. A. Zatsepin, D. Wang, D. James, S. Basu, S. Roy-Chowdhury, C. Conrad, J. Coe, H. Liu, S. Lisova, C. Kupitz, I. Grotjohann, R. Fromme, Y. Jiang, M. Tan, H. Yang, J. Li, M. Wang, Z. Zheng, D. Li, N. Howe, Y. Zhao, J. Standfuss, K. Diederichs, Y. Dong, C. S. Potter, B. Carragher, M. Caffrey, H. Jiang, H. N. Chapman, J. C. H. Spence, P. Fromme, U. Weierstall, O. P. Ernst, V. Katritch, V. V. Gurevich, P. R. Griffin, W. L. Hubbell, R. C. Stevens, V. Cherezov, K. Melcher & H. E. Xu, Crystal structure of rhodopsin bound to arrestin by femtosecond X-ray laser. *Nature* **523**, 561-567 (2015).
- [2.16] M. Sugahara, E. Mizohata, E. Nango, M. Suzuki, T. Tanaka, T. Masuda, R. Tanaka, T. Shimamura, Y. Tanaka, C. Suno, K. Ihara, D. Pan, K. Kakinouchi, S. Sugiyama, M. Murata, T. Inoue, K. Tono, C. Song, J. Park, T. Kameshima, T. Hatsui, Y. Joti, M. Yabashi & S. Iwata, Grease matrix as a versatile carrier of proteins for serial crystallography. *Nat. Methods* **12**, 61-63 (2015).
- [2.17] H. Zhang, H. Unal, C. Gati, G. W. Han, W. Liu, N. A. Zatsepin, D. James, D. Wang, G. Nelson, U. Weierstall, M. R. Sawaya, Q. Xu, M. Messerschmidt, G. J. Williams, S. Boutet, O. M. Yefanov, T. A. White, C. Wang, A. Ishchenko, K. C. Tirupula,

- R. Desnoyer, J. Coe, C. E. Conrad⁵, P. Fromme, R. C. Stevens, V. Katritch, S. S. Karnik & V. Cherezov, Structure of the angiotensin receptor revealed by serial femtosecond crystallography. *Cell* **161**, 833-844 (2015).
- [2.18] L. C. Johansson, B. Stauch, A. Ishchenko & V. Cherezov, A bright future for serial femtosecond crystallography with XFELs. *Trends Biochem. Sci.* **42**(9), 749-762 (2017).
- [2.19] B.W. Matthews, Solvent content of protein crystals. *J. Mol. Biol.* **33**, 491-497 (1968).
- [2.20] M. Chruszcz, W. Potrzebowski, M. D. Zimmerman, M. Grabowski, H. Zheng, P. Lasota & W. Minor, Analysis of solvent content and oligomeric states in protein crystals—does symmetry matter? *Protein Sci.* **17**, 623-632 (2008).
- [2.21] K. Hirata, K. Shinzawa-Ito, N. Yano, S. Takemura, K. Kato, M. Hatanaka, K. Muramoto, T. Kawahara, T. Tsukihara, E. Yamashita, K. Tono, G. Ueno, T. Hikima, H. Murakami, Y. Inubushi, M. Yabashi, T. Ishikawa, M. Yamamoto, T. Ogura, H. Sugimoto, J.-R. Shen, S. Yoshikawa & H. Ago, Determination of damage-free crystal structure of an X-ray-sensitive protein using an XFEL. *Nat. Methods* **11**(7), 734-736 (2014).
- [2.22] E. F. Garman, Radiation damage in macromolecular crystallography: what is it and why should we care? *Acta Cryst. D* **66**, 339-351 (2010).
- [2.23] E. F. Garman & M. Weik, Radiation damage to macromolecules: kill or cure? *J. Synchrotron Rad.* **22**, 195-200 (2015).
- [2.24] J. C. H. Spence, Diffract-and-destroy: Can X-ray lasers 'solve' the radiation damage problem? *Ultramicroscopy* **108**, 1502-1503 (2008).
- [2.25] H. N. Chapman, C. Caleman & N. Timneanu, Diffraction before destruction. *Phil. Trans. R. Soc. B* **369**, 20130313 (2014).
- [2.26] M. Amin, M. Askerka, V. S. Batista, G. W. Brudvig, M. R. Gunner, X-ray free electron laser radiation damage through the S-state cycle of the oxygen-evolving complex of photosystem II. *J. Phys. Chem. B* **121**, 9382-9388 (2017).
- [2.27] C. Caleman, N. Timneanu, A. V. Martin, H. O. Jönsson, A. Aquila, A. Barty, H. A. Scott, T. A. White & H. N. Chapman, Ultrafast self-gating Bragg diffraction of exploding nanocrystals in an X-ray laser. *Opt. Express* **23**, 1213-1231 (2015).
- [2.28] H. O. Jönsson, N. Timneanu, C. Östlin, H. A. Scott & C. Caleman, Simulations of radiation damage as a function of the temporal pulse profile in femtosecond X-ray protein crystallography. *J. Synchrotron Rad.* **22**, 256-266 (2015).
- [2.29] R. Neutze, R. Wouts, D. van der Spoel, E. Weckert & J. Hajdu, Potential for biomolecular imaging with femtosecond X-ray pulses. *Nature* **406**, 752-757 (2000).
- [2.30] L. Lomb, T. R. M. Barends, S. Kassemeyer, A. Aquila, S. W. Epp, B. Erk, L. Foucar, R. Hartmann, B. Rudek, D. Rolles, A. Rudenko, R. L. Shoeman, J. Andreasson, S. Bajt, M. Barthelmeß, A. Barty, M. J. Bogan, C. Bostedt, J. D. Bozek, C. Caleman, R. Coffee, N. Coppola, D. P. DePonte, R. B. Doak, T. Ekeberg, H. Fleckenstein, P. Fromme, M. Gebhardt, H. Graafsma, L. Gumprecht, C. Y. Hampton, A. Hartmann, G. Hauser, H. Hirsemann, P. Holl, J. M. Holton, M. S. Hunter, W. Kabsch, N. Kimmel, R. A. Kirian, M. Liang, F. R. N. C. Maia, A. Meinhart, S. Marchesini, A. V. Martin, K. Nass, C. Reich, J. Schulz, M. Marvin Seibert, R. Sierra, H. Soltau, J. C. H. Spence, J. Steinbrener, F. Stellato, S. Stern, N. Timneanu, X. Wang, G. Weidenspointner, U. Weierstall, T. A. White, C. Wunderer, H. N. Chapman, J. Ullrich, L. Strüder & I. Schlichting, Radiation damage in protein serial femtosecond crystallography using an X-ray free-electron laser. *Phys. Rev. B* **84**, 214111 (2011).
- [2.31] L. Galli, S.-K. Son, M. Klinge, S. Bajt, A. Barty, R. Bean, C. Betzel, K. R. Beyerlein, C. Caleman, R. B. Doak, M. Duszenko, H. Fleckenstein, C. Gati, B. Hunt, R. A. Kirian, M. Liang, M. H. Nanao, K. Nass, D. Oberthür, L. Redecke, R. Shoeman, F. Stellato, C. H. Yoon, T. A. White, O. Yefanov, J. Spence & H. N. Chapman, Electronic damage in S atoms in a native protein crystal induced by an intense X-ray free-electron laser pulse. *Struct. Dyn.* **2**, 041703 (2015).
- [2.32] H. N. Chapman, P. Fromme, A. Barty, T. A. White, R. A. Kirian, A. Aquila, M. S. Hunter, J. Schulz, D. P. DePonte, U. Weierstall, R. B. Doak, F. R. N. C. Maia, A. V. Martin, I. Schlichting, L. Lomb, N. Coppola, R. L. Shoeman, S. W. Epp, R. Hartmann, D. Rolles, A. Rudenko, L. Foucar, N. Kimmel, G. Weidenspointner, P. Holl, M. Liang, M. Barthelmeß, C. Caleman, S. Boutet, M. J. Bogan, J. Krzywinski,

- C. Bostedt, S. Bajt, L. Gumprecht, B. Rudek, B. Erk, C. Schmidt, A. Hömke, C. Reich, D. Pietschner, L. Strüder, G. Hauser, H. Gorke, J. Ullrich, S. Herrmann, G. Schaller, F. Schopper, H. Soltau, K.-U. Kühnel, M. Messerschmidt, J. D. Bozek, S. P. Hau-Riege, M. Frank, C. Y. Hampton, R. G. Sierra, D. Starodub, G. J. Williams, J. Hajdu, N. Timneanu, M. M. Seibert, J. Andreasson, A. Rocker, O. Jönsson, M. Svenda, S. Stern, K. Nass, R. Andritschke, C.-D. Schröter, F. Krasniqi, M. Bott, K. E. Schmidt, X. Wang, I. Grotjohann, J. M. Holton, T. R. M. Barends, R. Neutze, S. Marchesini, R. Fromme, S. Schorb, D. Rupp, M. Adolph, T. Gorkhover, I. Andersson, H. Hirsemann, G. Potdevin, H. Graafsma, B. Nilsson & J. C. H. Spence, Femtosecond X-ray protein nanocrystallography. *Nature* **470**, 73-77 (2011).
- [2.33] A. Barty, C. Caleman, A. Aquila, N. Timneanu, L. Lomb, T. A. White, J. Andreasson, D. Arnlund, S. Bajt, T. R. M. Barends, M. Barthelmess, M. J. Bogan, C. Bostedt, J. D. Bozek, R. Coffee, N. Coppola, J. Davidsson, D. P. DePonte, R. B. Doak, T. Ekeberg, V. Elser, S. W. Epp, B. Erk, H. Fleckenstein, L. Foucar, P. Fromme, H. Graafsma, L. Gumprecht, J. Hajdu, C. Y. Hampton, R. Hartmann, A. Hartmann, G. Hauser, H. Hirsemann, P. Holl, M. S. Hunter, L. Johansson, S. Kassemeyer, N. Kimmel, R. A. Kirian, M. Liang, F. R. N. C. Maia, E. Malmerberg, S. Marchesini, A. V. Martin, K. Nass, R. Neutze, C. Reich, D. Rolles, B. Rudek, A. Rudenko, H. Scott, I. Schlichting, J. Schulz, M. M. Seibert, R. L. Shoeman, R. G. Sierra, H. Soltau, J. C. H. Spence, F. Stellato, S. Stern, L. Strüder, J. Ullrich, X. Wang, G. Weidenspointner, U. Weierstall, C. B. Wunderer & H. N. Chapman, Self-terminating diffraction gates femtosecond X-ray nanocrystallography measurements. *Nat. Photonics* **6**, 35-40 (2012).
- [2.34] C. David, P. Karvinen, M. Sikorski, S. Song, I. Vartiainen, C. J. Milne, A. Mozzanica, Y. Kayser, A. Diaz, I. Mohacsi, G. A. Carini, S. Herrmann, E. Färm, M. Ritala, D. M. Fritz & A. Robert, Following the dynamics of matter with femtosecond precision using the X-ray streaking method. *Sci. Rep.* **5**, 7644 (2015).
- [2.35] P. Emma, R. Akre, J. Arthur, R. Bionta, C. Bostedt, J. Bozek, A. Brachmann, P. Bucksbaum, R. Coffee, F.-J. Decker, Y. Ding, D. Dowell, S. Edstrom, A. Fisher, J. Frisch, S. Gilevich, J. Hastings, G. Hays, P. Hering, Z. Huang, R. Iverson, H. Loos, M. Messerschmidt, A. Miahnahri, S. Moeller, H. - D. Nuhn, G. Pile, D. Ratner, J. Rzeplia, D. Schultz, T. Smith, P. Stefan, H. Tompkins, J. Turner, J. Welch, W. White, J. Wu, G. Yocky & J. Galayda, First lasing and operation of an Ångstrom-wavelength free-electron laser. *Nat. Photonics* **4**, 641-647 (2010).
- [2.36] P. Karvinen, S. Rutishauser, A. Mozzanica, D. Greiffenberg, P. N. Juranić, A. Menzel, A. Lutman, J. Krzywinski, D. M. Fritz, H. T. Lemke, M. Cammarata & C. David, Single-shot analysis of hard X-ray laser radiation using a noninvasive grating spectrometer. *Opt. Lett.* **37**(24), 5073-5075 (2012).
- [2.37] C. David, S. Gorelick, S. Rutishauser, J. Krzywinski, J. Vila-Comamala, V. A. Guzenko, O. Bunk, E. Färm, M. Ritala, M. Cammarata, D. M. Fritz, R. Barrett, L. Samoylova, J. Grünert & H. Sinn, Nanofocusing of hard X-ray free electron laser pulses using diamond based Fresnel zone plates. *Sci. Rep.* **1**: 57 (2011).
- [2.38] M. Makita, I. Vartiainen, I. Mohacsi, C. Caleman, A. Diaz, H. O. Jönsson, P. Juranić, N. Medvedev, A. Meents, A. Mozzanica, N. Opara, C. Padeste, V. Panneels, V. Saxena, M. Sikorski, S. Song, L. Vera, P. R. Willmott, P. Beaud, C.J. Milne, B. Ziaja-Motyka & C. David, Femtosecond phase-transition in hard X-ray excited bismuth. Available online since 2018, e-print: arXiv:1807.06865v2, also as Appendix A.
- [2.39] P. Hart, S. Boutet, G. Carini, A. Dragone, B. Duda, D. Freytag, G. Haller, R. Herbst, S. Herrmann, C. Kenney, J. Morse, M. Nordby, J. Pines, N. van Bakel, M. Weaver, G. Williams, The Cornell-SLAC Pixel Array Detector at LCLS. SLAC-PUB-15284, *IEEE NSS/MIC*, **538** (2012).
- [2.40] G. Blaj, P. Caragiulo, G. Carini, S. Carron, A. Dragone, D. Freytag, G. Haller, P. Hart, J. Hasi, R. Herbst, S. Herrmann, C. Kenney, B. Markovic, K. Nishimura, S. Osier, J. Pines, B. Reese, J. Segal, A. Tomada & M. Weaver, X-ray detectors at the Linac Coherent Light Source. *J. Synchrotron Rad.* **22**, 577-583 (2015).
- [2.41] T. C. Huang, H. Toraya, T. N. Blanton, Y. Wu, X-ray powder diffraction analysis of silver behenate, a possible low-angle diffraction standard. *J. Appl. Cryst.* **26**, 180-184 (1993).

- [2.42] N. Opara, I. Martiel, S. A. Arnold, T. Braun, H. Stahlberg, M. Makita, C. David & C. Padeste, Direct protein crystallization on ultrathin membranes for diffraction measurements at X-ray free-electron lasers. *J. Appl. Cryst.* **50**, 909-918 (2017).
- [2.43] A. Casanas, R. Warshamanage, A. D. Finke, E. Panepucci, V. Olieric, A. Nöll, R. Tampé, S. Brandstetter, A. Förster, M. Mueller, C. Schulze-Briese, O. Bunk & M. Wang, EIGER detector: application in macromolecular crystallography. *Acta Cryst. D* **72**, 1036-1048 (2016).
- [2.44] F. Cipriani, M. Röwer, C. Landret, U. Zander, F. Felisaz, & J. A. Márquez, CrystalDirect: a new method for automated crystal harvesting based on laser-induced photoablation of thin films. *Acta Cryst. D* **68**, 1393-1399 (2012).
- [2.45] I. Inoue, Y. Inubushi, T. Sato, K. Tono, T. Katayama, T. Kameshima, K. Ogawa, T. Togashi, S. Owada, Y. Amemiya, T. Tanaka, T. Hara & M. Yabashi, Observation of femtosecond X-ray interactions with matter using an X-ray–X-ray pump-probe scheme. *Proc. Natl. Acad. Sci. U.S.A.* **113**, 1492-1497 (2016).
- [2.46] T. Pardini, J. Alameda, A. Aquila, S. Boutet, T. Decker, A. E. Gleason, S. Guillet, P. Hamilton, M. Hayes, R. Hill, J. Koglin, B. Koziemiński, J. Robinson, K. Sokolowski-Tinten, R. Soufli, and S. P. Hau-Riege, Delayed Onset of Nonthermal Melting in Single-Crystal Silicon Pumped with Hard X Rays. *Phys. Rev. Lett.* **120**, 265701 (2018).
- [2.47] T. Pardini, R. Hill, T. Decker, J. Alameda, R. Soufli, A. Aquila, S. Guillet, S. Boutet, S. P. Hau-Riege, The MEL-X project at the Lawrence Livermore National Laboratory: a mirror-based delay line for X-rays. *Proc. SPIE* **9589**, X-Ray Lasers and Coherent X-Ray Sources: Development and Applications XI, 95890T (2015).
- [2.48] T. Hirano, T. Osaka, Y. Morioka, Y. Sano, Y. Inubushi, T. Togashi, I. Inoue, S. Matsuyama, K. Tono, A. Robert, J. B. Hastings, K. Yamauchi & M. Yabashi, Performance of a hard X-ray split-and-delay optical system with a wavefront division. *J. Synchrotron Rad.* **25**, 20-25 (2018).
- [2.49] N. Shimizu, K. Hirata, K. Hasegawa, G. Ueno & M. Yamamoto, Dose dependence of radiation damage for protein crystals studied at various X-ray energies. *J. Synchrotron Rad.* **14**, 4-10 (2007).
- [3.1] R. Neutze, R. Wouts, D. van der Spoel, E. Weckert & J. Hajdu, Potential for biomolecular imaging with femtosecond X-ray pulses. *Nature* **406**, 752-757 doi:10.1038/35021099 (2000).
- [3.2] H. N. Chapman, P. Fromme, A. Barty, T. A. White, R. A. Kirian, A. Aquila, M. S. Hunter, J. Schulz, D. P. DePonte, U. Weierstall, R. B. Doak, F. R. N. C. Maia, A. V. Martin, I. Schlichting, L. Lomb, N. Coppola, R. L. Shoeman, S. W. Epp, R. Hartmann, D. Rolles, A. Rudenko, L. Foucar, N. Kimmel, G. Weidenspointner, P. Holl, M. Liang, M. Barthelmeß, C. Caleman, S. Boutet, M. J. Bogan, J. Krzywinski, C. Bostedt, S. Bajt, L. Gumprecht, B. Rudek, B. Erk, C. Schmidt, A. Hömke, C. Reich, D. Pietschner, L. Strüder, G. Hauser, H. Gorke, J. Ullrich, S. Herrmann, G. Schaller, F. Schopper, H. Soltau, K.-U. Kühnel, M. Messerschmidt, J. D. Bozek, S. P. Hau-Riege, M. Frank, C. Y. Hampton, R. G. Sierra, D. Starodub, G. J. Williams, J. Hajdu, N. Timneanu, M. M. Seibert, J. Andreasson, A. Rocker, O. Jönsson, M. Svenda, S. Stern, K. Nass, R. Andritschke, C.-D. Schröter, F. Krasniqi, M. Bott, K. E. Schmidt, X. Wang, I. Grotjohann, J. M. Holton, T. R. M. Barends, R. Neutze, S. Marchesini, R. Fromme, S. Schorb, D. Rupp, M. Adolph, T. Gorkhover, I. Andersson, H. Hirsemann, G. Potdevin, H. Graafsma, B. Nilsson & J. C. H. Spence, Femtosecond X-ray protein nanocrystallography. *Nature* **470**, 73-77 doi:10.1038/nature09750 (2011).
- [3.3] M. Suga, F. Akita, K. Hirata, G. Ueno, H. Murakami, Y. Nakajima, T. Shimizu, K. Yamashita, M. Yamamoto, H. Ago & J.-R. Shen, Native structure of photosystem II at 1.95 Å resolution viewed by femtosecond X-ray pulses. *Nature* **517** (7532), 99–103 doi:10.1038/nature13991 (2015).
- [3.4] I. Schlichting, Serial femtosecond crystallography: the first five years. *IUCrJ.* **2**, 246-255 doi:10.1107/S205225251402702X (2015).
- [3.5] C. Mueller, A. Marx, S. W. Epp, Y. Zhong, A. Kuo, A. R. Balo, J. Soman, F. Schotte, H. T. Lemke, R. L. Owen, E. F. Pai, A. R. Pearson, J. S. Olson, P. A. Anfinrud, O. P. Ernst, & R. J. Dwayne Miller, Fixed target matrix for femtosecond time-resolved

- and *in situ* serial micro-crystallography. *Struct. Dyn.* **2**, 054302 doi: 10.1063/1.4928706 (2015).
- [3.6] S. Oghbaey, A. Sarracini, H. M. Ginn, O. Pare-Labrosse, A. Kuo, A. Marx, S. W. Epp, D. A. Sherrell, B. T. Eger, Y. Zhong, R. Loch, V. Mariani, R. Alonso-Mori, S. Nelson, H. T. Lemke, R. L. Owen, A. R. Pearson, D. I. Stuart, O. P. Ernst, H. M. Mueller-Werkmeister and R. J. D. Miller, Fixed target combined with spectral mapping: approaching 100% hit rates for serial crystallography. *Acta Cryst.* **D72**, 944–955 doi:10.1107/S2059798316010834 (2016).
- [3.7] P. Roedig, I. Vartiainen, R. Duman, S. Panneerselvam, N. Stübe, O. Lorbeer, M. Warmer, G. Sutton, D. I. Stuart, E. Weckert, C. David, A. Wagner, & A. Meents, A micro-patterned silicon chip as sample holder for macromolecular crystallography experiments with minimal background scattering. *Sci. Rep.* **5**, 10451 doi:10.1038/srep10451 (2015).
- [3.8] N. Opara, I. Martiel, S. A. Arnold, T. Braun, H. Stahlberg, M. Makita, C. David & C. Padeste, Direct protein crystallization on ultrathin membranes for diffraction measurements at X-ray free-electron lasers. *J. Appl. Cryst.* **50**, 909-918 doi:10.1107/S1600576717005799 (2017).
- [3.9] A. E. Cohen, S. M. Soltis, A. González, L. Aguila, R. Alonso-Mori, C. O. Barnes, E. L. Baxter, W. Brehmer, A. S. Brewster, A. T. Brunger, G. Calero, J. F. Chang, M. Chollet, P. Ehrensberger, T. L. Eriksson, Y. Feng, J. Hattne, B. Hedman, M. Hollenbeck, J. M. Holton, S. Keable, B. K. Kobilka, E. G. Kovaleva, A. C. Kruse, H. T. Lemke, G. Lin, A. Y. Lyubimov, A. Manglik, I. I. Mathews, S. E. McPhillips, S. Nelson, J. W. Peters, N. K. Sauter, C. A. Smith, J. Song, H. P. Stevenson, Y. Tsai, M. Uerirojngankoon, V. Vinetsky, S. Wakatsuki, W. I. Weis, O. A. Zadvornyy, O. B. Zeldin, D. Zhu & K. O. Hodgson, Goniometer-based femtosecond crystallography with X-ray free electron lasers. *Proc. Natl Acad. Sci. USA*, **111**, 17122–17127 doi:10.1073/pnas.1418733111 (2014).
- [3.10] J. A. Wojdyla, E. Panepucci, I. Martiel, S. Ebner, C.-Y. Huang, M. Caffrey, O. Bunk & M. Wang, Fast two-dimensional grid and transmission X-ray microscopy scanning methods for visualizing and characterizing protein crystals. *J. Appl. Cryst.* **49**, 944–952 doi:10.1107/S1600576716006233 (2016).
- [3.11] A. J. Warren, W. Armour, D. Axford, M. Basham, T. Connolley, D. R. Hall, S. Horrell, K. E. McAuley, V. Mykhaylyk, A. Wagner, A. & G. Evans, Visualization of membrane protein crystals in lipid cubic phase using X-ray imaging. *Acta Cryst.* **D69**, 1252–1259, doi:10.1107/S0907444913011359 (2013).
- [3.12] G. Calero, A. E. Cohen, J. R. Luft, J. Newman & E. H. Snell, Identifying, studying and making good use of macromolecular crystals, *Acta Cryst.* **F70**, 993–1008 doi:10.1107/S2053230X14016574 (2014).
- [3.13] J. T. Madden, S. J. Toth, C. M. Dettmar, J. A. Newman, R. A. Oglesbee, H. G. Hedderich, R. M. Everly, M. Becker, J. A. Ronau, S. K. Buchanan, V. Cherezov, M. E. Morrow, S. Xu, D. Ferguson, O. Makarov, C. Das, R. Fischetti & G. J. Simpson, Integrated nonlinear optical imaging microscope for on-axis crystal detection and centering at a synchrotron beamline. *J. Synchrotron Rad.* **20**, 531–40 doi:10.1107/S0909049513007942 (2013).
- [3.14] D. A. Sherrell, A. J. Foster, L. Hudson, B. Nutter, J. O’Hea, S. Nelson, O. Pare-Labrosse, S. Oghbaey, R. J. D. Miller & R. L. Owen, A modular and compact portable mini-endstation for high-precision, high-speed fixed target serial crystallography at FEL and synchrotron sources. *J. Synchrotron Rad.* **22**, 1372–1378, doi: 10.1107/S1600577515016938 (2015).
- [3.15] P. Roedig, H. M. Ginn, T. Pakendorf, G. Sutton, K. Harlos, T. S. Walter, J. Meyer, P. Fischer, R. Duman, I. Vartiainen, B. Reime, M. Warmer, A. S. Brewster, I. D. Young, T. Michels-Clark, N. K. Sauter, A. Kotecha, J. Kelly, D. J. Rowlands, M. Sikorski, S. Nelson, D. S. Damiani, R. Alonso-Mori, J. Ren, E. E. Fry, C. David, D. I. Stuart, A. Wagner & A. Meents, High-speed fixed-target serial virus crystallography. *Nat. Methods* **14**, 805–810, doi:10.1038/nmeth.4335 (2017).
- [3.16] D. E. Newbury, The new X-ray mapping: X-ray spectrum imaging above 100 kHz output count rate with the silicon drift detector. *Microsc. Microanal.* **12**, 26–35 doi:10.1017/S143192760606020X (2006).

- [3.17] C. J. Milne, T. Schietinger, M. Aiba, A. Alarcon, J. Alex, A. Anghel, V. Arsov, C. Beard, P. Beaud, S. Bettoni, M. Bopp, H. Brands, M. Brönnimann, I. Brunnenkant, M. Calvi, A. Citterio, P. Craievich, M. Csatari Divall, M. Dällenbach, M. D'Amico, A. Dax, Y. Deng, A. Dietrich, R. Dinapoli, E. Divall, S. Dordevic, S. Ebner, C. Erny, H. Fitze, U. Flechsig, R. Follath, F. Frei, F. Gärtner, R. Ganter, T. Garvey, Z. Geng, I. Gorgisyan, C. Gough, A. Hauff, C. P. Hauri, N. Hiller, T. Humar, S. Hunziker, G. Ingold, R. Ischebeck, M. Janousch, P. Juranić, M. Jurcevic, M. Kaiser, B. Kalantari, R. Kalt, B. Keil, C. Kittel, G. Knopp, W. Koprek, H. T. Lemke, T. Lippuner, D. Llorente Sancho, F. Löhl, C. Lopez-Cuenca, F. Märki, F. Marcellini, G. Marinkovic, I. Martiel, R. Menzel, A. Mozzanica, K. Nass, G. Luca Orlandi, C. Ozkan-Loch, E. Panepucci, M. Paraliev, B. Patterson, B. Pedrini, M. Pedrozzi, P. Pollet, C. Pradervand, E. Prat, P. Radi, J.-Y. Raguin, S. Redford, J. Rehanek, J. Réhault, S. Reiche, M. Ringele, J. Rittmann, L. Rivkin, A. Romann, M. Ruat, C. Ruder, L. Sala, L. Schebacher, T. Schilcher, V. Schlott, T. Schmidt, B. Schmitt, X. Shi, M. Stadler, L. Stingelin, W. Sturzenegger, J. Szlachetko, D. Thattil, D. M. Treyer, A. Trisorio, W. Tron, S. Vetter, C. Vicario, D. Voulot, M. Wang, T. Zamofing, C. Zellweger, R. Zennaro, E. Zimoch, R. Abela, L. Patthey, & H.-H. Braun, SwissFEL: The swiss X-ray free electron laser. *Appl. Sci.* **7**, 720 doi:10.3390/app7070720 (2017).
- [3.18] J. Kern, V. K. Yachandra & J. Yano, Metalloprotein structures at ambient conditions and in real-time: Biological crystallography and spectroscopy using X-ray free electron lasers. *Curr. Opin. Struct. Biol.* **34**, 87–98 doi:10.1016/j.sbi.2015.07.014 (2015).
- [3.19] L. Strüder, S. Epp, D. Rolles, R. Hartmann, P. Holl, G. Lutz, H. Soltau, R. Eckart, C. Reich, K. Heinzinger, C. Thamm, A. Rudenko, F. Krasniqi, K.-U. Kühnel, C. Bauer, C.-D. Schröter, R. Moshhammer, S. Techert, D. Miessner, M. Porro, O. Hälker, N. Meidinger, N. Kimmel, R. Andritschke, F. Schopper, G. Weidenspointner A. Ziegler, D. Pietschner, S. Herrmann, U. Pietsch, A. Walenta, W. Leitenberger, C. Bostedt, T. Möller, D. Rupp, M. Adolph, H. Graafsma, H. Hirsemann, K. Gärtner, R. Richter, L. Foucar, R. L. Shoeman, I. Schlichting, J. Ullrich, Large-format, high-speed, X-ray pnCCDs combined with electron and ion imaging spectrometers in a multipurpose chamber for experiments at 4th generation light sources. *Nucl. Instrum. Methods Phys. Res. A*, **614**, 483–496 doi: 10.1016/j.nima.2009.12.053 (2010)
- [3.20] T. Hatsui & H. Graafsma, X-ray imaging detectors for synchrotron and XFEL sources. *IUCrJ* **2**, 371–383 doi:10.1107/S205225251500010X (2015).
- [3.21] R. Dinapoli, A. Bergamaschi, B. Henrich, R. Horisberger, I. Johnson, A. Mozzanica, E. Schmid, B. Schmitt, A. Schreiber, X. Shi & G. Theidel, EIGER: Next generation single photon counting detector for X-ray applications. *Nucl. Instrum. Methods Phys. Res. A*, **650**, 79–83 doi:10.1016/j.nima.2010.12.005 (2011).
- [3.22] R. Ballabriga, M. Campbell, E. Heijne, X. Llopart, L. Tlustos & W. Wong, Medipix3: A 64k pixel detector readout chip working in single photon counting mode with improved spectrometric performance. *Nucl. Instr. and Meth. in Phys. Res. A* **633**, S15–S18 doi:10.1016/j.nima.2010.06.108 (2011).
- [3.23] M. Bochenek, S. Bottinelli, C. Brönnimann, P. Livi, T. Loeliger, V. Radicci, R. Schnyder & P. Zambon, IBEX: Versatile readout ASIC with spectral imaging capability and high-count rate capability, *IEEE Trans. Nucl. Sci.* **65**, 1285–1291. doi:10.1109/TNS.2018.2832464 (2018).
- [3.24] C. Brönnimann & P. Trüb, Hybrid pixel photon counting X-ray detectors for synchrotron radiation. In *Synchrotron Light Sources and Free-Electron Lasers*, edited by E. J. Jaeschke, S. Khan, J. R. Schneider & J. B. Hastings, Cham: Springer International Publishing. 995–1027. doi:10.1007/978-3-319-14394-1 (2018).
- [3.25] F. Leonarski, S. Redford, A. Mozzanica, C. Lopez-Cuenca, E. Panepucci, K. Nass, D. Ozerov, L. Vera, V. Olieric, D. Buntschu, R. Schneider, G. Tinti, E. Froejdh, K. Diederichs, O. Bunk, B. Schmitt & M. Wang, Fast and accurate data collection for macromolecular crystallography using the JUNGFRÄU detector. *Nat. Methods*, **15**, 799–804 doi:10.1038/s41592-018-0143-7 (2018).
- [3.26] S. Redford, M. Andrä, R. Barten, A. Bergamaschi, M. Brückner, R. Dinapoli, E. Fröjdth, D. Greiffenberg, C. Lopez-Cuenca, D. Mezza, A. Mozzanica, M. Ramilli, M. Ruat, C. Ruder, B. Schmitt, X. Shi, D. Thattil, G. Tinti, S. Vetter & J. Zhang, First full dynamic range calibration of the JUNGFRÄU photon detector. *JINST* **13**, C01027

- doi:10.1088/1748-0221/13/01/C01027 (2018).
- [3.27] M. R. Fuchs, C. Pradervand, V. Thominet, R. Schneider, E. Panepucci, M. Grunder, J. Gabadinho, F. S. N. Dworkowski, T. Tomizaki, J. Schneider, A. Mayer, A. Curtin, V. Olieric, U. Frommherz, G. Kotrle, J. Welte, X. Wang, S. Maag, C. Schulze-Briese & M. Wang, D3, the new diffractometer for the macromolecular crystallography beamlines of the Swiss Light Source. *J. Synchrotron Rad.* **21**, 340–351 doi:10.1107/S160057751400006X (2014).
- [3.28] G. Ingold, R. Abela, C. Arrell, P. Beaud, P. Böhler, M. Cammarata, Y. Deng, C. Erny, V. Esposito, U. Flechsig, R. Follath, C. Hauri, S. Johnson, P. Juranić, G. F. Mancini, R. Mankowsky, A. Mozzanica, R. A. Oggenfuss, B. D. Patterson, L. Patthey, B. Pedrini, J. Rittmann, L. Sala, M. Savoini, C. Svetina, T. Zamofing, S. Zerdane & H. T. Lemke, Experimental station Bernina at SwissFEL: condensed matter physics on femtosecond time scales investigated by X-ray diffraction and spectroscopic methods. *J. Synchrotron Rad.* **26**, 874–886 doi:10.1107/S160057751900331X (2019).
- [3.29] P. Aller, J. Sanchez-Weatherby, J. Foadi, G. Winter, C. M. C. Lobley, D. Axford, A. W. Ashton, D. Bellini, J. Brandao-Neto, S. Culurgioni, A. Douangamath, R. Duman, G. Evans, S. Fisher, R. Flaig, D. R. Hall, P. Lukacik, M. Mazzorana, K. E. McAuley, V. Mykhaylyk, R. L. Owen, N. G. Paterson, P. Romano, J. Sandy, T. Sorensen, F. von Delft, A. Wagner, A. Warren, M. Williams, D. I. Stuart & M. A. Walsh, Application of *in situ* diffraction in high-throughput structure determination platforms. In *Structural Proteomics: High-Throughput Methods* Second Edition, *Methods in Molecular Biology*, edited by R. Owens, **1261**, 233–253. doi:10.1007/978-1-4939-2230-7_13 (2015).
- [3.30] I. Martiel, V. Olieric, M. Caffrey & M. Wang, Practical approaches for *in situ* X-ray crystallography: from high-throughput screening to serial data collection. *Protein Crystallography: Challenges and Practical Solutions*, edited by K. Beis & G. Evans, 1–27. Cambridge: Royal Society of Chemistry (2018).
- [3.31] P. Karvinen, S. Rutishauser, A. Mozzanica, D. Greiffenberg, P. N. Juranić, A. Menzel, A. Lutman, J. Krzywinski, D. M. Fritz, H. T. Lemke, M. Cammarata & C. David, Single-shot analysis of hard X-ray laser radiation using a noninvasive grating spectrometer. *Opt. Lett.* **37**(24), 5073–5075 doi: 10.1364/OL.37.005073 (2012).
- [3.32] K. Tono, T. Togashi, Y. Inubushi, T. Sato, T. Katayama, K. Ogawa, H. Ohashi, H. Kimura, S. Takahashi, K. Takeshita, H. Tomizawa, S. Goto, T. Ishikawa & M. Yabashi, Beamline, experimental stations and photon beam diagnostics for the hard X-ray free electron laser of SACLA. *New J. Phys.* **15**, 083035 doi: 10.1088/1367-2630/15/8/083035 (2013).
- [3.33] D. Zhu, M. Cammarata, J. M. Feldkamp, D. M. Fritz, J. B. Hastings, S. Lee, H. T. Lemke, A. Robert, J. L. Turner & Y. Feng, A single-shot transmissive spectrometer for hard X-ray free electron lasers. *Appl. Phys. Lett.* **101**, 034103 doi: 10.1063/1.4736725 (2012).
- [3.34] P. Juranić, J. Rehanek, C. A. Arrell, C. Pradervand, R. Ischebeck, C. Erny, P. Heimgartner, I. Gorgisyan, V. Thominet, K. Tiedtke, A. Sorokin, R. Follath, M. Makita, G. Seniutinas, C. David, C. J. Milne, H. Lemke, M. Radovic, C. P. Hauri & L. Patthey, SwissFEL Aramis beamline photon diagnostics. *J. Synchrotron Rad.* **25**, 1238–1248 doi:10.1107/S1600577518005775 (2018).
- [3.35] R. Brun & F. Rademakers, ROOT — An object-oriented data analysis framework. *Nucl. Instrum. Methods Phys. Res. A* **389**, 81–86 doi:10.1016/S0168-9002(97)00048-X (1997).
- [3.36] F. L. Edelman, B. N. Zaitsev, V. Z. Latuta & A. A. Khoromenko, The structure of silicon nitride films. II. Non-stoichiometric silicon nitride. *Phys. Stat. Sol.* **51**, 49–56 doi:10.1002/pssa.2210510104 (1979).
- [3.37] G. Evans & R. F. Pettifer, CHOOCH: A program for deriving anomalous-scattering factors from X-ray fluorescence spectra. *J. Appl. Cryst.* **34**, 82–86 doi:10.1107/S0021889800014655 (2001).
- [3.38] S. Gorelick, V. A. Guzenko, J. Vila-Comamala & C. David, Direct e-beam writing of dense and high aspect ratio nanostructures in thick layers of PMMA for electroplating. *Nanotechnology* **21**, 295303 doi:10.1088/0957-4484/21/29/295303 (2010).
- [3.39] K. Hili, D. Fan, V. A. Guzenko & Y. Ekinci, Nickel electroplating for high-

resolution nanostructures. *Microelectronic Engineering* **141**, 122–128 doi:10.1016/j.mee.2015.02.031 (2015).

[3.40] C.-Y. Huang, V. Olieric, P. Ma, N. Howe, L. Vogeley, X. Liu, R. Warshamanage, T. Weinert, E. Panepucci, B. Kobilka, K. Diederichs, M. Wang, & M. Caffrey, *In meso in situ* serial X-ray crystallography of soluble and membrane proteins at cryogenic temperatures. *Acta Cryst. D* **72**, 93–112 doi:10.1107/S2059798315021683 (2016).

[3.41] H. P. Löbl & M. Huppertz, Thermal stability of nonstoichiometric silicon nitride films made by reactive dc magnetron sputter deposition. *Thin Solid Films* **317**, 153–156 doi:10.1016/S0040-6090(97)00512-9 (1998).

[3.42] S. Redford, M. Andrä, R. Barten, A. Bergamaschi, M. Brückner, S. Chiriotti, R. Dinapoli, E. Fröjdh, D. Greiffenberg, F. Leonarski, C. Lopez-Cuenca, D. Mezza, A. Mozzanica, C. Ruder, B. Schmitt, X. Shi, D. Thattil, G. Tinti, S. Vetter, & J. J. Zhang, Operation and performance of the JUNGFRUAU photon detector during first FEL and synchrotron experiments. *JINST* **13**, C11006 doi:10.1088/1748-0221/13/11/C11006 (2018).

[3.43] O. B. Zeldin, M. Gerstel & E. F. Garman, RADDOS-3D: time- and space-resolved modelling of dose in macromolecular crystallography. *J. Appl. Cryst.* **46**, 1225–1230 doi:10.1107/S0021889813011461 (2013).

[4.1] H. M. El-Kaderi, J.R. Hunt, J.L. Mendoza-Cortés, A.P. Côté, R.E. Taylor, M. O'Keeffe, O.M. Yaghi, Designed Synthesis of 3D Covalent Organic Frameworks. *Science* **316**, 268–272 (2007).

[4.2] M. Eddaoudi, J. Kim, N. Rosi, D. Vodak, J. Wachter, M. O'Keeffe, O.M. Yaghi, Systematic Design of Pore Size and Functionality in Isoreticular MOFs and Their Application in Methane Storage. *Science* **295**, 469–472 (2002).

[4.3] L. Grill, M. Dyer, L. Lafferentz, M. Persson, M. V. Peters, S. Hecht, Nano-architectures by covalent assembly of molecular building blocks. *Nat. Nano.* **2**, 687–691 (2007).

[4.4] L. Lafferentz, V. Eberhardt, C. Dri, C. Africh, G. Comelli, F. Esch, S. Hecht, L. Grill, Controlling on-surface polymerization by hierarchical and substrate-directed growth. *Nat. Chem.* **4**, 215–220 (2012).

[4.5] N. Zhang, T. Wang, X. Wu, C. Jiang, T. Zhang, B. Jin, H. Ji, W. Bai, R. Bai, From 1D polymers to 2D polymers: preparation of free-standing single-monomer-thick two-dimensional conjugated polymers in water. *ACS Nano* **11**, 7223–7229 (2017).

[4.6] T. Bauer, Z. Zheng, A. Renn, R. Enning, A. Stemmer, J. Sakamoto, A. D. Schlüter, Synthesis of free-standing, monolayered organometallic sheets at the air/water interface. *Angew. Chem. Int. Ed.* **50**, 7879–7884 (2011).

[4.7] K. Baek, G. Yun, Y. Kim, D. Kim, R. Hota, I. Hwang, D. Xu, Y. H. Ko, G. H. Gu, J. H. Suh, C. G. Park, B. J. Sung, K. Kim, Free-standing, single-monomer-thick two-dimensional polymers through covalent self-assembly in solution. *J. Am. Chem. Soc.* **135**, 6523–6528 (2013).

[4.8] A. Shchyrba, C. Wäckerlin, J. Nowakowski, S. Nowakowska, J. Björk, S. Fatayer, J. Girovsky, T. Nijs, S. C. Martens, A. Kleibert, M. Stöhr, N. Ballav, T. A. Jung, L. H. Gade, Controlling the dimensionality of on-surface coordination polymers via endo- or exoligation. *J. Am. Chem. Soc.* **136**, 9355–9363 (2014).

[4.9] M. Moradi, L. G. Tulli, J. Nowakowski, M. Baljozovic, T. A. Jung, P. Shahgaldian, Two dimensional calix[4]arene-based metal-organic coordination networks of tunable crystallinity. *Angew. Chem. Int. Ed.* **56**, 14395–14399 (2017).

[4.10] R. Dong, T. Zhang, X. Feng, Interface-Assisted Synthesis of 2D Materials: Trend and Challenges. *Chem. Rev.* **118**, 6189–6235 (2018).

[4.11] J. L. Atwood, L. J. Barbour, M. J. Hardie, C. L. Raston, Metal sulfonatocalix[4,5]arene complexes: bi-layers, capsules, spheres, tubular arrays and beyond. *Coord Chem Rev.* **222**, 3–32 (2001).

[4.12] S. J. Dalgarno, J. L. Atwood, C. L. Raston, Sulfonatocalixarenes: molecular capsule and 'Russian doll' arrays to structures mimicking viral geometry. *Chem. Commun.* **44**, 4567–4574 (2006).

- [4.13] P. A. Wood, S. J. Borwick, D. J. Watkin, W. D. S. Motherwell, F. H. Allen, Dipolar C≡N...C≡N interactions in organic crystal structures: database analysis and calculation of interaction energies. *Acta Cryst. B* **64**, 393-396 (2008).
- [4.14] J. F. Moulder, W. F. Stickle, P. E. Sobol, K. D. Bomben, Handbook of X-ray Photoelectron Spectroscopy. J. Chastain, Ed., (Perkin-Elmer Corporation Physical Electronics Division, USA, 1992).
- [4.15] A. Chernenkaya, K. Medjanik, P. Nagel, M. Merz, S. Schuppler, E. Canadell, J. Pouget, G. Schönhense, Nature of the empty states and signature of the charge density wave instability and upper Peierls transition of TTF-TCNQ by temperature-dependent NEXAFS spectroscopy. *Eur. Phys. J. B* **88**, 13 (2015).
- [4.16] S. Yu, S. Ahmadi, M. Zuleta, H. Tian, K. Schulte, A. Pietzsch, F. Hennies, J. Weissenrieder, X. Yang, M. Göthelid, Adsorption geometry, molecular interaction, and charge transfer of triphenylamine-based dye on rutile TiO₂(110). *J. Chem. Phys.* **133**, 224704 (2010).
- [4.17] J. Stöhr, NEXAFS Spectroscopy; Springer series in surface sciences. (Springer, Berlin, ed. 1st, 1996).
- [4.18] U. Flechsig, F. Nolting, A. Fraile Rodríguez, J. Krempaský, C. Quitmann, T. Schmidt, S. Spielmann, D. Zimoch, Performance measurements at the SLS SIM beamline. *AIP Conf. Proc.* **1234**, 319-322 (2010).
- [4.19] M. Pfeiffermann, R. Dong, R. Graf, W. Zajaczkowski, T. Gorelik, W. Pisula, A. Narita, K. Müllen, X. Feng, Free-standing monolayer two-dimensional supramolecular organic framework with good internal order. *J. Am. Chem. Soc.* **137**, 14525-14532 (2015).
- [4.20] Q. An, Q. Chen, W. Zhu, Y. Li, C. Tao, H. Yang, Z. Li, L. Wan, H. Tian, G. Li, A facile method for preparing one-molecule-thick free-standing organic nanosheets with a regular square shape. *Chem. Commun.* **46**, 725-727 (2010).
- [4.21] W. Bai, Z. Jiang, A. E. Ribbe, S. Thayumanavan, Smart organic 2D materials based on a rational combination of non-covalent interactions. *Angew. Chem. Int. Ed. Engl.* **55**, 10707-10711 (2016).
- [4.22] I. Müllerová, M. Hovorka, L. Frank, A method of imaging ultrathin foils with very low energy electrons. *Ultramicroscopy* **119**, 78-81 (2012).
- [4.23] R. Dong, M. Pfeiffermann, H. Liang, Z. Zheng, X. Zhu, J. Zhang, X. Feng, Large-area, free-standing, two-dimensional supramolecular polymer single-layer sheets for highly efficient electrocatalytic hydrogen evolution. *Angew. Chem. Int. Ed.* **54**, 12058-12063 (2015).
- [4.24] D. Zhang, Y. Zhu, L. Liu, X. Ying, C. Hsiung, R. Sougrat, K. Li, Y. Han, Atomic-resolution transmission electron microscopy of electron beam-sensitive crystalline materials. *Science* **359**, 675-679 (2018).
- [4.25] J. Miao, T. Ishikawa, I. K. Robinson, M. M. Murnane, Beyond crystallography: Diffractive imaging using coherent x-ray light sources. *Science* **348**, 530-535 (2015).
- [4.26] M. H. Düker, R. Gómez, C. M. L. Vande Velde, V. A. Azov, Upper rim tetrathiafulvalene-bridged calix[4]arenes. *Tetrahedron Lett.* **52**, 2881-2884 (2011).
- [4.27] C. D. Gutsche, K. C. Nam, Calixarenes. 22. Synthesis, properties, and metal complexation of aminocalixarenes. *J. Am. Chem. Soc.* **110**, 6153-6162 (1988).
- [4.28] N. Moridi, C. Wäckerlin, V. Rullaud, R. Schelldorfer, T. A. Jung, P. Shahgaldian, Langmuir-Blodgett monolayer stabilization using supramolecular clips. *Chem. Commun.* **49**, 367-369 (2013).
- [4.29] X. Llopart, R. Ballabriga, M. Campbell, L. Tlustos, W. Wong, Timepix, a 65k programmable pixel readout chip for arrival time, energy and/or photon counting measurements. *Nucl. Instr. Meth. Phys. Res. A* **581**, 485-494 (2007).
- [4.30] E. van Genderen, M. T. B. Clabbers, P. P. Das, A. Stewart, I. Nederlof, K. C. Barentsen, Q. Portillo, N. S. Pannu, S. Nicolopoulos, T. Gruene, J. P. Abrahams, *Ab initio* structure determination of nanocrystals of organic pharmaceutical compounds by electron diffraction at room temperature using a Timepix quantum area direct electron detector. *Acta Cryst. A* **72**, 236-242 (2016).
- [4.31] M. T. B. Clabbers, E. van Genderen, W. Wan, E. L. Wiegers, T. Gruene, J. P. Abrahams, Protein structure determination by electron diffraction using a single three-dimensional nanocrystal. *Acta Cryst. D* **73**, 738-748 (2017)

- [4.32] K. Suwinska, O. Shkurenko, C. Mbemba, A. Leydier, S. Jebors, A. W. Coleman, R. Matar, P. Falson, Trianionic calix[4]arene monoalkoxy derivatives: synthesis, solid-state structures and self-assembly properties. *New J. Chem.* **32**, 1988-1998 (2008).
- [5.1] P. Roedig, H. M. Ginn, T. Pakendorf, G. Sutton, K. Harlos, T. S. Walter, J. Meyer, P. Fischer, R. Duman, I. Vartiainen, B. Reime, M. Warmer, A. S. Brewster, I. D. Young, T. Michels-Clark, N. K. Sauter, A. Kotecha, J. Kelly, D. J. Rowlands, M. Sikorski, S. Nelson, D. S. Damiani, R. Alonso-Mori, J. Ren, E. E. Fry, C. David, D. I. Stuart, A. Wagner, A. Meents, High-speed fixed-target serial virus crystallography. *Nat. Methods* **14**, 805-810 (2017).
- [5.2] M. Gel, S. Kandasamy, K. Cartledge, D. Hay-lock, Fabrication of freestanding microporous COC membranes optimized for in vitro barrier tissue models. *Sensors Actuators A* **215**, 51-55 (2014).
- [5.3] N. Lengweiler *et al.*, Calixarene-based freestanding nanomembranes as a protein specimen composite support for electron microscopy. Manuscript in preparation (unpublished results).
- [5.4] P. Nogly, T. Weinert, D. James, S. Carbajo, D. Ozerov, A. Furrer, D. Gashi, V. Borin, P. Skopintsev, K. Jaeger, K. Nass, P. Báth, R. Bosman, J. Koglin, M. Seaberg, T. Lane, D. Kekilli, S. Brünle, T. Tanaka, W. Wu, C. Milne, T. White, A. Barty, U. Weierstall, V. Panneels, E. Nango, S. Iwata, M. Hunter, I. Schapiro, G. Schertler, R. Neutze, J. Standfuss, Retinal isomerization in bacteriorhodopsin captured by a femtosecond X-ray laser. *Science* **361**, eaat0094 10.1126/science.aat0094 (2018)
- [5.5] N.Coquelle, M. Sliwa, J. Woodhouse, G. Schirò, V. Adam, A. Aquila, T. R. M. Barends, S. Boutet, M. Byrdin, S. Carbajo, E. De la Mora, R. B. Doak, M. Feliks, F. Fieschi, L. Foucar, V. Guillon, M. Hilpert, M. S. Hunter, S. Jakobs, J. E. Koglin, G. Kovacsova, T. J. Lane, B. Lévy, M. Liang, K. Nass, J. Ridard, J. S. Robinson, C. M. Roome, C. Ruckebusch, M. Seaberg, M. Thepaut, M. Cammarata, I. Demachy, M. Field, R. L. Shoeman, D. Bourgeois, J.-P. Colletier, I. Schlichting, M. Weik, Chromophore twisting in the excited state of a photoswitchable fluorescent protein captured by time-resolved serial femtosecond crystallography. *Nat. Chem.* **10**, 31-37 (2018).
- [5.6] K. Pande, C. D. M. Hutchison, G. Groenhof, A. Aquila, J. S. Robinson, J. Tenboer, S. Basu, S. Boutet, D. P. DePonte, M. Liang, T. A. White, N. A. Zatsepin, O. Yefanov, D. Morozov, D. Oberthuer, C. Gati, G. Subramanian, D. James, Y. Zhao, J. Koralek, J. Brayshaw, C. Kupitz, C. Conrad, S. Roy-Chowdhury, J. D. Coe, M. Metz, P. L. Xavier, T. D. Grant, J. E. Koglin, G. Ketawala, R. Fromme, V. Šrajer, R. Henning, J. C. H. Spence, A. Ourmazd, P. Schwander, U. Weierstall, M. Frank, P. Fromme, A. Barty, H. N. Chapman, K. Moffat, J. J. van Thor M. Schmidt, Femtosecond structural dynamics drives the trans/cis isomerization in photoactive yellow protein. *Science* **352**, 725–729 doi:10.1126/science.aad5081 (2016).
- [5.7] M. Suga, F. Akita, M. Sugahara, M. Kubo, Y. Nakajima, T. Nakane, K. Yamashita, Y. Umena, M. Nakabayashi, T. Yamane, T. Nakano, M. Suzuki, T. Masuda, S. Inoue, T. Kimura, T. Nomura, S. Yonekura, L.-J. Yu, T. Sakamoto, T. Motomura, J.-H. Chen, Y. Kato, T. Noguchi, K. Tono, Y. Joti, T. Kameshima, T. Hatsui, E. Nango, R. Tanaka, H. Naitow, Y. Matsuura, A. Yamashita, M. Yamamoto, O. Nureki, M. Yabashi, T. Ishikawa, S. Iwata, J.-R. Shen, Light-induced structural changes and the site of O=O bond formation in PSII caught by XFEL. *Nature* **543**, 131-135 (2017).



Abbreviations

α , β , γ – angle
2D – two-dimensional
3D – three-dimensional
Å – angstrom
ACN – acetonitrile
adc – analog to digital converter
a.k.a. – also known as
AFM – Atomic Force Microscopy
arb. u. – arbitrary units
ASIC – application-specific integrated circuit
ATP – adenosine triphosphate
BAK – Balzers Aufdampf Kammer
BAM – Brewster angle microscopy
CC1/2 – correlation coefficient between intensity estimates from half data sets
CAD – Computer Assisted Design
C-CINA – Center for Imaging and NanoAnalytics
cf. – *confer* (Latin) compare
CF – crystallization facility
COC – cyclic olefin copolymer
COFs – covalent-organic frameworks
cSAXS – coherent small-angle X-ray scattering
CSPAD – Cornell-SLAC Pixel Array Detector
CVD – chemical vapour deposition
 ΔG_0 – Gibbs' free energy
DECP – displacive excitation of coherent photons
DESY – Deutsches Elektronen-Synchrotron
e.g. – *exempli gratia* (Latin) = for example
EG – ethylene glycol
EM – electron microscopy
EPFL – École Polytechnique Fédérale de Lausanne
eV – electronvolt
 \emptyset – diameter symbol
Fig. – figure
fs – femtosecond
FUN – freestanding ultrathin nanomembranes
FWHM – full width at half maximum
HCl – hydrochloric acid
HD – hanging drop
HOPG – highly oriented pyrolytic graphite
i.e. – *id est* (Latin) = in other words
IMISX – *in meso in situ* crystallography
JUNGFRAU – adjusting gain detector for the Aramis user station
K – kelvin
KOH – potassium hydroxide
LCLS – Linac Coherent Light Source

LCP – lipidic cubic phase
LD – linear dichroism
LS – Langmuir Schaefer method
MAD – multi-wavelength anomalous dispersion
MAGIC – multiwell array generated for in situ crystallization
MFX – macromolecular femtosecond crystallography beamline
MGy – megagray
mJ – millijoule
MO – molecular orbital
MOFs – metal-organic frameworks
mrad – milliradian
MX – macromolecular crystallography
 μm – micrometer
NaAc – sodium acetate
NaCl – sodium chloride
n. d. – not determined
NEXAFS – near-edge X-ray absorption fine structure
nl – nanoliter
non-LTE – non-local thermodynamic equilibrium
NMR – nuclear magnetic resonance
OTS – octadecyltrichlorosilane
PDB – protein data bank
PEG – polyethylene glycol
PSI – Paul Scherrer Institute
PVA – polyvinyl alcohol
PX-I – protein crystallography beamline no. 1
PMMA – poly(methyl methacrylate)
RIE – reactive ion etching
RMS – root mean square
ROI – region of interest
RPM – revolutions per minute
RT – room temperature
R – reservoir
SAD – single-wavelength anomalous diffraction
SASE – self-amplified spontaneous emission
SBR – signal-over-background ratio
s.c.cm – standard cubic cm
SD – sitting drop
SDD – silicon drift detector
SEM – scanning electron microscope
SFX – serial femtosecond crystallography
SLAC – accelerator laboratory
SLS – Swiss Light Source
SNR – signal-to-noise ratio
S-S – disulfide bond
SSMMS – solid stainless steel metal microspheres
TEM – transmission electron microscopy
UV – ultraviolet radiation
VDX – vapor diffusion crystallization
vs – *versus* (Latin) = against
YAG – Yttrium Aluminum Garnet
X-CHIP – crystallization chip
XCS – X-ray correlation spectroscopy instrument
XDS – X-ray Detector Software
XFEL – X-ray free electron laser
XPS – X-ray photoelectron spectroscopy



Acknowledgements

“Życie jest spotkaniem”

“Life is a meeting”

(from Collection of memories about Prof. Stanisława Hejwowska
by Dr. Justyna Staluszka)

It is very important in life to realize which bridge to cross, which to build and which to burn. On this bumpy road through my doctoral studies, I have met many people who should be mentioned here.

First and foremost I would like to express my special appreciation to my advisor Prof. Henning Stahlberg, for all the support and given freedom and for allowing me to grow and develop skills in a new research field, as well as for valuable comments and suggestions to the thesis.

I would like to thank my Advisory Committee, especially Prof. Timm Maier for fulfilling the role of Co-referee, as well as Dr. Carolin Seuring for participation in my PhD thesis committee. Also, Prof. Jan Pieter Abrahams for kindly chairing the examination.

Further, I would like to acknowledge all the past and current colleagues working at C-CINA in Basel as well as at Paul Scherrer Institute in Villigen for creating non-forgettable, friendly atmosphere: Mina, Daniel, Michael, Deepika, Waiz, Matthias, Joka, Stefan, Benjamin, Claudio, Anastasia, Cedric, Paula, Raphael, Andy, Stefan, Pooja, Max, Inay, Ricardo, Paolo, Luca, Stefan, Ricardo, Thomas, Patrick, Stefano, Rosie, Amanda, Andrej, Andri, ... Thank you, to all of you met along the way.

Special thanks go to Dr. Shirely Müller for carefully proofreading the manuscript and all the given advice, as well as to Ashraf Al-Amoudi and Michael Wharmby for correcting a chapter of this thesis.

I would like to thank all Co-authors for their contribution to the presented results as parts of this thesis. Especially support from the researches and staff at large-scale facilities: LCLS, ESRF, SLS and DESY is greatly acknowledged.

I am grateful for all the technical cleanroom support to Dario Marty and Christopher Wild as well as for taking attentive care of the CINA equipment to Ariane Fecteau-LeFebvre, Kenny Goldie, Mohamed Chami, and sharing their knowledge and expertise on electron microscopy and sample preparation to Eric van Genderen, Philippe Ringler, Daniel Castano-Diez, Lubomir Kovacik, Thorsten Blum, Vitaliy Guzenko.

Many thanks to Karen Bergmann and Claudia Wirth who were dealing with the administrative work connected with the PhD studies.

I would also like to thank my family, all of my friends who supported me in writing, and my husband for constant encouragement to strive towards my goal.

Finally, I would like to thank again everyone, without the support of whom the work presented in this thesis would not have been possible.

The financial support from the Swiss Nanoscience Institute (SNI), and U.S. Department of Energy (LCLS experiments) is gratefully acknowledged.

Publications and meetings

Manuscripts covered in the doctoral thesis

"Direct protein crystallization on ultrathin membranes for diffraction measurements at X-ray free electron lasers",

N. Opara, I. Martiel, S. A. Arnold, T. Braun, H. Stahlberg, M. Makita, C. David, and C. Padeste, *Journal of Applied Crystallography*, 50, 909-918, **2017**. DOI:10.1107/S1600576717005799.

"Demonstration of femtosecond X-ray pump X-ray probe diffraction on protein crystals",

N. L. Opara, I. Mohacsi, M. Makita, D. Castano-Diez, A. Diaz, P. Juranić, M. Marsh, A. Meents, C. J. Milne, A. Mozzanica, C. Padeste, V. Panneels, M. Sikorski, S. Song, H. Stahlberg, I. Vartiainen, L. Vera, M. Wang, P. R. Willmott, and C. David *Structural Dynamics*, 5, 054303, **2018**. DOI:10.1063/1.5050618.

"X-ray fluorescence detection for serial macromolecular crystallography using a JUNGFRÄU pixel detector",

I. Martiel, A. Mozzanica, N. L. Opara, E. Panepucci, F. Leonarski, S. Redford, I. Mohacsi, V. A. Guzenko, B. Schmitt, B. Pedrini, and M. Wang *Journal of Synchrotron Radiation*, 27, 329-339, **2020**. DOI:10.1107/S1600577519016758.

"Supramolecular architectures of molecularly thin yet robust free-standing layers",

M. Moradi, N. L. Opara, L. G. Tulli, C. Wäckerlin, S. J. Dalgarno, S. J. Teat, M. Baljozovic, O. Popova, E. Van Genderen, A. Kleibert, H. Stahlberg, J. P. Abrahams, P. F.-X. Corvini, T. A. Jung, & P. Shahgaldian *Science Advances* 5, eaav4489, **2019**. DOI:10.1126/sciadv.aav4489.

"Femtosecond phase-transition in hard X-ray excited bismuth",

M. Makita, I. Vartiainen, I. Mohacsi, C. Caleman, A. Diaz, H. O. Jönsson, P. Juranić, N. Medvedev, A. Meents, A. Mozzanica, N. Opara, C. Padeste, V. Panneels, V. Saxena, M. Sikorski, S. Song, L. Vera, P. R. Willmott, P. Beaud, C. J. Milne, B. Ziaja-Motyka and C. David *Scientific Reports*, 9, 602, **2019**. DOI: 10.1038/s41598-018-36216-3.

Additional peer-reviewed articles

M. Moradi, N. L. Lengweiler, C. Housecroft, L. Tulli, H. Stahlberg, T. Jung, P. Shahgaldian, "Coordination-Driven Monolayer-to-Bilayer Transition in 2D Metal-Organic Networks", accepted in *Journal of Physical Chemistry B*, **2021**.

A. Tolstikova M. Levantino, O. Yefanov, V. Hennicke, P. Fischer, J. Meyer, A. Mozzanica, S. Redford, E. Crosas, N. L. Opara, M. Barthelmess, J. Lieske, D. Oberthuer, E. Wator, I. Mohacsi, M. Wulff, B. Schmitt, H. N. Chapman, and A. Meents

"1 kHz fixed-target serial crystallography using a multilayer monochromator and an integrating pixel detector",

IUCrJ, 6, 1-11, **2019**. DOI: 10.1107/S205225251900914X.

M. Ł. Górzny, N. L. Opara, V. A. Guzenko, V. J. Cadarso, H. Schiff, X. D. Li and C. Padeste

"Microfabricated silicon chip as lipid membrane sample holder for serial protein crystallography", *Micro and Nano Engineering*, 3, **2019**, 31-36. DOI: 10.1016/j.mne.2019.03.002

S. A. Arnold, S. Albiez, N. L. Opara, M. Chami, C. Schmidli, A. Bieri, C. Padeste, H. Stahlberg and T. Braun,

"Total sample conditioning and preparation of nanoliter volumes for electron microscopy", *ACS Nano*, 10 (5), 4981-4988, **2016**. DOI: 10.1021/acsnano.6b01328.

C. Rytka, N. Opara, N. Korsgaard Andersen, P. M. Kristiansen, A. Neyer,

"On the role of wetting, structure width and flow characteristics in polymer replication on micro- and nanoscale", *Macromol. Mater. Eng.* 5, 597-609, **2016**. DOI: 10.1002/mame.201500350.

Oral presentations

Nadia Opara, "In *situ* protein crystallization on microfabricated chips for serial crystallography", presented at:

- 41st Micro and Nano Engineering Conference, Hague, The Netherlands, September 21-24, **2015**, as contributed presentation (<http://mne2015.org/wp-content/uploads/2014/09/Program-overview-compact-for-website-color-2015-9-09.pdf>);
- 9th International Nanoscience Student Conference, University of Basel, Switzerland, August 11-14, **2015**, student talk
- Swiss Nanoscience Institute - Annual Meeting, Lenzerheide, Switzerland, September 3-4, **2015** – Distinguished with best talk award.

Nadia Opara, Thomas Braun, Henning Stahlberg, Mikako Makita, Christian David, Celestino Padeste, "Fixed target approach to time-resolved measurements on protein crystals at Free Electron Lasers", SLS Symposium, 19th April **2016**, SLS-PSI, Villigen-PSI

Nadia Opara *et al.*, "Delivery methods for Free Electron Lasers: direct protein crystallization on solid supports economizes sample consumption in serial femtosecond crystallography", 9th International Conference on Structural Biology, Zürich, Switzerland, September 18-20, **2017** (<https://structuralbiology.conferenceseries.com/speaker/2017/nadia-l-opara-paul-scherrer-institute-switzerland>)

Nadia Opara, Istvan Mohacsi, Mikako Makita, Daniel Castano-Diez, Ana Diaz, Pavle Juranic, May Marsh, Alke Meents, Christopher J Milne, Aldo Mozzanica, Celestino Padeste, Valerie Panneels, Marcin Sikorski, Sanghoon Song, Henning Stahlberg, Ismo Vartiainen, Laura Vera, Meitian Wang, Phillip R Willmott, Christian David,

"Demonstration of femtosecond time-resolved X-ray diffraction on protein crystals", 32nd Rhine-Knee Regional Meeting on Structural Biology, Emmetten, Switzerland, September 26-28, **2018** (https://indico.psi.ch/event/6339/attachments/11483/14747/2018_Regio_Book_of_Abstracts.pdf)

"Demonstration of femtosecond X-ray pump X-ray probe diffraction on protein crystals", 6th BioXFEL International Conference, San Diego, USA, February 11-14, **2019**, (https://www.bioxfel.org/resources/1670/download/Speaker_Abstracts_2019.pdf)

Poster presentations

Nadia Opara, Celestino Padeste, Thomas Braun, Henning Stahlberg
"Membrane supports for X-FEL based protein crystallography", SGK/SSCr Annual Meeting, EMPA Dübendorf, Switzerland 8th of Sep **2014** – Distinguished with best poster award.

N. Opara, C. Padeste, T. Braun, H. Stahlberg,
"Membrane supports for X-FEL based protein crystallography", Multi-Pole II Approach to Structural Science Meeting, Warsaw, Poland, 10-13 May, **2015** – Awarded a prize for an outstanding poster.

Nadia Opara, Celestino Padeste, Thomas Braun, Henning Stahlberg,
"Solid supports for serial protein crystallography at free electron lasers", Swiss NanoConvention, Neuchâtel, Switzerland, May 27-28, **2015**

Stefan A. Arnold, Stefan Albiez, Nadia Opara, Claudio Schmidli, Andrej Bieri, Rosmarie Sütterlin, Henning Stahlberg and Thomas Braun,
"Electron microscopy sample preparation from nanoliter volumes", Annual SNI Meeting, Lenzerheide, Switzerland, **2015** – Distinguished with poster award.

Stefan A. Arnold, Stefan Albiez, Anastasia Syntychaki, Nadia Opara, Andrej Bieri, Henning Stahlberg, and Thomas Braun,
"Electron microscopy sample preparation from nanoliter volumes", Global Engage Microscopy Congress, London, United Kingdom, **2016**

Nadia Opara, Stefan Arnold, Thomas Braun, Henning Stahlberg, Celestino Padeste, “Fixed Target Approach for Protein Crystal Delivery at X-ray Free Electron Lasers” (“Time-Resolved X-ray Crystallography of Enzymes with an X-ray Free Electron laser”), 3rd International Conference BioXFEL, San Juan, Puerto Rico, 12th Jan-15th Jan **2016** – Distinguished with 3rd poster award.

Nadia Opara, Celestino Padeste, Thomas Braun, Henning Stahlberg, “Microfabricated nanomembrane chips for serial femtosecond crystallography at X-ray free electron lasers”, Swiss NanoConvention, Basel, Switzerland, June 30-July 1, **2016**

Nadia Opara, Stefan Arnold, Thomas Braun, Henning Stahlberg, Celestino Padeste, “Ultrathin membrane chips as X-ray transparent supports for serial crystallography”, ECM-30, 30th European Crystallographic Meeting, 28th August - 1st September **2016**, Congress Center Basel, Switzerland

Project P1305,
“Ultrathin film supports for protein crystals in diffraction studies”, Nano in the snow: SNI PhD school meeting, Zermatt, Jan 25-27, **2017**

Paolo Oliva, Benjamin Bircher, Nadia Opara, Jenifer Sen, Christoph Gerber, Hans Peter Lang, Henning Stahlberg, Ernst Meyer, Thomas Braun, “Nanomechanical mass and viscosity measurement-platform for cell imaging”, Nano in the snow: SNI PhD school meeting, Zermatt, Jan 25-27, **2017** – Distinguished with poster award.

N. Opara *et al.* “Ultrathin film supports for protein crystals in diffraction studies”, Swiss NanoConvention Fribourg June 1-2, **2017**

Marcin Ł. Górzny, Nadia Opara, Xiao-Dan Li, Victor J Cadarso, Vitaliy Guzenko, Helmut Schiff, Celestino Padeste, “Silicon chip as lipid membrane sample holder for crystallography experiments”, Swiss NanoConvention Fribourg June 1-2, **2017** – Distinguished with the poster award.

Nadia Opara, Mina Moradi, Henning Stahlberg, Thomas Braun, Celestino Padeste, “Solid supports for protein nanocrystallography”, Annual SNI Meeting, Lenzerheide (CH), Sept 7-8, **2017**

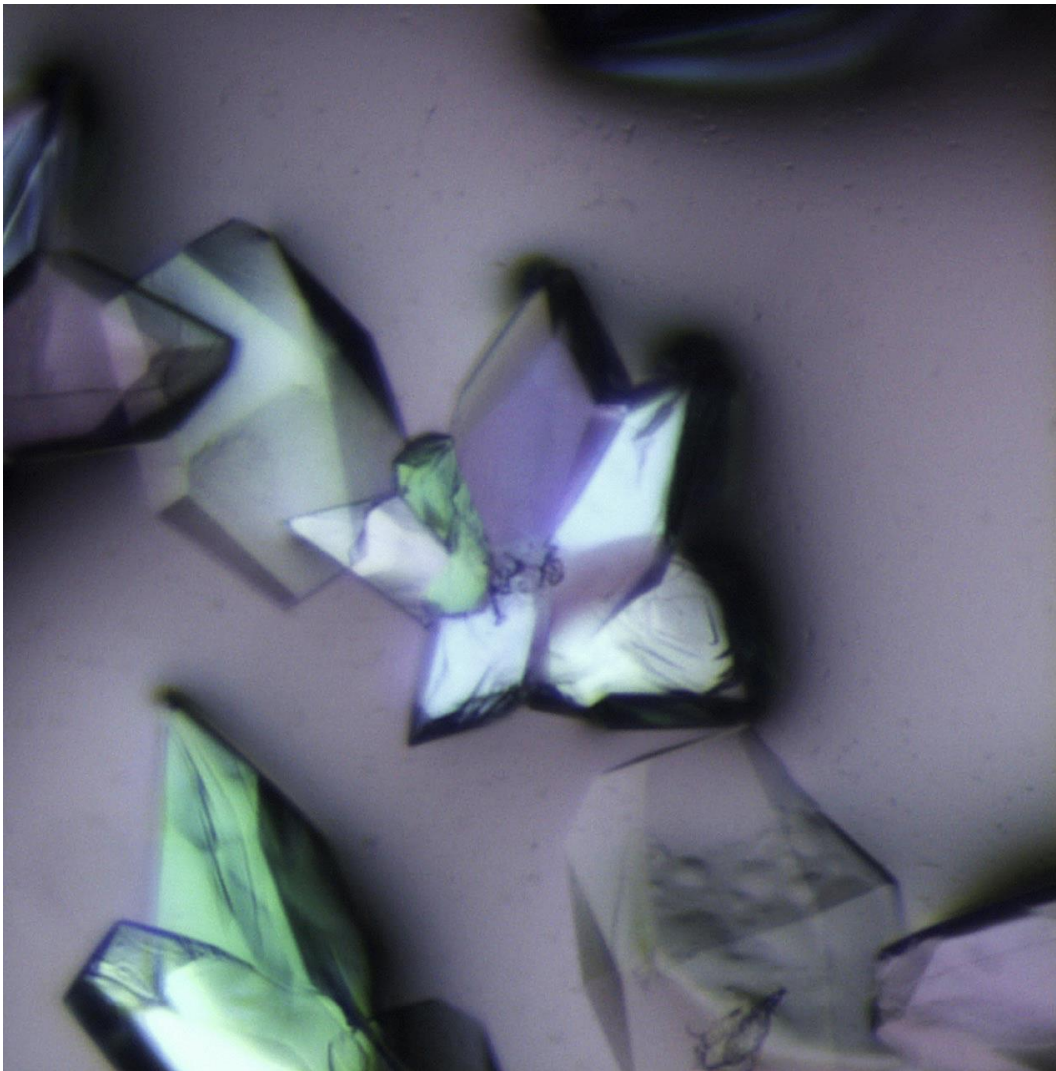
Nadia Opara, Istvan Mohacsi, Mikako Makita, Thomas Braun, Ana Diaz, Pavle Juranic, May Marsh, Alke Meents, Christopher Milne, Celestino Padeste, Valerie Panneels, Marcin Sikorski, Sanghoon Song, Henning Stahlberg, Meitian Wang, Phillip Willmott, Ismo Vartiainen, Laura Vera, Christian David, “X-ray pump / X-ray multiprobe delay line to study interaction of femtosecond ultrabright X-rays with protein crystals”, presented at:

- EUCALL workshop: Biology at Advanced Laser Light Sources, Hamburg (D), EuXFEL Facility, Nov 30 - Dec 1, **2017** and
- First Photon Science Division’s New Year’s apero, SLS, Villigen, Jan 10, **2018**

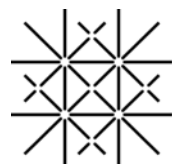
Nadia Opara, Istvan Mohacsi, Mikako Makita, Ana Diaz, Pavle Juranic, May Marsh, Alke Meents, Christopher Milne, Aldo Mozzanica, Celestino Padeste, Valerie Panneels, Marcin Sikorski, Sanghoon Song, Henning Stahlberg, Ismo Vartiainen, Laura Vera, Meitian Wang, Phillip Willmott, Christian David, “Demonstration of femtosecond time-resolved X-ray diffraction on protein crystals”, Protein dynamics workshop, Les Houches, May 27 – Jun 1, **2018**.

Freestanding Ultrathin Nanomembranes as Sample Supports for Structural Studies

Inauguraldissertation
Supplementary material



*"(...) ad astra" ****



University
of Basel

*** About the book cover:

Image source: Nadia Opara *et al.*, *J. Appl. Cryst.* (2017),
<https://doi.org/10.1107/S1600576717005799>.

Scale: height of the star-shaped crystal $\approx 172 \mu\text{m}$.

The image shows lysozyme crystals grown on the silicon nitride freestanding membrane; they were captured during sample preparation for the XFEL exposures at LCLS in March 2015.

Freestanding Ultrathin Nanomembranes as Sample Supports for Structural Studies

Inauguraldissertation Supplementary Material

zur
Erlangung der Würde eines Doktors der Philosophie
vorgelegt der
Philosophisch-Naturwissenschaftlichen Fakultät
der Universität Basel

von

**Nadia Linda Lengweiler
aus Polen**

Basel 2021

Originaldokument gespeichert auf dem Dokumentenserver der Universität Basel
<https://edoc.unibas.ch>



Appendix A

Femtosecond phase-transition in hard X-ray excited bismuth

Mikako Makita^{*,a}, Ismo Vartiainen^a, Istvan Mohacsi^{a,b}, Carl Caleman^{c,d}, Ana Diaz^a, Hans O. Jönsson^{d,e}, Pavle Juranica^a, Nikita Medvedev^{f,g}, Alke Meents^c, Aldo Mozzanica^a, Nadia L. Opara^{a,h}, Celestino Padeste^a, Valérie Panneels^a, Vikrant Saxena^{c,i}, Marcin Sikorski^j, Sanghoon Song^j, Laura Vera^a, Philip R. Willmott^a, Paul Beaud^a, Christopher J. Milne^a, Beata Ziaja-Motyka^{c,k} & Christian David^a

^a Paul Scherrer Institut, CH-5232 Villigen PSI, Switzerland

^b Synchrotron SOLEIL, L'Orme des Merisiers, 91190, Saint-Aubin, France

^c CFEL, Deutsches Elektronen-Synchrotron DESY, 22607 Hamburg, Germany

^d Department of Physics and Astronomy, Uppsala University, SE-751 24 Uppsala, Sweden

^e Department of Applied physics, KTH Royal Institute of Technology, SE-106 91 Stockholm, Sweden

^f Institute of Physics, Czech Academy of Sciences, 182 21 Prague 8, Czech Republic

^g Institute of Plasma Physics, Czech Academy of Sciences, 182 00 Prague 8, Czech Republic

^h C-CINA Biozentrum, University of Basel, CH-4058, Basel, Switzerland

ⁱ Institute for Plasma Research, Bhat, Gandhinagar 382428, India

^j Linac Coherent Light Source, SLAC National Accelerator Laboratory, 2575 Sand Hill Road, Menlo Park, California, 94025, USA

^k Institute of Nuclear Physics, Polish Academy of Sciences, 31-342 Kraków, Poland

Available online: <https://www.nature.com/articles/s41598-018-36216-3>
Scientific Reports 9, 602 (2019).

This article is licensed under a Creative Commons Attribution 4.0 International License,

and also, earlier version is available as a preprint in the repository:
<https://arxiv.org/ftp/arxiv/papers/1807/1807.06865.pdf>

Abstract

The evolution of bismuth crystal structure upon excitation of its A_{1g} phonon has been intensely studied with short pulse optical lasers. Here we present the first-time observation of a hard X-ray induced ultrafast phase transition in bismuth single crystal at high intensities ($\sim 10^{14}$ W/cm²). The lattice evolution was followed using a recently demonstrated X-ray single-shot probing setup. The time evolution of the (111) Bragg peak intensity showed strong dependence on the excitation fluence. After exposure to a sufficiently intense X-ray pulse, the peak intensity dropped to zero within 300 fs, *i.e.* faster than one oscillation period of the A_{1g} mode at room temperature. Our analysis indicates a nonthermal origin of a lattice disordering process, and excludes interpretations based on electron-ion equilibration process, or on thermodynamic heating process leading to a plasma formation.

The typical response time of the internal microscopic degrees of freedom in a solid, such as the arrangement of the electrons and atoms ranges between few fs to few ps. Ultrashort laser pulses can excite materials on time scales that are faster than those response times, often revealing unique behavior [A1-A5] and furthering the understanding of the interactions between electrons and atomic lattice [A6-A8]. In the case of ultrafast melting, photoexcitation drives the material in a highly non-equilibrium state where the electrons are excited while the lattice is still cold. As the electrons thermalize, the lattice disorders in hundreds of femtoseconds due to a significant shift in the atomic potential energy surface (PES) driven by the excited electrons. Bismuth (Bi), well known for its Peierls distorted lattice structure, is an important example of such a phase transition.

The crystal lattice of Bi can be readily excited by an ultrashort laser pulses to promote electronic excitations that typically trigger a coherent oscillation of the optical Γ -point A_{1g} phonon mode [A1-A4, A9]. The characteristic parameters of this oscillation, for example its frequency (~ 2.9 THz [A10, A11]), are strongly dependent on the excitation intensity and are directly correlated with the out-of-equilibrium potential energy surface [A12] (PES). Results from a pioneering infrared-pump experiment [A13] and subsequently from theoretical models [A8], suggested presence of a non-thermal melting process in Bi at an absorbed dose above its melting threshold. To date, however, to the best of our knowledge, neither experiments nor calculations have been able to describe the dynamics in a range above an absorbed dose of 1.2 eV/atom [A13], which is still well below a strong fast ionisation regime. In the interest of time-resolved studies, several experiments explored excitation regimes up to the regime of nonthermal melting in Bi [A3, A9, A14] and in other materials with state-of-the-art techniques [A15, A16]. Up to now, structural studies at high temporal resolution (< 100 fs) sensitive to the excitation of phonon modes in Bi have never been carried out neither in the non-thermal

melting regime or above it. It is therefore of a fundamental interest to investigate the time-resolved dynamical lattice response of Bi to intense electronic excitations, with high temporal resolution.

To address this question, we performed a study of the ultrafast lattice dynamics of a bismuth bulk crystal, excited with a femtosecond hard X-ray pulse. The advantages of using hard X-rays, instead of optical lasers, are: (i) X-rays allow to highly excite the material with negligible non-linear effects from electric and magnetic fields of the focused laser [A17]. In this way a purely electronic response of the material can be studied, and (ii) X-ray irradiation creates a low photoelectron density gradient within the pump pulse penetration depth under an incidence close to normal, yielding a relatively homogeneous secondary electron density therein. The technical difficulties typically associated with an X-ray pump and X-ray probe experiment using SASE pulses [A18] were overcome by using a novel X-ray splitting setup [A19]. As a result, an extremely high temporal resolution was achieved, limited only by the XFEL pulse duration. Importantly, this technique allows for combined characteristics which: (1) is free of any timing and spatial jitter between the pump and the probe, or between the probe beams, (2) provides consecutive probing (8 in this work) from a single X-ray pulse, thus eliminating stochastic effects, and (3) allows for independent focusing between pump and the probe pulses.

Results

The experiment was performed at the XCS station [A20] of the Linac Coherent Light Source (LCLS) [A21], using an X-ray photon energy of 5 keV, a nominal pulse energy of 2 mJ and a nominal pulse duration of 35 fs FWHM. The schematic arrangement of the transmission gratings is illustrated in Fig. A1a. The transmitted part of the X-ray pulse through the gratings acted as a “pump”, whilst those diffracted by the gratings “probed” the sample at precise time delays determined by their extended optical paths relative to the transmitted pulse. On the sample, half of the probe beams are spatially overlapped with the pump pulse, while the other half was separated by 70 μm from the pumped region. The uniqueness of the setup has been demonstrated previously [A19]. The two major differences from the previous work in this experiment are: finer time steps of 20-50 fs for an overall coverage of 300 fs, allowing higher probing time resolution, and, 2-5 times higher grating diffraction efficiency resulting in better signal-to-noise ratio. Further details about the setup can be found in the Methods and in references [A19, A22]. To ensure the spatial overlap, spot sizes of the pump and the probe pulses were focused to a FWHM of $35 \pm 5 \mu\text{m}$ and $12.5 \pm 2.5 \mu\text{m}$, respectively. The sample was oriented so as to direct the Bragg reflections of all the pulses onto a 2D detector.

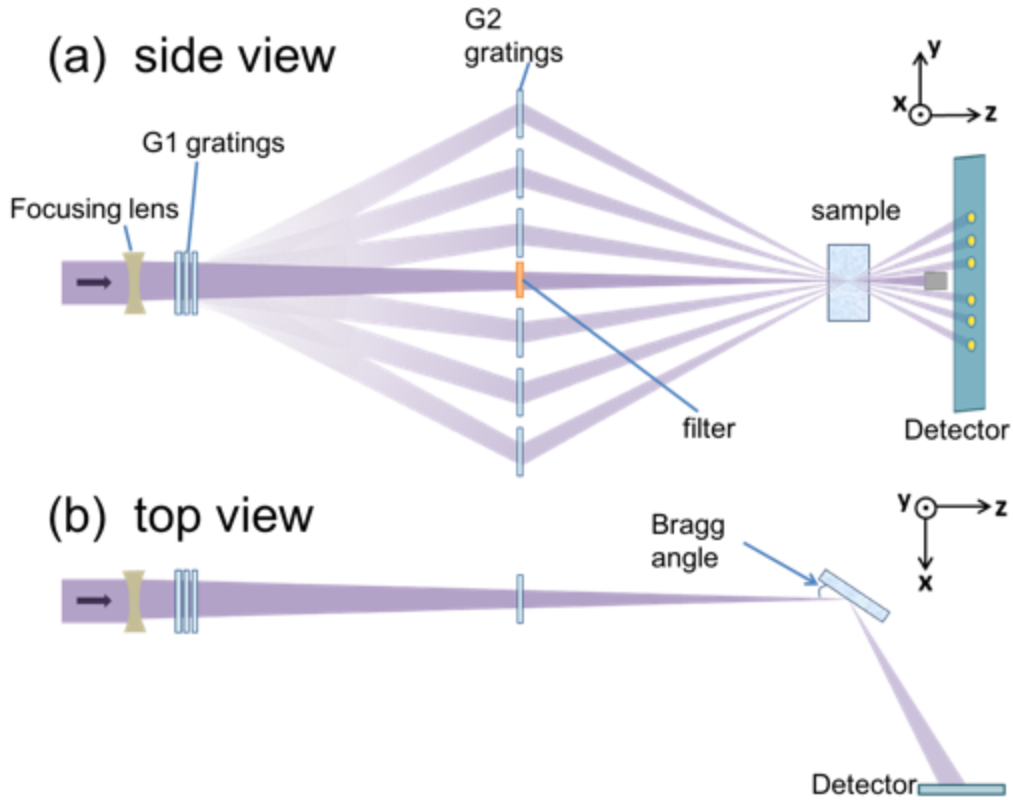


Figure A1 (a) Y-Z plane view of the setup. The label “G1 gratings” denotes a stack of 10 different diamond gratings. Only three are shown here for simplicity. Each of these gratings diffracts a small portion of the incoming X-ray pulse in the y-z plane, at varying angles defined by their pitch. The diffracted pulses are then re-diffracted back by the G2-gratings, to overlap with the transmitted primary pulse within $\pm 3 \mu\text{m}$ precision. (b) X-Z plane view of the setup. All the transmitted and diffracted pulses satisfy the Bragg condition of the sample in the x-z plane. The pulses that diffract from the sample are separated along the y-axis and aligned along the x-axis. They are then recorded on a 2D detector (JUNGFRAU).

Figure A2a, A2b show typical single-shot images of the Bi (111) Bragg peak reflection, which is sensitive to the A_{1g} phonon mode, as recorded on the detector. Diffraction patterns with and without the pump pulse are compared (Fig. A2a, A2b). For both images, the group of signals on the left-hand side, marked as “reference”, probed the unpumped region of the sample; while that marked as “probe” on the right, probed the excited area of the sample. The delay time increases as the signal distance increase from the (blocked) pump pulse at the center of the image. The flare caused by the pump beam was fitted with a 1D Gaussian profile for background removal (Fig. A2c).

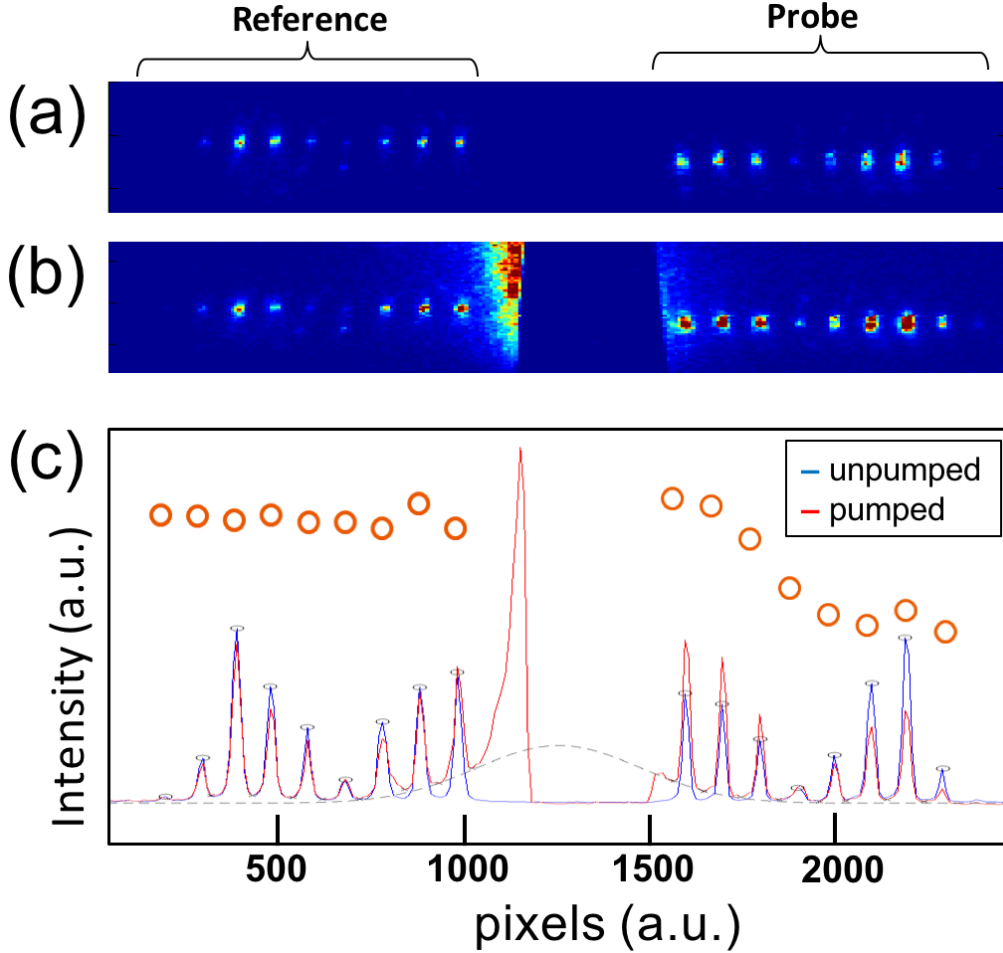


Figure A2 (a, b) Typical raw images showing (a) unpumped, and (b) pumped events of Bragg reflection signals. The pump pulse is blocked in front of the detector. The integrated plots of these images are shown in (c), red (pumped) and blue (unpumped) lines. The time delay increases symmetrically left and right from the pump pulse at the centre. A dashed grey line indicates the 1D Gaussian background level in the pumped case. After background removal, the pumped signals are then integrated and normalised by their counterpart from unpumped signals. The normalised signals are plotted as red open circles.

Figure A3 shows the time evolution of the (111) reflection recorded for different X-ray pump fluences, with the relative pump incidence at time zero (center of the pump pulse). The fluence levels are 2.46 J/cm^2 , 1.48 J/cm^2 , and 0.91 J/cm^2 , corresponding to the average absorbed dose values of 3.5 eV/atom , 2.1 eV/atom , and 1.3 eV/atom , respectively. (The chosen X-ray energy does not induce a resonant absorption by inner-shell electrons). Prior to the pump events, probe pulse intensities were measured and confirmed low enough not to damage or affect the crystal. On average, 50 ± 10 selected shots for each fluence level were used. We emphasize here that the signal dynamics seen in Fig. A3 cannot be due to X-ray intensity and spectral fluctuation, or due to crystal imperfections, since the time sequences were taken from the same pulse in single shot and from the same region of the crystal.

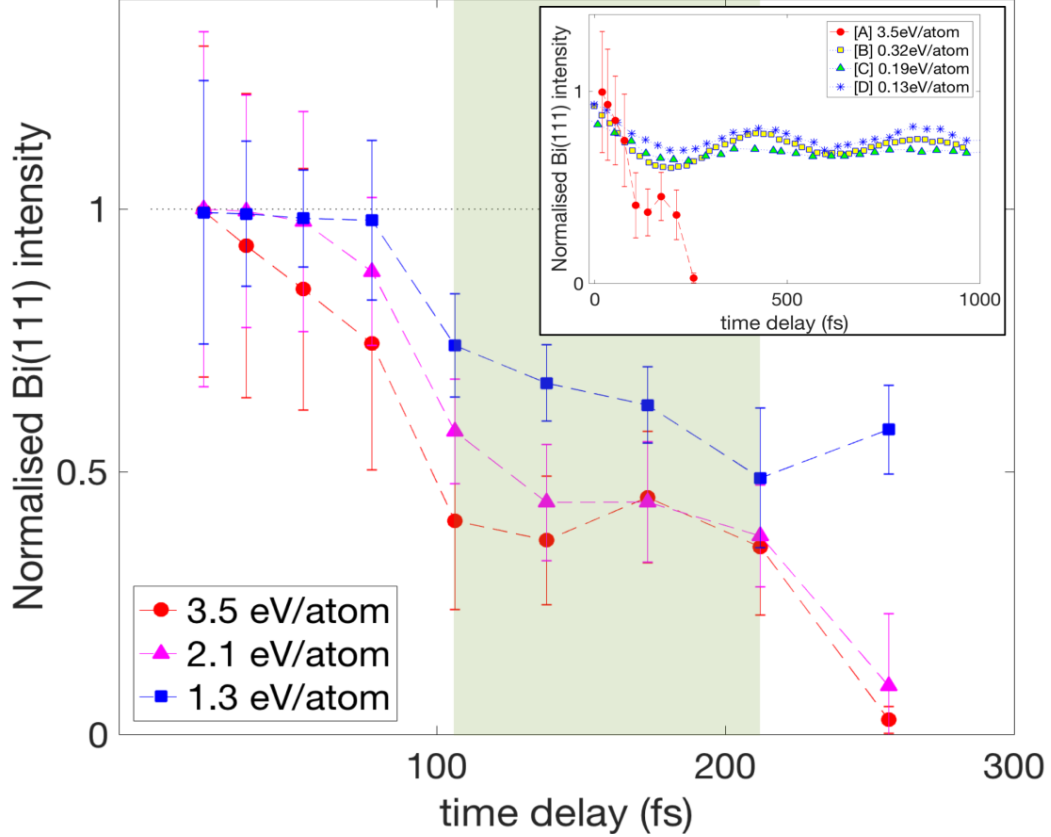


Figure A3 Temporal evolution of the normalised signals from X-ray irradiated Bi crystal at three different absorbed doses: 3.5 eV/atom (red circles), 2.1 eV/atom (magenta triangles) and 1.3 eV/atom (blue squares). Error bars are taken from standard deviation. Dashed lines are guides for the eye. The green shaded area marks roughly the plateau region discussed in the text. The inset graph shows the comparison of the case with [A] 3.5 eV/atom absorbed dose from 5 keV X-ray pulse, with the extrapolated data from previous reports on optical excitation of Bi at various absorbed doses: [B] Harmand *et al.* [A6], [C] Fritz *et al.* [A2], and [D] Johnson *et al.* [A3].

The dynamics at the lowest absorption dose of 1.3 eV/atom (at 0.91 J/cm^2) in our case could be considered similar to the highest dose cases presented in ref. [A13] (1.2 eV/atom for Bi) and in ref. [A23] (0.35 eV/atom for Sb) – implying that the PES map at this X-ray dose should be highly anharmonic and described by a single-minimum-well. For such a case, it is expected that the disordering of the lattice follows a relatively direct path, possibly by a direct anharmonic coupling of the initially excited A_{1g} motion coordinate to that of the degenerate E_g optical mode [A8, A13].

For the absorbed doses of 2.1 eV/atom and 3.5 eV/atom, the intensity drops to zero within ~ 300 fs, faster than one oscillation period of the unperturbed Bi A_{1g} phonon mode (342 fs, 2.92 THz) [A10-A12]. This is also highlighted in the inset graph in Fig. A3, which compares our observation to previous Bi (111) diffraction experiments in which bond softening or lattice damage at later times were observed [A2, A3, A9]. Our signal decays in less than half a picosecond ruling out the possibility of thermal melting process. We also note that the observed femtosecond transition triggered by $10^{13} \sim 10^{14} \text{ W/cm}^2$ pump intensity,

excludes the possibility of collisional heating through photoexcited electrons [A24] as a dominant heating process. More details about these analyses will be given in the discussion below.

An intermediate signal plateau present for all fluence cases shown in Fig. A3 (shaded green area) has been observed at a comparable timescale in X-ray irradiated diamond, within its transient transmission of optical pulses [A25]. An exponential fitting to extrapolate the decay time constant is possible for reflections from lattice insensitive to optical phonon-modes [A5-A13]. In our case, however, due to the sensitivity of (111) reflection to the A_{1g} phonon mode, we cannot uniquely exclude the possible origin of the plateau in Fig. A3 from a damped oscillatory motion along the distortion coordinate [A26, A27]. In such a case the major initial atomic potential shift would be along the (111) direction, leading to minima of diffracted intensity when Bi atomic potential passes through or near the lower symmetry equilibrium position of the parent cubic lattice. A possibility of such a process could be validated in the future by performing dedicated experiments with a longer time delay window.

Discussion

In the thermal melting regime, dramatic changes in the crystal structure can only be observed after significant atomic heating due to the electron-ion energy exchange. This process takes time typically of the order of ps [A28, A29] at the pump pulse fluences considered here. Therefore, the complete signal drop within 300 fs, seen in Fig. A3, casts out the lattice disorder through its thermalisation as a possible cause. If, on the other hand, the diffraction signal drop is due to strong ionisation only, one would expect a significant change of the Bi atomic scattering factor due to ionisation of core-electrons. However an ionisation degree estimated with the non-local thermodynamic-equilibrium (non-LTE) radiation transfer code, CRETIN30, points to less than 1 electron per atom being excited in the first 100 fs after the pump, at our highest intensity of 10^{14} W/cm² (equivalent to 3.5 eV/atom) (see Supplementary Fig. Aii). Indeed, an estimate of the scattered intensity based on XATOM code [A31] suggest that, to realise the observed signal drop, the normalised scattering factors of Bi should be at least ~ 0.8 . This corresponds to an average ionisation degree of more than ~ 10 per atom in the initial state (see Supplementary Fig. Ai). To reach such a degree of ionisation would require orders of magnitude higher X-ray intensity than we have in this experiment, which would push the sample into a plasma state.

This leaves a non-thermal melting process as the most likely interpretation of the observed transition, where a modification of interatomic potential due to high electronic excitation induces a lattice instability [A13, A32]. Given the average absorbed pump doses (1.3~3.5 eV/atom) in our cases, we conclude that 0.3~1.4 atoms for every 1000 atoms underwent photoabsorption. Therefore, $\sim 0.1\%$ of the atoms have one inner-shell hole due to photoexcitation, which is

immediately filled through an Auger process occurring in a sub-fs timescale [A31]. Immediately after photoexcitation, this process creates only $\sim 0.1\%$ holes in the valence or conduction bands, and the core holes are promptly filled. We can then assume that in the first instants after photoexcitation the interatomic potential is not significantly perturbed. Meanwhile the free energy of the sample increases by the amount of the absorbed energy, which is stored in high energy ($>keV$) photoelectrons. In a conventional non-thermal melting processes, the following dynamics has been discussed, especially for the case of semiconductors [A5, A32, A33]. A fast electron distributes its energy through collisional interactions repetitively until it settles down into bound states. At the same time the electron cascading processes further excite electrons from the valence to the conduction band, altering the electron density distribution and thus the interatomic potential, and consequently leading to lattice disorder.

Given that X-ray diffraction is mainly sensitive to the changes in core electron density, it should be noted that Bragg diffraction signal is, in principle, not directly sensitive to the PES. Indeed, for hard X-ray excited Si with similar absorbed doses to our case [A5], the start of the Bragg diffraction signal decay was observed after ~ 110 fs from the incidence of the pump. The similar excitation condition in Bi in our case also implies a significantly low ionisation degree, thus low photoelectron population, despite the absorbed dose is up to a few times higher than its damage threshold [A13]. For reflections insensitive to optical modes, similarly to the Si or diamond cases [A5, A25, A33], one could expect a short period of delay until the onset of signal drop can be observed. However, from Bi (111) the onset of the signal decay is almost immediate, especially for the highest excitation case. It indicates an atomic dislocation process occurring in parallel to non-thermal melting process.

The fluence dependence of our measurements (as seen in Fig. A3), carries additional information on the possible phenomena occurring upon photoexcitation. Scenarios such as thermal excitation of the lattice (Debye-Waller) would exhibit a fluence dependence only in the amplitude of the exponentially decreasing diffracted intensity. In contrast, here both the amplitude and the gradient leading to the normalised intensity of ~ 0.5 in Fig. A3 show fluence dependence – an observation compatible with the displacive excitation of coherent phonons (DECP) [A12]. Theoretical modelling of the DECP process is primarily dependent on the pump pulse duration (shorter than the phonon oscillation period) and on the absorbed power density. Presence of energetic excited electrons leads to excitation of many outer electrons; thus, a coherent motion of the lattice is induced as a result of changes of PES, likely contributing to the building up of a non-thermal melting process.

Assuming that DECP process is initiated, the potential implication following here is a strong anharmonic coupling between the A_{1g} and the E_g optical modes leading to a phase transition on the

timescale less than one period of the A_{1g} mode, as discussed also in ref. [A8]. We therefore speculate that this coherent lattice motion could be the precursor to the observed non-thermal melting process on such a rapid timescale. These stages of transition dynamics initiated by hard X-rays are thus most likely relevant for materials with A_1 optical modes in general.

In conclusion, we have performed the first-time observation of X-ray induced lattice disordering in Bi occurring within less than 300 fs. The (111) Bragg peak dynamics indicates that the phase transition proceeds as a complex multistep process. Our data set an important benchmark for future experiments and modelling of the hard X-ray induced ultrafast phase-transition in Bi, which should reproduce the observed fluence dependence. For that purpose, there is a strong need for a development of dedicated theoretical models capable of following such complex non-equilibrium dynamics in time. Promising candidates currently being developed are time-dependent Density Functional Theory or Hartree-Fock based schemes.

Methods

Experimental Setup

The schematic arrangement of the transmission gratings is illustrated in Fig. A1a. A set of 10 linear gratings (G1 gratings), made of diamond, was placed 0.3 m downstream from the beamline exit window. A set of 20 linear gratings (G2 gratings), made of Ir and SiO_2 , was positioned 3.3 m downstream of the G1 gratings to receive the diffracted beams from the G1 gratings. All the gratings were fabricated by means of electron-lithography and reactive ion etching, at the Laboratory for Micro- and Nanotechnology, Paul Scherrer Institut. The sample was positioned 6.6 m downstream of the G1 gratings, accepting both the transmitted (pump) beam and 20 diffracted (probe) beams from the G2 gratings. On the sample, half of the probe beams spatially overlap with the pump pulse, while the other half is separated by $70 \mu\text{m}$ to the unpumped region. In this way, the whole sequence of pumped and unpumped signals are obtained simultaneously, from a single X-ray pulse. In this experiment, the grating efficiencies are enhanced by factors of 2~5 compared to those reported earlier. The grating pitches were optimized to sequentially increase the delay timings with precisely defined intervals of 20 fs to 50 fs. This small time steps were continued up to ~ 300 fs delay, with the probe focus on early-onset of the damage to the crystal.

The Bragg angle for the (111) reflection in Bi at 5 keV is 18° with a measured rocking curve width of 0.2° . The varying incident angles in y-z plane of the pump and probe beams do not affect the Bragg condition, because the diffraction angle from the sample is only sensitive to the angle in the x-z plane, which is perpendicular to the gratings' diffraction plane (Fig. A1b). Each pulse is then incident at the detector at spatially separated locations due to the angular separations

in the y-z planes created by the diffraction gratings, thus retaining the delay-time information. Fresh sample surface was used for every shot.

The Bragg reflected probe beam signals were recorded using the JUNGFRU detector, an integrating two-dimensional pixel detector comprised of arrays of $75 \times 75 \mu\text{m}^2$ pixels, with single photon sensitivity over a dynamic range of 2.5×10^4 for 5 keV photons. More details about the JUNGFRU detector can be found in [A34]. The intensity of each diffracted peak on the detector was determined by integrating the counts up to half the distance to the neighbouring peaks. The integrated peak intensities were then normalised against the unpumped counterparts, which were then rescaled using the normalised and averaged “reference” signals.

The size of the pump beam spot was determined by observing the attenuated X-ray beam on a YAG screen at the sample position, using a microscope lens and a Charge Coupled Device (CCD) detector. The different spot sizes of the pump and the probe pulses were achieved by using Be focusing lenses positioned at two places. The first set was placed upstream of the G1 gratings and therefore affected the focusing of the direct pump beam and the probe beams. The other set was placed on the optical axis at the G2 grating position (not shown in the figure) and only affected the focusing of the pump pulse. This arrangement allowed us to choose the size of the pump and the probe beams independently.

The unattenuated pump pulse energy at the sample position (after passing through the gratings and the focusing lenses) was measured with a calorimeter to be $\sim 100 \mu\text{J}$, which is $\sim 5\%$ of the nominal total emitted pulse energy. In order to vary the fluence level, but not the probe intensities, the pump pulse was attenuated using $10 \mu\text{m}$ and $20 \mu\text{m}$ Al foils placed on the optical axis of the transmitted beam, close to the G2 grating (Fig. A1a). With these conditions, the pump beam fluence varied from 0.9 to 2.5 J/cm^2 . The energy of each probe beam was 0.01 to 0.2% of the pump beam at the sample position. In the absence of the pump beam, the crystal structure remains intact, confirming that the probe pulses are sufficiently weak to not damage the crystal.

Acknowledgements

We thank Dr. Steve Johnson, Dr. Stephen Fahy, and Dr. Éamonn Murray for insightful advice and discussions. The research leading to these results has received funding from the European Community’s Seventh Framework Programme (FP7/2007-2013) under grant agreement no. 290605 (PSI-FELLOW/COFUND). The diamond membranes used for the gratings were provided by the Diamond Materials GmbH. Silicon-nitride membranes used for the gratings were fabricated by N. L. Opara and J. Lehmann. Partial financial support from the Czech Ministry of Education (Grants LTT17015 and LM2015083) is acknowledged by N. Medvedev.

C. Caleman thanks Swedish Research Council (2013-3940) and Helmholtz Association, through Center for Free-Electron Laser Science at DESY. Support from Swiss Nanoscience Institute via project P1305 is acknowledged by N. L. Opara. Preliminary experiments were conducted at the cSAXS beamline at the Swiss Light Source, Paul Scherrer Institut, Villigen, Switzerland, as preparation for the experiment at the FEL. Use of the Linac Coherent Light Source (LCLS), SLAC National Accelerator Laboratory, is supported by the U.S. Department of Energy, Office of Science, Office of Basic Energy Sciences under Contract No. DE-AC02-76SF00515.

Author Contributions

C.D. conceived and planned the project together with M.M. The time-resolved sequential-probing with singleshot setup was built by C.D., M.M., I.V., I.M., and A.Mo. C.D. treated the Bi samples. M.M. fabricated the gratings used for the experiment. M.M., I.V., I.M., A.D., P.J., A.Me., A.Mo., N.L.O., C.P., V.P., L.V., P.R.W., C.J.M., and C.D. carried out the experiment. M.S. and S.S. supported the use of the XCS beamline at the LCLS facility. A. Mo operated the JUNGFRÄU detector. C.C. and H.O.J. operated the CRETIN code. B.Z.-M., and V.S. operated the XATOM code. M.M. analysed the data together with B.Z.-M., N.M., C.M., and P.B. The manuscript was written by M.M. with inputs from all the co-authors.

References

- [A1] K. Sokolowski-Tinten, C. Blome, J. Blums, A. Cavalleri, C. Dietrich, A. Tarasevitch, I. Uschmann, E. Förster, M. Kammler, M. Horn-von-Hoegen, D. von der Linde, Femtosecond X-ray measurement of coherent lattice vibrations near the Lindemann stability limit. *Nature* **422**, 287-289 (2003).
- [A2] D. M. Fritz, D. A. Reis, B. Adams, R. A. Akre, J. Arthur, C. Bolme, P. H. Bucksbaum, A. L. Cavalieri, S. Engemann, S. Fahy, R. W. Falcone, P. H. Fuoss, K. J. Gaffney, M. J. George, J. Hajdu, M. P. Hertlein, P. B. Hillyard, M. Horn-Von Hoegen, M. Kammler, J. Kaspar, R. Kienberger, P. Krejčík, S. H. Lee, A. M. Lindenberg, B. McFarland, D. Meyer, T. Montagne, É. D. Murray, A. J. Nelson, M. Nicoul, R. Pahl, J. Rudati, H. Schlarb, D. P. Siddons, K. Sokolowski-Tinten, T. Tschentscher, D. Von Der Linde, J. B. Hastings, Ultrafast bond softening in bismuth: mapping a solid's interatomic potential with X-rays. *Science* **315**, 633-636 (2007).
- [A3] S. L. Johnson, P. Beaud, E. Vorobeva, C. J. Milne, É. D. Murray, S. Fahy, G. Ingold, Directly observing squeezed phonon states with femtosecond X-ray diffraction. *Phys. Rev. Lett.* **102**, 175503 (2009).
- [A4] S. L. Johnson, P. Beaud, C. J. Milne, F. S. Krasniqi, E. S. Zijlstra, M. E. Garcia, M. Kaiser, D. Grolimund, R. Abela, G. Ingold, Nanoscale depth-resolved coherent femtosecond motion in laser-excited bismuth. *Phys. Rev. Lett.* **100**, 155501 (2008).
- [A5] T. Pardini, J. Alameda, A. Aquila, S. Boutet, T. Decker, A. E. Gleason, S. Guillet, P. Hamilton, M. Hayes, R. Hill, J. Koglin, B. Koziowski, J. Robinson, K. Sokolowski-Tinten, R. Soufli, S. P. Hau-Riege, Delayed onset of nonthermal melting in single-crystal silicon pumped with hard X-rays. *Phys. Rev. Lett.* **120**, 265701 (2018).

- [A6] É. D. Murray and S. Fahy, First-principles calculation of femtosecond symmetry-breaking atomic forces in photoexcited bismuth. *Phys. Rev. Lett.* **114**, 055502 (2015).
- [A7] S. Fahy, É. D. Murray, D. A. Reis, Resonant squeezing and the anharmonic decay of coherent phonons. *Phys. Rev. B* **93**, 134308 (2016).
- [A8] E. S. Zijlstra, L. L. Tatarinova, M. E. Garcia, Laser-induced phonon-phonon interactions in bismuth. *Phys. Rev. B* **74**, 220301 (2006).
- [A9] M. Harmand, R. Coffee, M. R. Bionta, M. Chollet, D. French, D. Zhu, D. M. Fritz, H. T. Lemke, N. Medvedev, B. Ziaja, S. Toleikis, M. Cammarata, Achieving few-femtosecond time-sorting at hard X-ray free-electron lasers. *Nat. Photonics* **7**, 215-218 (2013).
- [A10] P. Fischer, I. Sosnowska, M. Szymanski, Debye-Waller factor and thermal expansion of arsenic, antimony and bismuth. *J. Phys. C: Solid State Phys.* **11**, 1043-1051 (1978).
- [A11] X. Gonze, J.-P. Michenaud, J.-P. Vigneron, First-principles study of As, Sb, and Bi electronic properties. *Phys. Rev. B* **41**, 11827 (1990).
- [A12] H. J. Zeiger, J. Vidal, T. K. Cheng, E. P. Ippen, G. Dresselhaus, M. S. Dresselhaus, Theory for displacive excitation of coherent phonons. *Phys. Rev. B* **45**, 768-778 (1992).
- [A13] G. Sciaini, M. Harb, S. G. Kruglik, T. Payer, C. T. Hebeisen, F.-J. M. zu Heringdorf, M. Yamaguchi, M. Horn-von Hoegen, R. Ernstorfer, R. J. D. Miller, Electronic acceleration of atomic motions and disordering in bismuth. *Nature* **458**, 56-60 (2009).
- [A14] A. M. Lindenberg, J. Larsson, K. Sokolowski-Tinten, K. J. Gaffney, C. Blome, O. Synnergren, J. Sheppard, C. Coleman, A. G. MacPhee, D. Weinstein, D. P. Lowney, T. K. Allison, T. Matthews, R. W. Falcone, A. L. Cavalieri, D. M. Fritz, S. H. Lee, P. H. Bucksbaum, D. A. Reis, J. Rudati, P. H. Fuoss, C. C. Kao, D. P. Siddons, R. Pahl, J. Als-Nielsen, S. Duesterer, R. Ischebeck, H. Schlarb, H. Schulte-Schrepping, Th. Tschentscher, J. Schneider, D. von der Linde, O. Hignette, F. Sette, H. N. Chapman, R. W. Lee, T. N. Hansen, S. Techert, J. S. Wark, M. Bergh, G. Huldt, D. van der Spoel, N. Timneanu, J. Hajdu, R. A. Akre, E. Bong, P. Krejcik, J. Arthur, S. Brennan, K. Luening, J. B. Hastings, Atomic-scale visualization of inertial dynamics. *Science* **308**, 392-395 (2005).
- [A15] P. Musumeci, D. Cesar, J. Maxson, Double-shot MeV electron diffraction and microscopy. *Struct. Dyn.* **4**, 044025 (2017).
- [A16] M. R. Otto, L. P. René de Cotret, M. J. Stern, B. J. Siwick, Solving the jitter problem in microwave compressed ultrafast electron diffraction instruments: Robust sub-50 fs cavity-laser phase stabilization. *Struct. Dyn.* **4**, 051101 (2017).
- [A17] P. Gibbon and E. Förster, Short-pulse laser-plasma interactions. *Plasma Phys. Control. Fusion* **38**, 769-793 (1996).
- [A18] P. Emma, K. Bane, M. Cornacchia, Z. Huang, H. Schlarb, G. Stupakov, D. Walz, Femtosecond and subfemtosecond x-ray pulses from a self-amplified spontaneous-emission-based free-electron laser. *Phys. Rev. Lett.* **92**, 074801 (2004).
- [A19] C. David, P. Karvinen, M. Sikorski, S. Song, I. Vartiainen, C. J. Milne, A. Mozzanica, Y. Kayser, A. Diaz, I. Mohacsi, G. A. Carini, S. Herrmann, E. Färm, M. Ritala, D. M. Fritz, A. Robert, Following the dynamics of matter with femtosecond precision using the X-ray streaking method. *Sci. Rep.* **5**, 7644 (2015).
- [A20] R. Alonso-Mori, C. Caronna, M. Chollet, R. Curtis, D. S. Damiani, J. Defever, Y. Feng, D. L. Flath, J. M. Glowia, S. Lee, H. T. Lemke, S. Nelson, E. Bong, M. Sikorski, S. Song, V. Srinivasan, D. Stefanescu, D. Zhu, A. Robert, The X-ray correlation spectroscopy instrument at the Linac Coherent Light Source. *J. Synchrotron Radiat.* **22**, 508-513 (2015).
- [A21] P. Emma, R. Akre, J. Arthur, R. Bionta, C. Bostedt, J. Bozek, A. Brachmann, P. Bucksbaum, R. Coffee, F.-J. Decker, Y. Ding, D. Dowell, S. Edstrom, A. Fisher, J. Frisch, S. Gilevich, J. Hastings, G. Hays, P. Hering, Z. Huang, R. Iverson, H. Loos, M. Messerschmidt, A. Miahnahri, S. Moeller, H.-D. Nuhn, G. Pile, D. Ratner, J. Rzepiela, D. Schultz, T. Smith, P. Stefan, H. Tompkins, J. Turner, J. Welch, W. White, J. Wu, G. Yocky, J. Galayda, First lasing and operation of an ångström-wavelength free-electron laser. *Nat. Photonics* **4**, 641-647 (2010).

- [A22] N. L. Opara, I. Mohacsi, M. Makita, D. Castano-Diez, A. Diaz, P. Juranić, M. Marsh, A. Meents, C. J. Milne, A. Mozzanica, C. Padeste, V. Panneels, M. Sikorski, S. Song, H. Stahlberg, I. Vartiainen, L. Vera, M. Wang, P. R. Willmott, C. David, Demonstration of femtosecond X-ray pump X-ray probe diffraction on protein crystals. *Struct. Dyn.* **5**, 054303 (2018).
- [A23] B. Bauerhenne, E. S. Zijlstra, M. E. Garcia, Molecular dynamics simulations of a femtosecond-laser-induced solid-to-solid transition in antimony. *Appl. Phys. A* **123**, 608 (2017).
- [A24] S. M. Vinko, O. Ciricosta, B. I. Cho, K. Engelhorn, H.-K. Chung, C. R. D. Brown, T. Burian, J. Chalupský, R. W. Falcone, C. Graves, V. Hájková, A. Higginbotham, L. Juha, J. Krzywinski, H. J. Lee, M. Messerschmidt, C. D. Murphy, Y. Ping, A. Scherz, W. Schlotter, S. Toleikis, J. J. Turner, L. Vysin, T. Wang, B. Wu, U. Zastra, D. Zhu, R. W. Lee, P. A. Heimann, B. Nagler, J. S. Wark, Creation and diagnosis of a solid-density plasma with an X-ray free-electron laser. *Nature* **482**, 59-63 (2012).
- [A25] F. Tavella, H. Höppner, V. Tkachenko, N. Medvedev, F. Capotondi, T. Golz, Y. Kai, M. Manfredda, E. Pedersoli, M. J. Prandolini, N. Stojanovic, T. Tanikawa, U. Teubner, S. Toleikis, B. Ziaja, Soft x-ray induced femtosecond solid-to-solid phase transition. *High Energy Density Phys.* **24**, 22-27 (2017).
- [A26] P. Beaud, A. Caviezel, S. O. Mariager, L. Rettig, G. Ingold, C. Dornes, S.-W. Huang, J. A. Johnson, M. Radovic, T. Huber, T. Kubacka, A. Ferrer, H. T. Lemke, M. Chollet, D. Zhu, J. M. Glowina, M. Sikorski, A. Robert, H. Wadati, M. Nakamura, M. Kawasaki, Y. Tokura, S. L. Johnson, U. Staub, A time-dependent order parameter for ultrafast photoinduced phase transitions. *Nat. Mater.* **13**, 923-927 (2014).
- [A27] T. Huber, S. O. Mariager, A. Ferrer, H. Schafer, J. A. Johnson, S. Grubel, A. Lubcke, L. Huber, T. Kubacka, C. Dornes, C. Laulhe, S. Ravy, G. Ingold, P. Beaud, J. Demsar, S. L. Johnson, Coherent structural dynamics of a prototypical charge-density-wave-to-metal transition. *Phys. Rev. Lett.* **113**, 026401 (2014).
- [A28] K. Sokolowski-Tinten, R. K. Li, A. H. Reid, S. P. Weathersby, F. Quirin, T. Chase, R. Coffee, J. Corbett, A. Fry, N. Hartmann, C. Hast, R. Hettel, M. Horn von Hoegen, D. Janoschka, J. R. Lewandowski, M. Ligges, F. M. zu Heringdorf, X. Shen, T. Vecchione, C. Witt, J. Wu, H. A. Dürr, X. J. Wang, Thickness-dependent electron-lattice equilibration in laser-excited thin bismuth films. *New J. Phys.* **17**, 113047 (2015).
- [A29] B. Arnaud and Y. Giret, Electron cooling and Debye-Waller effect in photoexcited bismuth. *Phys. Rev. Lett.* **110**, 016405 (2013).
- [A30] H. A. Scott, Cretin—a radiative transfer capability for laboratory plasmas. *J. Quant. Spectrosc. Radiat. Transf.* **71**, 689-701 (2001).
- [A31] S.-K. Son, L. Young, R. Santra, Impact of hollow-atom formation on coherent X-ray scattering at high intensity. *Phys. Rev. A* **83**, 033402 (2011).
- [A32] N. Medvedev, H. O. Jeschke, B. Ziaja, “Nonthermal phase transitions in semiconductors induced by a femtosecond extreme ultraviolet laser pulse”, *New J. Phys.* **15**, 015016 (2013).
- [A33] N. Medvedev, Z. Li, B. Ziaja, Thermal and nonthermal melting of silicon under femtosecond x-ray irradiation. *Phys. Rev. B* **91**, 054113 (2015).
- [A34] A. Mozzanica, A. Bergamaschi, M. Brueckner, S. Cartier, R. Dinapoli, D. Greiffenberg, J. Jungmann-Smith, D. Maliakal, D. Mezza, M. Ramilli, C. Ruder, L. Schaedler, B. Schmitt, X. Shi, G. Tinti, Characterization results of the JUNGFRUA full scale readout ASIC. *J. Instrum.* **11**, C02047–C02047 (2016).

Supplementary information

Available online:

https://static-content.springer.com/esm/art%3A10.1038%2Fs41598-018-36216-3/MediaObjects/41598_2018_36216_MOESM1_ESM.pdf

Table of Contents:

- 1) Scattering factor and ionisation degree estimate with XATOM
- 2) Ionisation degree calculation with CRETIN

1) Scattering factor and ionisation degree estimate with XATOM

Assuming that the diffracted Bragg signal scales with the scattering factor, the expected average photoionization degree of atoms within the X-ray irradiated Bi bulk is estimated with XATOM code [A1.1].

The X-ray excited Bi was treated iteratively (up to ~100 iterations for convergence), for each charge state of Bi, in a spherical coordinate system. For each iteration, effective single-electron Schrödinger equation is solved within Hartree-Fock-Slater (HFS) model, with Latter's correction in the asymptotic behaviour of the HFS potential. To calculate atomic data for all individual electronic configurations, called Self Consistent Field (SCF) procedure, an energy error threshold of $1e^{-8}$ atomic units (a.u.), was used. This error includes multiple-hole states of arbitrary atomic species, as well as the cross sections and rates of X-ray-induced atomic processes. For this calculation, we have used approximately 200 grid points in the radial direction (more than 0-50 a.u. radius) and about 100 grid points in the angular direction (over 0-20 a.u. momentum).

Figure Ai shows the atomic scattering factors for different charge states of Bi, as the functions of momentum transfer. Based on this result, the required degree of ionisation in the initial state, to reach the observed intensity drop, is estimated to be at least 10 - which is contradictory to the low pump intensity, and thus photoabsorption probabilities corresponding to the fluence used in the experiment.

2) Ionisation degree calculation with CERTIN

Ionisation degree of Bi under 5 keV x-ray excitation was estimated using the non-local thermodynamic equilibrium (non-LTE) plasma simulation code CRETIN [A2.1]. For the experiment condition presented in the manuscript, the plasma model is expected to provide an overview description of the material under X-ray excitation, such as the ionisation state, or electron temperature, as a function of time (more examples could be found in refs. [A3.1, A4.1]).

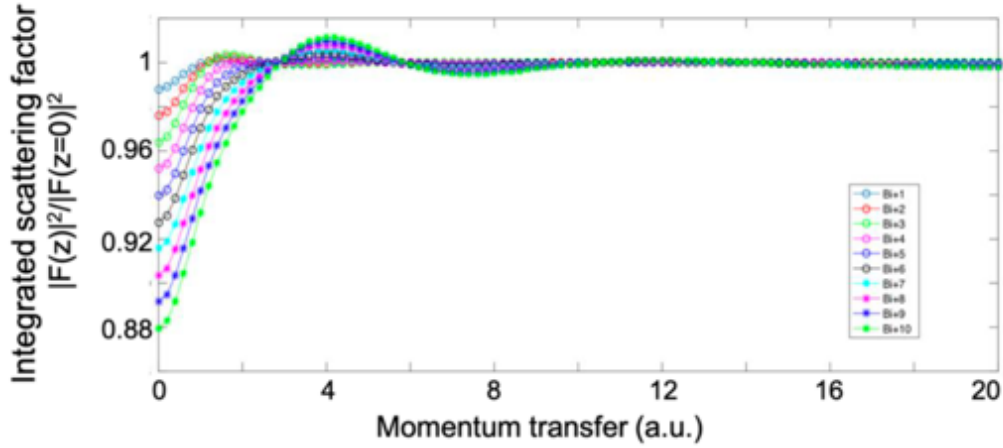


Figure Ai The scattering factors (y-axis) for various Bi ions. The y-axis is the integrated scattering factor (ISF) for different charge states, normalised by the ISF for neutral Bi. The x-axis is the momentum transfer in a.u. The plot suggests that the average ionization degree in Bi bulk would have to increase significantly within the 300 fs timescale, in order to explain the observed Bragg peak decay seen in Fig. A3 of the main manuscript as due to the decrease in scattering factor.

The simulation parameters are matched with the fluence and photon energy in the experiment, *i.e.* photon energy of 5 keV, pulse duration of 35 fs with a flat-top X-ray pulse model. The structure is not explicitly modelled in this code and the material is treated as a continuum. Instead, the sample is simulated in nanometre-sized zones, where continuum lowering governed by Stewart-Pyatt degeneracy is applied to compensate for the lowering of ionisation potentials. The code allows electron and ion temperatures to be different but assume a Maxwellian distribution of kinetic energies within those populations. Using this concept, rate equations are solved to calculate the time evolution of the system with changing population of electronic states, radiation transport including energy dependent absorption and opacity changes.

The calculation keeps track of the average ionisation and temperatures of electrons and ions separately, while excluding any local structural information assuming that the local density of the atoms is homogeneous within the simulation duration (~ 100 fs). It was found that even at the highest fluence case, the average ionisation degree per atom was around 0.8 after 100 fs, where the primary modes of ionisation were direct photoionisation and Auger ionisation. It also suggests that many of the capabilities of the code related to highly ionized plasma states were not activated even for the highest dose case.

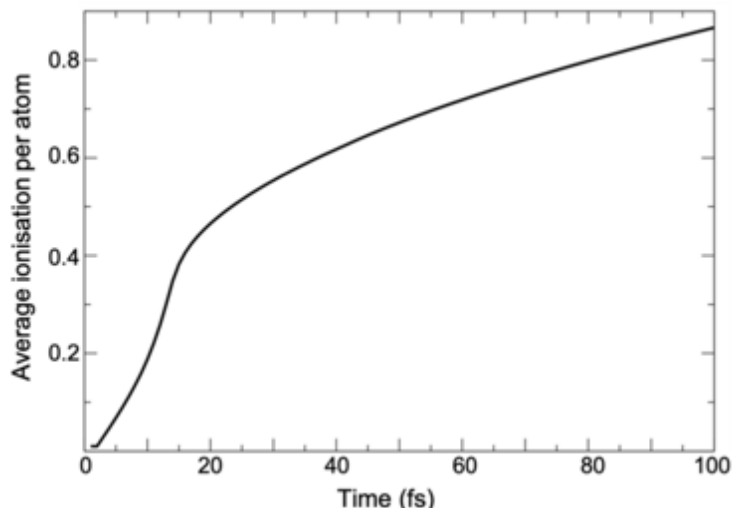


Figure Aii Average ionization degree per atom of bismuth for the highest fluence case (3.5 eV/atom). Time zero denotes the pump pulse incidence. The average ionisation degree is less than 1, at 100 fs after the laser incidence, indicating that the sample to reach plasma state on the timescale of < 300 fs unlikely.

[A1.1] S.-K. Son, L. Young, R. Santra, Impact of hollow-atom formation on coherent X-ray scattering at high intensity. *Phys. Rev. A* **83**, 033402 (2011).

[A2.1] H. A. Scott, Cretin—a radiative transfer capability for laboratory plasmas. *J. Quant. Spectrosc. Radiat. Transf.* **71**, 689-701 (2001).

[A3.1] K. R. Beyerlein, H. O. Jönsson, R. Alonso-Mori, A. Aquila, S. Bajt, A. Barty, R. Bean, J. E. Koglin, M. Messerschmidt, D. Ragazzon, D. Sokaras, G. J. Williams, S. Hau-Riege, S. Boutet, H. N. Chapman, N. Timneanu, C. Caleman, Ultrafast nonthermal heating of water initiated by an X-ray Free-Electron Laser. *Proc. Natl. Acad. Sci. U. S. A.* **115**, 5652–5657 (2018).

[A4.1] K. Nass, L. Foucar, T. R. M. Barends, E. Hartmann, S. Botha, R. L. Shoeman, R. B. Doak, R. Alonso-Mori, A. Aquila, S. Bajt, A. Barty, R. Bean, K. R. Beyerlein, M. Bublitz, N. Drachmann, J. Gregersen, H. O. Jönsson, W. Kabsch, S. Kassemeyer, J. E. Koglin, M. Krumrey, D. Mattle, M. Messerschmidt, P. Nissen, L. Reinhard, O. Sitsel, D. Sokaras, G. J. Williams, S. Hau-Riege, N. Timneanu, C. Caleman, H. N. Chapman, S. Boutet, I. Schlichting, Indications of radiation damage in ferredoxin microcrystals using high-intensity X-FEL beams. *J. Synchrotron Radiat.* **22**, 225–238 (2015).



Appendix B

**Supplementary Information for:
Direct protein crystallization on ultrathin
membranes for diffraction measurements
at X-ray free electron lasers**

Nadia Opara^{a,b,c}, Isabelle Martiel^a, Stefan A. Arnold^{b,c}, Thomas Braun^{b,c}, Henning Stahlberg^{b,c}, Mikako Makita^a, Christian David^a, and Celestino Padeste^{a,c}

^a Paul Scherrer Institute (PSI), 5232 Villigen, Switzerland

^b Center for Cellular Imaging and NanoAnalytics (C-CINA), Biozentrum, University of Basel, 4058 Basel, Switzerland

^c Swiss Nanoscience Institute, University of Basel, 4056 Basel, Switzerland

Available online:

<http://journals.iucr.org/j/issues/2019/06/00/yr9015/yr9015sup1.pdf>

Journal of Applied Crystallography **50**, 909-918 (2017).

Reproduced with permission of the International Union of Crystallography.

Table BS1 Parameters of the crystallization conditions tested for producing large crystals for X-FEL experiments. Unless otherwise stated (SD) experiments were carried out in hanging drop (HD) geometry. Loaded chips were mounted on the lid of the ibidi® box and the reservoir of the chamber was charged with 1 or 0.5 ml of 0.6 M NaCl, 0.1 M NaAc, pH 4.5 (reservoir solution; referred to as “R” in the table). They were incubated at room temperature (20-22°C), at approximately 55% relative humidity. Sizes shapes and densities of crystals were assessed by light microscopy. Chips that were selected, mounted to the aluminium holder and exposed to the FEL beam are indicated by bold type, chip 48 was used for the synchrotron diffraction data collection.

Chip no.	Window size [μm^2]	Si_xN_y layer thickness [nm]	Crystallization condition: protein concentration and precipitating agent composition	Volume deposited (μl)
1	300 x 300	30	90 μl (50 mg/ml H_2O) + 10 μl “R”	20
2 (SD)	300 x 300	30	90 μl (50 mg/ml H_2O) + 10 μl “R”	20
3	400 x 400	30	50 mg/ml H_2O	20
4	400 x 400	30	90 μl (50 mg/ml H_2O) + 5 μl “R”	20
5	500 x 500	85	100 mg/ml H_2O	20
6	500 x 500	85	90 μl (100 mg/ml H_2O) + 10 μl “R”	20
7	200 x 200	30	90 μl (50 mg/ml H_2O) + 10 μl “R”	5
8	200 x 200	30	90 μl (50 mg/ml H_2O) + 5 μl “R”	5 vs 0.5 ml R
9	300 x 300	30	90 μl (50 mg/ml H_2O) + 10 μl “R”	5 vs 0.5 ml R
10	200 x 200	30	90 μl (50 mg/ml H_2O) + 10 μl “R”	20
11	200 x 200	30	90 μl (50 mg/ml H_2O) + 20 μl “R”	20
12	300 x 300	250	90 μl (50 mg/ml H_2O) + 10 μl B1 + 10 μl PEG 50%	20
13	200 x 200	250	90 μl (50 mg/ml H_2O) + 20 μl “R” + 5 μl 100% EG	20

14	400 x 400	30	50 mg/ml 50 mM NaAc	20
15	300 x 300	250	50 mg/ml 50 mM NaAc	20 vs 0.5 ml R
16	200 x 200	250	50 mg/ml 50 mM NaAc	20 vs 0.5 ml R
17	300 x 300	250	90 µl (50 mg/ml H ₂ O) + 10 µl „R“ + 10 µl PEG 50%	20 vs 0.5 ml R
18	400 x 400	250	90 µl (50 mg/ml H ₂ O) + 10 µl „R“ + 10 µl EG 1%	20 vs 0.5 ml R
20	200 x 200	250	50 mg/ml 50 mM NaAc; fresh	20 vs 0.5 ml R
21	300 x 300	250	50 mg/ml 50 mM NaAc; fresh	20 vs 0.5 ml R
22	400 x 400	250	50 mg/ml 50 mM NaAc; fresh	20 vs 0.5 ml R
23	200 x 200	250	90 µl (50 mg/ml H ₂ O) + 10 µl „R“ + 10 µl 50% PEG; fresh	20 vs 0.5 ml R
24	300 x 300	250	90 µl (50 mg/ml H₂O) + 10 µl „R“ + 10 µl 50% PEG; fresh	20 vs 0.5 ml R
25	400 x 400	250	90 µl (50 mg/ml H ₂ O) + 10 µl „R“ + 10 µl 50% PEG; fresh	20 vs 0.5 ml R
26	200 x 200	250	90 µl (70 mg/ml H₂O) + 10 µl „R“ + 10 µl PEG 50%; fresh	20 vs 0.5 ml R
27	300 x 300	250	90 µl (70 mg/ml H₂O) + 10 µl „R“ + 10 µl PEG 50%; fresh	20 vs 0.5 ml R
28	400 x 400	250	90 µl (70 mg/ml H ₂ O) + 10 µl „R“ + 10 µl PEG 50%; fresh	20 vs 0.5 ml R
29	400 x 400	250	70 mg/ml 50 mM NaAc; fresh	20 vs 0.5 ml R
30	200 x 200	250	50 mg/ml 50 mM NaAc; fresh	20 vs 0.5 ml R
31	300 x 300	250	50 mg/ml 50 mM NaAc; fresh	20 vs 0.5 ml R
32	400 x 400	250	50 mg/ml 50 mM NaAc; fresh	20 vs 0.5 ml R

33	200 x 200	250	90 µl (70 mg/ml H ₂ O) + 10 µl „R“ + 10 µl PEG 50%; fresh	20 vs 0.5 ml R
34	300 x 300	250	90 µl (70 mg/ml H ₂ O) + 10 µl „R“ + 10 µl PEG 50%; fresh	20 vs 0.5 ml R
35	400 x 400	250	90 µl (70 mg/ml H ₂ O) + 10 µl „R“ + 10 µl PEG 50%; fresh	20 vs 0.5 ml R
36	200 x 200	250	50 mg/ml 50mM NaAc; stored at 4°C	20 vs 0.5 ml R
37	200 x 200	250	90 µl (70 mg/ml H ₂ O) + 10 µl „R“ + 10 µl PEG 50%; stored at 4°C	20 vs 0.5 ml R
38	300 x 300	250	90 µl (70 mg/ml H ₂ O) + 10 µl „R“ + 10 µl PEG 50%; stored at 4°C	20 vs 0.5 ml R
39	400 x 400	250	50 mg/ml 50mM NaAc; stored at 4°C	20 vs 0.5 ml R
40	200 x 200	250	50 mg/ml 50 mM NaAc; fresh	20 vs 0.5 ml R
41	300 x 300	250	50 mg/ml 50 mM NaAc; fresh	20 vs 0.5 ml R
42	200 x 200	250	90 µl (70 mg/ml H ₂ O) + 10 µl „R“ + 10 µl PEG 50%; fresh	20 vs 0.5 ml R
43	300 x 300	250	90 µl (70 mg/ml H ₂ O) + 10 µl „R“ + 10 µl PEG 50%; fresh	20 vs 0.5 ml R
44	200 x 200	250	50 mg/ml 50 mM NaAc; stored at 4°C	20 vs 0.5 ml R
45	300 x 300	250	50 mg/ml 50 mM NaAc; stored at 4°C	20 vs 0.5 ml R
46	200 x 200	250	90 µl (70 mg/ml H ₂ O) + 10 µl „R“ + 10 µl PEG 50%; stored at 4°C	20 vs 0.5 ml R
47	400 x 400	250	90 µl (70 mg/ml H ₂ O) + 10 µl „R“ + 10 µl PEG 50%; fresh	20 vs 0.5 ml R
48	300 x 300	250	90 µl (50mg/ml H ₂ O) + 20 µl „R“ + 10 µl 25% EG	20
49	100 x 100	30	5 nl (50 mg/ml H ₂ O) on top of 8 nl „R“	13 nl in each well

Table BS2 Parameters of the diffraction data collected on EIGER X 16M detector at PX-I beamline, SLS on lysozyme microcrystals grown *in situ* on the silicon nitride membranes and preserved from dehydration by sandwich-type enclosure in between two chips.

Data collection	
Temperature (K)	293
Beamline	Swiss Light Source PXI X06SA
Wavelength (Å)	1.00
Flux of the full beam; transmission; exposure;	1.5e11 ph/s; 0.005; 0.1 s/frame
Total range collected per crystal (°); per frame	50; 0.1
Crystal-to-detector distance [mm]	200
Number of crystals merged	2
Phasing method	Molecular replacement (search model PDB: 2lyz)
Space group	P4 ₃ 2 ₁ 2
Unit cell parameter <i>a</i> (Å)	79.50
Unit cell parameter <i>b</i> (Å)	79.50
Unit cell parameter <i>c</i> (Å)	37.81
<i>a</i> = <i>b</i> = <i>γ</i> (°)	90
Resolution (Å)	50-1.57 (1.61-1.57)
R _{meas}	0.05 (0.847)
<I/σ(I)>	13.74 (1.04)
Completeness	0.954 (0.952)
CC _{1/2}	99.9 (70.5)
Mosaicity (°)	0.033
Refinement	
Resolution (Å)	39.75-1.57
No. of reflections R _{work} /R _{free}	16960/849
R _{work} /R _{free}	0.1656/0.1819
No. of non-hydrogen atoms:	
Protein	1020
Ions	5
Water	65
Bond lengths RMS (Å)	0.005
Bond angles RMS (°)	0.77
Ramachandran favored (%)	99.25
Ramachandran allowed (%)	0.75
Ramachandran outliers (%)	0
Rotamer outliers (%)	0
Clashscore	1.00
B-factors (Å ²):	
Protein	30.44
Ions	42.11
Water	41.05
PBD ID	5ne0

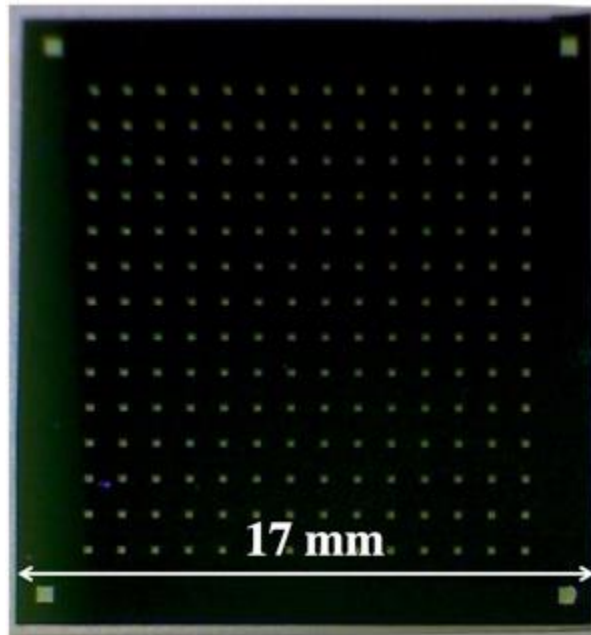


Figure BS1 Microfabricated chip with Si_3N_4 windows (here: $200\ \mu\text{m} \times 200\ \mu\text{m}$) designed for serial femtosecond crystallography time-resolved experiments. Large ($400\ \mu\text{m} \times 400\ \mu\text{m}$) membranes placed in the corners were knocked-out and served as alignment marks.

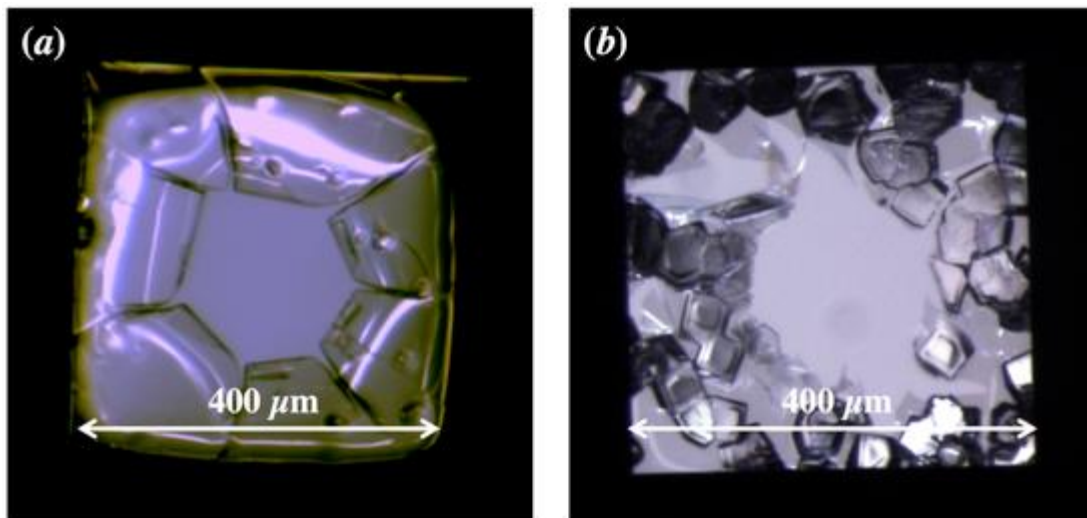


Figure BS2 Inadequate crystallization conditions led to membrane damage. Thin membranes ($30\ \text{nm}$) are prone to damage during (a) or after (b) crystallization – due to the tension created on the membrane.

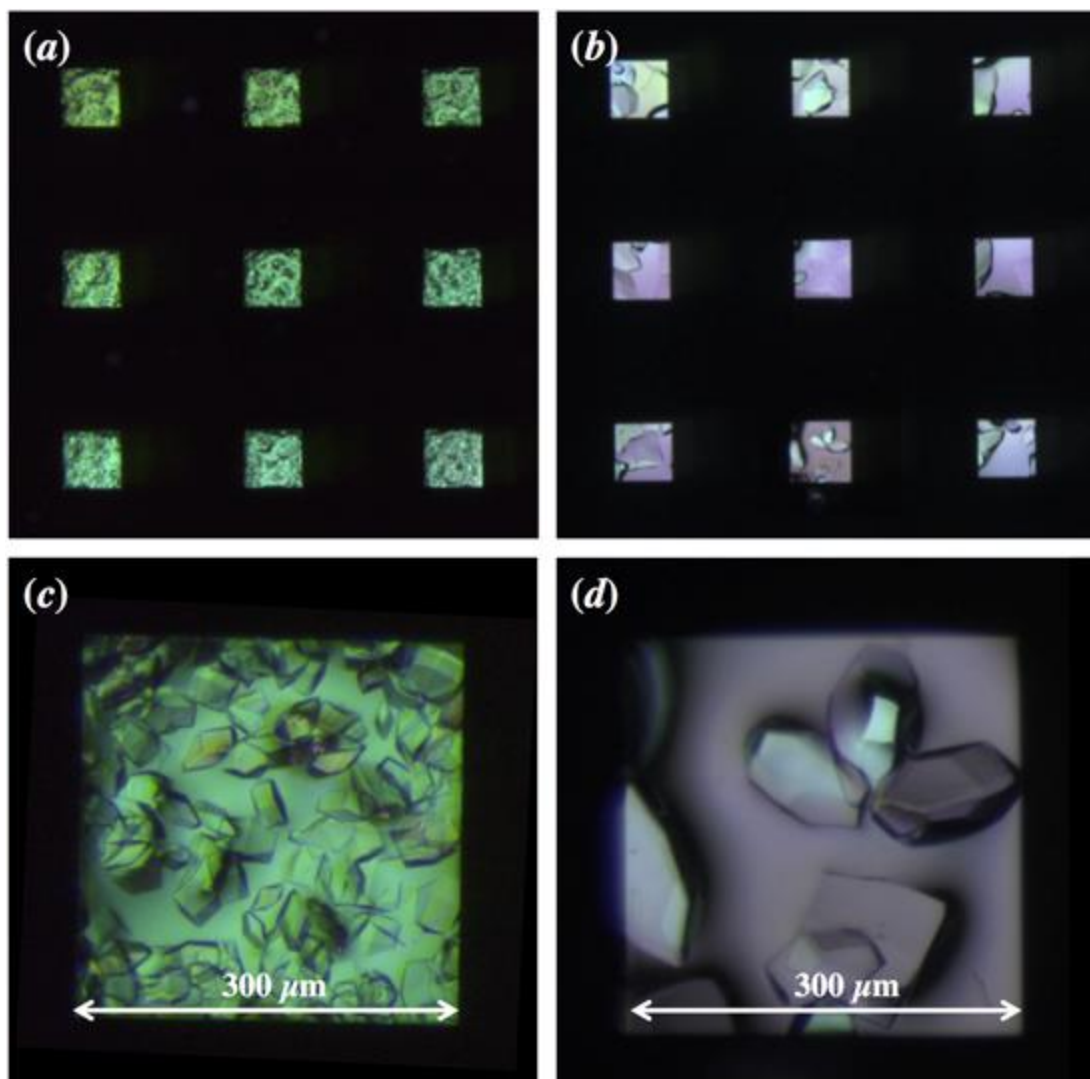


Figure BS3 Protein crystals grown on Si_3N_4 membranes. (a) and (b): overview, (c) and (d): zoomed in view of selected wells. (a) and (c): Crystals grown at RT from mixture previously stored at 4°C overnight, chip 12, chemical composition: $90\ \mu\text{l}$ $50\ \text{mg/ml}$ H_2O + $10\ \mu\text{l}$ R + $10\ \mu\text{l}$ PEG 50%. (b) and (d): Crystals grown at RT from fresh solutions, chip 24: chemical composition: $90\ \mu\text{l}$ $50\ \text{mg/ml}$ H_2O + $10\ \mu\text{l}$ R + $10\ \mu\text{l}$ PEG 50%. The chip reference numbers refer to Table S1.

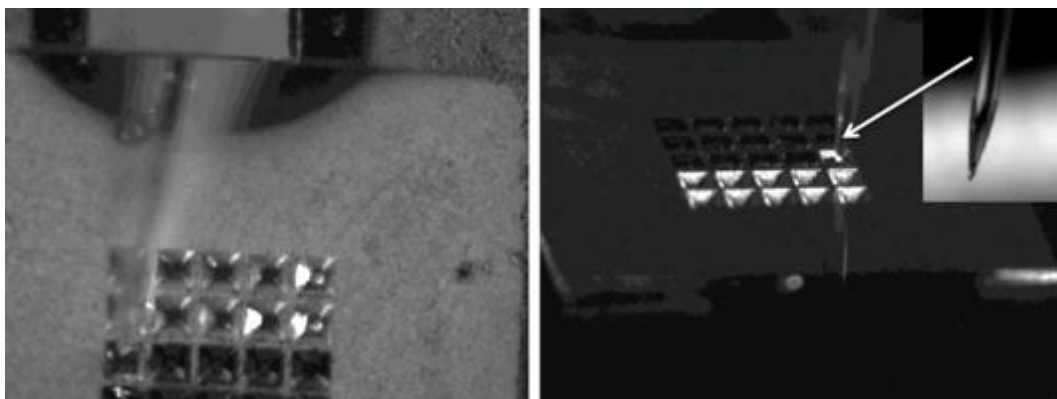


Figure BS4 Microfabricated chip on the dew point stage as the nano-wells are filled with protein (crystallization) solution, with nanoliter accuracy. Left – top view; right – side view. The 5 x 5 well array is 2 mm x 2 mm in size. The automatic method was used to load each well with 15 nl of liquid. It took about 2 min to load all 25 wells. See here: <https://doi.org/10.1107/S1600576717005799/yr5015sup2.mov> the Supplementary Movie for a demonstration.

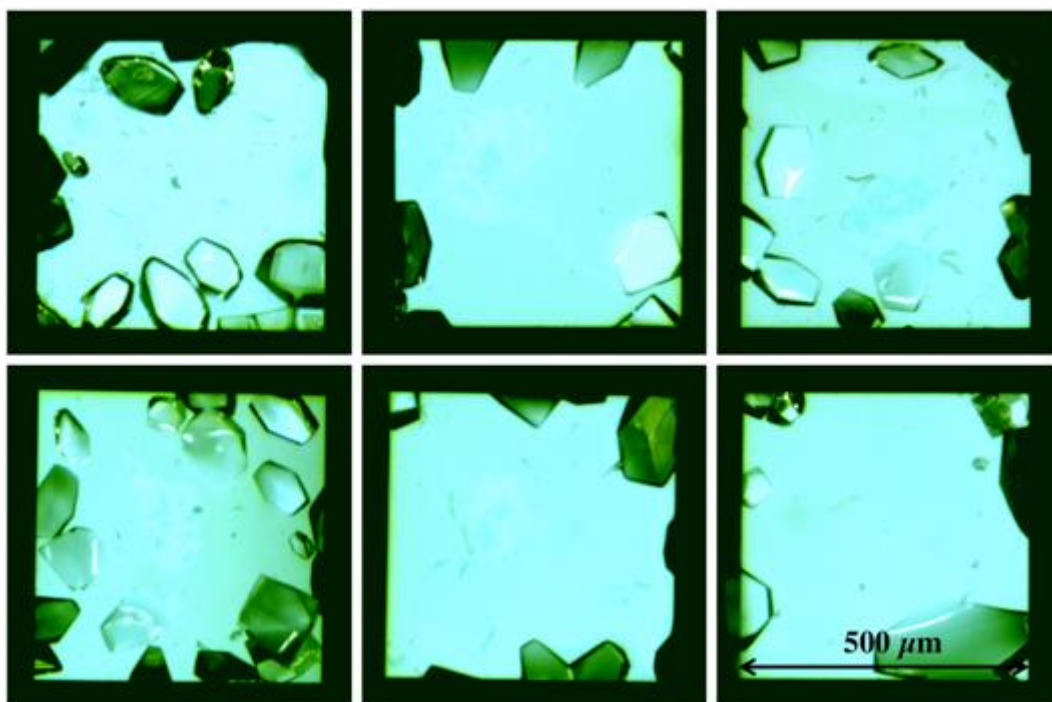


Figure BS5 Protein crystals grown on Si_xN_y membranes. Crystals are clustering in the corners and close to the edges of the membranes resulting in poor coverage of the windows. Growth from 20 μl of the solutions mixture (50 mg/ml H_2O lysozyme and 0.6 M NaCl, 0.1 M NaAc, pH 4.5 in proportion 9:1) in HD geometry against 1 ml of reservoir solution. Growth observed after 17 h under light microscope.

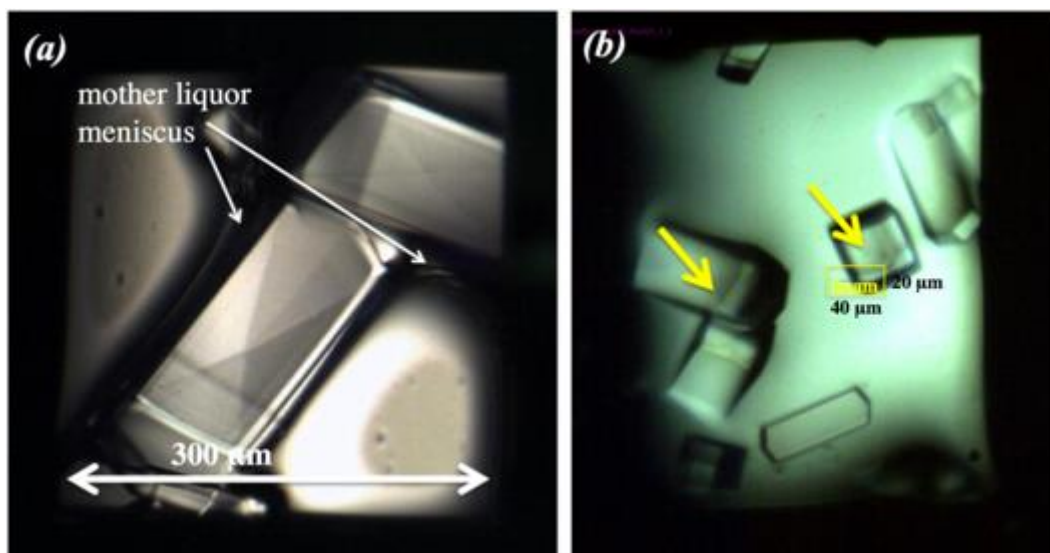


Figure BS6 Protein crystals grown at RT from fresh solutions on 250 nm thick Si_3N_4 membranes: (a) observed in the sandwich 1h after the enclosure showing minute amounts of mother liquor around the crystals. (No water rings were observed in the diffraction pattern); (b) microscope view of the sandwich placed on the goniometer of the SLS PX-I; data used for structure refinement are originating from the crystals indicated by arrows.

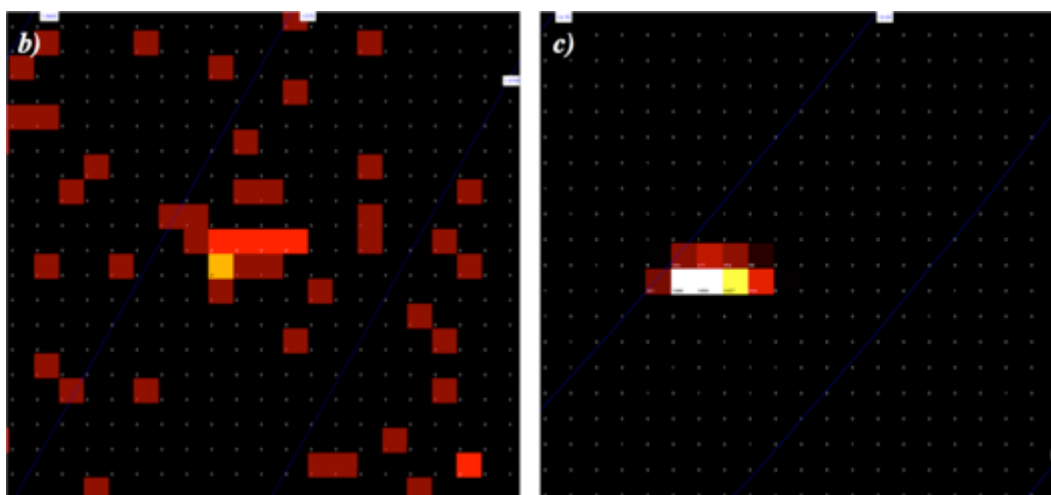
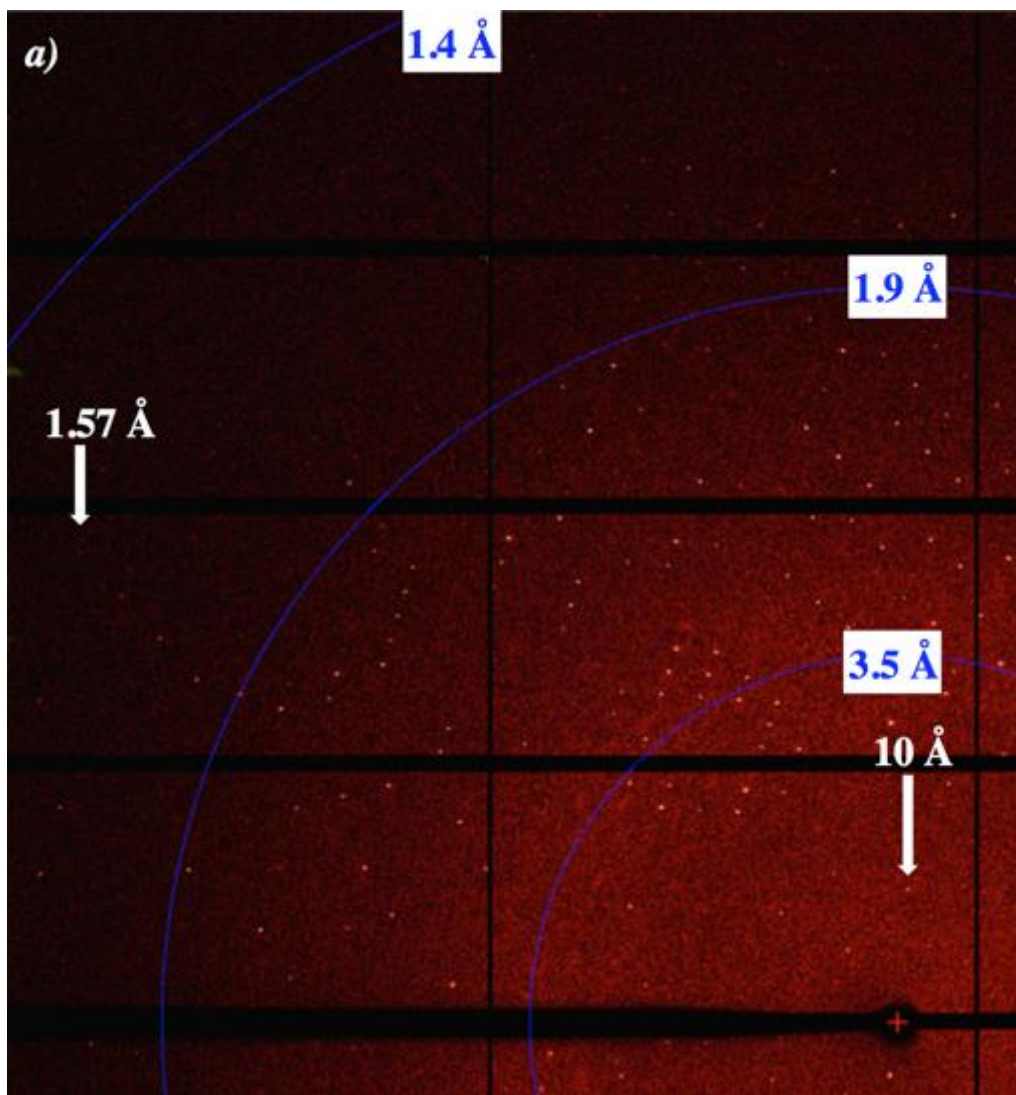


Figure BS7 (a): Representative diffraction pattern of a lysozyme crystal between silicon nitride membranes. Only a quarter of the Eiger 16M detector is shown. Transmission for this testshot was 5%. (b): Close up on a spot at 1.57 Å resolution (testshot with transmission 5%). Maximum counts value: 3. (c): Close up on a spot at about 10Å resolution (similar to Bragg peaks used at LCLS for the delay experiments), in a dataset collected at the Swiss Light Source (transmission 0.3%). Counts are up to about 2000.

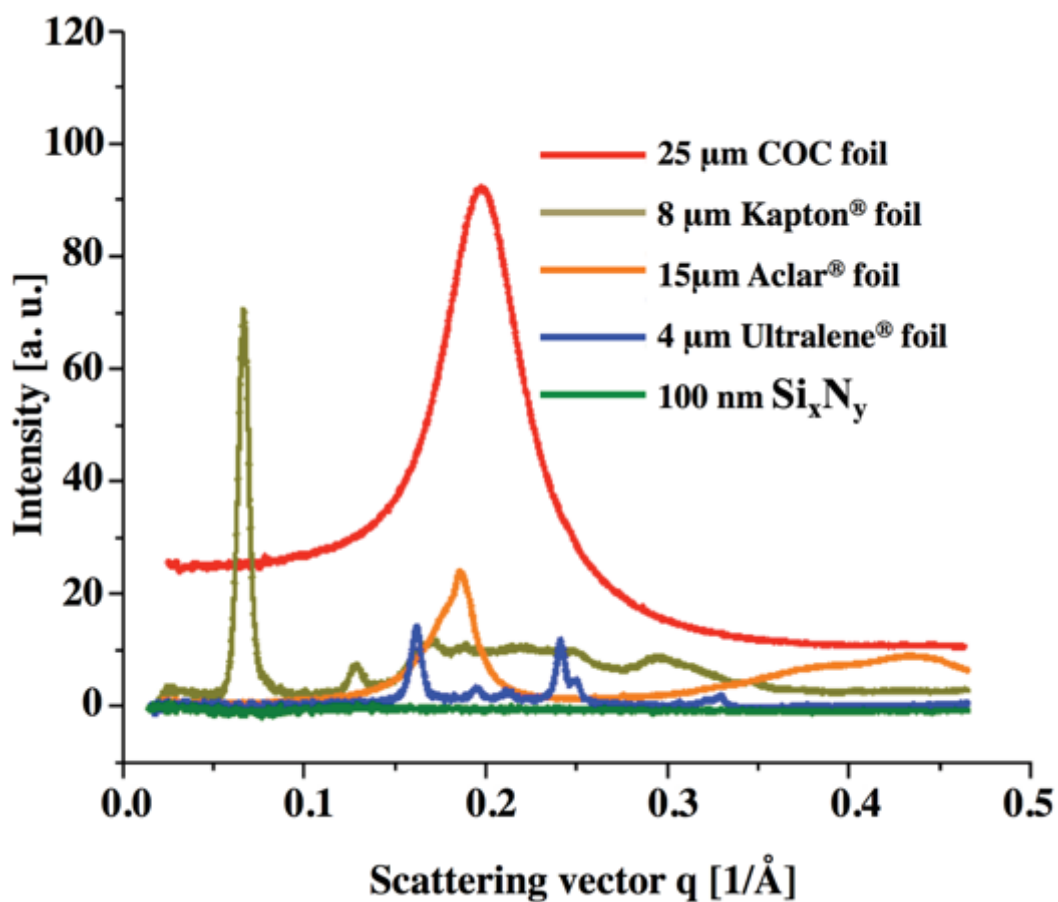


Figure BS8 Comparison of the silicon nitride background signal to commonly used, commercial ultrathin support materials. Intensity of X-ray scattering from investigated samples has been collected at 12.7 keV photon energy, 1 s exposure and full flux ($4e11$ photons/s), detector distance 400 mm. Data recorded at PX-I beamline, SLS, Switzerland.



Appendix C

Supplementary information for: Demonstration of femtosecond X-ray pump X-ray probe diffraction on protein crystals

Nadia L. Opara^{a,b,c,*}, Istvan Mohacsi^{a,d}, Mikako Makita^{a,e}, Daniel Castano-Diez^b, Ana Diaz^a, Pavle Juranić^a, May Marsh^a, Alke Meents^d, Christopher J. Milne^a, Aldo Mozzanica^a, Celestino Padeste^a, Valérie Panneels^a, Marcin Sikorski^f, Sanghoon Song^f, Henning Stahlberg^{b,c}, Ismo Vartiainen^a, Laura Vera^a, Meitian Wang^a, Philip R. Willmott^a, Christian David^a

^a Paul Scherrer Institut, CH-5232 Villigen-PSI, Switzerland

^b C-CINA, Biozentrum, University of Basel, CH-4058 Basel, Switzerland

^c Swiss Nanoscience Institute, CH-4056 Basel, Switzerland

^d Deutsches Elektronen-Synchrotron DESY, Notkestrasse 85, D-22607 Hamburg, Germany

^e European XFEL GmbH, Holzkoppel 4, D-22869, Schenefeld, Germany

^f LCLS, SLAC National Accelerator Laboratory, 2575 Sand Hill Road, CA94025 Menlo Park, USA

Available online: <https://aca.scitation.org/doi/suppl/10.1063/1.5050618>
Structural Dynamics 5, 054303 (2018).

All article content, except where otherwise noted, is licensed under a Creative Commons Attribution (CC BY) license.

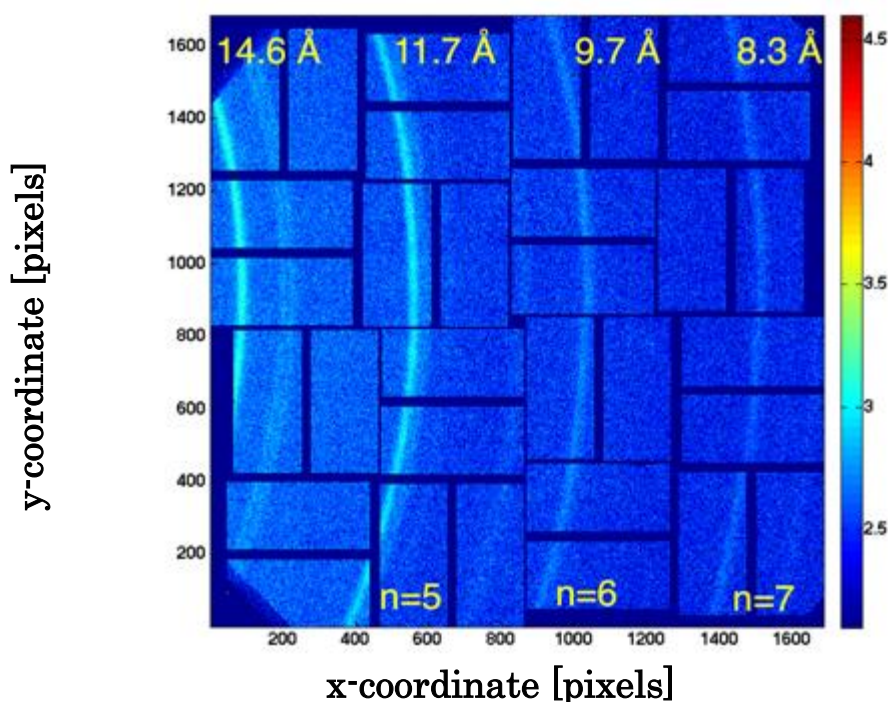


Figure CS1 Powder diffraction pattern of silver behenate used for calibration of the setup (sum of 45 images with XFEL exposures). The silver behenate rings show equal spacing in reciprocal space. Resulting in arcs of the powder rings at 8.3, 9.7 and 11.7 and 14.6 Å resolution. The center of the detector was calculated from this image to be offset in horizontal direction by an angle of 13° with respect to the unscattered beam. This detector position allowed for the observation of Bragg peaks in the resolution range between 15 Å and 8 Å (q -range between 0.4 Å⁻¹ and 0.7 Å⁻¹). Image plotted in logarithmic scale: $\log_{10}(I)$, I - signal intensity.

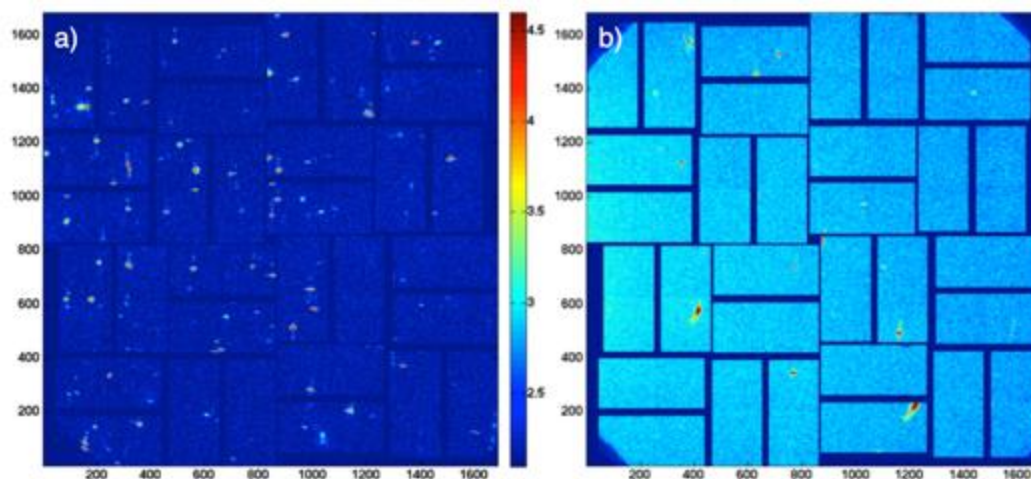
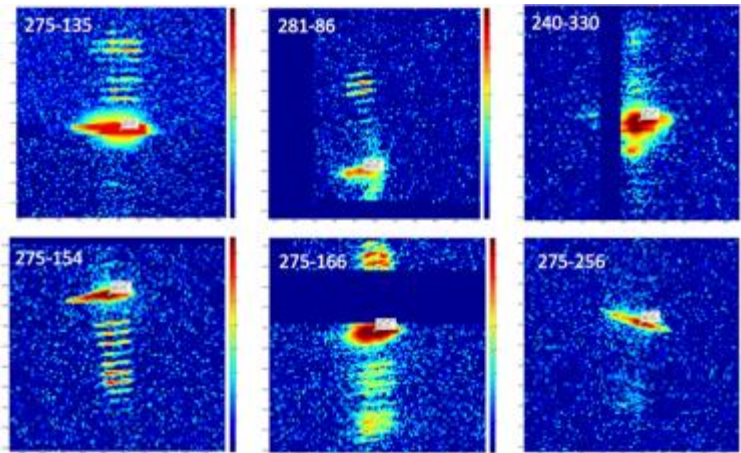


Figure CS2 Comparison of the background signals for different sample preparation methods. a) Sum of the 102 snapshots collected on 2 x 250-nm thick silicon nitride membranes, which are almost completely transparent to the X-ray beam. b) Sum of 102 snapshots collected from microtiter plates. The 25- μ m thick each, Kapton and COC foil gives significant increase in the background signal of about one order of magnitude. High intensity Bragg peaks and delayed peaks are originating from lysozyme crystals grown on these supports. Images are plotted in logarithmic scale: $\log_{10}(I)$, I - signal intensity.



Grade A

Grade B

Grade C

Figure CS3 Illustration of the applied grading criteria to the obtained diffraction signals. Grade A: clear, visible, well-resolved peaks of delays, easy to process; Grade B: weak or blurred peaks of delays, missing part of the signal, deformation, difficult to interpret; Grade C: inexistent or very weak, blurred peaks of delays, impossible to process. Intensities are plotted in the logarithmic scale for better visibility of the signal, as delayed peaks are much weaker than the main Bragg peak. Registered signals were considered separately for the pump (top) and reference (bottom) side of the signal to create subsets with larger (only with complete signal cases) amounts of data.

a)

b)

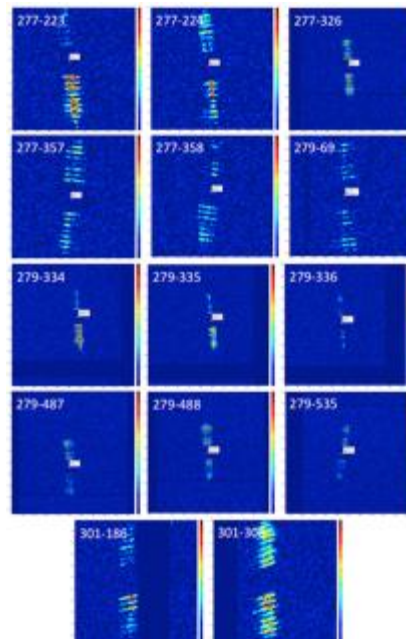
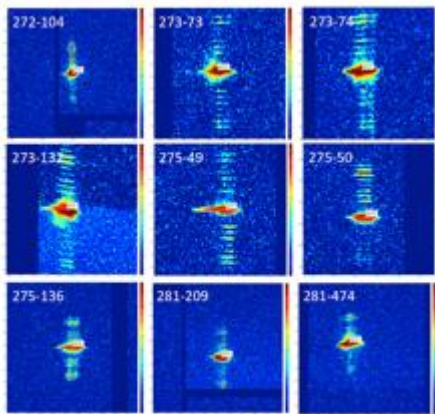


Figure CS4 Complete signals a) population of the registered signals with Bragg peak visible (pumped) b) population of the registered signals without Bragg peak (unpumped). Both sets are consisting of only a few data elements, *i.e.*, they are very small. Therefore, caution has to be taken while attempting statistical analysis on these data sets. Numbers in the top left corners indicates run no-shot no.

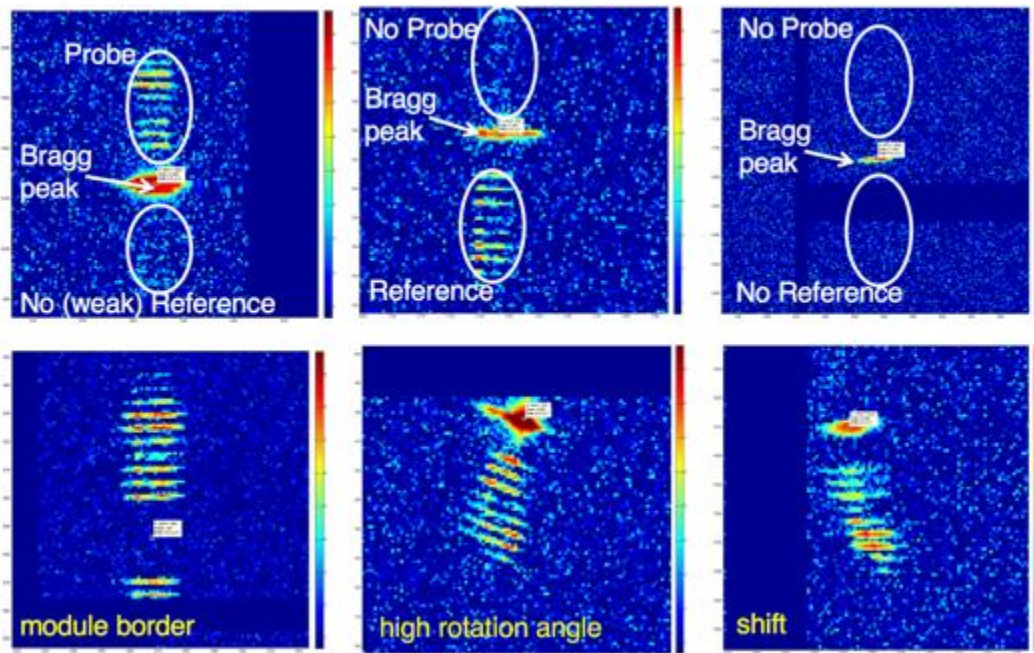


Figure CS5 Imperfections in recorded signal.

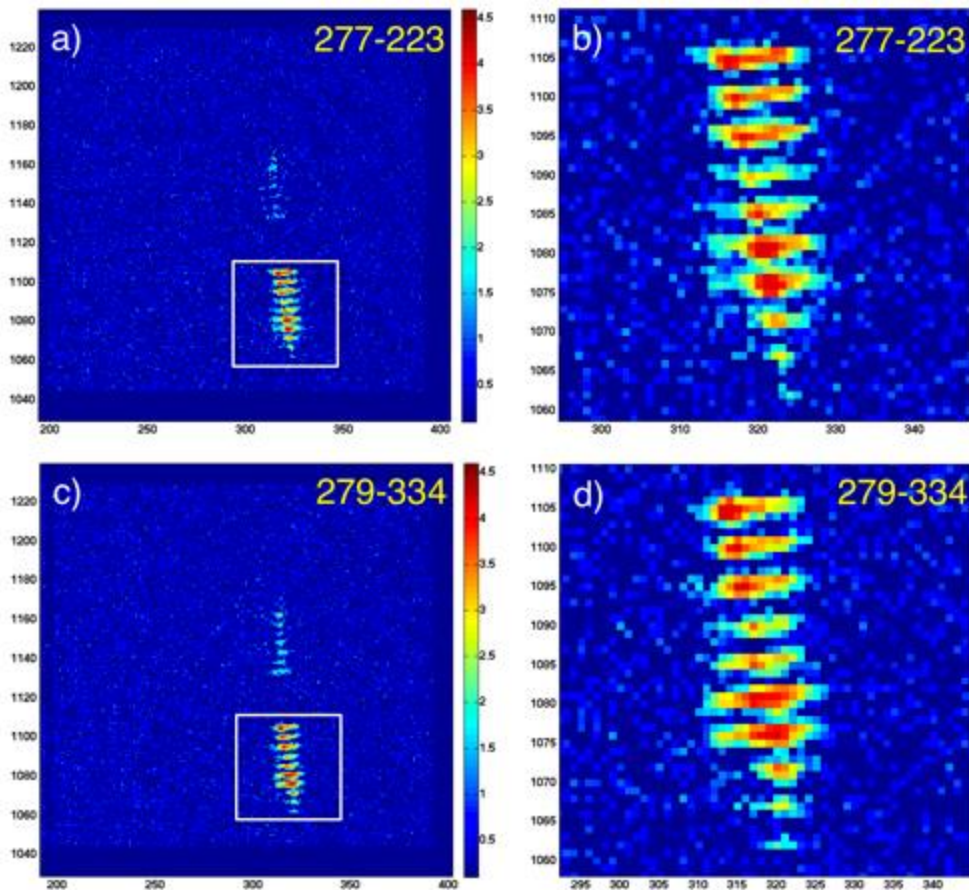
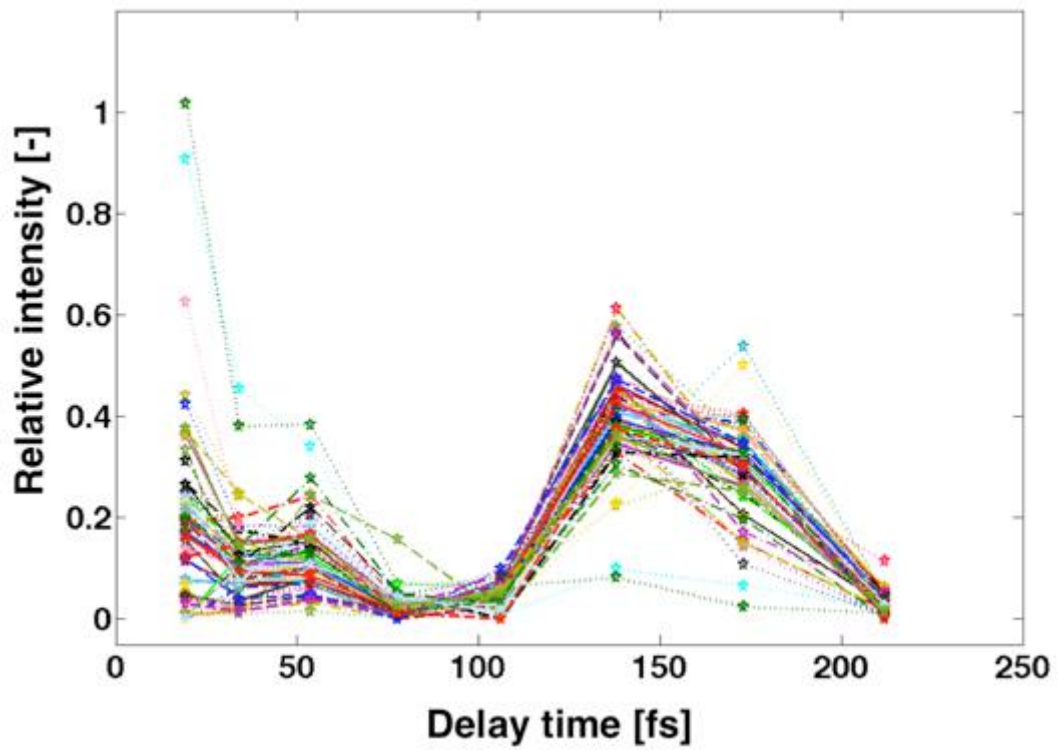
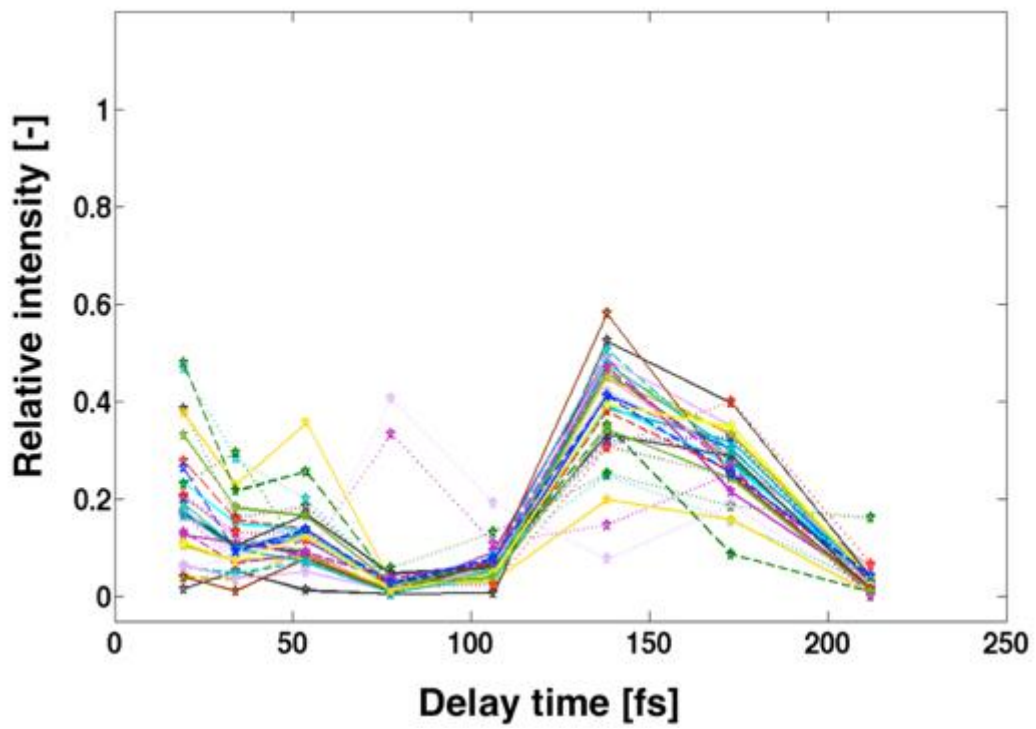


Figure CS6 High intensity of the delayed peaks acquired from the same large lysozyme crystal in two runs (277 and 279) in the unpumped scenario (with attenuator present, showing reflections up to the 10th delay), b) and d) – zoomed view of white square area marked on a) and c) respectively. Images are plotted in logarithmic scale: $\log_{10}(I)$, I - signal intensity.

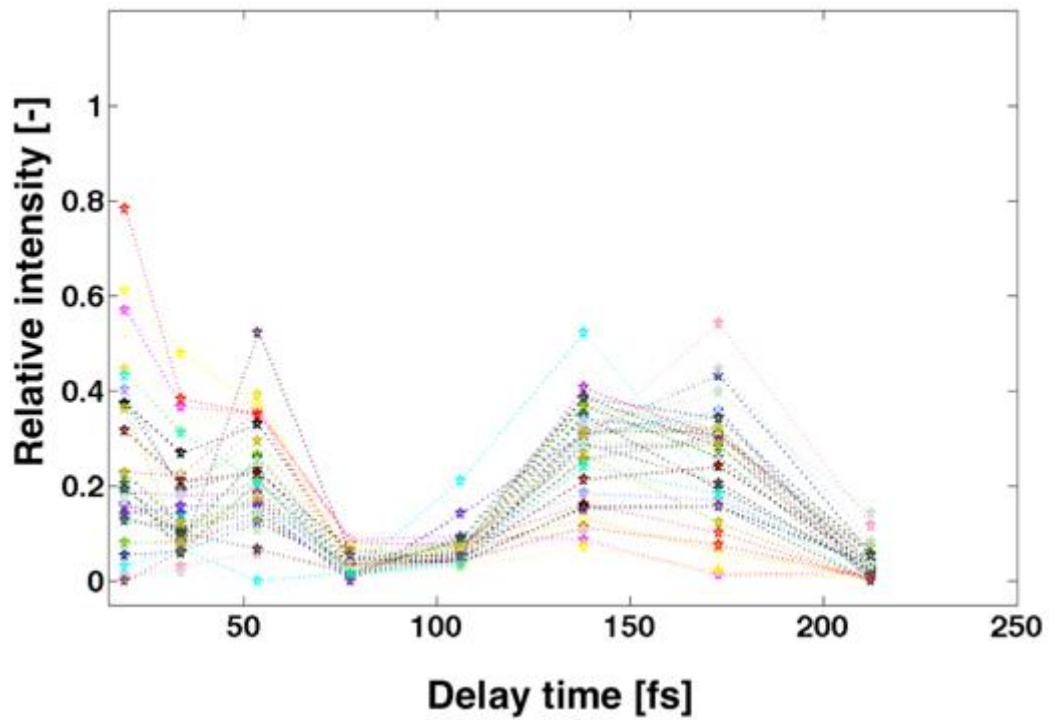
a)



b)



c)



d)

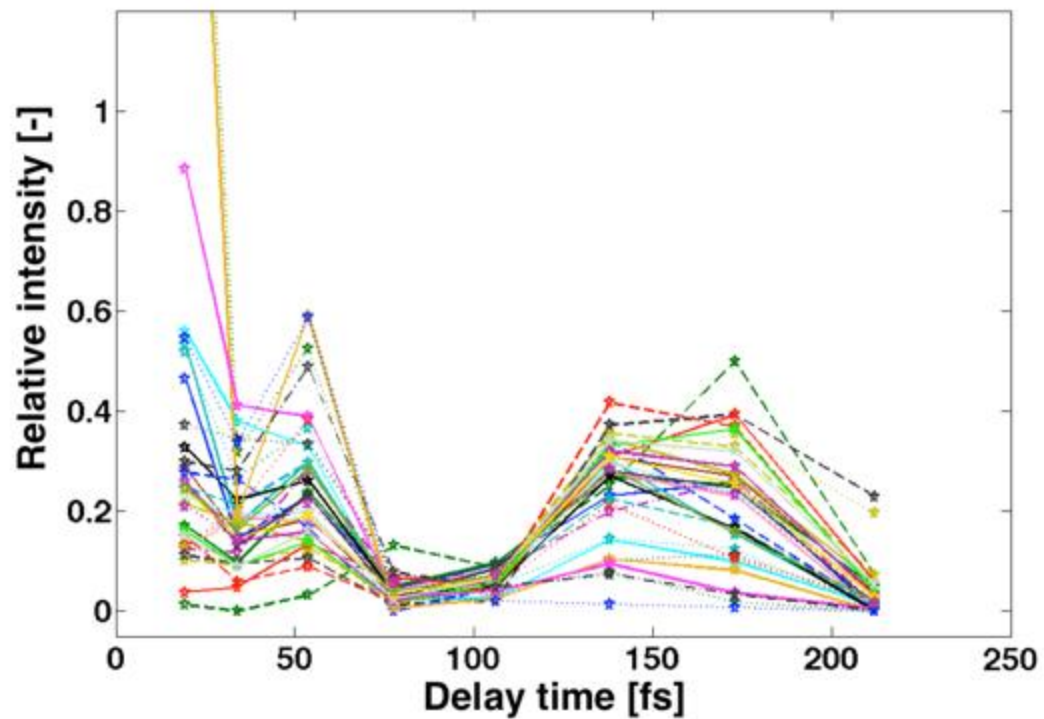
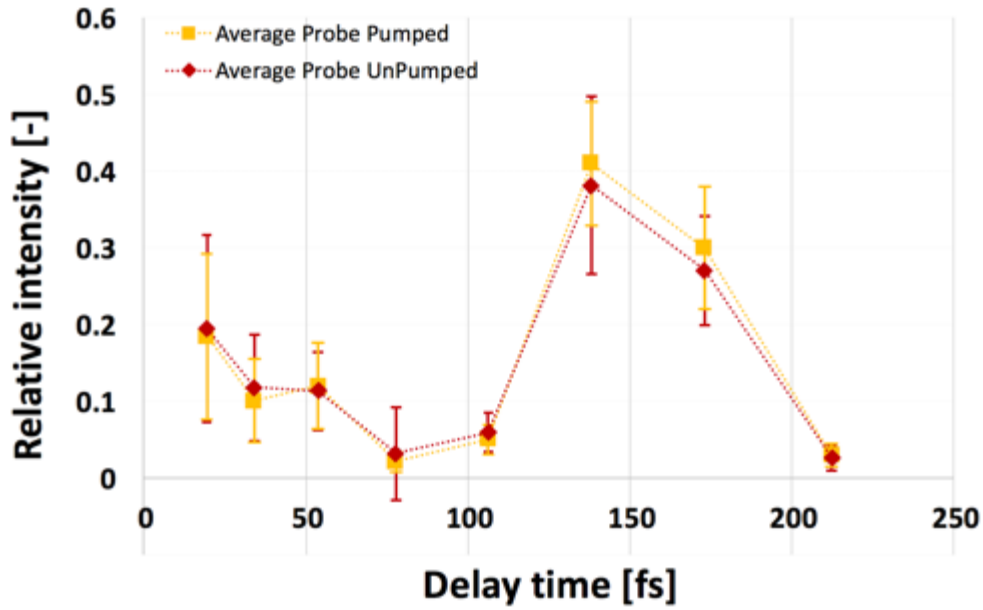


Figure CS7 Relative intensities (scaled with the sum of the intensity of the first 8 peaks as internal reference) of each processed shot in 4 sets a) 60 shots of pumped probe, b) 29 shots of unpumped probe, c) 37 shots pumped reference, d) 33 shots of unpumped reference part of the signal. Most of the data points follow the shape of the average (*cf.* Fig. CS8); outliers are mostly lower quality/saturating detector shots. Data points indicated as stars; lines are visual guide.

a)



b)

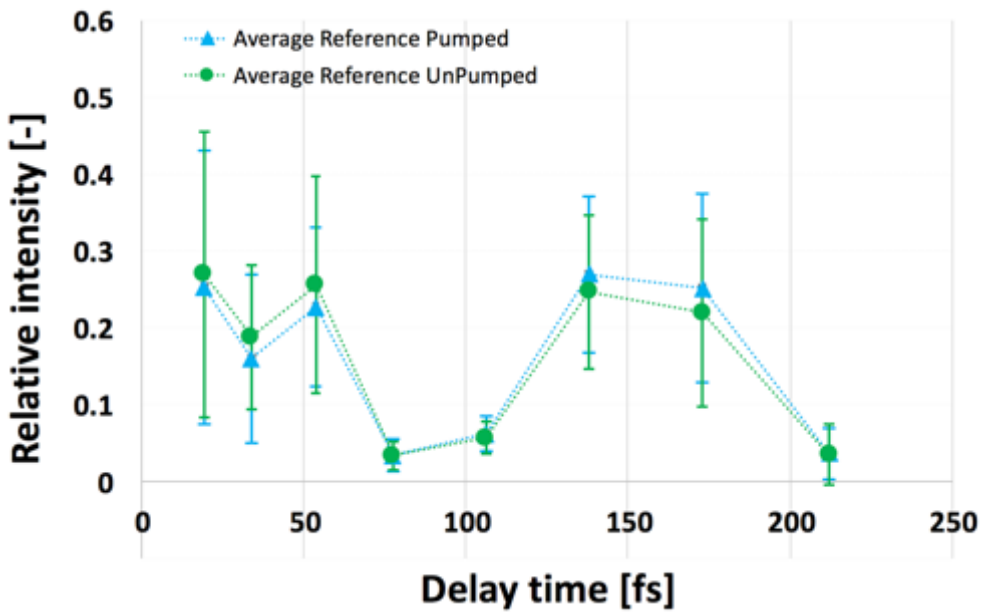


Figure CS8 Average relative (scaled with internal reference of the sum of the intensity of the first 8 peaks) intensities based on shot populations consisting of A-graded exposures (*cf.* Fig. CS7). Error bars are corresponding standard deviations. a) Probe and b) reference part of the signal registered on CSPAD (intensities approximately 10^6 times fainter than the pump beam). Experimental data are marked by geometric figures; dotted lines are guide for an eye. The shape of plotted curves follows the efficiencies of the setup's X-ray optics elements.

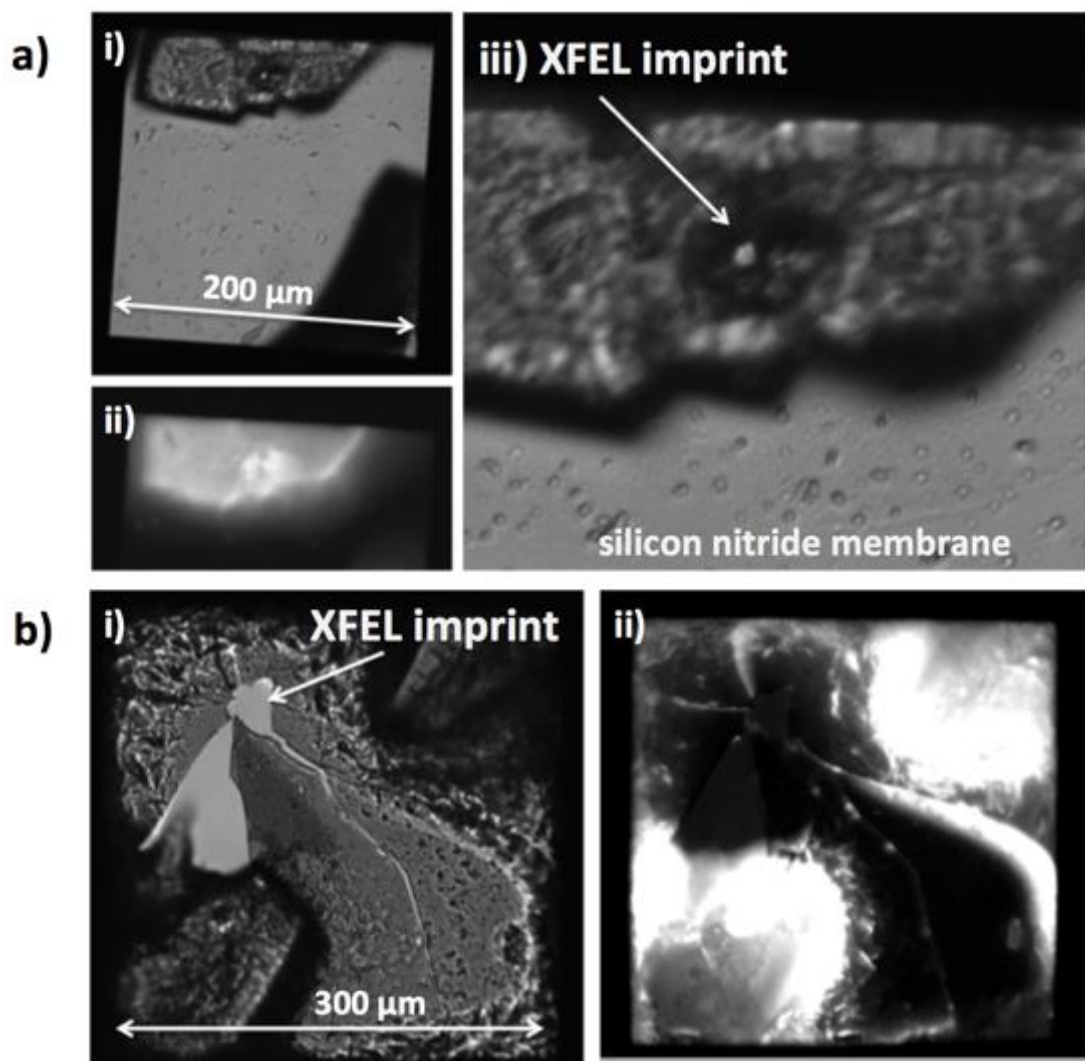


Figure CS9 UV-imaging of the crystals sandwiched between silicon nitride membranes, exposed to XFEL, LCLS during LE86 experiment. UV-positive signal confirms presence of tryptophan in the crystals, thus their protein origin. i) Bright field image of the crystal grown on the membrane; ii) UV-signal registered by means of JANSi UVEX microscope, Molecular Dimensions with technical assistance from Valérie Panneels; iii) Zoomed view of i). Crystals grown on a) chip no. 30; b) chip no. 43 (*cf.* Supplementary Information for Opara *et al.*, 2017, Appendix B).

Table CS1: Calibration values of the intensity for each time point based on Si-data collection on X-ray optics setup utilized for protein crystal diffraction. Data collected on JUNGFRU detector. These factors are scaling down to equal value the efficiencies of the individual channels.

#	Delay [fs]	Si-based calibration for probe	Si-based calibration for reference
1.	19.4	0.2942/1.33	0.30655/1.33
2.	34	0.15282/1.33	0.16923/1.33
3.	53.8	0.14965/1.33	0.24609/1.33
4.	77.7	0.02869/1.33	0.04714/1.33
5.	106.3	0.0689/1.33	0.0878/1.33
6.	138.1	0.54712/1.33	0.34961/1.33
7.	173	0.41686/1.33	0.33447/1.33
8.	212.2	0.04136/1.33	0.04124/1.33



Appendix D

Supplementary Information for: X-ray fluorescence detection for serial macromolecular crystallography using a JUNGFRU pixel detector

Isabelle Martiel^a, Aldo Mozzanica^a, Nadia L. Opara^{a,b,c}, Ezequiel Panepucci^a, Filip Leonarski^a, Sophie Redford^a, Istvan Mohacsi^a, Vitaliy Guzenko^a, Dmitry Ozerov^a, Bernd Schmitt^a, Bill Pedrini^a, Meitian Wang^a

^a Paul Scherrer Institute, Forschungsstrasse 111, Villigen, 5232, Switzerland

^b Center for Cellular Imaging and NanoAnalytics (C-CINA), Biozentrum, University of Basel, Basel, 4058, Switzerland

^c Swiss Nanoscience Institute, University of Basel, Basel, 4056, Switzerland

Available online:

<https://journals.iucr.org/s/issues/2020/02/00/ig5086/ig5086sup1.pdf>

Journal of Synchrotron Radiation **27**, (2020).

All article content, except where otherwise noted, is licensed under a Creative Commons Attribution (CC-BY) license.

Section DS1. Materials and methods for the fluorescence maps experiments

DS1.1. Fabrication of gold and nickel model structures by electroplating

Metal markers of 1 and 2 μm thickness were fabricated on a 250 nm thick non-stoichiometric amorphous silicon nitride (Si_xN_y) membrane [D1, D2] of 2 mm x 2 mm in size, suspended on a silicon frame (6 mm x 6 mm). The 250 μm thick silicon wafer was processed as previously described [D3] by wet chemical etching using 20% KOH in water at 85°C to create freestanding Si_xN_y membranes. The pattern layout is divided into several areas, corresponding to markers of different shape and size (1 and 2 μm diameter disks and 3 μm wide crosses), and various spacing and arrangement (regular spacing of 20, 50 and 100 μm , and randomization of these positions). The main fabrication steps are pictured in Figure DS1 and pattern layout details are given in Figure DS2.

The wafer with Si_xN_y membranes was initially cleaned with oxygen plasma (RIE, Oxford Instruments, 150 W forward power, 90 mTorr pressure, 30 sccm flow O_2 , for 2 min). The chips with membranes were subsequently coated with Cr/Ge/Cr layers of respective thicknesses 5 nm/30 nm/5 nm in a Balzers BAK 600 evaporator (Evatec AG, Switzerland), to form a seed layer for electroplating. The growth rate of the layers was 0.1 nm/s for chromium and 0.23 nm/s for germanium, with the substrate placed 40 cm from the evaporation source. The upper Cr layer serves as an adhesion promoter for the PMMA structures. A PMMA (molecular mass: 950k, Microchem) layer was spincoated (Laurell spincoater WS-400-6NPP-LITE) from an anisole solution with spin speeds of 3500 rpm and 2000 rpm to reach thicknesses of at least 1 μm and 2 μm respectively. The samples were baked out for 15 min at 180°C on a hot plate and gradually cooled down to room temperature. The designed pattern was written in the PMMA layer by electron beam lithography with a Vistec EBPG 5000 PlusES machine using a dose of 3000 $\mu\text{C}/\text{cm}^2$, in so-called undersize-overdose conditions [D4]. Subsequently, the PMMA layer was developed for about 20 s in a 3:7 mixture of H_2O of ultrapure quality (resistivity 18.2 M Ωcm) and isopropanol (ultrapure, Technic, France), rinsed for 30 s in deionized H_2O , and dried using a flash of pressurized N_2 gas. After development, the membranes were briefly cleaned with oxygen plasma (15 s with 150 W forward power, 30 sccm, 90 mTorr pressure). The upper chromium layer was removed with a 25 s chlorine plasma-etching step (CMA-4, BMP-Plasmatechnologie GmbH, Germany, mixture of 50 sccm O_2 and 20 sccm Cl_2). The gold structures were electroplated from a potassium gold cyanide ($\text{K}[\text{Au}(\text{CN})_2]$) buffered electrolyte bath (Autronex™ GVC) of min. 68.1 wt. % of gold, and the nickel structures from a 185 g/l nickel sulphamate electrolyte solution (SEL-REX ELECTRONIC 10-03 S, ERNE surface AG, Switzerland), as described by Hili *et al.* [D5]. In the

final step, the PMMA layer surrounding the electroplated pillars was removed by washing in acetone heated up to approx. 40°C.

The quality of the formed pillar structures was investigated by scanning electron microscopy at 5 keV accelerating voltage with a Zeiss Supra VP55 (Zeiss, Germany) equipped with both the in-lens and the Everhart-Thorneley secondary electron detectors.

DS1.2. Preparation of fluorescent samples for the scanning maps

The model samples consisted of the gold or nickel structures described above. The frame surrounding the membrane carrying metal markers was inserted in the slit of a magnetic chip pin (Figure 3.3a) and glued with cyanoacrylate Cementit CA10 glue (merz+benteli AG, Niederwangen, Switzerland). Cementit glue can be dissolved in acetone for reusing the chip pins.

The representative samples, containing lipidic cubic phase (LCP) with embedded protein crystals, were prepared by sandwiching LCP containing crosslinked lysozyme microcrystals between Si_xN_y membranes. The LCP (about 20 μl total volume) was prepared by mixing monoolein (Nu-Check Prep, USA) and the aqueous phase in 60:40 ratio with coupled Hamilton syringes. The aqueous phase consisted of a suspension of lysozyme microcrystals, obtained by batch crystallisation by mixing 500 μl of 20 mg/ml lysozyme (Sigma-Aldrich) solution in 100 mM NaAc pH 3.0 and 500 μl of precipitant solution (68% dilution of the stock solution 28% NaCl, 8% PEG 6000, 100 mM NaAc pH 3.0), crosslinked by suspending the centrifuged crystals (2 min at 2600 g) overnight in a 2.5% solution glutaraldehyde. The size of the crystals ranged from 5 to 20 μm in size. For sandwiching, a marker-free 1000 nm-thick Si_xN_y membrane with a 5 mm x 5 mm frame and a 1.5 mm x 1.5 mm membrane (Silson, Southam, United Kingdom) was fixed to a microscope slide. A double-sided sticky tape 140 μm spacer (MiTeGen, Ithaca, USA) cut to form a hole of the membrane size was stuck on top. A small LCP bolus was deposited on the flat membrane side, and the sandwich was closed by sticking a second Si_xN_y membrane on top, with the flat side facing the mesophase. The sandwich was separated from the glass slide and affixed to a standard protein crystallography sample pin with a double-sided sticky tape piece as described by Huang *et al.* [D6]. The fluorescent markers were introduced in the representative protein-containing samples either by replacing the upper Si_xN_y membrane with a metal marker carrying membrane described above, or by replacing half of the aqueous phase with a 5% wt. suspension of steel microbeads (stainless steel metal microspheres 1-22 μm , SSMMS-7.8, Cospheric, Santa Barbara, USA) in milliQ water. The steel bead suspension was briefly sonicated in a bath to separate aggregates and agitated just before sampling to minimize bead decantation. Alternatively, instead of commercial Si_xN_y membranes, the steel bead samples were prepared between two 25- μm thick cyclic olefin copolymer (COC) films, following the IMISX setup reported by Huang *et al.* [D6]. The samples were

snap-cooled in liquid nitrogen. Micrographs of the samples prior to snap-cooling are presented in Figure DS3.

DS1.3. Data processing

The raw data from the JUNGFRÄU detector was processed with the standard correction algorithm presented by Redford *et al.* [D7]. Due to the low incoming flux, the automatic gain switching feature was never engaged and all pixels remained in the highest gain. The pedestal raw analog-to-digital converter (ADC) output from the pixel matrix was determined in a dedicated dark measurement, and subtracted pixel by pixel from the raw ADC pixel matrix output. Then the result was corrected with a pixel-wise gain correction factor determined independently, to obtain the measured energy per pixel [D7].

Due to the critical dependence of this measurement to the stability of the recorded energy at the SLS, a tracking procedure to follow slow drifts in the pedestal values was applied to the data [D7]: a subsample of empty pixels was used in each frame to track the pedestal. The peak around zero of this distribution, corresponding to pixels without photon hits, was fitted with a Gaussian curve, and the mean value of said curve was used to obtain a global value to correct for pedestal shifts. This is a simple and effective way to correct for common mode fluctuations (which were generally small) and also (stronger) global temperature/sensor effects. At SwissFEL this tracking procedure is not necessary thanks to the short integration time.

Further processing was performed using ROOT [D8] and customized python scripts. In selected cases, a clustering procedure was carried out to correct for charge-sharing effects between neighboring pixels, when a photon hits the corner or edge of a pixel. On the pedestal subtracted and gain corrected 2D-array, square 4-pixel clusters were selected around local maxima, over which the energies were summed. After photon energy extraction, the cluster was set to zero to avoid a new cluster being found on the same pixels while analyzing the remaining of the 2D-array.

The measured energy values of all pixels (or pixel clusters) within a defined spatial region of interest on the detector were used to compute a histogram showing the number of pixels having received a given energy within the exposure, cumulative on all images corresponding to a grid cell. Examples of spectra obtained are shown in Figure 3.2b. For each metal element, counts were integrated within a region of interest (ROI) in energy corresponding to the fluorescence energy of the metal: 8.5-10.3 keV for Au, 6.2-8.2 keV for Ni and 5.3-7.2 keV for Fe. The ROI counts for each grid cell are displayed as fluorescence maps. In the case of the XFEL measurements, the Ni ROI counts were normalized by the counts in a direct beam ROI (8.3-9.3 keV), to eliminate pulse-to-pulse variations of the intensity in SASE mode. Signal-over-background ratios (SBR) were calculated by dividing average counts in the few cells of the map with high counts

(where metal is present) by average counts from a large area of the map with low counts (where metal is absent). Standard deviations on the SBR were calculated using SBRs either from several different metal markers in the same map at the SLS, or from several independent measurements of the same marker at SwissFEL. Briefly, for EIGER 16M scanning maps, pixel counts were summed over a defined area of the detector (a square area centered around the beam center, covering the same solid angle as the JUNGFRÄU 1M geometry, see Supporting Information Figure DS10).

Dose calculations were performed using RADDPOSE-3D v1.2.467 [D9], not using any particular heavy atom content, but a safety factor was included by considering the max. beamline flux of 10^{12} photons s^{-1} .

The distance measurements between metal markers were carried out either by taking horizontal and vertical slices in the map, or by projecting the signal from each marker in both scanning directions by summing all rows or columns in the marker area. A calculated overlap model was then fitted to the experimental signal by scale optimization and translation (0.05 μm steps). The deviation from the theoretical distance was calculated as the absolute value of the difference between the measured distance and the distance on the photolithography mask pattern design. In the oversampled maps, a small offset was introduced every other line to account for a small triggering delay in the rastering setup (see Figure DS7 in the Supporting Information).

Section DS2. Absorption edge scan experiments

DS2.1. Materials and methods

DS2.1.1. Selenium-containing crystal

Crystals were kindly provided by Jérôme Basquin (Max Planck Institute of Biochemistry, Martinsried). The selenomethionine substituted CWC22-CWC27-EIF4A3 complex was set up for crystallization at 20 mg/ml in SEC buffer (20 mM Tris pH 7.4, 250 mM NaCl, 2mM DTT) by sitting-drop vapor diffusion in 0.2 μL drops obtained by mixture of equal volumes of protein and crystallization solutions. Crystals appeared after 2 days at 4°C as monoclinic prism after mixing with 20% (w/v) PEG20000, 50 mM MES pH 6.5 and were cryoprotected in reservoir solution containing 33% (v/v) ethylene glycol prior to flash freezing in liquid nitrogen. The protein crystallized in the $P2_12_12_1$ space group with cell parameters of $a=152$ Å, $b=165$ Å, $c=181$ Å, $\alpha=\beta=\gamma=90^\circ$. The asymmetric unit contained 4 molecules of the complex, with 12 Se atoms per molecule (for 514 amino acids in the sequence).

DS2.1.2. Mercury-soaked lysozyme crystals

Chicken egg white lysozyme from Sigma Aldrich (10837059001) was dissolved at a concentration of 50 mg/mL in 50 mM Na Acetate pH 4.5. The crystallisation experiment was carried out in a CrysChem sitting drop vapor diffusion plate with protein drops of 2 μL and 2 μL of

precipitant against 500 μL of precipitant consisting of 5% PEG MME 5000, 2 M NaCl, 50 mM Na Acetate pH 4.5, 25% ethylene glycol. The plate was stored at 20°C, crystals appeared overnight and kept growing for 3 days. A 1 μL drop of Mercury(II) acetate dissolved at 10 mM in water was added to the crystallisation drops 10 minutes before cryo-cooling crystals in liquid nitrogen.

DS2.1.3. Data collection and analysis

For the absorption edge scanning experiments, the beam transmission was set to 5% for Se and 0.5% for Hg. The Si(111) monochromator energy was stepped by 5 eV or 2 eV increments depending on the distance to the theoretical edge. At each energy reached by the monochromator, a series of 5000 images for Se, or of 9000 images for Hg was recorded at 2.2 kHz repetition rate with a 50 μm integration time, but reliable results were obtained already using the first 1000, respectively 3000 images, corresponding respectively to 0.45 s and 1.4 s total shutter opening time at each energy. The sample-to-detector distance was of 55 mm and the sample-to-beamstop distance was of 15 mm. The beam was defocused to a size of 50 μm x 50 μm .

For the absorption edge scanning experiment, energy histograms were calculated over the two furthest corners of the detector from the beamstop, between -2 and 30 keV with 500 bins. The spectra obtained are shown in Figure DS8 in the Supporting Information. The counts in the metal ROI (9 to 10 keV for Hg and 10-11 keV for Se) were normalized by the maximum of counts at the direct beam energy to account for the beam intensity decrease caused by the absence of beam optimization during energy scanning. The program *chooch* [D10] was used for obtaining anomalous scattering coefficients f' and f'' from the relative fluorescence signal. For comparison, standard edge scan data was recorded on the exact same selenomethionine crystal using a typical beamline configuration with the beamline-integrated SDD (Ketek AXIS) placed in backscattering geometry with an angle of 45° [D11], at beamlines X06SA and X06DA, using a transmission of 1% and 1 s exposure time at each energy.

DS2.2. Results

Representative data for the absorption edge scans is given in Figure DS8, using 1000 images for Se and 3000 images for Hg. Adding more of the recorded images resulted in smoother curves, but no major change in edge profile and *chooch* results. The absence of a peak around 25 keV in Figure DS8a shows that each pixel received at most one photon during the integration time. JF spectra display wider peaks than SDD spectra due to electronic noise, and a continuous background from charge sharing is observed.

Table DS1 shows the results from *chooch* for the Se-containing sample. Peak and inflection energies are within 1 eV from the determinations using an SDD at 2 different beamlines, which is lower

than the typical energy resolution of the beamlines. The values of the scattering coefficients f' and f'' are within 2 electrons, which is comparable to the difference observed between SDD measurements at 2 different beamlines. We conclude that the edges scan measurement is of similar quality compared to the SDD measurements, in spite of the reduced sharpness of the obtained spectra compared to SDD spectra.

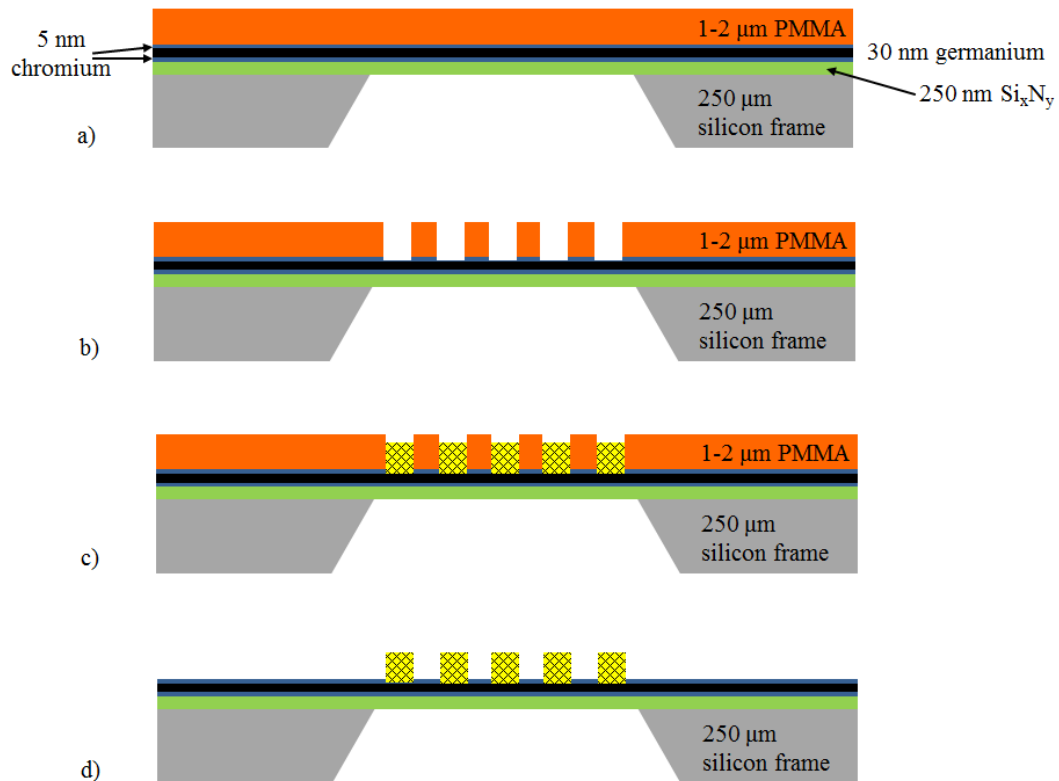


Figure DS1 Scheme of metal markers fabrication on silicon nitride membranes by electroplating: a) silicon nitride membrane over a silicon frame covered with a stack of 5 nm Cr, 30 nm Ge, 5 nm Cr and 1-2 μm PMMA, *cf.* Materials and Methods section, b) e-beam exposure, development and opening of the chromium layer c) electroplating the structures in the PMMA mold, filling of the formed cavities with metal, d) PMMA removal in the acetone bath, leaving the formed markers on the freestanding silicon nitride membrane.

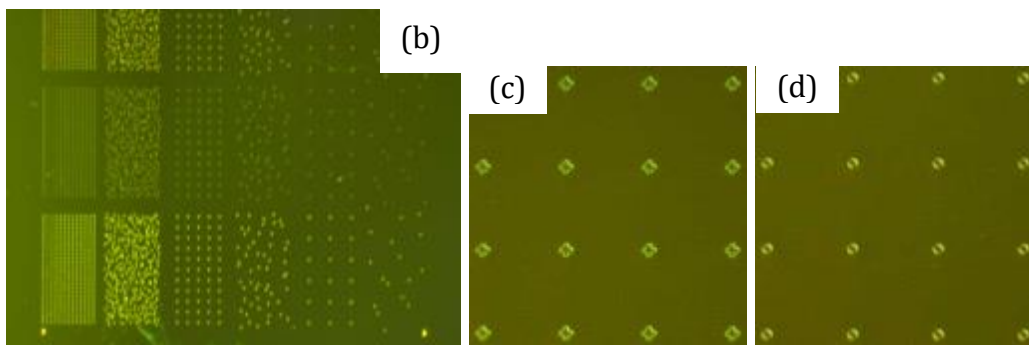
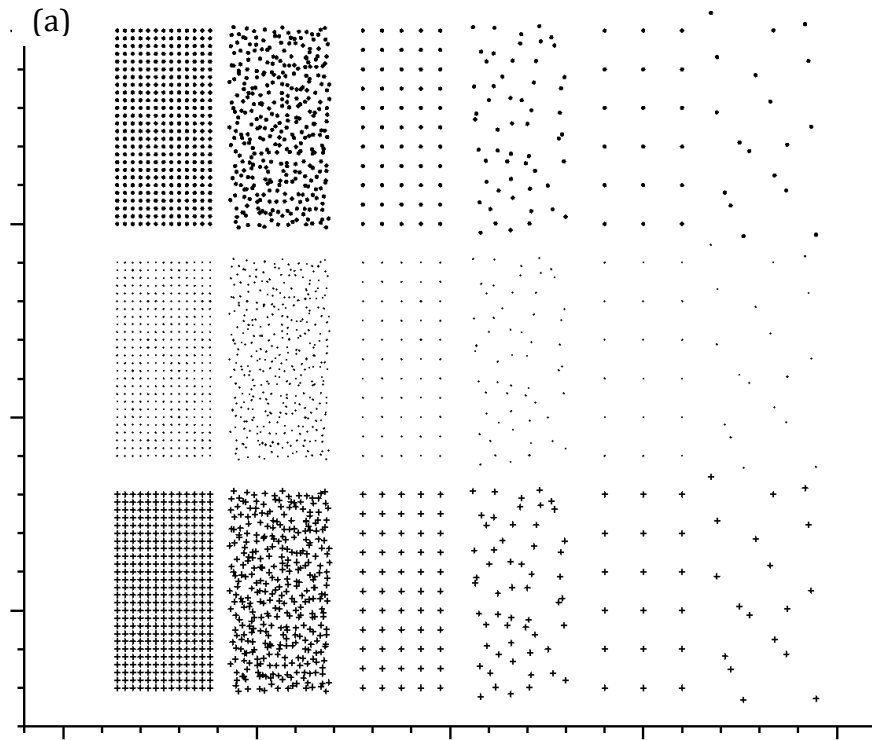


Figure DS2 (a) Arrangement of the electroplated model metal samples. For visibility, the markers are drawn larger than their actual size. The pattern is divided in 9 zones in a 3 by 3 layout. Each zone contains a set of regular markers on the left and randomly distributed markers on the right. The randomly distributed marks were obtained by randomizing the positions of the regular arrays within the same surface area. In the upper 3 zones, markers were 2 μm wide disks. In the 3 zones in the middle (horizontally), markers were 1 μm disks. In the bottom 3 zones, markers were 3 μm wide crosses. The spacing between markers in the regular arrays was of 20 μm on the left, 50 μm in the middle (vertically), and 100 μm on the right. In the figure, the major ticks are spaced out by 500 μm , and the minor ticks by 100 μm . (b) Optical micrographs of a metal sample, with close-ups on the regular 20 μm spaced crosses area (c) and 2 μm circles area (d).

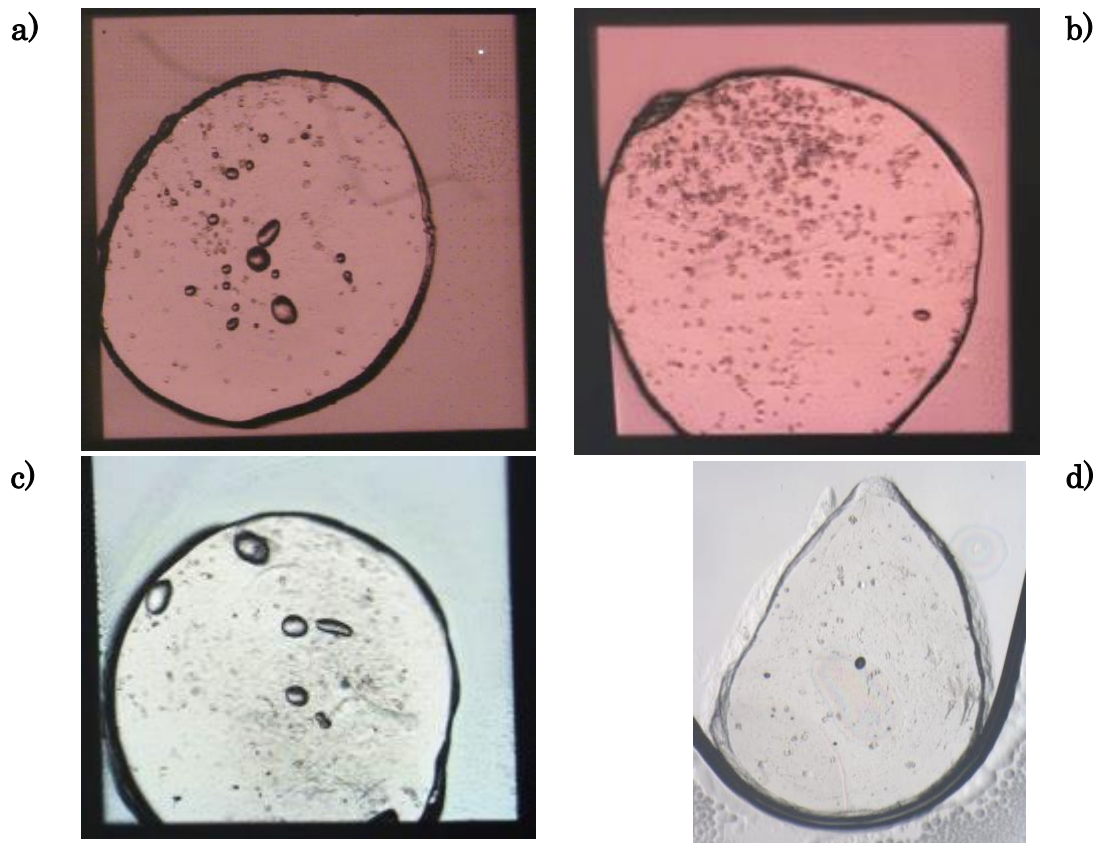


Figure DS3 Optical microscopy pictures of the samples with the protein crystal containing LCP media prior to snap-cooling: (a) silicon nitride sandwich with gold markers, (b) silicon nitride sandwich with nickel markers, (c) silicon nitride sandwich with steel beads, (d) COC sandwich with steel beads. For scale, the size of the silicon nitride window, visible as a black frame in a)-c), is 2 mm x 2 mm, and picture (d) is taken at the same magnification.

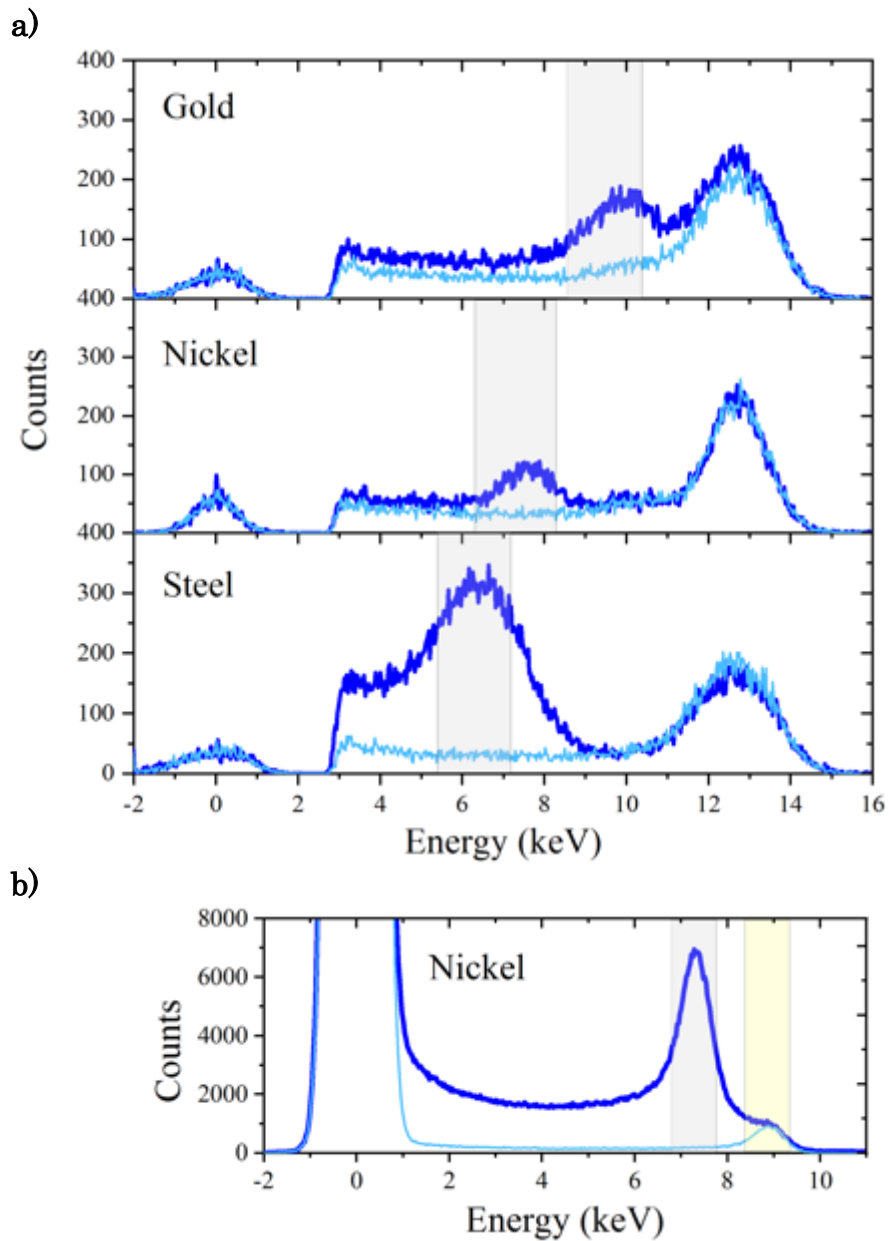


Figure DS4 Full range representative spectra from the fluorescence maps obtained at SLS (a) and SwissFEL (b), corresponding to the curves shown respectively in Fig. 3.2b) and (d) of the main manuscript. The additional peak centered around 0 keV is the noise peak from the detector and contains no information from the sample. In the case of the SLS data, the signal below 3 keV has been filtered out to 1% for better visibility and use in pedestal tracking.

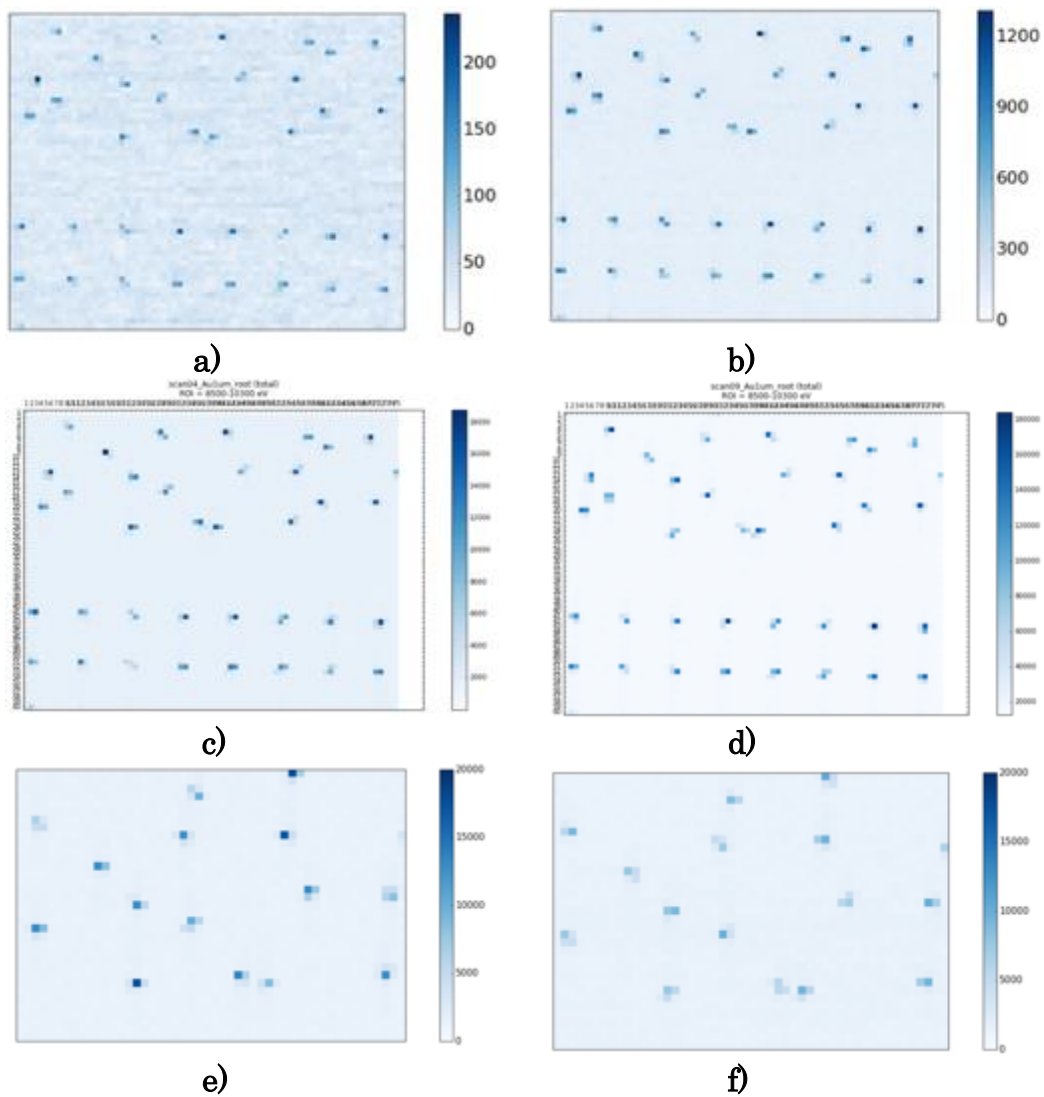


Figure DS5 Fluorescence maps obtained from gold model samples while varying the transmission: 0.04% (a), 0.4% (b), 4% (c) and 40% (d), and while varying the rastering speed: 10 Hz-10 images/cell (e) and 10 Hz-100 images/cell (f). (e) and (f) are plotted on the same scale.

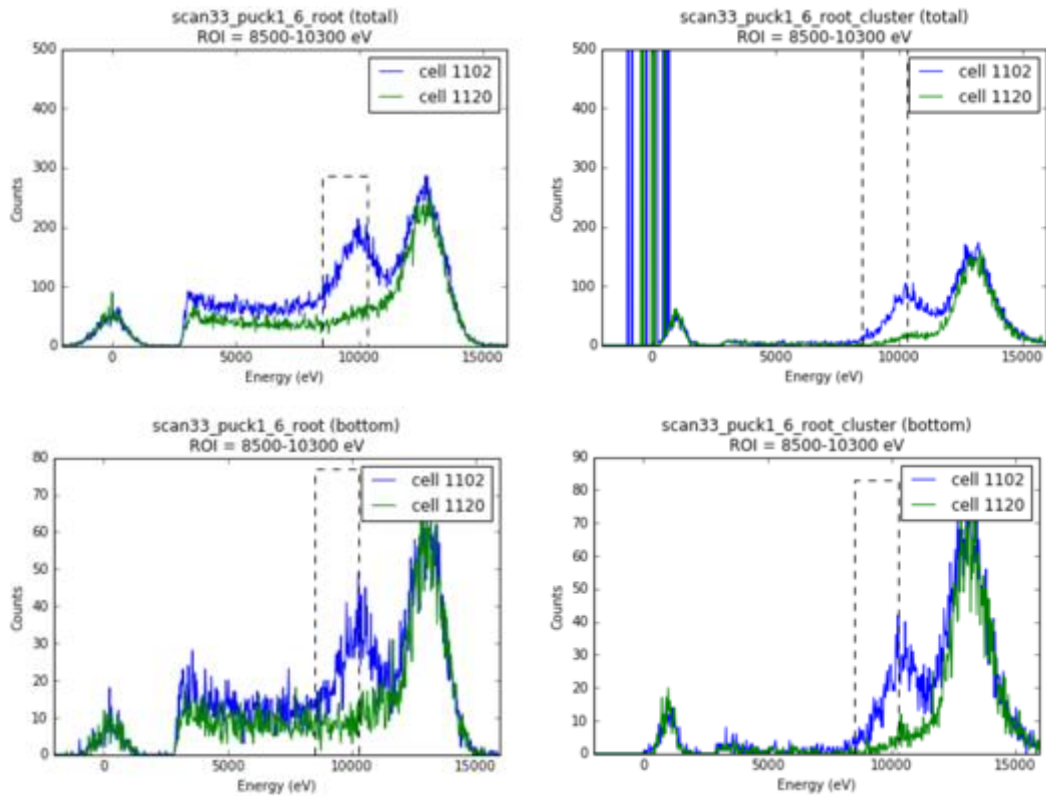


Figure DS6 Representative spectra from a gold real sample (silicon nitride sandwich), obtained by using the full detector area (top) versus only the lower half of the lower module (bottom), *i.e.* only a quarter of the detector area. The left column shows spectra obtained using individual pixels information, while the right column shows spectra obtained by clustering. The spectra from 2 different cells in a fluorescence map grid are shown. Cell 1102 is a cell where the fluorescence intensity was maximum, and cell 1120 had no metal present.

a)



b)

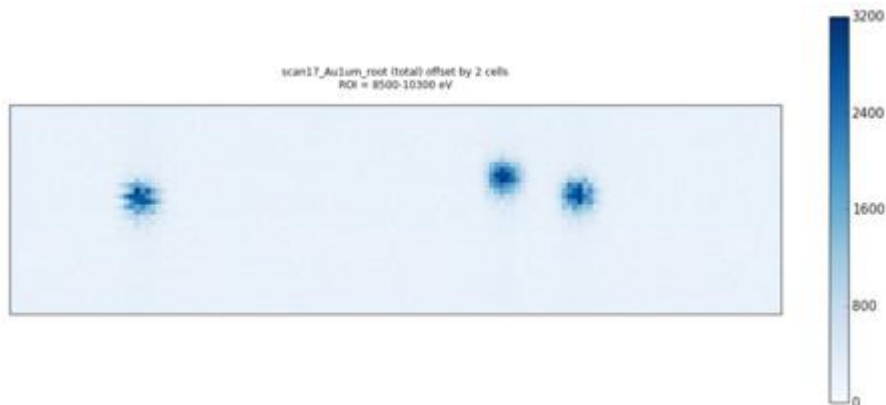


Figure DS7 Oversampled maps with 1 μm cell size, before (a) and after (b) the offset correction. This offset correction consisted in offsetting every other line by 2 cells, in order to compensate for a systematic triggering error.

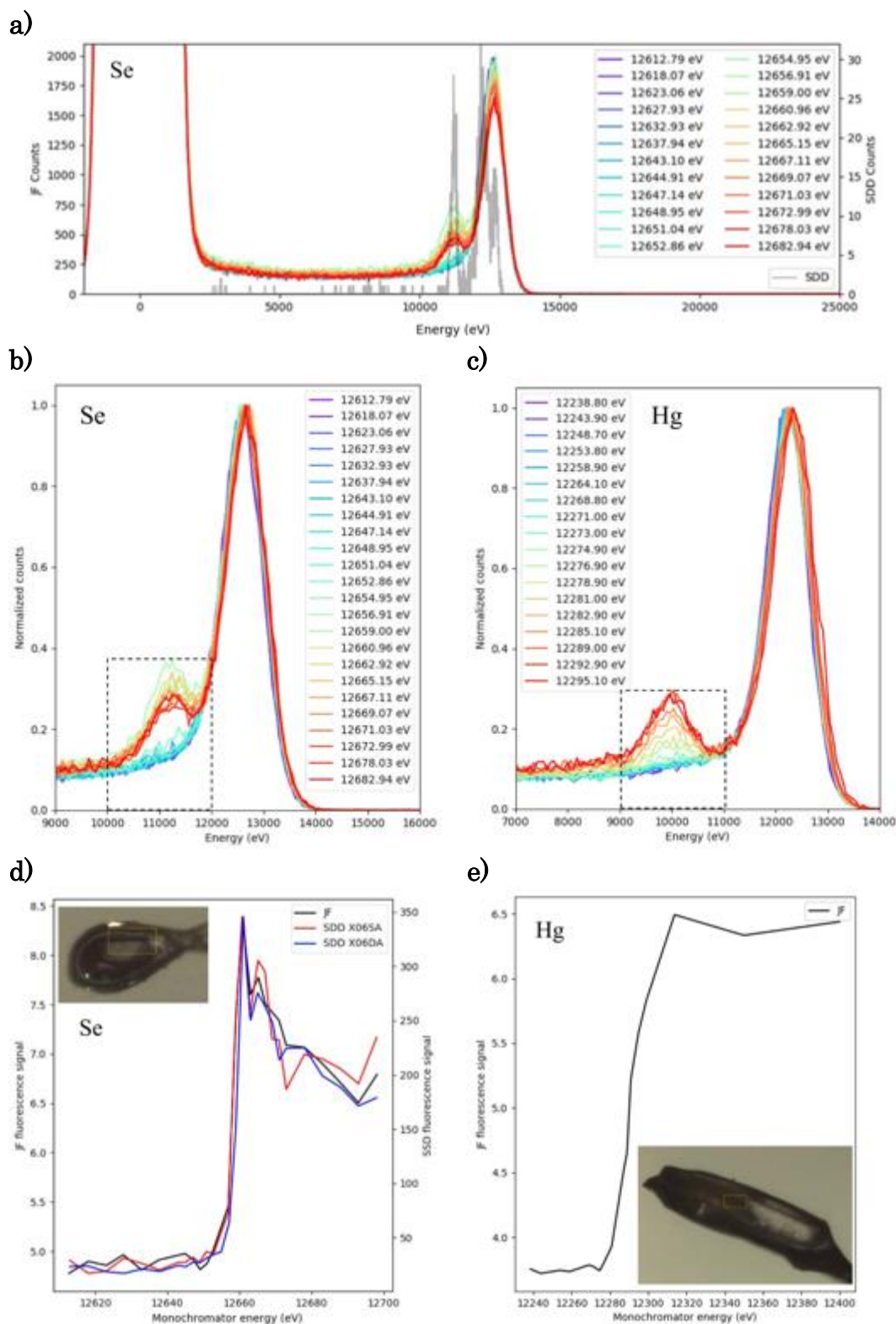


Figure DS8 Absorption edge scans: (a) Raw histograms from the Se edge scan for the different monochromator energies, in comparison to an SDD spectrum taken above the edge. (b, c) Portions of the histograms normalized to the height of the direct beam energy peak, Se in (b), Hg in (c). The integration range is shown as a dashed line. (d) JUNGFRAU edge profile for the Se-containing sample, compared to edges measured on the same sample with SDDs at the X06SA and X06DA beamlines of the SLS. (e) JUNGFRAU edge profile for the Hg-containing sample. Insets in (d, e) show the crystals measured. The yellow box is 90 μm x 50 μm . 1000 images were used for Se, 3000 images for Hg.

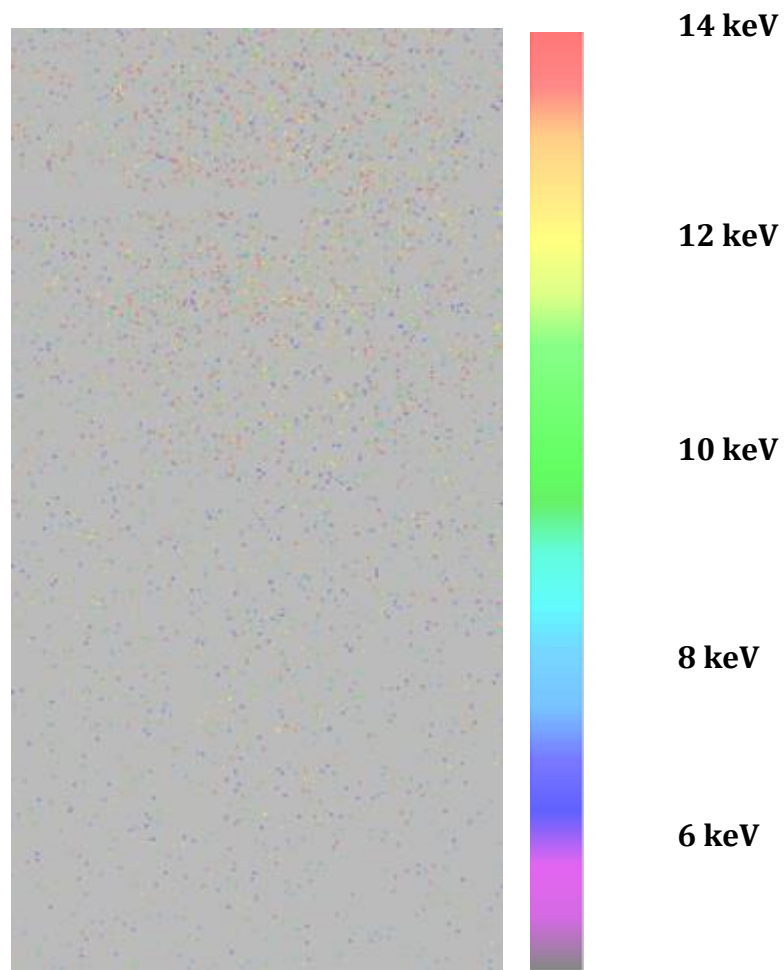
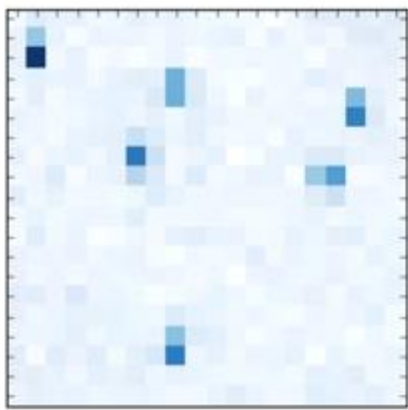
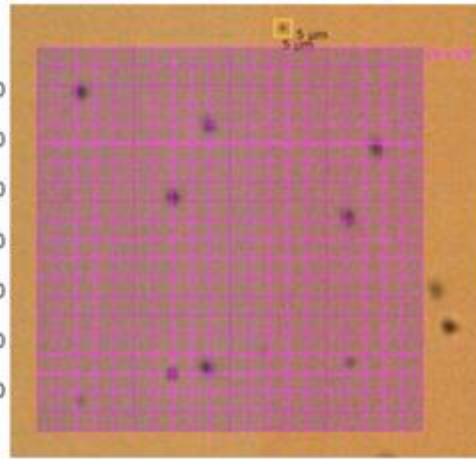
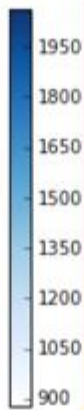


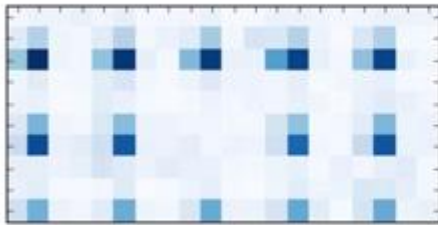
Figure DS9 Example of readout image from the JUNGRAU detector, recorded on a fluorescent nickel marker with 2 % transmission: 20 images were summed (to cover the complete cell), with 2.5 keV threshold. Only a about 1/8 of the detector is shown, from beam center to detector edge, for visibility of the small pixels. The beamstop shadow is visible in the upper part.



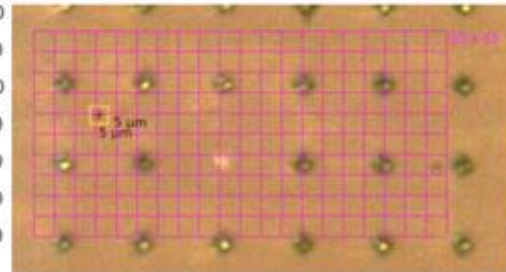
a)



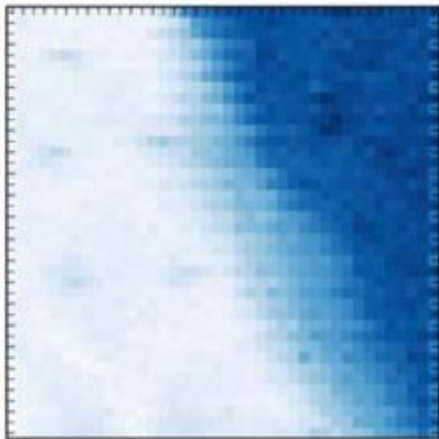
b)



c)



d)



e)



f)

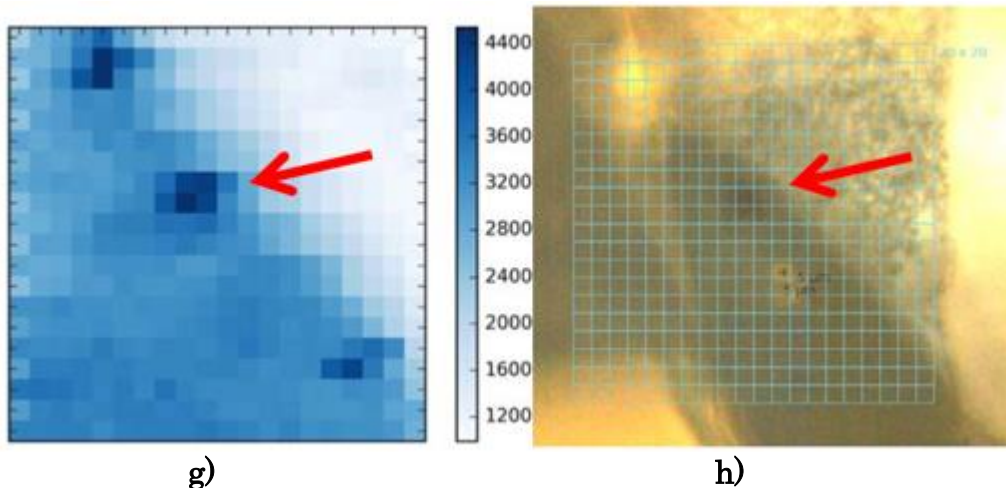


Figure DS10 Examples of EIGER 16M maps on model samples (a, c) and real samples (e, g) based on total counts summed over a large detector area, a square in size of 3376 pixels centered on the beam center. The exposure was 0.1 s (10 Hz rastering), and the beam transmission was 0.01% for the model samples, and 0.01 s (100 Hz rastering) with 0.1% transmission for the real-life samples, *i.e.* the number of photons per cell is identical to the JUNGFRAU reference maps, and between scans. For the nickel model sample (a), the SBR obtained was 1.7 ± 0.2 . For the gold sample (c), the SBR was 4.2 ± 0.1 . (b, d, f, h) corresponding areas on the model and real samples. For the gold real sample (e), the scanning area overlaps the LCP bolus on the right side. The markers are detectable only in the left area, where no LCP is present. For the real sample with steel beads mixed in LCP and enclosed in a silicon nitride sandwich, the red arrow shows the only effectively present steel bead in the scanning area. Other high-counts features are artifacts illustrating the unreliability of the detection with EIGER in presence of LCP.

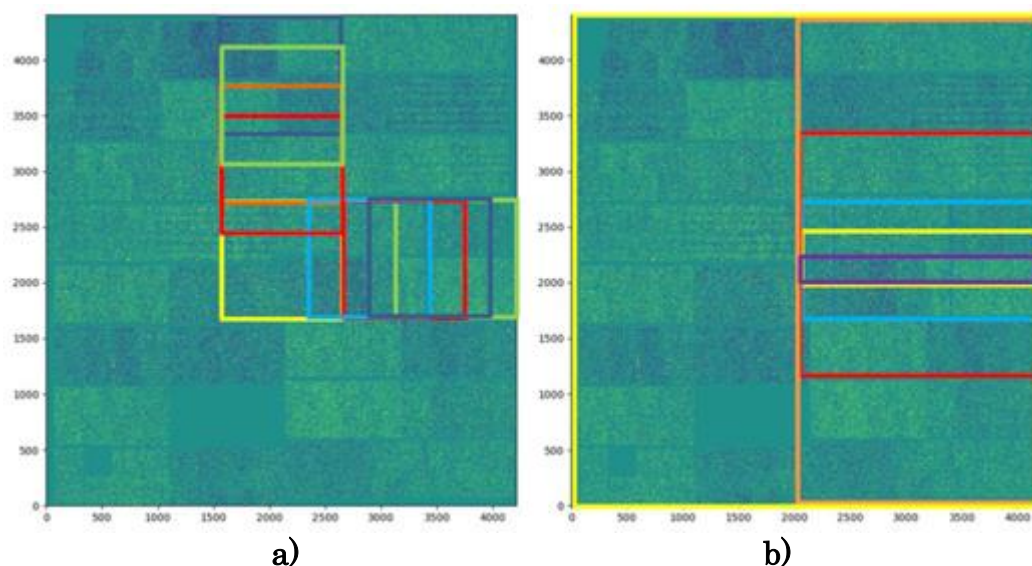


Figure DS11 Spatial ROIs used on the JUNGFRAU 16M for the SwissFEL data analysis, viewed in the direction opposite to the beam propagation. The right and top areas were predominantly used because of the absence of any bad module or shadow from devices such as the cryojet and post-sample tube. (a) 1M ROIs with the vertical and horizontal offset used for Figure 3.4b in the main manuscript. (b) ROIs of variable size used for Figure 3.4c. For clarity, ROIs smaller than 0.5M are not shown, and the rectangles are very slightly offset for visibility of their overlapping edges.

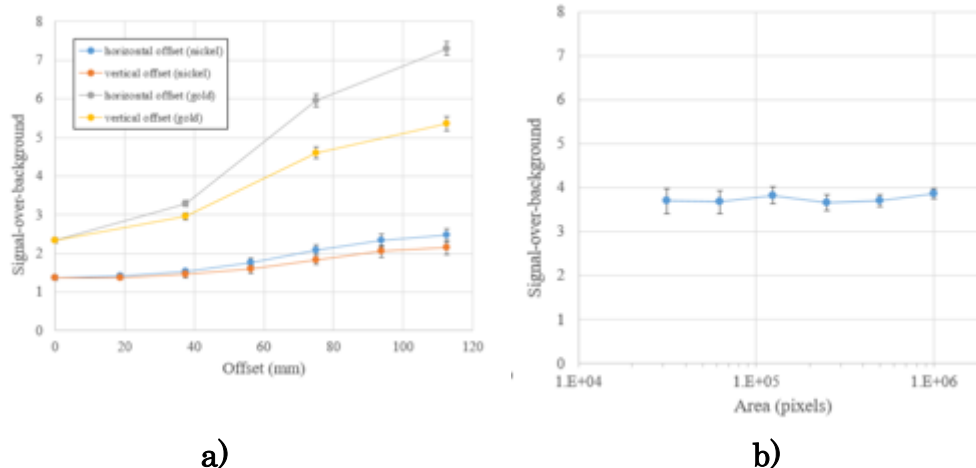


Figure DS12 Results from measurements with the EIGER 16M detector, using total counts on regions of interest defined similarly as in Figure DS11. (a) SBR as a function of the offset horizontally and vertically to the beam center for gold and nickel model samples, using a square 1 Mpix ROI. The SBR depends highly on the position of the ROI. At larger offsets, the SNB becomes higher thanks to the isotropy of fluorescence. At low offsets, the SBR decreases and makes the detection difficult. The separation between vertical and horizontal offsets arises from the beam polarization. (b) SBR as a function of the area of the ROI, for the nickel model sample. The SBR is maintained even for small ROIs, but the standard error increases.

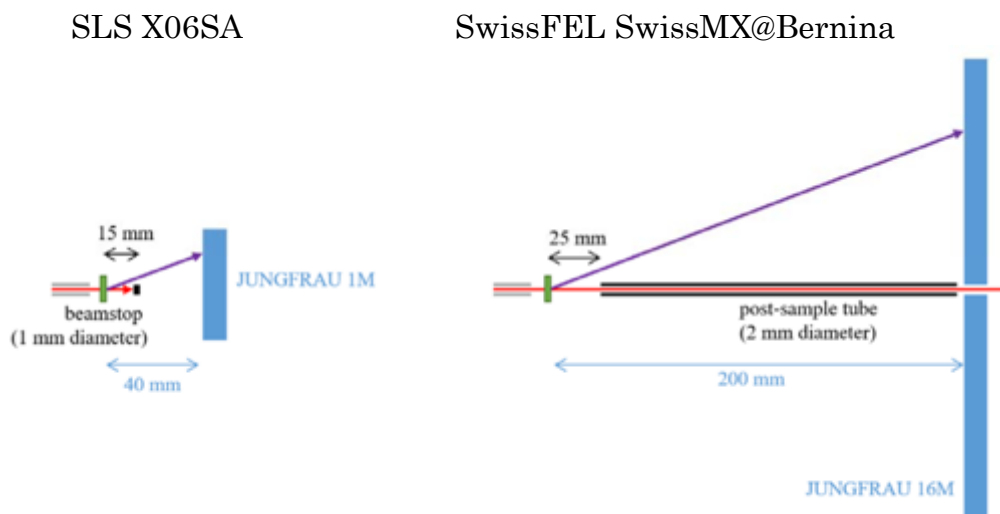


Figure DS13 Schematics of the experimental setups with relevant distances noted. The direct X-ray beam is shown in red, a diffracted ray in purple. Not indicated for clarity is the collimator (grey) to sample (green) distance, of about 4 mm in both cases. Schematics are approximately to scale.

Table DS1 Edge scan results for Se, obtained using 1000 images

		Energy (eV)	$f''(e)$	$f'(e)$
JUNGFRAU	Peak	12660.80	5.98	-7.88
	Inflection	12659.00	4.38	-9.66
SDD X06SA	Peak	12661.18	5.25	-7.48
	Inflection	12658.35	2.88	-9.34
SDD X06DA	Peak	12661.34	4.65	-7.49
	Inflection	12659.58	2.80	-8.85

Table DS2 Edge scan results for Hg, obtained using 3000 images

		Energy (eV)	f''(e)	f'(e)
JUNGFRAU	Peak	12313.80	9.87	-13.44
	Inflection	12291.00	7.19	-16.17

References

- [D1] F. L. Edelman, B. N. Zaitsev, V. Z. Latuta & A. A. Khoromenko, The structure of silicon nitride films. II. Non-stoichiometric silicon nitride. *Phys. Stat. Sol.* **51**, 49–56 doi:10.1002/pssa.2210510104 (1979).
- [D2] H. P. Löbl & M. Huppertz, Thermal stability of nonstoichiometric silicon nitride films made by reactive dc magnetron sputter deposition. *Thin Solid Films* **317**, 153–156 doi:10.1016/S0040-6090(97)00512-9 (1998).
- [D3] N. Opara, I. Martiel, S. A. Arnold, T. Braun, H. Stahlberg, M. Makita, C. David & C. Padeste, Direct protein crystallization on ultrathin membranes for diffraction measurements at X-ray free-electron lasers. *J. Appl. Cryst.* **50**, 909–918 doi:10.1107/S1600576717005799 (2017).
- [D4] S. Gorelick, V. A. Guzenko, J. Vila-Comamala & C. David, Direct e-beam writing of dense and high aspect ratio nanostructures in thick layers of PMMA for electroplating. *Nanotechnology* **21**, 295303 doi:10.1088/0957-4484/21/29/295303 (2010).
- [D5] K. Hili, D. Fan, V. A. Guzenko & Y. Ekinici, Nickel electroplating for high-resolution nanostructures. *Microelectronic Engineering* **141**, 122–128 doi:10.1016/j.mee.2015.02.031 (2015).
- [D6] C.-Y. Huang, V. Olieric, P. Ma, N. Howe, L. Vogeley, X. Liu, R. Warshamanage, T. Weinert, E. Panepucci, B. Kobilka, K. Diederichs, M. Wang, & M. Caffrey, *In meso in situ* serial X-ray crystallography of soluble and membrane proteins at cryogenic temperatures. *Acta Cryst. D* **72**, 93–112 doi:10.1107/S2059798315021683 (2016).
- [D7] S. Redford, M. Andrä, R. Barten, A. Bergamaschi, M. Brückner, R. Dinapoli, E. Fröjd, D. Greiffenberg, C. Lopez-Cuenca, D. Mezza, A. Mozzanica, M. Ramilli, M. Ruat, C. Ruder, B. Schmitt, X. Shi, D. Thattil, G. Tinti, S. Vetter & J. Zhang, First full dynamic range calibration of the JUNGFRAU photon detector. *JINST* **13**, C01027 doi:10.1088/1748-0221/13/01/C01027 (2018).
- [D8] R. Brun & F. Rademakers, ROOT — An object-oriented data analysis framework. *Nucl. Instr. and Meth. in Phys. Res. A* **389** (1–2): 81–86 doi:10.1016/S0168-9002(97)00048-X (1997).
- [D9] O. B. Zeldin, M. Gerstel & E. F. Garman, RADDOS-3D: time- and space-resolved modelling of dose in macromolecular crystallography. *J. Appl. Cryst.* **46**, 1225–1230 doi:10.1107/S0021889813011461 (2013).
- [D10] G. Evans & R. F. Pettifer, CHOOCH: A Program for deriving anomalous-scattering factors from X-ray fluorescence spectra. *J. Appl. Cryst.* **34**, 82–86 doi:10.1107/S0021889800014655 (2001).
- [D11] M. R. Fuchs, C. Pradervand, V. Thominet, R. Schneider, E. Panepucci, M. Grunder, J. Gabadinho, F. S. N. Dworkowski, T. Tomizaki, J. Schneider, A. Mayer, A. Curtin, V. Olieric, U. Frommherz, G. Kotrle, J. Welte, X. Wang, S. Maag, C. Schulze-Briese & M. Wang, D3, the new diffractometer for the macromolecular crystallography beamlines of the Swiss Light Source. *J. Synchrotron Rad.* **21**, 340–351 doi:10.1107/S160057751400006X (2014).



Appendix E

Supplementary Information for: **Supramolecular Architectures of Molecularly Thin Yet Robust Free- Standing Layers**

Mina Moradi^{a,b}, Nadia L. Oparab^{b,c}, Ludovico G. Tullia^a, Christian Wäckerlin^d, Scott J. Dalgarno^e, Simon J. Teat^f, Milos Baljovic^b, Olha Popova^g, Eric Van Genderen^c, Armin Kleibert^h, Henning Stahlberg^c, Jan Pieter Abrahams^{i,j}, Philippe F.-X. Corvini^a, Thomas A. Jung^{b,g,*}, & Patrick Shahgaldian^{a,*}

^aInstitute of Chemistry and Bioanalytics, School of Life Sciences, University of Applied Sciences and Arts Northwestern Switzerland, Hofackerstrasse 35, CH-4132 Muttenz, Switzerland.

^bLaboratory for Micro- and Nano-technology, Paul Scherrer Institute, Villigen CH-5232, Switzerland.

^cCenter for Cellular Imaging and NanoAnalytics (C-CINA), Biozentrum, University of Basel, Mattenstrasse 26, CH-4058 Basel, Switzerland.

^dEmpa – Swiss Federal Laboratories for Materials Science and Technology, CH-8600 Dübendorf, Switzerland.

^eInstitute of Chemical Sciences, Heriot-Watt University, Riccarton, Edinburgh, Scotland EH14 4AS, UK.

^fAdvanced Light Source, Lawrence Berkeley National Laboratory, 1 Cyclotron Rd, MS6R2100, Berkeley, CA 94720, USA.

^gDepartment of Physics, University of Basel, Klingelbergstrasse 82, 4056 Basel, Switzerland

^hSwiss Light Source, Paul Scherrer Institute, CH-5232 Villigen, Switzerland.

ⁱBiozentrum, University of Basel, Switzerland and Laboratory of Biomolecular Research, Paul Scherrer Institute, Villigen, Switzerland.

^jInstitute of Biology Leiden, Leiden University, Sylviusweg 72, 2333 BE Leiden, Netherlands.

Available online:

advances.sciencemag.org/cgi/content/full/5/2/eaav4489/DC1

Science Advances **5**, eaav4489 (2019).

Distributed under a Creative Commons Attribution NonCommercial License 4.0 (CC BY-NC).

Section ES1. Materials and methods

All chemicals were purchased as reagent grade from Sigma-Aldrich (Switzerland) and used without further purification. Solvents (analytical grade) were used without any further purification. 5,11,17,23-tetrakis(chloromethyl)-25,26,27,28-tetrapropoxy calix[4]arene (Cl-C4A-OC₃) was synthesized as previously reported [26].

Synthesis of 5,11,17,23-tetramethylcyano-25,26,27,28-tetrapropoxy calix[4]arene (**1**) was achieved by following a modified literature procedure [27].

A Millipore Synergy purification system was used to produce nanopure water with resistivity of 18.2 MΩ.cm. Deuterated solvents for NMR spectroscopic analyses were used as received from Arma AG (Switzerland). ¹H and ¹³C NMR spectra were recorded with a Bruker spectrometer 300 and 75 MHz, respectively. All the NMR peaks are reported as chemical shift in parts per million (ppm) using tetramethylsilane as internal standard. All coupling constants (J) are quoted in Hertz (Hz). The abbreviations s (singlet), d (doublet), t (triplet) and m (multiplet) are used to describe multiplicities. Electrospray ionization mass spectra were recorded in positive ion mode on a thermoquest LCQ Deca instrument. Elemental analysis was measured on a Leco CHN900 microanalyser. Melting points were measured using a Büchi 530 apparatus as triplicates to ensure the reproducibility of the result.

Section ES2. Contact angle measurement

Contact angles were measured using a commercial Krüss® Easy drop optical system (Krüss, GmbH, Germany). Drops of 3 µL of nanopure water were used for measuring static water contact angle on samples. To ensure reproducibility, the measurements were repeated at five different positions on each sample.

Section ES3. Spectroscopic ellipsometry

Ellipsometry measurements were carried out using an imaging and spectroscopic system (EP3 Ellipsometer Accurion) in a nulling PCSA (polarizer-compensator-sample-analyzer) set-up. For all the ellipsometry experiments, OTS-coated silicon wafers were used [28].

Section ES4. X-ray photoelectron spectroscopy

X-ray photoelectron spectroscopy (XPS) spectra were acquired using Specs FOCUS 500 monochromatic Al K_α (hν = 1486.7 eV) with XR 50 M excitation source in normal emission using a Specs PHOIBOS 150 electron analyzer. The C1s core level of HOPG was used as reference for the binding energies and was assigned to 284.5 eV. The measurements were performed in ultra-high vacuum system with base pressure of 10⁻¹¹ mbar.

Section ES5. Atomic force microscopy

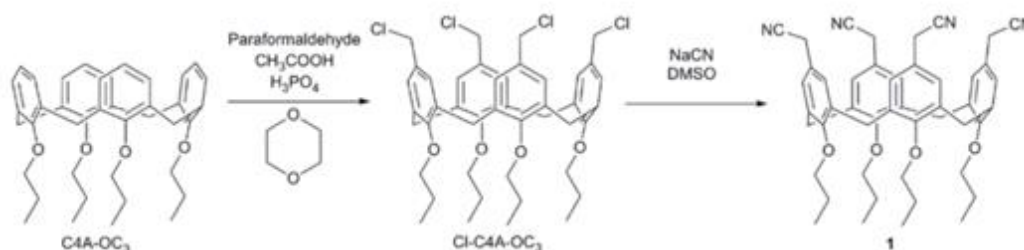
Atomic force microscopy experiments were carried out in the PeakForce Tapping® mode using a Multimode 8 instrument (Bruker) equipped with a Nanoscope V controller with a scanasyst-air-HR silicon tip on silicon nitride lever.

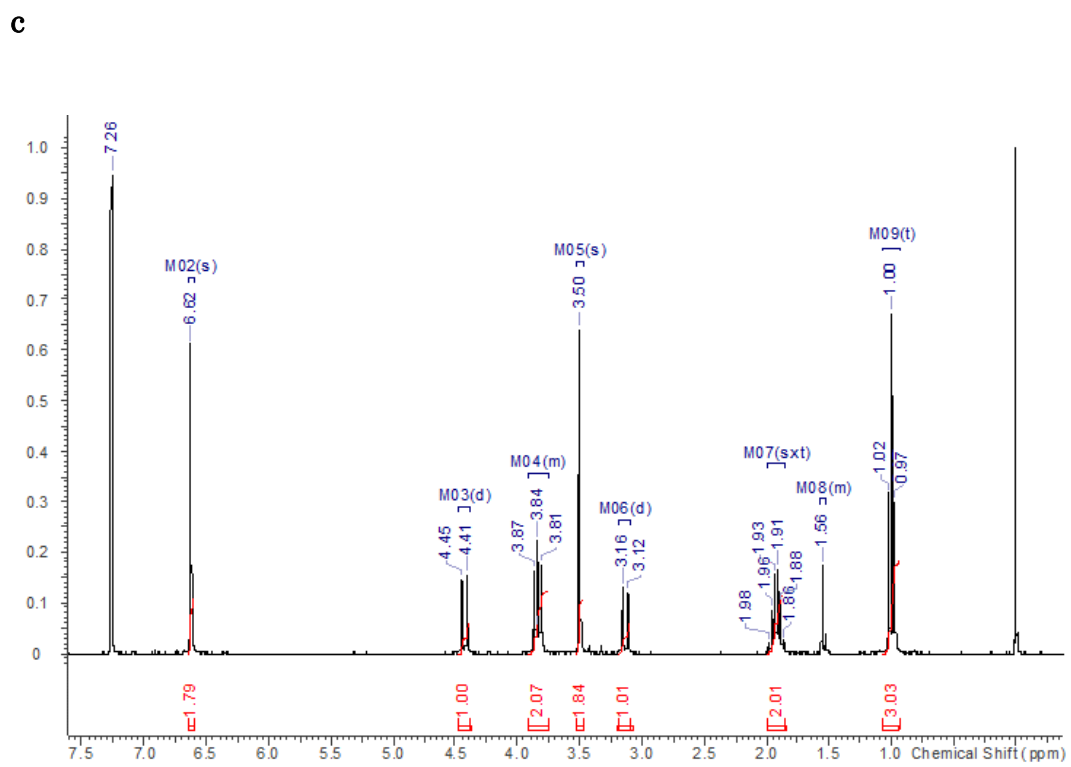
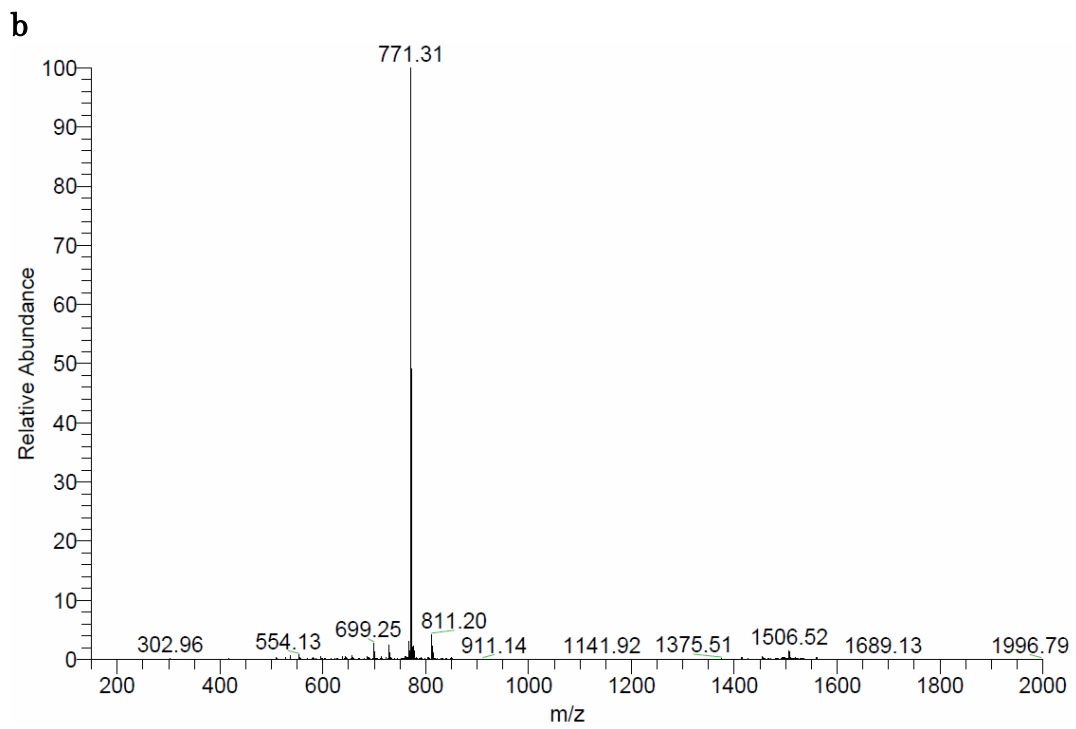
Section ES6. Transmission electron microscopy

The monolayer of **1**, prepared as detailed above, was transferred via the LS method on an electron microscopy grid (copper grid with lacey carbon, Ted Pella Inc., USA) placed on the designed and fabricated polydimethylsiloxane support of required geometry. The TEM imaging and diffraction data collection were done with a TEM system equipped with CCD camera Ceta (16M Pixel CMOS) and Timepix direct electron detector [29-31]. The images were collected in cryo-conditions (sample placed on the cryoholder, inserted to the microscope and cooled down with liquid nitrogen before illumination by the electrons) with Talos (FED) machine operating at 200 keV accelerating voltage (high accelerating voltages are necessary to reduce melting of the material in the electron beam and enable the imaging) and vacuum of 3.5×10^{-8} Torr. The exposure parameters for imaging were adjusted to achieve sufficient visibility of the ultrathin material: to increase the contrast image was strongly defocused ($> 100 \mu\text{m}$); gun lens set to the level 5; spot size set to the level 5; electron beam intensity 63.1% and objective lens: 82.1%. Additionally, SA and objective apertures were retracted. The diffraction image shows a stack of the 300 frames. Each frame was an exposure to the electrons of the $\lambda = 2.51 \text{ pm}$ for 0.5 s. The detector distance was calibrated with aluminum grid and theoretical camera length was determined to be 1890 mm.

Supplementary Figures and Tables

a





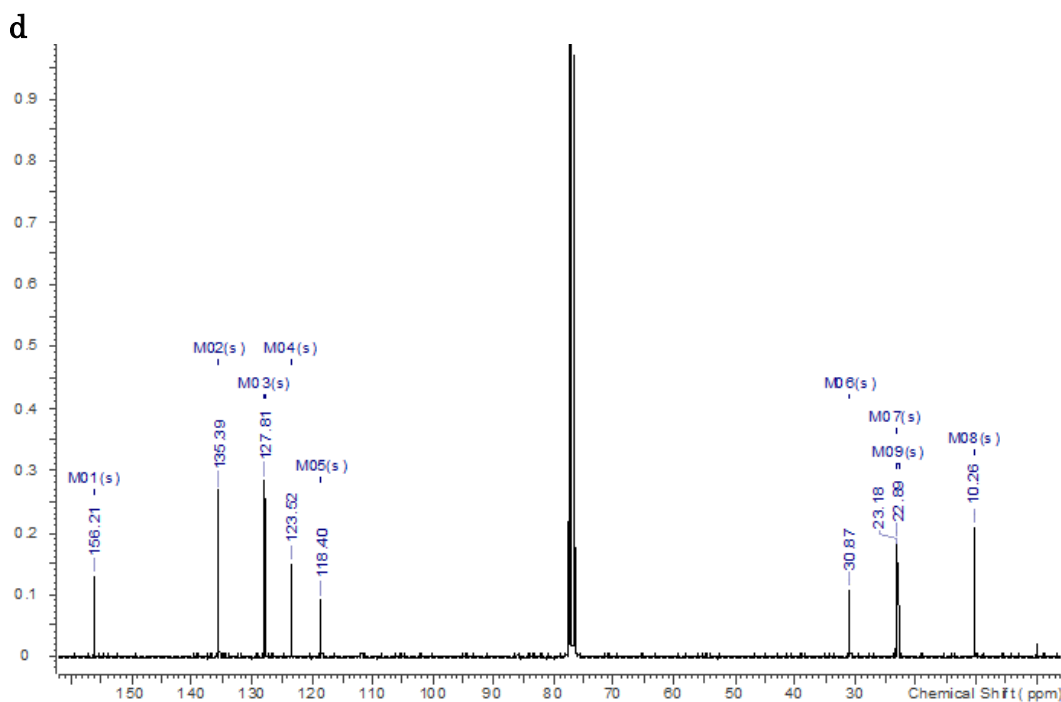


Figure ES1 Synthetic route to 5,11,17,23-tetramethyloxy-25,26,27,28-tetrapropoxy calix[4]arene (1) and spectroscopic details of 1. (a) Synthetic route to 1 through the chloro-methylation of the parent tetra-propyloxy-calix[4]arene (C4A-OC₃), locked in the cone conformation, to yield the tetrachloromethyl derivative (Cl-C4A-OC₃) followed by the nucleophilic substitution of chlorine atoms using NaCN to yield 1. (b) ESI mass chromatogram of 1. (c) ¹H NMR spectrum of 1. (d) ¹³C NMR spectrum of 1.

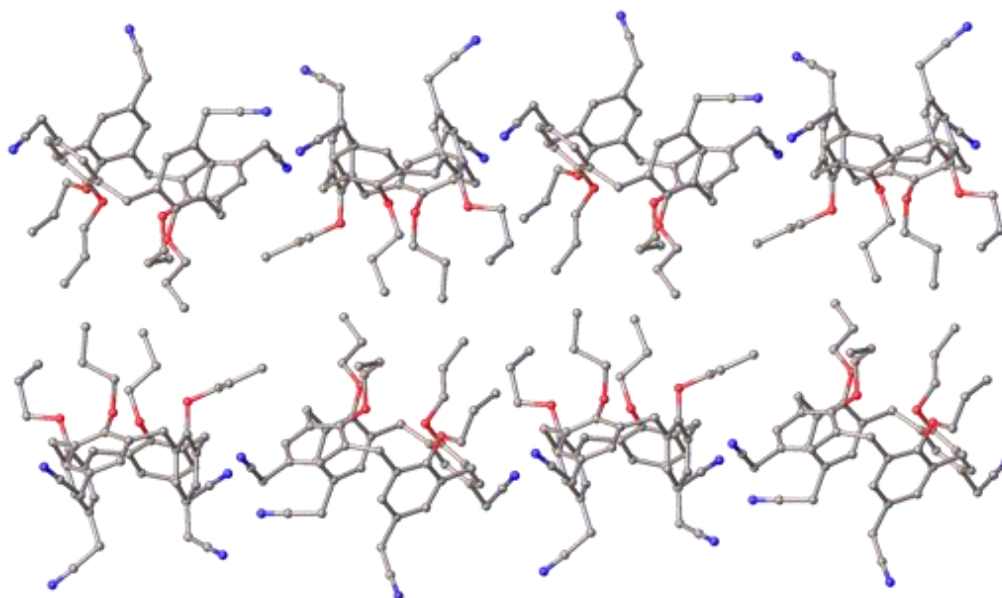


Figure ES2 X-ray crystal structure determination details of 1. Crystal Data for 1 (CCDC 1586569): C₉₆H₁₀₄N₈O₈, M = 1497.87 g/mol, triclinic, space group P-1 (no. 2), a = 14.6702(7) Å, b = 14.7632(7) Å, c = 20.0756(9) Å, α = 82.227(3)°, β = 76.317(2)°, γ = 89.982(3)°, V = 4183.5(3) Å³, Z = 2, T = 100(2) K, 34673 reflections measured (4.28° ≤ 2θ ≤ 57.33°), 16006 unique (R_{int} = 0.0659, R_{sigma} = 0.0909) which were used in all calculations. The final R₁ was 0.0799 (I > 2σ(I)) and wR₂ was 0.1982 (all data). Symmetry expanded structure of 1 showing bilayer formation by association of hydrophobic chains at the macrocycle lower rim.

The asymmetric unit contains two molecules of **1**, as well as diffuse density associated with badly disordered solvent of crystallization; this was removed during refinement using a solvent mask, greatly improving the agreement indices. The density associated with the disordered solvent of crystallization occupies space within the hydrophobic layer of the extended structure, generated by the packing of symmetry equivalents (s.e.) of **1**. There is no indication of the presence of significant intermolecular interactions between the peaks in the density map and atoms of neighboring s.e. of **1**, so one may assume that the presence of the solvent is very unlikely to influence bilayer assembly; this lack of interactions likely promotes the severe disorder that in fact compromises modelling. We identified two crystallographically unique CH \cdots N interactions with distances of 2.612 and 2.664 Å, and one CH \cdots π interaction with a CH \cdots aromatic centroid distance of 2.611 Å. It is noteworthy that a search of the Cambridge structural database for upper-rim methyl-cyano functionalized calix[4]arenes returned just 6 hits, and these structures display similar intermolecular interactions as those observed in the present case [32].

Table ES1 X-ray crystal structure determination detail of 1. Crystal data and structure refinement for compound 1 (CCDC 1586569).

Empirical formula	C ₉₆ H ₁₀₄ N ₈ O ₈
Formula weight	1497.87
Temperature/K	100(2)
Crystal system	triclinic
Space group	P-1
a/Å	14.6702(7)
b/Å	14.7632(7)
c/Å	20.0756(9)
α /°	82.227(3)
β /°	76.317(2)
γ /°	89.982(3)
Volume/Å ³	4183.5(3)
Z	2
$\rho_{\text{calc}}/\text{cm}^3$	1.189
μ/mm^{-1}	0.090
F(000)	1600.0
Crystal size/mm ³	0.08 × 0.06 × 0.05
Radiation	synchrotron ($\lambda = 0.7749$)
2 θ range for data collection/°	4.28 to 57.33
Index ranges	-18 ≤ h ≤ 18, -18 ≤ k ≤ 18, -24 ≤ l ≤ 24
Reflections collected	34673
Independent reflections	16006 [R _{int} = 0.0659, R _{sigma} = 0.0909]
Data/restraints/parameters	16006/0/1017
Goodness-of-fit on F ²	1.055
Final R indexes [I ≥ 2 σ (I)]	R ₁ = 0.0799, wR ₂ = 0.1818
Final R indexes [all data]	R ₁ = 0.1132, wR ₂ = 0.1982
Largest diff. peak/hole / e Å ⁻³	0.56/-0.48

Table ES2 X-ray crystal structure determination detail of 1. Fractional atomic coordinates ($\times 10^4$) and equivalent isotropic displacement parameters ($\text{\AA}^2 \times 10^3$) for 1 (CCDC 1586569). U_{eq} is defined as 1/3 of the trace of the orthogonalised U_{ij} tensor.

Atom	<i>x</i>	<i>y</i>	<i>z</i>	$U(\text{eq})$
O7	-1473.9(14)	3841.3(14)	2219.1(11)	19.9(5)
O1	8339.2(14)	8842.2(14)	2215.0(11)	20.1(5)
O8	945.7(15)	4481.6(14)	1785.4(11)	20.7(5)
O6	170.1(15)	2305.5(14)	2341.3(12)	21.8(5)
O5	2391.7(15)	2832.6(14)	1659.7(11)	21.4(5)
O3	4859.7(15)	7834.2(14)	1584.8(11)	20.5(5)
O2	6607.1(15)	7306.5(14)	2316.1(11)	20.3(5)
O4	6220.0(15)	9458.6(14)	1752.6(12)	21.1(5)
N2	6038(2)	2722(2)	4075.4(16)	31.6(7)
N6	-449(2)	-2261(2)	4098.5(16)	30.6(7)
N4	5073(2)	14024(2)	2190.1(18)	35.5(8)
N8	1727(2)	9042(2)	2306.9(18)	36.4(8)
C54	2307(2)	2919(2)	2349.6(16)	17.6(6)
C13	6517(2)	6567(2)	2828.7(16)	18.5(6)
C25	5923(2)	11494(2)	2623.6(17)	21.4(7)
N3	1547(2)	8738(2)	4535.3(16)	36.9(8)
N5	3828(2)	3778(2)	4571.9(17)	37.9(8)
C68	-1268(2)	3855(2)	2856.6(17)	18.3(6)
C75	1165(2)	5209(2)	2086.4(16)	18.1(6)
C6	7697(2)	8854(2)	2842.4(16)	17.9(6)
C9	7058(2)	5698(2)	3748.0(17)	20.2(7)
C66	-631(2)	4636(2)	3622.4(18)	21.7(7)
C10	6273(2)	5111(2)	3889.7(17)	20.4(7)
C4	6867(2)	8075(2)	3942.8(17)	20.8(7)
C5	7516(2)	8060(2)	3324.2(17)	18.5(7)
C49	2532(2)	3759(2)	2534.5(17)	19.1(7)
C70	435(2)	5750(2)	2370.3(16)	18.2(6)
C26	6342(2)	10758(2)	2324.7(16)	18.5(7)
C53	1965(2)	2168(2)	2858.3(18)	20.6(7)
C14	4929(2)	6261(2)	2612.7(17)	21.5(7)
C1	7197(2)	9646(2)	2967.6(17)	18.9(7)
C8	7183(2)	6442(2)	3226.0(17)	18.7(7)
C59	-1238(2)	703(2)	3771.9(17)	21.6(7)
C11	5593(2)	5286(2)	3515.6(17)	20.5(7)
C22	4850(2)	10330(2)	2099.1(17)	19.9(7)
C63	-1418(2)	3061(2)	3338.3(17)	19.0(7)
C57	383(2)	306(2)	3570.0(17)	22.3(7)
C71	642(2)	6488(2)	2682.0(17)	20.1(7)
C56	629(2)	1032(2)	3037.2(17)	20.0(7)
C27	5809(2)	10206(2)	2039.0(17)	19.1(7)
C2	6555(2)	9640(2)	3598.2(17)	22.0(7)
C16	4097(2)	7254(2)	3473.3(17)	21.9(7)
C24	4984(2)	11670(2)	2657.2(17)	21.7(7)
C74	2077(2)	5336(2)	2171.5(16)	18.6(7)
C15	4488(2)	7153(2)	2787.9(17)	19.4(7)
C20	4495(2)	7910(2)	2275.5(17)	19.6(7)
C92	-605(2)	-1562(2)	4275.0(18)	23.4(7)
C28	7303(2)	10458(2)	2400.4(18)	21.0(7)
C72	1558(2)	6667(2)	2727.8(17)	20.3(7)
C51	2198(2)	3066(2)	3732.7(17)	21.7(7)
C19	4171(2)	8753(2)	2455.6(17)	19.3(7)

C73	2253(2)	6073(2)	2493.8(17)	20.9(7)
C23	4451(2)	11073(2)	2410.5(18)	21.4(7)
C67	-841(2)	4639(2)	2978.8(17)	19.1(7)
C62	-1736(2)	2170(2)	3159.0(18)	21.6(7)
C76	2805(2)	4615(2)	2009.6(17)	20.0(7)
C12	5699(2)	6015(2)	2987.1(17)	18.8(7)
C58	-546(2)	125(2)	3929.3(17)	22.2(7)
C21	4248(2)	9605(2)	1923.4(18)	21.4(7)
C7	7954(2)	7166(2)	3150.0(18)	20.7(7)
C65	-810(2)	3864(2)	4118.3(17)	22.4(7)
C44	6086(2)	3425(2)	4247.8(18)	24.7(7)
C17	3728(2)	8076(2)	3660.4(17)	22.6(7)
C48	4835(2)	13349(2)	2543.4(19)	26.0(8)
C52	1923(2)	2257(2)	3544.6(18)	21.9(7)
C55	1644(2)	1277(2)	2672.3(18)	22.3(7)
C61	-85(2)	1579(2)	2858.7(17)	18.5(6)
C3	6390(2)	8871(2)	4092.7(17)	20.7(7)
C69	-564(2)	5453(2)	2418.3(17)	19.9(7)
C18	3789(2)	8820(2)	3148.9(17)	20.6(7)
C50	2474(2)	3817(2)	3225.8(17)	21.0(7)
C89	2211(2)	3145(2)	4476.8(18)	27.7(8)
C43	6144(2)	4318(2)	4479.1(18)	25.0(7)
C60	-1016(2)	1440(2)	3247.3(17)	20.3(7)
C64	-1195(2)	3079(2)	3969.5(18)	22.0(7)
C29	9279(2)	9150(2)	2220.6(18)	23.8(7)
C95	1765(2)	7468(2)	3071.0(19)	25.6(7)
C93	-591(3)	3861(2)	4821.7(18)	28.9(8)
C35	4252(2)	7361(2)	1267.7(18)	25.8(7)
C90	3117(2)	3507(2)	4529.1(18)	26.6(8)
C46	2301(3)	8497(2)	4478.6(18)	27.4(8)
C96	1739(2)	8356(2)	2641(2)	26.9(8)
C80	-135(2)	2230(2)	1719.6(18)	25.8(7)
C83	-2401(2)	4164(2)	2197.2(19)	24.9(7)
C81	520(2)	1704(2)	1225.8(18)	27.2(8)
N1	6527(3)	9435(3)	5673.9(19)	52.3(10)
C38	6447(2)	9550(2)	1012.8(18)	27.0(8)
C32	7321(2)	7242(2)	1694.4(18)	24.9(7)
C41	5695(2)	8869(2)	4784.7(18)	27.9(8)
C30	9888(2)	9157(2)	1503.9(18)	26.4(7)
C45	3258(2)	8161(3)	4405.7(18)	29.8(8)
C91	-803(2)	-671(2)	4513.2(18)	26.6(8)
C47	4542(2)	12478(2)	2990.7(18)	23.8(7)
N7	-2040(3)	4448(3)	5664(2)	56(1)
C86	1312(2)	4524(2)	1051.0(17)	26.1(7)
C31	10023(3)	8212(2)	1276.6(19)	29.5(8)
C36	3557(3)	7979(3)	1008(2)	31.5(8)
C42	6144(3)	9187(3)	5292(2)	33.7(9)
C39	7402(3)	9993(2)	681.6(19)	33.1(8)
C84	-2517(3)	4183(2)	1471.6(19)	30.6(8)
C33	6965(2)	6765(2)	1176.2(18)	29.0(8)
C87	650(3)	4956(2)	633.3(19)	29.2(8)
C82	148(3)	1632(3)	589(2)	35.2(9)
C88	627(3)	5995(2)	572(2)	33.7(9)
C85	-2483(3)	3245(3)	1228(2)	34.8(9)
C94	-1388(3)	4190(3)	5309(2)	35.7(9)
C37	2934(3)	7456(3)	666(2)	42.3(10)
C34	7744(3)	6731(3)	529(2)	45.2(10)

C40	7665(3)	9995(3)	-98(2)	42(1)
C77	3329(3)	2687(3)	1283(2)	40.5(10)
C79	4359(3)	1724(3)	506(2)	52.1(12)
C78	3399(3)	1887(3)	932(3)	55.3(13)

Table ES3 X-ray crystal structure determination detail of 1. Anisotropic displacement parameters ($\text{\AA}^2 \times 10^3$) for 1. The anisotropic displacement factor exponent takes the form: $-2\pi^2[h^2a^*U_{11}+2hka^*b^*U_{12}+\dots]$.

Atom	U_{11}	U_{22}	U_{33}	U_{23}	U_{13}	U_{12}
O7	16.2(11)	21.8(11)	25.5(12)	-7.4(9)	-10.1(9)	5.6(9)
O1	15.1(11)	21.7(11)	25.0(12)	-7.0(9)	-5.5(9)	3.4(9)
O8	21.5(11)	18.0(11)	24.8(12)	-5.8(9)	-8.1(10)	2.9(9)
O6	22.4(11)	16.2(11)	25.3(12)	0.6(9)	-4.9(10)	-0.9(9)
O5	20.0(11)	20.4(11)	24.3(12)	-5.4(9)	-4.9(10)	5.1(9)
O3	20.2(11)	19.4(11)	23.3(12)	-3.4(9)	-7.7(9)	-0.2(9)
O2	21.2(11)	16.8(11)	22.5(12)	-0.5(9)	-5.9(9)	2.1(9)
O4	21.7(11)	16.0(11)	26.5(13)	-5.8(9)	-6(1)	4.5(9)
N2	32.2(17)	26.1(16)	37.6(18)	-0.7(14)	-12.6(14)	2.7(13)
N6	28.3(16)	25.5(16)	36.8(18)	-1.2(14)	-7.3(14)	2.6(13)
N4	30.8(17)	20.6(16)	55(2)	-5.4(15)	-9.7(16)	5.8(13)
N8	33.8(17)	23.9(16)	55(2)	-7.2(15)	-16.4(16)	2.0(13)
C54	13.4(14)	19.7(15)	21.4(17)	-3.2(13)	-6.9(13)	6.1(12)
C13	21.1(16)	12.3(14)	21.9(17)	-3.1(12)	-4.1(13)	5.4(12)
C25	18.4(15)	16.8(15)	30.3(19)	-4.2(13)	-7.7(14)	1.7(12)
N3	31.5(18)	48(2)	29.5(18)	-2.0(15)	-5.6(14)	9.2(15)
N5	32.2(18)	49(2)	31.3(18)	-0.1(15)	-8.6(15)	-6.0(15)
C68	12.4(14)	17.5(15)	26.4(18)	-6.4(13)	-5.4(13)	5.0(12)
C75	21.4(16)	13.5(14)	20.6(17)	-2.4(12)	-7.4(13)	0.5(12)
C6	16.1(15)	17.7(15)	23.0(17)	-7.6(13)	-7.9(13)	1.6(12)
C9	20.3(16)	17.7(15)	26.4(18)	-7.5(13)	-10.8(14)	7.1(13)
C66	18.5(16)	16.9(15)	31.4(19)	-7.6(14)	-7.2(14)	3.3(12)
C10	24.4(17)	15.4(15)	21.9(17)	-3.1(13)	-6.1(14)	4.8(13)
C4	20.4(16)	17.8(15)	26.5(18)	-3.5(13)	-9.7(14)	3.9(13)
C5	14.7(15)	19.2(15)	25.4(17)	-7.4(13)	-9.8(13)	4.5(12)
C49	13.6(14)	18.1(15)	26.0(18)	-2.2(13)	-6.1(13)	6.2(12)
C70	17.7(15)	14.9(15)	22.0(17)	-0.4(13)	-6.1(13)	1.4(12)
C26	17.9(15)	13.5(14)	23.6(17)	-0.6(13)	-5.0(13)	2.4(12)
C53	13.9(15)	18.6(15)	31.9(19)	-4.9(14)	-9.9(14)	6.2(12)
C14	21.2(16)	20.1(16)	24.6(18)	-4.2(13)	-7.7(14)	3.4(13)
C1	15.2(15)	17.3(15)	27.0(18)	-4.9(13)	-9.7(13)	-0.1(12)
C8	17.6(15)	13.7(14)	26.2(18)	-5.9(13)	-6.3(13)	6.6(12)
C59	19.9(16)	17.4(15)	27.5(18)	-6.4(13)	-4.0(14)	-2.8(13)
C11	18.6(15)	15.5(15)	28.1(18)	-4.7(13)	-5.7(14)	1.4(12)
C22	18.4(15)	15.9(15)	25.8(18)	1.4(13)	-8.4(14)	0.8(12)
C63	10.4(14)	18.2(15)	28.9(18)	-6.6(13)	-3.8(13)	1.8(12)
C57	23.5(17)	16.6(15)	28.4(19)	-5.0(13)	-8.1(14)	3.5(13)
C71	19.3(16)	15.3(15)	25.9(18)	-3.5(13)	-5.6(14)	1.5(12)
C56	18.8(16)	17.4(15)	26.1(18)	-6.5(13)	-7.7(14)	0.8(12)
C27	19.7(16)	11.5(14)	25.5(18)	-0.7(13)	-5.2(13)	2.1(12)
C2	19.9(16)	18.6(16)	29.1(19)	-8.5(14)	-6.0(14)	3.8(13)
C16	16.9(15)	23.1(16)	27.2(18)	0.1(14)	-10.4(14)	3.2(13)
C24	22.1(16)	16.2(15)	26.9(18)	-3.0(13)	-5.8(14)	4.1(13)
C74	18.4(15)	15.1(15)	20.5(17)	0.9(12)	-3.0(13)	-0.4(12)
C15	13.0(14)	18.2(15)	28.3(18)	-3.2(13)	-7.6(13)	2.0(12)

C20	16.0(15)	19.1(15)	23.7(17)	-1.1(13)	-5.9(13)	-0.5(12)
C92	20.0(16)	23.3(18)	25.2(18)	3.1(14)	-5.4(14)	0.8(13)
C28	17.2(15)	15.2(15)	32.1(19)	-4.6(13)	-8.5(14)	3.0(12)
C72	22.6(16)	14.9(15)	24.7(18)	-3.5(13)	-7.5(14)	0.6(13)
C51	13.0(15)	25.2(17)	27.0(18)	-4.9(14)	-4.6(13)	3.1(13)
C19	14.7(15)	17.6(15)	29.0(18)	-1.9(13)	-12.8(14)	2.0(12)
C73	18.0(15)	18.6(15)	27.6(18)	-1.8(13)	-9.4(14)	-1.7(13)
C23	15.4(15)	17.4(15)	31.8(19)	-2.2(14)	-7.1(14)	4.7(12)
C67	13.1(14)	15.6(15)	30.0(18)	-5.7(13)	-6.6(13)	5.6(12)
C62	18.3(15)	17.6(15)	30.9(19)	-5.3(14)	-8.6(14)	1.6(13)
C76	16.9(15)	18.7(15)	24.1(17)	-3.7(13)	-4.2(13)	1.1(12)
C12	17.7(15)	14.7(14)	25.0(17)	-4.3(13)	-6.4(13)	5.7(12)
C58	24.1(17)	17.5(16)	25.2(18)	-3.8(13)	-5.6(14)	0.4(13)
C21	20.1(16)	16.7(15)	29.9(19)	-3.3(13)	-10.8(14)	1.2(13)
C7	14.0(15)	19.3(16)	30.4(19)	-5.3(14)	-7.5(14)	4.0(12)
C65	22.0(16)	22.4(16)	24.8(18)	-6.9(14)	-7.5(14)	2.5(13)
C44	24.4(17)	20.8(17)	28.8(19)	4.2(14)	-10.5(15)	3.1(14)
C17	19.3(16)	25.3(17)	27.3(18)	-4.6(14)	-12.9(14)	3.3(13)
C48	18.8(16)	22.3(18)	42(2)	-12.7(16)	-12.0(15)	8.2(14)
C52	15.2(15)	20.5(16)	27.9(18)	1.1(14)	-3.5(13)	1.5(12)
C55	17.2(15)	17.5(15)	32.0(19)	-3.9(14)	-5.1(14)	4.3(13)
C61	18.2(15)	14.9(15)	22.8(17)	-4.5(13)	-4.6(13)	-1.3(12)
C3	16.0(15)	23.3(16)	24.1(17)	-6.3(14)	-5.2(13)	0.9(13)
C69	16.1(15)	17.1(15)	27.4(18)	-3.3(13)	-6.7(13)	4.2(12)
C18	20.3(16)	17.1(15)	27.8(18)	-5.9(13)	-11.3(14)	5.3(13)
C50	18.1(15)	17.8(15)	28.5(18)	-6.4(13)	-6.2(14)	5.7(12)
C89	23.1(17)	34.6(19)	23.4(18)	-1.0(15)	-3.2(14)	-4.7(15)
C43	29.4(18)	20.9(16)	26.7(19)	-1.6(14)	-12.0(15)	0.9(14)
C60	18.1(15)	18.7(16)	27.3(18)	-8.1(13)	-9.1(14)	1.6(13)
C64	20.2(16)	18.3(16)	26.9(18)	-2.1(13)	-5.2(14)	1.3(13)
C29	14.4(15)	24.8(17)	34(2)	-7.9(15)	-7.0(14)	3.2(13)
C95	24.2(17)	22.6(17)	32(2)	-8.8(15)	-8.7(15)	2.4(14)
C93	32.4(19)	27.2(18)	31(2)	-4.0(15)	-14.7(16)	0.6(15)
C35	28.4(18)	29.2(18)	23.1(18)	-5.6(14)	-11.2(15)	-3.3(15)
C90	27.2(19)	28.7(18)	22.2(18)	1.2(14)	-5.3(15)	0.9(15)
C46	31(2)	27.6(18)	23.5(19)	-1.3(15)	-7.5(15)	1.5(15)
C96	22.2(17)	20.8(18)	42(2)	-12.1(16)	-11.7(16)	0.2(14)
C80	25.0(17)	25.2(17)	25.6(18)	0.3(14)	-5.0(15)	4.7(14)
C83	18.8(16)	23.3(17)	37(2)	-6.3(15)	-13.5(15)	6.6(13)
C81	31.1(19)	21.5(17)	30(2)	-3.9(14)	-8.4(16)	5.6(14)
N1	63(3)	58(2)	35(2)	-12.9(18)	-8.0(19)	-6(2)
C38	29.6(18)	25.4(17)	26.9(19)	-8.1(15)	-6.0(15)	5.6(14)
C32	20.7(16)	25.1(17)	26.6(19)	-0.2(14)	-2.9(14)	1.6(14)
C41	24.8(18)	24.2(17)	34(2)	-5.0(15)	-4.3(15)	4.1(14)
C30	21.7(17)	25.5(17)	29.7(19)	-1.2(15)	-3.1(15)	1.8(14)
C45	29.2(19)	35(2)	28(2)	-7.1(16)	-10.7(16)	8.2(16)
C91	28.9(18)	21.3(17)	28.3(19)	-3.0(14)	-4.6(15)	2.3(14)
C47	20.3(16)	21.2(16)	32.3(19)	-6.6(14)	-9.1(15)	6.7(13)
N7	72(3)	63(3)	37(2)	-14.8(19)	-16(2)	25(2)
C86	28.8(18)	26.9(18)	24.8(19)	-8.2(14)	-8.1(15)	8.7(15)
C31	29.0(19)	29.3(19)	28(2)	-6.8(15)	-1.8(16)	5.0(15)
C36	30.4(19)	39(2)	29(2)	-8.3(16)	-11.3(16)	3.1(16)
C42	40(2)	30.6(19)	28(2)	-5.3(16)	-1.4(17)	2.7(17)
C39	33(2)	27.5(19)	36(2)	-4.3(16)	-4.1(17)	1.9(16)
C84	26.0(18)	32.3(19)	36(2)	0.3(16)	-15.7(16)	0.6(15)
C33	29.5(19)	30.1(19)	28(2)	-7.3(15)	-5.5(15)	4.3(15)
C87	36(2)	30.2(19)	26.3(19)	-8.6(15)	-14.4(16)	7.5(16)

C82	41(2)	35(2)	33(2)	-7.8(17)	-12.9(18)	8.5(17)
C88	41(2)	31.0(19)	32(2)	-3.9(16)	-14.3(17)	6.8(17)
C85	34(2)	42(2)	33(2)	-7.1(17)	-15.6(17)	0.8(17)
C94	52(2)	32(2)	28(2)	-7.3(17)	-17.8(19)	10.1(18)
C37	45(2)	42(2)	48(3)	-6.7(19)	-27(2)	-2.5(19)
C34	44(2)	53(3)	36(2)	-15(2)	-0.6(19)	2(2)
C40	41(2)	41(2)	39(2)	-6.2(19)	0.1(19)	5.9(19)
C77	27(2)	63(3)	32(2)	-16(2)	-2.4(17)	16.2(19)
C79	56(3)	47(3)	41(3)	-1(2)	10(2)	21(2)
C78	42(3)	65(3)	65(3)	-35(3)	-11(2)	13(2)

Table ES4 X-ray crystal structure determination detail of 1. Bond Lengths for 1.

Atom	Atom	Length/Å	Atom	Atom	Length/Å
O7	C68	1.385(4)	C22	C23	1.396(4)
O7	C83	1.449(4)	C22	C21	1.517(4)
O1	C6	1.385(4)	C63	C62	1.512(4)
O1	C29	1.455(4)	C63	C64	1.386(5)
O8	C75	1.374(4)	C57	C56	1.389(4)
O8	C86	1.437(4)	C57	C58	1.390(5)
O6	C61	1.372(4)	C71	C72	1.396(4)
O6	C80	1.440(4)	C56	C55	1.516(4)
O5	C54	1.384(4)	C56	C61	1.406(4)
O5	C77	1.436(4)	C2	C3	1.384(5)
O3	C20	1.383(4)	C16	C15	1.388(5)
O3	C35	1.441(4)	C16	C17	1.390(5)
O2	C13	1.379(4)	C24	C23	1.391(4)
O2	C32	1.441(4)	C24	C47	1.518(4)
O4	C27	1.386(4)	C74	C73	1.392(4)
O4	C38	1.430(4)	C74	C76	1.520(4)
N2	C44	1.145(4)	C15	C20	1.411(4)
N6	C92	1.142(4)	C20	C19	1.395(4)
N4	C48	1.144(4)	C92	C91	1.465(5)
N8	C96	1.140(4)	C72	C73	1.382(4)
C54	C49	1.403(4)	C72	C95	1.512(4)
C54	C53	1.406(4)	C51	C52	1.387(4)
C13	C8	1.398(4)	C51	C50	1.388(5)
C13	C12	1.399(4)	C51	C89	1.518(5)
C25	C26	1.385(4)	C19	C21	1.522(4)
C25	C24	1.389(4)	C19	C18	1.389(5)
N3	C46	1.145(5)	C67	C69	1.515(4)
N5	C90	1.144(4)	C62	C60	1.532(4)
C68	C63	1.396(4)	C58	C91	1.522(5)
C68	C67	1.394(4)	C65	C64	1.387(4)
C75	C70	1.393(4)	C65	C93	1.520(5)
C75	C74	1.404(4)	C44	C43	1.465(5)
C6	C5	1.397(4)	C17	C18	1.386(4)
C6	C1	1.400(4)	C17	C45	1.514(5)
C9	C10	1.392(4)	C48	C47	1.466(5)
C9	C8	1.392(4)	C61	C60	1.403(4)
C66	C67	1.397(5)	C3	C41	1.516(5)
C66	C65	1.389(5)	C89	C90	1.465(5)
C10	C11	1.388(4)	C29	C30	1.503(5)
C10	C43	1.524(4)	C95	C96	1.474(5)
C4	C5	1.377(5)	C93	C94	1.464(5)

C4	C3	1.400(4)	C35	C36	1.505(5)
C5	C7	1.515(4)	C46	C45	1.470(5)
C49	C76	1.519(4)	C80	C81	1.505(5)
C49	C50	1.384(5)	C83	C84	1.503(5)
C70	C71	1.395(4)	C81	C82	1.521(5)
C70	C69	1.508(4)	N1	C42	1.148(5)
C26	C27	1.394(4)	C38	C39	1.508(5)
C26	C28	1.513(4)	C32	C33	1.518(5)
C53	C52	1.388(5)	C41	C42	1.462(5)
C53	C55	1.520(4)	C30	C31	1.523(5)
C14	C15	1.515(4)	N7	C94	1.150(5)
C14	C12	1.516(4)	C86	C87	1.514(5)
C1	C2	1.387(5)	C36	C37	1.531(5)
C1	C28	1.519(4)	C39	C40	1.520(5)
C8	C7	1.523(4)	C84	C85	1.527(5)
C59	C58	1.392(4)	C33	C34	1.522(5)
C59	C60	1.388(5)	C87	C88	1.524(5)
C11	C12	1.387(4)	C77	C78	1.445(6)
C22	C27	1.397(4)	C79	C78	1.503(6)

Table ES5 X-ray crystal structure determination detail of 1. Bond Angles for 1.

Atom	Atom	Atom	Angle/°	Atom	Atom	Atom	Angle/°
C68	O7	C83	113.2(2)	O3	C20	C19	118.9(3)
C6	O1	C29	113.1(2)	C19	C20	C15	120.9(3)
C75	O8	C86	116.9(2)	N6	C92	C91	179.0(4)
C61	O6	C80	115.3(2)	C26	C28	C1	109.5(3)
C54	O5	C77	114.6(3)	C71	C72	C95	119.8(3)
C20	O3	C35	114.8(2)	C73	C72	C71	119.1(3)
C13	O2	C32	115.5(2)	C73	C72	C95	121.0(3)
C27	O4	C38	115.7(2)	C52	C51	C50	119.0(3)
O5	C54	C49	119.9(3)	C52	C51	C89	121.5(3)
O5	C54	C53	119.2(3)	C50	C51	C89	119.5(3)
C49	C54	C53	120.8(3)	C20	C19	C21	122.4(3)
O2	C13	C8	119.9(3)	C18	C19	C20	118.6(3)
O2	C13	C12	118.3(3)	C18	C19	C21	119.0(3)
C8	C13	C12	121.4(3)	C72	C73	C74	121.8(3)
C26	C25	C24	121.1(3)	C24	C23	C22	121.5(3)
O7	C68	C63	119.4(3)	C68	C67	C66	118.1(3)
O7	C68	C67	118.9(3)	C68	C67	C69	121.1(3)
C67	C68	C63	121.4(3)	C66	C67	C69	120.7(3)
O8	C75	C70	117.9(3)	C63	C62	C60	109.5(2)
O8	C75	C74	120.5(3)	C49	C76	C74	109.6(3)
C70	C75	C74	121.2(3)	C13	C12	C14	119.6(3)
O1	C6	C5	119.6(3)	C11	C12	C13	118.5(3)
O1	C6	C1	119.4(3)	C11	C12	C14	121.8(3)
C5	C6	C1	120.9(3)	C59	C58	C91	120.0(3)
C8	C9	C10	121.1(3)	C57	C58	C59	119.4(3)
C65	C66	C67	121.1(3)	C57	C58	C91	120.5(3)
C9	C10	C43	119.7(3)	C22	C21	C19	109.3(3)
C11	C10	C9	119.3(3)	C5	C7	C8	109.5(2)
C11	C10	C43	120.9(3)	C66	C65	C93	121.3(3)
C5	C4	C3	120.9(3)	C64	C65	C66	119.5(3)
C6	C5	C7	121.0(3)	C64	C65	C93	119.2(3)
C4	C5	C6	119.2(3)	N2	C44	C43	179.1(4)
C4	C5	C7	119.6(3)	C16	C17	C45	121.1(3)

C54	C49	C76	122.6(3)	C18	C17	C16	118.7(3)
C50	C49	C54	118.6(3)	C18	C17	C45	120.2(3)
C50	C49	C76	118.8(3)	N4	C48	C47	179.1(4)
C75	C70	C71	118.8(3)	C51	C52	C53	121.5(3)
C75	C70	C69	119.3(3)	C56	C55	C53	111.5(3)
C71	C70	C69	121.4(3)	O6	C61	C56	118.0(3)
C25	C26	C27	118.7(3)	O6	C61	C60	121.1(3)
C25	C26	C28	121.3(3)	C60	C61	C56	120.5(3)
C27	C26	C28	119.3(3)	C4	C3	C41	119.5(3)
C54	C53	C55	121.6(3)	C2	C3	C4	118.9(3)
C52	C53	C54	118.3(3)	C2	C3	C41	121.6(3)
C52	C53	C55	120.1(3)	C70	C69	C67	109.2(2)
C15	C14	C12	111.7(3)	C17	C18	C19	121.7(3)
C6	C1	C28	120.2(3)	C49	C50	C51	121.5(3)
C2	C1	C6	118.4(3)	C90	C89	C51	111.7(3)
C2	C1	C28	121.2(3)	C44	C43	C10	112.9(3)
C13	C8	C7	120.6(3)	C59	C60	C62	120.7(3)
C9	C8	C13	118.2(3)	C59	C60	C61	119.0(3)
C9	C8	C7	120.7(3)	C61	C60	C62	119.7(3)
C60	C59	C58	120.9(3)	C63	C64	C65	120.9(3)
C12	C11	C10	121.2(3)	O1	C29	C30	107.7(3)
C27	C22	C21	120.3(3)	C96	C95	C72	112.7(3)
C23	C22	C27	117.7(3)	C94	C93	C65	110.5(3)
C23	C22	C21	121.4(3)	O3	C35	C36	112.8(3)
C68	C63	C62	121.2(3)	N5	C90	C89	179.1(4)
C64	C63	C68	118.9(3)	N3	C46	C45	178.4(4)
C64	C63	C62	119.7(3)	N8	C96	C95	179.4(4)
C56	C57	C58	121.2(3)	O6	C80	C81	113.4(3)
C70	C71	C72	120.8(3)	O7	C83	C84	108.4(3)
C57	C56	C55	121.8(3)	C80	C81	C82	110.8(3)
C57	C56	C61	118.7(3)	O4	C38	C39	113.4(3)
C61	C56	C55	119.4(3)	O2	C32	C33	112.8(3)
O4	C27	C26	118.8(3)	C42	C41	C3	111.2(3)
O4	C27	C22	119.2(3)	C29	C30	C31	113.8(3)
C26	C27	C22	121.7(3)	C46	C45	C17	111.9(3)
C3	C2	C1	121.6(3)	C92	C91	C58	112.8(3)
C15	C16	C17	121.7(3)	C48	C47	C24	111.9(3)
C25	C24	C23	119.1(3)	O8	C86	C87	113.1(3)
C25	C24	C47	120.0(3)	C35	C36	C37	111.2(3)
C23	C24	C47	120.9(3)	N1	C42	C41	177.6(4)
C75	C74	C76	120.4(3)	C38	C39	C40	112.2(3)
C73	C74	C75	118.0(3)	C83	C84	C85	114.1(3)
C73	C74	C76	121.0(3)	C32	C33	C34	110.3(3)
C16	C15	C14	119.8(3)	C86	C87	C88	114.7(3)
C16	C15	C20	118.2(3)	N7	C94	C93	176.3(4)
C20	C15	C14	121.9(3)	O5	C77	C78	113.3(4)
O3	C20	C15	120.1(3)	C77	C78	C79	115.5(4)

Table ES6 X-ray crystal structure determination detail of 1. Torsion angles for 1.

A	B	C	D	Angle/°	A	B	C	D	Angle/°
O7	C68	C63	C62	4.3(4)	C71	C72	C73	C74	4.4(5)
O7	C68	C63	C64	178.9(3)	C71	C72	C95	C96	-73.5(4)
O7	C68	C67	C66	-179.4(3)	C56	C57	C58	C59	-2.7(5)
O7	C68	C67	C69	-2.7(4)	C56	C57	C58	C91	-179.8(3)
O7	C83	C84	C85	63.4(4)	C56	C61	C60	C59	-5.7(5)
O1	C6	C5	C4	-179.2(3)	C56	C61	C60	C62	165.6(3)
O1	C6	C5	C7	-4.8(4)	C27	O4	C38	C39	87.0(3)
O1	C6	C1	C2	179.7(3)	C27	C26	C28	C1	-71.0(4)
O1	C6	C1	C28	4.7(4)	C27	C22	C23	C24	-0.3(5)
O1	C29	C30	C31	-64.9(3)	C27	C22	C21	C19	68.0(4)
O8	C75	C70	C71	179.6(3)	C2	C1	C28	C26	-45.7(4)
O8	C75	C70	C69	7.7(4)	C2	C3	C41	C42	-87.8(4)
O8	C75	C74	C73	-178.6(3)	C16	C15	C20	O3	-178.7(3)
O8	C75	C74	C76	-7.1(4)	C16	C15	C20	C19	3.8(4)
O8	C86	C87	C88	77.0(4)	C16	C17	C18	C19	2.9(5)
O6	C61	C60	C59	-179.1(3)	C16	C17	C45	C46	-124.9(3)
O6	C61	C60	C62	-7.8(5)	C24	C25	C26	C27	1.7(5)
O6	C80	C81	C82	178.8(3)	C24	C25	C26	C28	-168.7(3)
O5	C54	C49	C76	4.4(4)	C74	C75	C70	C71	6.6(5)
O5	C54	C49	C50	-177.6(3)	C74	C75	C70	C69	-165.3(3)
O5	C54	C53	C52	177.3(3)	C15	C14	C12	C13	-65.8(4)
O5	C54	C53	C55	-2.9(4)	C15	C14	C12	C11	110.2(3)
O5	C77	C78	C79	177.6(4)	C15	C16	C17	C18	-2.7(5)
O3	C20	C19	C21	-3.1(4)	C15	C16	C17	C45	176.7(3)
O3	C20	C19	C18	178.9(3)	C15	C20	C19	C21	174.4(3)
O3	C35	C36	C37	179.2(3)	C15	C20	C19	C18	-3.7(4)
O2	C13	C8	C9	178.7(3)	C20	O3	C35	C36	84.8(3)
O2	C13	C8	C7	6.3(4)	C20	C19	C21	C22	-118.8(3)
O2	C13	C12	C14	-2.1(4)	C20	C19	C18	C17	0.2(4)
O2	C13	C12	C11	-178.2(3)	C28	C26	C27	O4	-8.1(4)
O2	C32	C33	C34	179.1(3)	C28	C26	C27	C22	165.1(3)
O4	C38	C39	C40	174.2(3)	C28	C1	C2	C3	173.7(3)
C54	O5	C77	C78	126.3(4)	C73	C74	C76	C49	103.0(3)
C54	C49	C76	C74	116.0(3)	C73	C72	C95	C96	110.4(4)
C54	C49	C50	C51	-0.2(4)	C23	C22	C27	O4	178.0(3)
C54	C53	C52	C51	0.8(4)	C23	C22	C27	C26	4.8(5)
C54	C53	C55	C56	-121.4(3)	C23	C22	C21	C19	-103.3(3)
C13	O2	C32	C33	87.5(3)	C23	C24	C47	C48	-107.8(4)
C13	C8	C7	C5	60.0(4)	C67	C68	C63	C62	-170.1(3)
C25	C26	C27	O4	-178.7(3)	C67	C68	C63	C64	4.4(4)
C25	C26	C27	C22	-5.5(5)	C67	C66	C65	C64	0.7(5)
C25	C26	C28	C1	99.4(3)	C67	C66	C65	C93	-179.4(3)
C25	C24	C23	C22	-3.3(5)	C62	C63	C64	C65	173.4(3)
C25	C24	C47	C48	75.1(4)	C76	C49	C50	C51	177.9(3)
C68	O7	C83	C84	175.9(3)	C76	C74	C73	C72	-171.3(3)
C68	C63	C62	C60	121.3(3)	C12	C13	C8	C9	5.9(5)
C68	C63	C64	C65	-1.3(5)	C12	C13	C8	C7	-166.5(3)
C68	C67	C69	C70	-131.0(3)	C12	C14	C15	C16	-56.6(4)
C75	O8	C86	C87	-91.3(3)	C12	C14	C15	C20	120.6(3)
C75	C70	C71	C72	-1.9(5)	C58	C59	C60	C62	-169.1(3)
C75	C70	C69	C67	72.1(4)	C58	C59	C60	C61	2.1(5)
C75	C74	C73	C72	0.1(5)	C58	C57	C56	C55	175.9(3)

C75	C74	C76	C49	-68.2(4)	C58	C57	C56	C61	-0.8(5)
C6	O1	C29	C30	-176.8(2)	C21	C22	C27	O4	6.4(4)
C6	C5	C7	C8	-121.7(3)	C21	C22	C27	C26	-166.8(3)
C6	C1	C2	C3	-1.2(5)	C21	C22	C23	C24	171.2(3)
C6	C1	C28	C26	129.2(3)	C21	C19	C18	C17	-177.9(3)
C9	C10	C11	C12	2.4(5)	C65	C66	C67	C68	2.3(5)
C9	C10	C43	C44	-121.0(3)	C65	C66	C67	C69	-174.5(3)
C9	C8	C7	C5	-112.2(3)	C17	C16	C15	C14	176.7(3)
C66	C67	C69	C70	45.6(4)	C17	C16	C15	C20	-0.6(4)
C66	C65	C64	C63	-1.3(5)	C52	C53	C55	C56	58.4(4)
C66	C65	C93	C94	87.7(4)	C52	C51	C50	C49	-3.7(5)
C10	C9	C8	C13	-2.3(5)	C52	C51	C89	C90	128.1(3)
C10	C9	C8	C7	170.1(3)	C55	C53	C52	C51	-179.0(3)
C10	C11	C12	C13	1.1(5)	C55	C56	C61	O6	1.9(4)
C10	C11	C12	C14	-175.0(3)	C55	C56	C61	C60	-171.7(3)
C4	C5	C7	C8	52.7(4)	C61	O6	C80	C81	-84.9(3)
C4	C3	C41	C42	93.2(4)	C61	C56	C55	C53	67.4(4)
C5	C6	C1	C2	3.6(4)	C3	C4	C5	C6	0.1(5)
C5	C6	C1	C28	-171.4(3)	C3	C4	C5	C7	-174.4(3)
C5	C4	C3	C2	2.2(5)	C69	C70	C71	C72	169.9(3)
C5	C4	C3	C41	-178.7(3)	C18	C19	C21	C22	59.2(4)
C49	C54	C53	C52	-4.8(4)	C18	C17	C45	C46	54.6(4)
C49	C54	C53	C55	175.0(3)	C50	C49	C76	C74	-61.9(4)
C70	C75	C74	C73	-5.7(5)	C50	C51	C52	C53	3.4(5)
C70	C75	C74	C76	165.7(3)	C50	C51	C89	C90	-51.4(4)
C70	C71	C72	C73	-3.5(5)	C89	C51	C52	C53	-176.1(3)
C70	C71	C72	C95	-179.7(3)	C89	C51	C50	C49	175.7(3)
C26	C25	C24	C23	2.6(5)	C43	C10	C11	C12	178.8(3)
C26	C25	C24	C47	179.7(3)	C60	C59	C58	C57	2.0(5)
C53	C54	C49	C76	-173.5(3)	C60	C59	C58	C91	179.1(3)
C53	C54	C49	C50	4.5(4)	C64	C63	C62	C60	-53.2(4)
C14	C15	C20	O3	4.1(4)	C64	C65	C93	C94	-92.4(4)
C14	C15	C20	C19	-173.4(3)	C29	O1	C6	C5	-94.3(3)
C1	C6	C5	C4	-3.0(4)	C29	O1	C6	C1	89.5(3)
C1	C6	C5	C7	171.4(3)	C95	C72	C73	C74	-179.5(3)
C1	C2	C3	C4	-1.6(5)	C93	C65	C64	C63	178.9(3)
C1	C2	C3	C41	179.3(3)	C35	O3	C20	C15	77.5(3)
C8	C13	C12	C14	170.9(3)	C35	O3	C20	C19	-105.0(3)
C8	C13	C12	C11	-5.3(5)	C80	O6	C61	C56	113.2(3)
C8	C9	C10	C11	-1.7(5)	C80	O6	C61	C60	-73.2(4)
C8	C9	C10	C43	-178.2(3)	C83	O7	C68	C63	95.3(3)
C59	C58	C91	C92	118.5(3)	C83	O7	C68	C67	-90.1(3)
C11	C10	C43	C44	62.6(4)	C38	O4	C27	C26	-106.5(3)
C63	C68	C67	C66	-4.9(4)	C38	O4	C27	C22	80.2(4)
C63	C68	C67	C69	171.8(3)	C32	O2	C13	C8	75.0(4)
C63	C62	C60	C59	111.5(3)	C32	O2	C13	C12	-112.0(3)
C63	C62	C60	C61	-59.6(4)	C45	C17	C18	C19	-176.5(3)
C57	C56	C55	C53	-109.2(3)	C47	C24	C23	C22	179.6(3)
C57	C56	C61	O6	178.7(3)	C86	O8	C75	C70	114.3(3)
C57	C56	C61	C60	5.0(5)	C86	O8	C75	C74	-72.6(4)
C57	C58	C91	C92	-64.5(4)	C77	O5	C54	C49	81.0(4)
C71	C70	C69	C67	-99.6(3)	C77	O5	C54	C53	-101.1(3)

Table ES7 X-ray crystal structure determination detail of 1. Hydrogen atom coordinates ($\text{\AA}\times 10^4$) and isotropic displacement parameters ($\text{\AA}^2\times 10^3$) for **1**.

Atom	x	y	z	U(eq)
H25	6284	11885	2809	26
H9	7515	5589	4012	24
H66	-362	5172	3722	26
H4	6742	7537	4272	25
H14A	5195	6315	2107	26
H14B	4439	5766	2742	26
H59	-1870	592	4027	26
H11	5046	4899	3624	25
H57	859	-74	3691	27
H71	155	6873	2865	24
H2	6221	10178	3693	26
H16	4082	6749	3824	26
H28A	7645	10969	2518	25
H28B	7670	10286	1957	25
H73	2866	6170	2555	25
H23	3801	11174	2455	26
H62A	-1801	2257	2675	26
H62B	-2356	1969	3466	26
H76A	2846	4465	1538	24
H76B	3429	4854	2027	24
H21A	4533	9453	1455	26
H21B	3615	9839	1925	26
H7A	8364	6964	3465	25
H7B	8344	7253	2669	25
H52	1702	1753	3893	26
H55A	1715	1335	2165	27
H55B	2047	779	2804	27
H69A	-621	5285	1969	24
H69B	-987	5963	2529	24
H18	3565	9391	3276	25
H50	2626	4382	3356	25
H89A	1709	3553	4667	33
H89B	2079	2534	4758	33
H43A	6677	4330	4702	30
H43B	5562	4402	4831	30
H64	-1306	2547	4305	26
H29A	9530	8731	2558	29
H29B	9264	9772	2355	29
H95A	1299	7458	3518	31
H95B	2394	7403	3169	31
H93A	-452	3232	5003	35
H93B	-29	4258	4773	35
H35A	3906	6857	1610	31
H35B	4639	7088	876	31
H80A	-194	2852	1481	31
H80B	-765	1924	1848	31
H83A	-2472	4784	2334	30
H83B	-2886	3750	2524	30
H81A	589	1083	1461	33
H81B	1147	2016	1083	33
H38A	5967	9920	840	32

H38B	6424	8937	870	32
H32A	7852	6902	1819	30
H32B	7559	7865	1475	30
H41A	5173	9271	4724	33
H41B	5430	8241	4959	33
H30A	10511	9431	1485	32
H30B	9605	9551	1172	32
H45A	3234	7556	4692	36
H45B	3637	8587	4581	36
H91A	-446	-598	4865	32
H91B	-1479	-655	4738	32
H47A	3850	12403	3093	29
H47B	4722	12490	3435	29
H86A	1442	3897	939	31
H86B	1914	4881	914	31
H31A	10444	8265	814	44
H31B	9414	7950	1265	44
H31C	10296	7814	1605	44
H36A	3898	8488	669	38
H36B	3158	8244	1400	38
H39A	7878	9661	887	40
H39B	7406	10631	782	40
H84A	-2016	4587	1152	37
H84B	-3127	4455	1444	37
H33A	6430	7099	1051	35
H33B	6740	6136	1387	35
H87A	8	4700	849	35
H87B	835	4781	162	35
H82A	574	1272	281	53
H82B	107	2246	344	53
H82C	-477	1331	730	53
H88A	218	6222	269	50
H88B	1263	6257	377	50
H88C	385	6176	1032	50
H85A	-2565	3312	754	52
H85B	-2986	2844	1534	52
H85C	-1874	2978	1240	52
H37A	3329	7168	292	63
H37B	2517	7881	475	63
H37C	2557	6983	1011	63
H34A	7504	6428	197	68
H34B	8267	6389	652	68
H34C	7965	7355	319	68
H40A	8272	10319	-294	63
H40B	7184	10303	-302	63
H40C	7710	9363	-199	63
H77A	3745	2621	1608	49
H77B	3555	3232	937	49
H79A	4537	2216	116	78
H79B	4351	1136	331	78
H79C	4814	1712	794	78
H78A	2957	1944	626	66
H78B	3193	1343	1284	66

Table ES8 X-ray crystal structure determination detail of 1. Solvent masks information for 1.

Number	X	Y	Z	Volume	Electron count	Content
1	0.500	0.500	0.000	180.6	43.0	-

Table ES9 Characteristic values of the surface pressure-area compression isotherm of 1.

Sample	A_0 ($\text{\AA}^2 \text{ molecule}^{-1}$)	A_{lim} ($\text{\AA}^2 \text{ molecule}^{-1}$)	A_c ($\text{\AA}^2 \text{ molecule}^{-1}$)	Π_c (mN m^{-1})
Monolayer on pure water	103	90	80	28

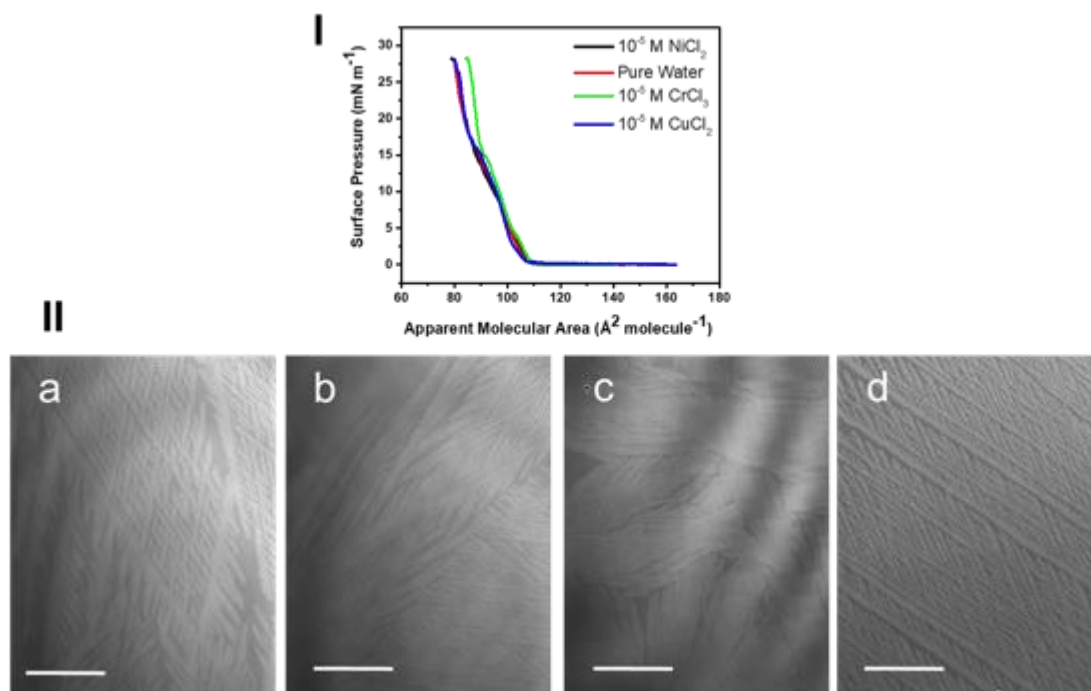


Figure ES3 Interfacial properties of the monolayer of 1 in the presence of transition metal ions in the subphase. (I) Surface pressure-area compression isotherms of 1 on a 10 μM NiCl₂ (black), CrCl₃ (green), CuCl₂ (blue) and pure water (red). 10 μM concentration of the salt solutions was chosen based on our recent results on the formation of metal-organic coordination network of calix[4]arene [9]. The isotherms show no difference in the take-off values of the monolayer of 1 in the presence of ions. (II), BAM images of the monolayer of 1 formed at the interface of a 10 μM (a) NiCl₂, (b) CrCl₃, (c) CuCl₂ and (d) pure water at π : 20 mN m^{-1} were shown.

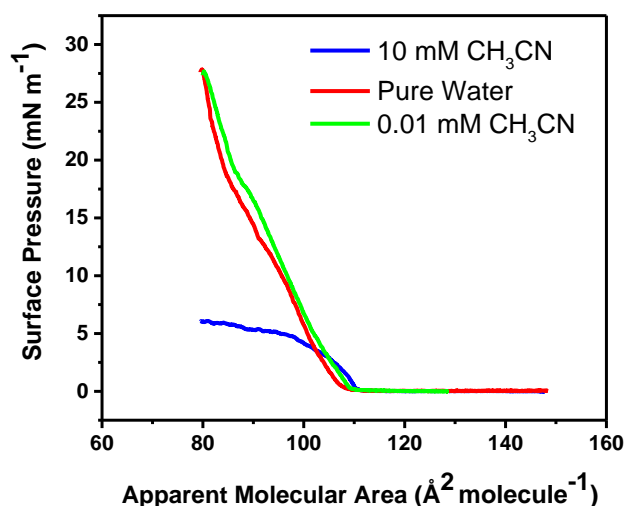
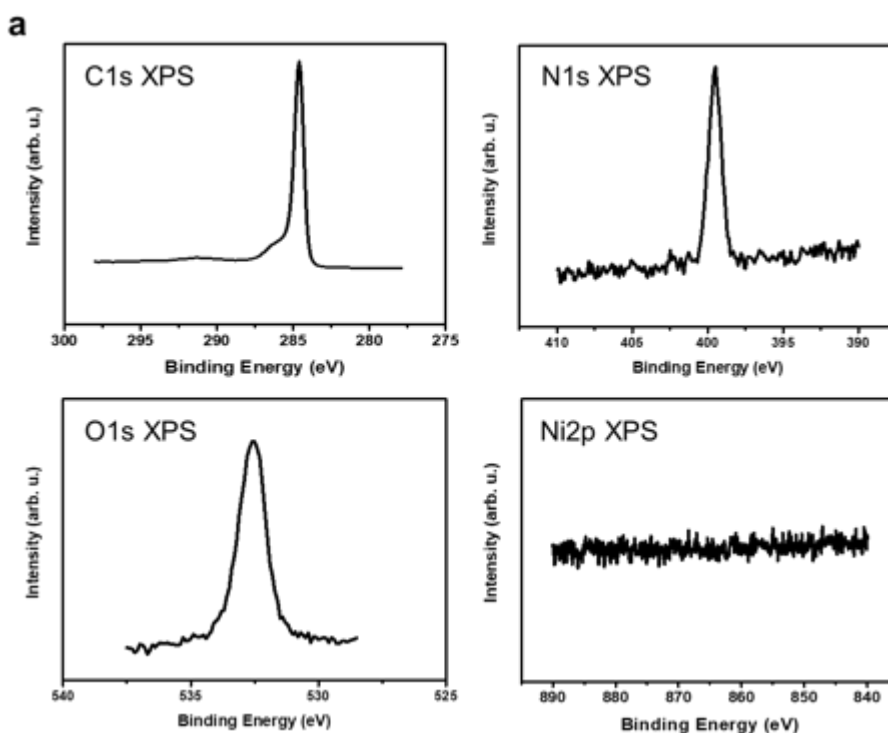
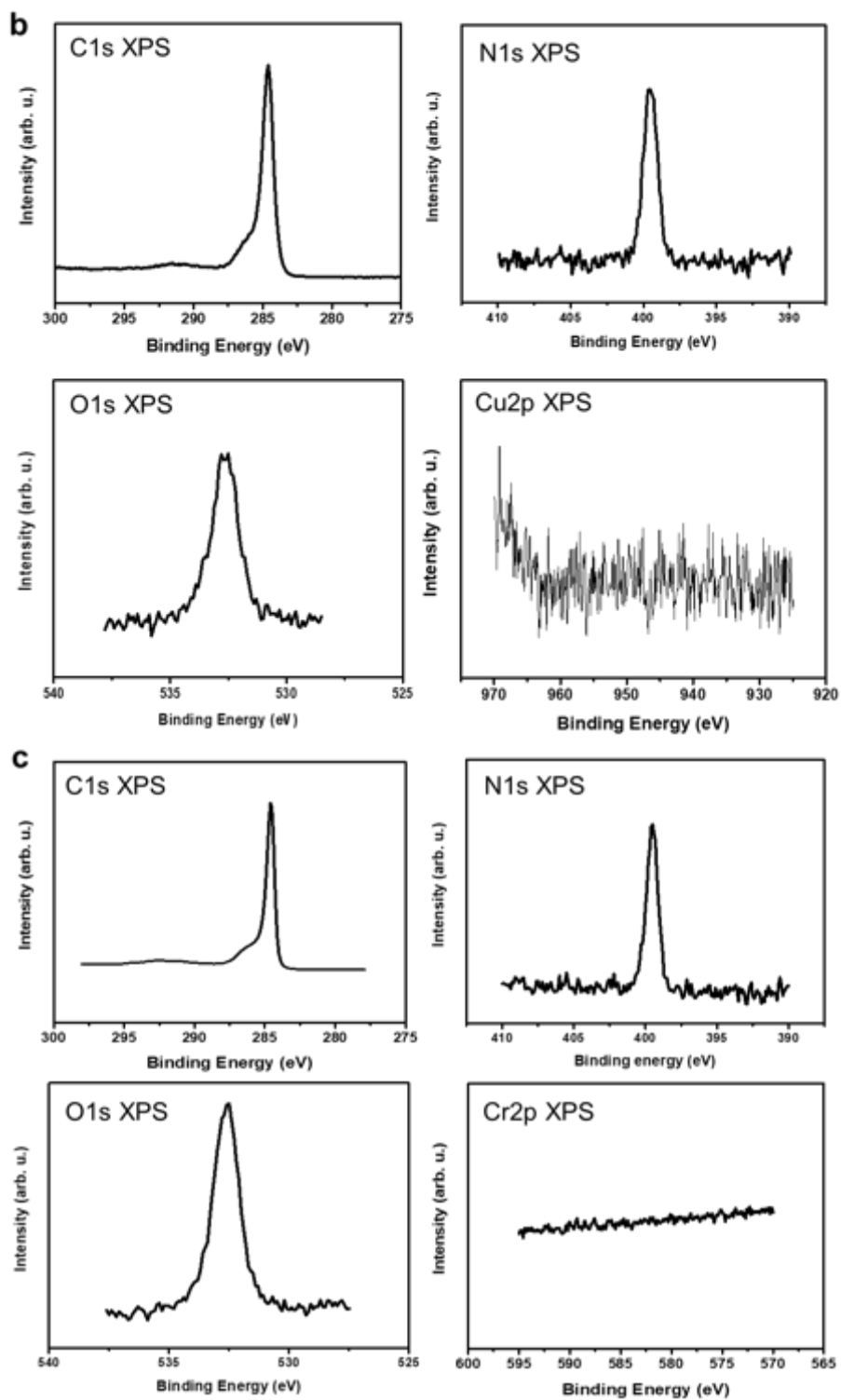


Figure ES4 Interfacial properties of the monolayer of **1** in the presence of ACN molecules as competitors with the CN functional groups of **1** for dipole-dipole interactions. Surface pressure-area compression isotherms of **1** on 0.01 and 10 mM CH₃CN solutions, compared to pure water subphase.

Table ES10 Contact Angle Measurements on the Monolayer of **1** transferred from the air-water interface onto HOPG. HOPG was considered as reference sample.

Sample	Contact Angle (°)
HOPG (reference sample)	98.8 ± 6
Monolayer of 1 transferred from pure water onto HOPG	80 ± 5





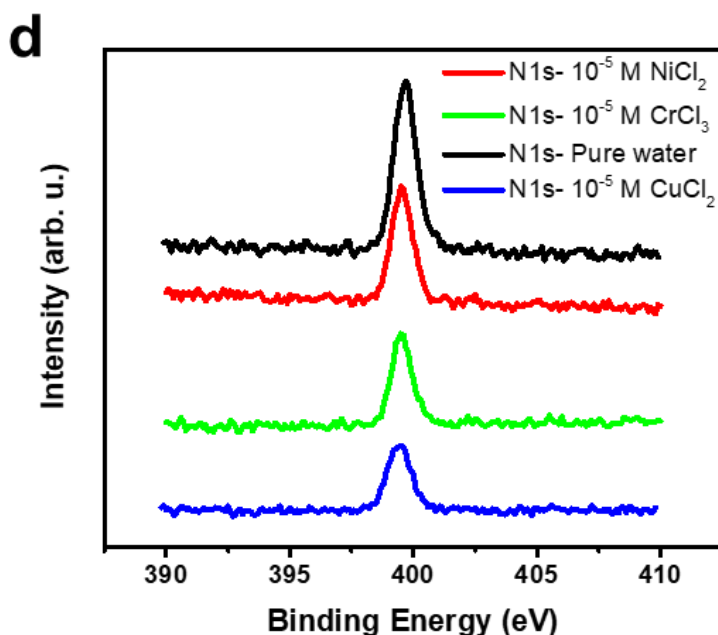


Figure ES5 Surface analysis of the monolayer of 1 in the presence of transition metal ions in the subphase. XP spectra of the monolayer of 1 transferred onto HOPG by the LS method for C1s, N1s and O1s peaks from a $10\ \mu\text{M}$ (a) NiCl_2 , (b) CuCl_2 and (c) CrCl_3 . Nitrogen XP spectra of the monolayer of 1 show one peak at 399.7 eV that is the characteristic feature of N in the CN functional group [14]. (d) There is no change in the N1s spectra of the transferred layer from different aqueous solutions onto HOPG. The absence of ions *i.e.* Ni^{2+} , Cu^{2+} and Cr^{3+} in the transferred layer confirms that the building units of 1 have a high tendency to interact with one another rather than metallic ions. Indeed, introducing the ions in the subphase cannot disturb the self-assembled network of 1 through dipole-dipole interaction.

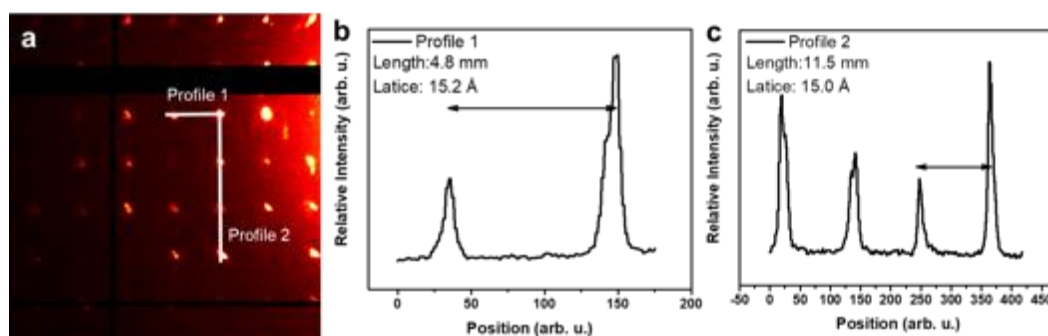


Figure ES7 Diffraction analysis of the free-standing monolayer of 1 by means of high-resolution cryo-TEM. (a) Zoomed image of the TEM electron diffraction pattern of the free-standing monolayer of 1. The diffraction pattern confirms the square packing structure of the crystalline layer. (b & c) The profile lines across the diffraction pattern, showing a unit cell size of $\sim 15\ \text{\AA}$.

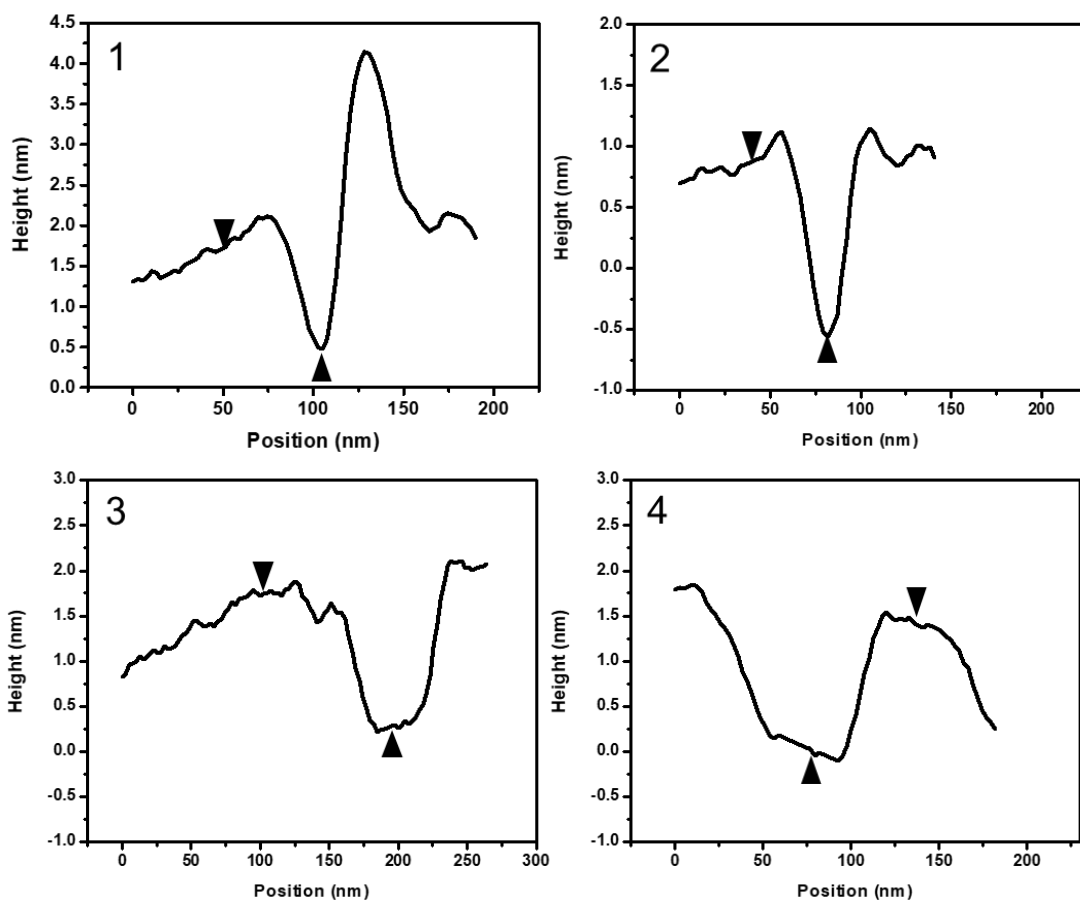
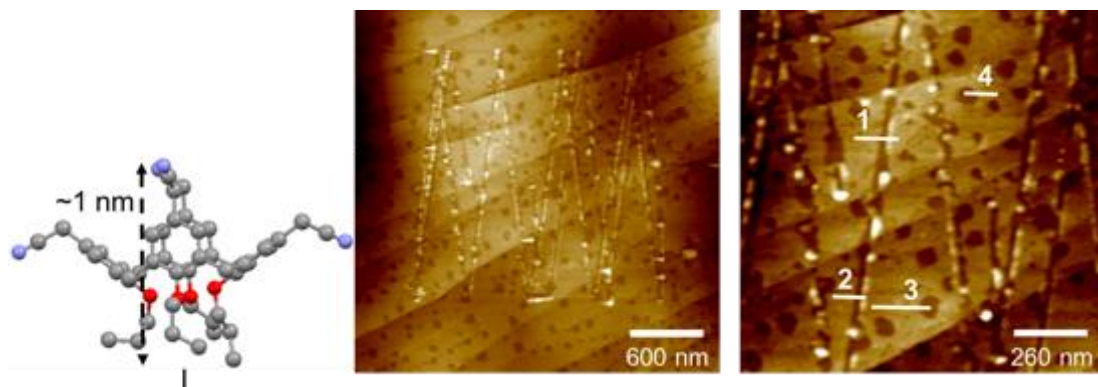


Figure ES6 AFM height analysis of the transferred monolayer of 1 from pure water subphase onto HOPG by the LS method. Height analysis of the monolayer of 1 was carried out in intentionally scratched layer (line profiles of 1 and 2) and on partially covered HOPG by the monolayer of 1 (line profiles of 3 and 4). The lines in the AFM images indicate where the height profiles were recorded. The AFM results confirmed the presence of a monomolecular layer of 1 with a height of 1.0 ± 0.4 nm. The measured height using AFM images is in a good agreement with the expected height of 1, derived from its crystalline structure (1.1 nm) (I). The deviation from 1.1 nm could originate from the ambient-condition AFM experiments [6] and also partially rearrangement of molecules because of water evaporation.